University of Sheffield

Department of Mechanical Engineering

Numerical Study of Trailing Edge Flow Control for Horizontal Axis Wind Turbines

by

Hao Chen

Supervised by Prof. N. Qin

This thesis is submitted to the University of Sheffield in partial fulfillment of the requirement for the degree of Doctor of Philosophy

June 2016

Abstract

Wind turbines have been developed for more than a century and nowadays wind turbines are still facing some challenges such as efficiency and maintenance problems. Load control is considered to be one of the most important parts for future horizontal axis wind turbine (HAWT) designs. Deploying effective flow control devices on the blades could either increase loads at off-design wind speed conditions or reduce the extreme loads, leading to either higher energy output or a more stable energy output from the wind turbine. This study reports a research into the performance of trailing edge flow control devices of HAWT by solving the Reynolds averaged Navier-Stokes equations. The validation case selected for this work is the NREL Phase VI blade with experimental data. The trailing edge flow control devices studied include microtabs and microjets installed near the trailing edge of the rotating blade. The divergent trailing edge is also included in the study as a passive flow control device due to its practical interest. These trailing edge devices are implemented on the fixed-pitch NREL Phase VI blade, using the original performance and flow characteristics as a benchmark. Both 2D and 3D simulations are carried out in order to investigate the suitability of the 2D blade sectional design analysis and control for the actual 3D rotating framework. Moreover, the study is extended to an active pitch-regulated offshore wind turbine, NREW 5MW wind turbine. Firstly the code to code comparison is carried out for validation purpose. Then the trailing edge flow control devices are also deployed on this wind turbine to find out their effectiveness. The results show there are significant differences when compared to the conclusions from the CFD study on the NREL Phase VI blade.

Acknowledgements

I want to express my sincere appreciation to my supervisor Professor Ning. Qin who gave me a lot of guidance in academic and personal suggestions for my research. I also strongly appreciate for his understanding and support during my second year of the PhD study when I faced some family difficulties during that time. Undoubtedly I would not be able to finish my PhD research without the support from him.

I would also like to thank my family (my wife, my new born daughter, my parents and my sister) who stand beside me and encourage me to finish my research. Their understanding and endless love is the biggest motivation to me.

Finally I want to thank my second supervisor Yang Zhang and all the colleagues in the aerodynamic group in the University of Sheffield (Zhaolin Chen, Wei Wang, Spiridon Siouris, Feng Zhu, Sheng Liu, Veronica Palma Gonzalez Garcia, Benjamin Hinchliffe, Guglielmo Vivarelli, Gabriele Luigi Mura, Raybin Yu and Feng Xie). Especially for Zhaolin Chen who gave me a lot of support at the beginning of my research when I faced some CFD difficulties.

Contents

Nomenclature

A	=	Swipe area of the wind turbine (m^2)
c	=	Chord length of the 2D Cross-sectional aerofoil
C_l	=	Lift coefficient, $C_l = L/(0.5\rho U_\infty^2 S_{ref})$
C_d	=	Drag coefficient, $C_d = D/(0.5\rho U_\infty^2 S_{ref})$
C_{power}	=	Power coefficient = $P/(0.5\rho U^3 A)$
C_p	=	Pressure coefficient, $C_p = (p - p_\infty)/(0.5\rho U_\infty^2)$
D	=	Drag force
$F_{effective}$	=	Target force at the rotational direction of the 2D cross-sectional aerofoil
L	=	Lift force
M_T	=	Momentum of the wind turbine in rotational direction, Nm
P	=	Power output of the wind turbine (MW)
r	=	Radial spanwise position of the aerofoil, m
R	=	Wind turbine blade radius
Re	=	Reynolds number, $Re = \rho U_\infty L/\mu$
T	=	Wind turbine Thrust (right to the rotational direction), N
U_∞	=	wind speed, m/s
U_r	=	Relative free stream wind speed
x	=	Chord position to the leading edge of the aerofoil
y^+	=	Nondimensional cell wall distance, $y^+ = \rho u_\tau y/\mu$

Greek Symbol

α	=	Angle of attack (AOA), °
β	=	Blade pitch angle, °
ϕ	=	Cross-sectional aerofoil twist angle
ω	=	Wind turbine rotational speed, rad/s
μ	=	Fluid viscosity, this study uses $\mu = 1.983 \times 10^5 Pa \cdot s$
ρ	=	Air density, this study uses $\rho = 1.225 kg/m^3$

Acronyms

2D	=	Two dimensional
3D	=	Three dimensional
CFD	=	Computational fluid dynamics
HAWT	=	Horizontal axis wind turbine
VAWT	=	Vertical axis wind turbine
NREL	=	National Renewable Energy Laboratory
GF	=	Gurney flap
DTE	=	Divergent trailing edge
TSR	=	Tip speed ratio of the wind turbine blade: $\lambda = \frac{\Omega \mathrm{R}}{U_\infty}$
TE	=	Trailing Edge

List of Tables

List of Figures

Chapter 1 Introduction

Energy has become the most important part in modern society. It exists in lots of forms such as electrical, chemical, heat, kinetic and so on. Nowadays fossil fuel is still the main energy source for human consumption but it is non-renewable and unsustainable. Therefore, in the recent years, scientists and engineers are devoting a lot of efforts in developing renewable energy technologies, such as bio-energy, solar energy, wind energy, tidal energy, geothermal energy and wave energy. Wind energy has some obvious advantages when compared to other renewable energies due to its huge reserves and it is wide spread and availability.

1.1 Wind Energy Today

Wind energy is holding a more and more important position in the world's energy consumption year after year. Wind turbine, which is the machine converting the wind energy to usable electric power, has been developed for more than a century. The first man who transferred the wind energy into electricity was James Blyth in 1887. In 1931 the French aeronautical engineer George Darrieus first used aerofoils to create rotation which pioneered the wind turbine design. Since then the wind turbine design has attracted the attention of engineers, who promoted the development of the modern wind turbines. In the past few decades wind energy has been developed significantly in the world because of the energy crisis and governmental policy.

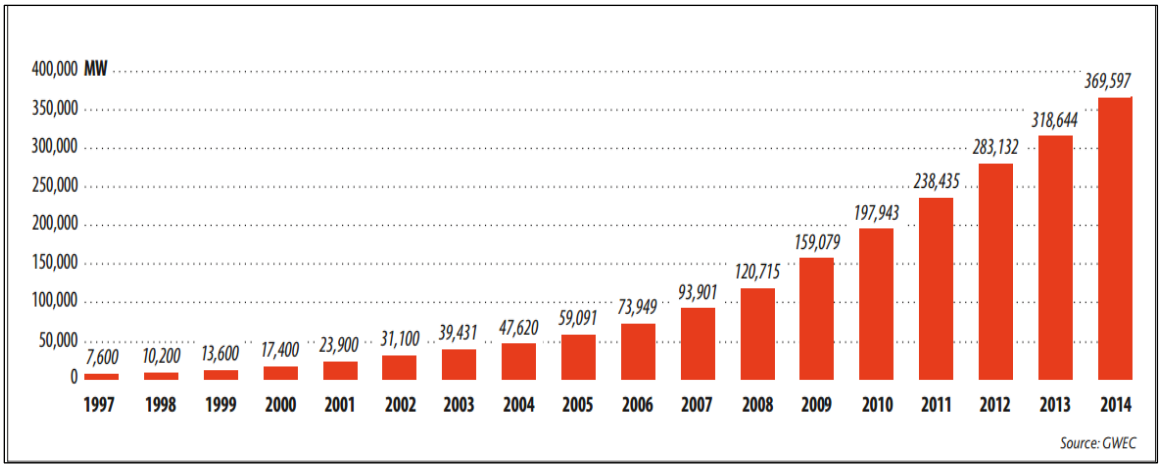

Figure 1. Global Cumulative Installed Wind Energy Production 1996-2014.

(Source from Global Wind Report 2014 by GWEC)

Figure 1 shows the outstanding development of the wind capacity in the world from 1996 to 2014. However there is still huge potential to explore more wind energy all over the world. According to the analysis from Lu et al. (2009) a network of land-based 2.5 MW wind turbines can supply more than five times of the total use of energy worldwide.

According to Table 1, China is the country with the biggest wind energy production at the moment. However, because of the huge electricity demand the wind-generated electricity only accounted for 2.78% of the country's total electricity output which was 153.4 billion kWh last year. It is significant to mention that there are six European countries in the top ten wind energy list.

Country	MW	% SHARE
PR China	23,196	45.1
Germany	5,279	10.2
USA	4,854	9.4
Brazil*	2,472	4.8
India	2,315	4.5
Canada	1,871	3.6
United Kingdom	1,736	3.4
Sweden	1,050	2.0
France	1,042	2.0
Turkey	804	1.6
Rest of the world	6,852	13.3
Total TOP 10	**44,620**	**87**
World Total	**51,473**	**100**

Table 1. Top 10 cumulative wind power production countries in the world

(Source from Global wind report 2014 by GWEC)

The United Kingdom has the best wind resources in Europe because of its long exposed coastlines and low mountain ranges. The UK installed 1,736 MW wind energy in 2014 which consisting of 813MW offshore and 924MW on shore wind energy. In December of 2014, the wind power contributed 14% of the national electricity consumption which was a new record and very close to the target ratio in 2020. The UK's government set up the Renewable Obligation (RO) to legally require the British electricity suppliers to provide a proportion of their sales from renewable energy such as wind power or they will be penalized (ofgem.gov.uk). With the

governmental support and huge wind resources, the UK is expected to have more than 28,000 MW in 2020 which secure 15% of the national energy consumption (Jowit, 2012).

1.2 Modern Wind Turbines

1.2.1 HAWTs and VAWTs

A wind turbine is a tool that in used to transform wind energy into electricity and it can be divided into two categories based on different constructions: vertical axis wind turbines and horizontal axis wind turbines (Figures 2). Nowadays HAWTs are the main type of wind turbines which are commercially manufactured around the world for generating wind energy. The reasons for this are: 1) the power coefficient of HAWT is considered higher than that for VAWT; 2) the rotor of HAWT is operated in the high Atmospheric Boundary Layer which can access higher wind speeds; 3) the size of HAWT can be very large (the diameter can be more than 120m so far) and its mechanical behaviour is more stable.

The modern HAWT's aerodynamic driving force is mainly a force in the direction of torque generated from the wind turbine blades. Nowadays some specific aerofoils are used as the blade's cross section in order to get a better C_l/C_d ratio, resulting in larger force in the direction of rotation. The working principle of the HAWT will be introduced in Chapter 2.

Figure 2. On-shore HAWTs (left) and a typical VAWT (right).

(Picture from: http://www.windenergyplanning.com/)

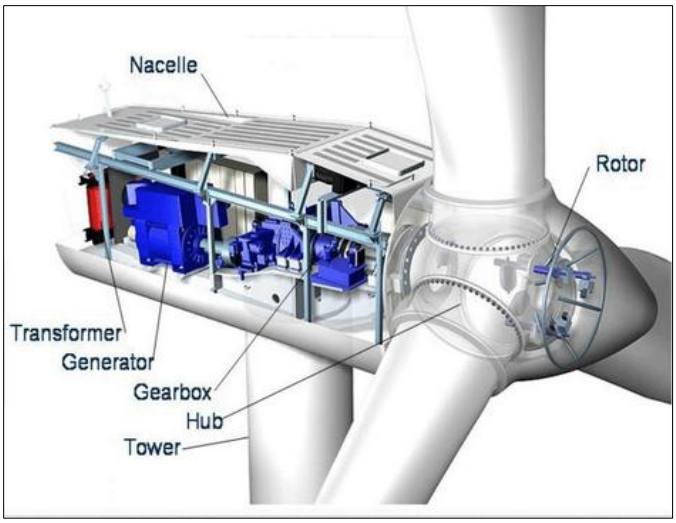

Figure 3. Components of HAWT. (Source from: http://www.windpoweralternators.co.uk)

A HAWT consists of some fundamental components as follows (Figure 3):

1. The rotor. It includes blades and hub of the wind turbine which is the most important part because it is the determinant of the development of the wind turbine's performance;

2. The drive train. It includes shafts, gearbox, brake system and generator. This part of HAWT is mainly used for transferring the mechanical power from the low-speed shaft to a high-speed shaft which leading to a suitable angular velocity to drive a generator and produce electricity.

3. Nacelle. This is the housing of the drive train and it can control the wind turbine's yaw angle.

4. Tower and foundation. Typically, the ratio between rotor diameter and tower height is 1 to 1.5 and it is also dependent on the local geography and weather conditions.

5. Control system. This part is mainly used for power control and wind turbine protection.

1.2.2 The Development of HAWTs

The technology of HAWTs, including both aerodynamically and electrically, has been developed for some decades. The capacity of a single HAWT has been developed significantly and the largest HAWT reaches a tip height of 220m (V164-8.0-MW prototype). Figure 4 shows that the size of HAWTs grows rapidly in recent years and from IPCC's prediction, the tip height of HAWT could grow to 300m and with a 250m diameter.

With the much higher power output of large HAWTs, the load control of the wind turbine is becoming more and more significant for both electrical requirement and wind turbine maintenance. Smaller wind turbines were mostly stall-controlled wind turbines and these wind turbines do not avoid stall and are commonly with a constant rotational speed. The stall-controlled wind turbines are small and easily controlled in their working wind speed range, however the power output of this type of HAWT is relatively small and the C_P is quite low out of the rated wind speed. For example, the NREL Phase VI wind turbine studied in the present work. Modern large HAWTs, especially for offshore HAWTs, are mostly with variable-speed and variable-pitch control system. This type of HAWT normally changes its rotational speed and pitch angle to fit the wind speed for the optimal AOA to reach the maximum C_P before the rated wind speed. Then if the wind speed exceeds the rated wind speed, the wind turbine would change its pitch angle to maintain its power output at a stable level. Hansen and Hansen (2007) classified the modern HAWTs into four types: fixed speed wind turbines, variable speed wind turbine concept with variable rotor resistance, variable speed wind turbine concept with partial-scale frequency converter and variable speed concept with full-scale frequency converter. The details including the differences of the gearbox among these types of HAWTs will not be presented here as this PhD study is mainly about the aerodynamics and flow control of the HAWTs.

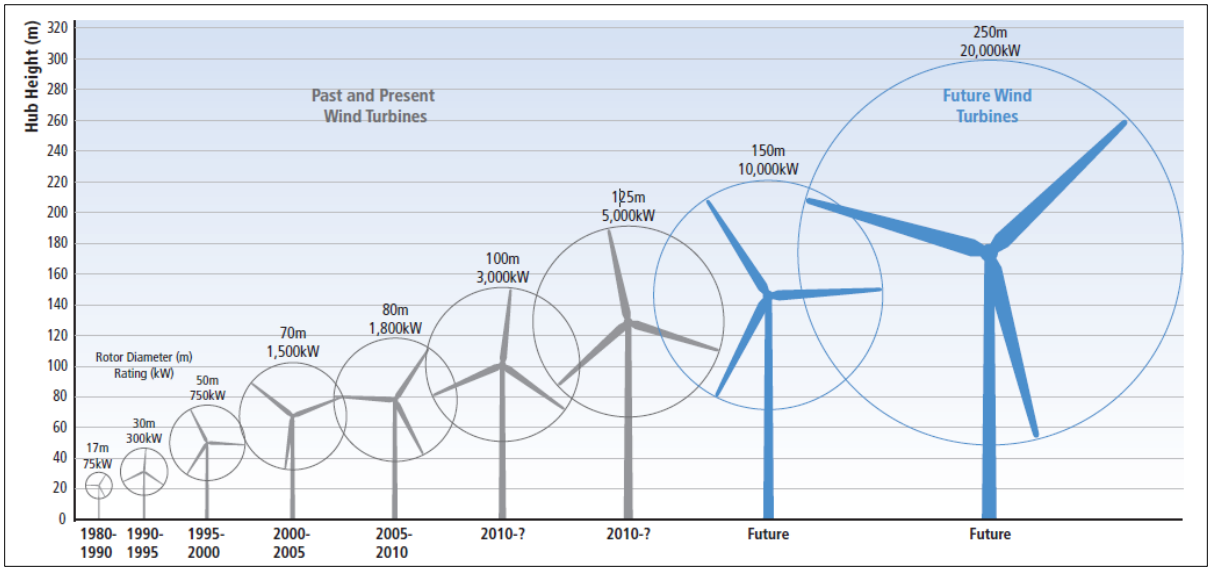

Figure 4. Development history of the size of HAWTs. (Source from IPCC 2011 report)

1.3 Motivation and Objectives

Improving the aerodynamic performance of the wind turbine blade is one of the most significant factors to maximize the efficiency of transforming wind energy into mechanical energy. Furthermore, load control is also important for the aerodynamic design and protection for HAWTs. Therefore flow control can play a significant role in both improving the aerodynamic performance and load alleviation for modern HAWTs.

So far the research work relative to this area has gained great achievements and as a result the efficiency has been improved to be nearly 50% today. CFD played an important and effective role in researching the flow around and downstream of a wind turbine, which is relatively cheaper than wind tunnel testing and provides more reliable results than analytical and semi-empirical models (Sørensen and Shen, 2002).

The comparison between CFD and experiments can be seen clearly in the following table.

Table 2. Comparison between CFD simulations and experiments

Experiments	**CFD**
1. For one quantity at a time	1. For all desire quantities
2. The points and time instants are limited	2. High resolution in space and time
3. For a laboratory-scale mode	3. For actual flow domain
4. The operating conditions and problems are in a limited range	4. Can simulate any problem and operating condition virtually
5. Error sources: measurement errors, flow disturbances by the probes	5. Error sources: modelling, discretization, iteration, turbulence model, implementation

However, the results of a CFD simulation are not fully reliable because: 1) the input data may involve uncertainties; 2) the mathematical model of the problem may be inadequate; 3) the computational resources may lead to the limitation of the accuracy of the results. Therefore the validation of the employed CFD methodology is necessary with comparing the CFD results with the actual experimental results.

1.3.1 Motivation

As mentioned above, the power coefficient of some modern wind turbines can reach as high as 50% in a particular wind speed. However, the wind speed is changing all the time which leads to lower power coefficient in both lower and higher wind speeds. For instance, in the high wind speed condition, the wind turbine blade begins to stall which leading to immediate reduction of the power coefficient. Under such situation, many flow control devices including both passive and active devices were researched and tested for higher efficiency of the wind turbine under various wind speeds. According to the literature review in chapter 2, in the past few decades many flow control devices such as microtabs, vortex generators, synthetic jets and moving flaps at the trailing edge were proved to be effective to increase the performance of the wind turbine in some specified conditions.

Researchers investigated into deploying different flow control devices on the wind turbine blades in both experimental and numerical ways. However, as compared above, the experiments are only with specific conditions and rotor models. Therefore if the CFD simulation can be used properly with reliable results it will be significantly beneficial for further design and modelling of the wind turbine blade.

So far most the CFD studies on the flow control devices on wind turbine blades are limited to 2D cases because of the huge mesh generation work and computational time of 3D full-scale simulation. However the 2D simulation can just explain the performance of cross-sectional aerofoils. Since the 3D effects can be significant for wind turbine flow physics, 3D full-scale simulation is more reliable and realistic. Therefore with sufficient computational resources, the motivation and aim of this study is to model the 3D full-scale wind turbine blade in the rotating frame with flow control devices in order to further optimize the blade design and improve the efficiency or for load control of the wind turbines.

1.3.2 Objectives

CFD simulation as an effective tool for optimizing the design of the wind turbine blade, the first steps of the study are as follows:

1) Understanding how CFD works and its limitations. This includes the governing equations and turbulence models, for example why choosing $k-\omega\ SST$ turbulence model, why the wall y^+ is important for computation accuracy.

2) Mastering the methodology of how to generate a proper mesh for the specified geometry for the 3D simulation. ICEM CFD is selected as the mesh generation tool for all of the cases. It is significant to find out the criterion of good mesh and how to make the mesh capture the flow details of the case.

3) Understanding the theoretical details of ANSYS FLUENT and relevant settings. This includes many factors such as whether the flow is steady or unsteady, the boundary conditions, solvers and time steps.

4) Post processing of the results. After the computation it is necessary to process the results to get the figures and data. Using proper software is able to export helpful figures which showing the flow structure and important details of the cases. In this study most of the figures come from ANSYS CFD-POST and a few of them are from TECPLOT360.

After understanding the common methodology, the objectives of this study are as follows:

1) Carrying out a reasonable validation of the employed CFD method. This can be done by comparing the CFD results with the experimental results. So the NREL Phase VI wind turbine, which is a stall-regulated small wind turbine, is chosen because of its sufficient experimental data. Another validation case is the NREL 5MW offshore wind turbine with 126m diameter, which is designed from a BEM (Blade Element Momentum theory, will be introduced in chapter 2) code. However there is no experimental data for this wind turbine so only code to code comparison is carried out in the study.

2) Investigating different turbulence models. There are many turbulence models so far and which one can predict the most accurate result in the specified conditions in this case should be studied. This part also includes the steady or unsteady flow condition study.

3) Researching into the modern flow control devices of the wind turbine blade, for example, the microtabs in the trailing edge, microjets and vortex generators on the suction side and so on. Investigation involves what is the design process of these devices and how they work.

4) Carrying out 3D CFD simulations on the rotating wind turbine blade with deploying different kinds of flow control devices. This is the eventual objective of the study to see how to improve the efficiency or control the loads of the wind turbine in relatively lower or higher wind speed. A good effort will be needed for the mesh generation work in this part because the geometry of the wind turbine is complicated.

1.3.3 Innovations of the study

After reviewing the literatures, the possible innovations of the PhD study are as follows:

1. Most of the existing CFD study on wind turbines underestimated the power coefficient when the stall happens under high wind speed using RANS turbulence modelling. Some researches using DES turbulence modelling can more accurately predict the torque of the wind turbine; however the utilized mesh size was huge such as Li el al. (2012). The mesh of this CFD simulation had more than 57 million grid points which was impossible to compute in most of the universities or companies. In this study a relatively coarser mesh (less than 4 million grid points) was employed in ANSYS FLUENT using the $k-\omega\ SST$ turbulence model and results show that with a good mesh and a proper unsteady RANS solution the CFD is still able to accurately predict the mechanic torque of the small stall-regulated wind turbine in higher wind speed where the stall is dominating on the suction side of the blade.

2. According to the literature review, so far there are still rare researches on the 3D full-scale wind turbine CFD modelling with different kind of flow control devices. 2D CFD studies or sectional span CFD studies and relevant experiments showed that (see chapter 2) some flow control devices including both passive and active devices such as microtabs, microjets and vortex generators can improve the wind turbine's efficiency in particular wind speeds. This PhD study will focus on the 3D full-scale CFD simulation of wind turbine with deploying different kind of flow control devices in various wind speeds to see how the wind turbine's performance change with the particular devices. Such simulations are more realistic than 2D CFD simulation. Moreover, when compared to the experimental researches, the CFD simulation can test different flow control devices and more flow conditions.

3. Other than the flow control devices, some innovative aerofoil design such the divergent trailing edge design proposed by Henne and Gregg (1991) or flatback aerofoils. These types of aerofoils can actually provide higher C_l than sharp trailing edge aerofoils however due to much higher

induced C_d they are not suitable for aircrafts or aerospace applications. For wind turbines, the torque and bending moment are the most important factors to be concerned in the design process. Therefore investigating and comparing the performance of these aerofoil designs on the wind turbine in 3D rotating frame is another novel aspect in this study.

Chapter 2 Literature Review: Aerodynamics of HAWTs and Relevant Flow Control Devices

This chapter firstly introduces the basic definition and equations of HAWTs including TSR, power coefficient, and sectional lift and drag forces. The numerical methodology and equations used for the CFD simulations are introduced in the second part. Lastly the literature reviews on the previous study on the flow control on HAWTs, including both numerical and experimental studies, are illustrated.

2.1 Basic Definitions and Equations

Tip speed ratio:

In the wind turbine design the tip speed ratio (TSR) is a very important parameter. It is the ratio between the blade tip speed and the wind speed which can be written as:

$$\lambda = \frac{\omega R}{U_\infty} \tag{2.1}$$

where λ is the TSR, ω is the wind turbine rotational angular velocity, R is the radius of the wind turbine disc and U_∞ is the absolute wind speed.

Power coefficient:

Theoretically the energy P_0 passing through a cross-section A per second is:

$$P_0 = \frac{1}{2}\rho {U_\infty}^3 A \tag{2.2}$$

where ρ is the air density, U_∞ is the wind speed and A is the cross-section area. Thus the power coefficient C_p which is the ratio between the actual power and the flow energy is:

$$C_P = \frac{P}{\frac{1}{2}\rho {U_\infty}^3 A} \tag{2.3}$$

According to Betz's limit (1966), the C_p has a maximum value of 16/27 = 0.593.

Lift and drag coefficients:

Lift and drag coefficients are the main characteristics of an aerofoil which can be calculated as:

$$C_l = \frac{\mathrm{L}}{\frac{1}{2}\rho \mathrm{U}^2 \mathrm{c}} \qquad C_d = \frac{\mathrm{D}}{\frac{1}{2}\rho \mathrm{U}^2 \mathrm{c}} \tag{2.4}$$

where c is the chord length, L is the lift force, D is the drag force and U is the relative flow speed around the aerofoil. In different span position of the wind turbine blade, the chord length, flow speed, angle of attack and Reynolds number are different, which are important to the wind turbine performance.

Pressure coefficient:

The pressure coefficient is a very important parameter to the aerofoil, and in many researches this parameter was used to validate the accuracy of the CFD simulation. The pressure coefficient can be calculated by the equation:

$$C_p = \frac{\mathrm{p} - p_\infty}{\frac{1}{2}\rho U^2} \tag{2.5}$$

where p is the surface pressure and p_∞ is the standard atmospheric pressure and U is the flow speed.

Blade Element Momentum (BEM) Theory:

The Blade Element Momentum (BEM) theory was developed by Betz and Glauert (1935) from Rankine and Froude's (1878) Actuator Disk theory. This theory combines blade element theory and momentum theory together. Practically, using BEM theory for wind turbine blade design is to divide the blade into finite elements along the span. In the rotational plane of the rotor, these elements will trace out annular regions across which the momentum balance takes place. Therefore with using existing 2D aerofoil data and the BEM theory it is able to predict the power output of the wind turbine. Nowadays many mainstream wind turbine design software are based on BEM theory because it can provide reasonably well results with short computing time. However its disadvantages are also obvious as: 1), it assumes the elements along the span work independently which ignoring the spanwise flow effects; 2), based on steady-state flow (non-turbulent); 3), ignoring the yaw effects of the blade; 4), requiring specific tip loss correction models for higher accuracy.

2.2 CFD Study on Wind Turbines

CFD enable us to solve the differential governing equations of fluid flows numerically with computers. As mentioned above, compared to experimental analysis CFD is much faster and cheaper but can also provide acceptable results if used properly.

In an integrated CFD study there are normally three steps which are preprocessor, flow solution and post-processing respectively. Preprocessor includes the computational domain setting and mesh generation. A good mesh is significant for getting good results. The flow solver is the core of a CFD study and most of the commercial CFD codes are based on a finite volume discretization such as ANSYS FLUENT which is used in this study. The post-processing work is for the analysis of solution results. There is some specific software for CFD post-processing such as CFD-POST and TECPLOT 360. With such software we can analysis different factors such as pressure, surface streamlines and so on.

The Unsteady/Reynolds-Averaged Navier-Stoke (URANS/RANS) methods is used for all the simulations in the present work as the LES (Large Eddy Simulation) and DNS (Direct Numerical Simulation) require huge computation time especially for the 3D simulations of wind turbines in this study. As for incompressible fluid solution, the pressure-based coupled solver is selected for all the simulations. Referring to the ANSYS FLUENT Theory Guide, there are some advantages for using the coupled approach comparing to the segregated approach as it obtains a robust and efficient single phase implementation for steady-state flows. In the present work, it is found that using the coupled approach is more robust and provides much better convergences than using the segregated algorithm. The research done by Chen & Przekwas (2010) can also be referred as a sample which showed that the coupled approach demonstrates good numerical convergence and computation time reduction.

2.2.1 Navier-Stokes equations:

The mathematical model of fluid dynamics is based on the fundamental mass, momentum and energy conservation principles. For incompressible flows the energy equation is decoupled from the mass and momentum conservation equations. Because the fluid properties are assumed to be constant (not changing with different temperature) for incompressible flow. With such condition means that we do not need the temperature to solve the mass and momentum conservation

equations for calculating the unknown velocity and pressure distribution. After solving the velocity and pressure field if the flow, the energy equation can be solved by itself to find the temperature distribution. For the simulations of wind turbines, heat transfer is not a primary concern as the flow around the wind turbine is assumed to be incompressible with constant temperature. Therefore in the present study only the mass and linear momentum equations are solved to obtain the velocity and pressure fields.

If we combine the continuity and momentum equations into a compact vector-variable form we can get:

$$\frac{\partial}{\partial_t}\int_{\Omega} \overrightarrow{W} d\Omega + \oint_{\partial\Omega}(\overrightarrow{F_C} - \overrightarrow{F_v})dS = 0 \tag{2.6}$$

where the vector of the conserved variables $\overrightarrow{W}$, the convection term $\overrightarrow{F_C}$ and the diffusion term $\overrightarrow{F_v}$ are as follows:

$$\overrightarrow{W} = \begin{bmatrix} \rho \\ \rho u \\ \rho v \\ \rho w \end{bmatrix} \qquad \overrightarrow{F_C} = \begin{bmatrix} \rho V \\ \rho u V + p n_x \\ \rho v V + p n_y \\ \rho w V + p n_z \end{bmatrix} \qquad \overrightarrow{F_v} = \begin{bmatrix} 0 \\ n_x \tau_{xx} + n_y \tau_{xy} + n_z \tau_{xz} \\ n_x \tau_{yx} + n_y \tau_{yy} + n_z \tau_{yz} \\ n_x \tau_{zx} + n_y \tau_{zy} + n_z \tau_{zz} \end{bmatrix} \tag{2.7}$$

The contravariant velocity V in equation 2.7 is introduced as:

$$V = \vec{v} \times \vec{n} = u n_x + v n_y + w n_z \tag{2.8}$$

Where p is the static pressure and for perfect gas: $p = \rho R_{specific} T$, here $R_{specific}$ is the specific gas constant which is 287.058 J/kg*K and T is the temperature ; τ is the stress term. For Newtonian fluid, the shear stress terms are introduced as follows:

$$\tau_{xx} = \frac{2}{3}\mu(2\frac{\partial u}{\partial x} - \frac{\partial v}{\partial y} - \frac{\partial w}{\partial z}) \tag{2.9}$$

$$\tau_{yy} = \frac{2}{3}\mu(2\frac{\partial v}{\partial y} - \frac{\partial u}{\partial x} - \frac{\partial w}{\partial z}) \tag{2.10}$$

$$\tau_{zz} = \frac{2}{3}\mu(2\frac{\partial w}{\partial z} - \frac{\partial u}{\partial x} - \frac{\partial v}{\partial z}) \tag{2.11}$$

$$\tau_{xy} = \tau_{yx} = \mu(\frac{\partial u}{\partial y} + \frac{\partial v}{\partial x}) \tag{2.12}$$

$$\tau_{xz} = \tau_{zx} = \mu(\frac{\partial w}{\partial x} + \frac{\partial u}{\partial z}) \tag{2.13}$$

$$\tau_{yz} = \tau_{zy} = \mu(\frac{\partial v}{\partial z} + \frac{\partial w}{\partial y}) \tag{2.14}$$

The equations of stress terms shown above are for general solutions. The present work uses the RANS solution for all cases using the finite volume method therefore the Reynolds averaged momentum equation is introduced below in the tensor format:

$$\rho \frac{\partial U_i}{\partial t} + \rho U_j \frac{\partial U_i}{\partial x_j} = -\frac{\partial p}{\partial x_i} + \frac{\partial}{\partial x_j}(2\mu S_{ji} - \overline{\rho u_i' u_j'}) \tag{2.15}$$

Where S_{ji} is a symmetric tensor called the strain-rate tensor: $S_{ji} = (\frac{\partial v_i}{\partial x_j} + \frac{\partial v_j}{\partial x_i})$. The Boussinesq eddy viscosity assumptions are used to model the unknown Reynolds stress terms:

$$\tau_{yz} = -\overline{\rho u_i' u_j'} = 2\mu_t S_{ij} - \frac{2}{3}\rho k \delta_{ij} \tag{2.16}$$

Where μ_t is calculated from turbulence models and $\delta_{ij} = \begin{pmatrix} 1 & i = j \\ 0 & i \neq j \end{pmatrix}$.

2.2.2 Turbulence models:

The laminar flow only exists at a very low Reynolds number which is:

$$Re = \frac{\rho \mathrm{UL}}{\mu} \tag{2.17}$$

Here L is the characteristic length scale (the aerofoil's chord length in this study), U is the flow velocity and μ is the viscosity of the fluid. When the Reynolds number is high the flow regime becomes turbulent and the flow situation is complex which leading to the existence of many turbulence model theories. Due to the non-closure condition of the RANS equations, different turbulence models have been developed to close the RANS equations. In the beginning of the present work, the Spalart-Allmaras, Realizable $k-\varepsilon$ model and $k-\omega$ SST turbulence models are selected for the computation. However after comparing the results with experimental data and the convergence history of these three turbulence models, the $k-\omega$ SST turbulence model provides more accurate results comparing to the other two models especially at the wind speeds higher than 10m/s where stall happens. Therefore all CFD simulations in the present work are using the $k-\omega$ SST turbulence model. The detail comparison and data will be found in chapter four.

The k − ω SST (shear stress transport) model:

Menter (1994) developed the shear-stress transport (SST) k − ω SST model which blends the robust and accurate formulation of the k − ω model in the near-all region with the freestream independence of the $k-\varepsilon$ model in the far field. The form of k − ω SST is similar as the standard k − ω model:

$$\frac{\partial}{\partial_t}(\rho k)+\frac{\partial}{\partial_{xi}}(\rho k u_i)=\frac{\partial}{\partial x_j}\left(\Gamma_k\frac{\partial k}{\partial x_j}\right)+G_k-Y_k+S_k \tag{2.18}$$

$$\frac{\partial}{\partial_t}(\rho \omega)+\frac{\partial}{\partial x_j}(\rho \omega u_j)=\frac{\partial}{\partial x_j}\left(\Gamma_\omega\frac{\partial \omega}{\partial x_j}\right)+G_\omega-Y_\omega+D_\omega+S_\omega \tag{2.19}$$

In the two equations shown above, the term G_k represents the productions of turbulence kinetic energy and G_ω represents the production of ω. The definitions of G_k and G_ω are as follows.

$$G_k=-\rho\overline{u_i'u_j'}\frac{\partial u_j}{\partial x_i} \qquad ; \qquad G_\omega=\frac{\alpha}{v_t}G_k \tag{2.20}$$

The coefficient α is given by:

$$\alpha=\frac{\alpha_\infty}{\alpha^*}\left(\frac{\alpha_0+Re_t/R_\omega}{1+Re_t/R_\omega}\right)\ ;\ \alpha^*=\alpha_\infty^*\left(\frac{\alpha_0^*+Re_t/R_k}{1+Re_t/R_k}\right) \tag{2.21}$$

Where $Re_t=\frac{\rho k}{\mu\omega}$. For the k − ω SST model the term α_∞ is defined as equation (2.23). The other model constants can be found below.

$$\alpha_\infty=F_1\alpha_{\infty,1}+(1-F_1)\alpha_{\infty,2} \tag{2.22}$$

$$\alpha_{\infty,1}=\frac{\beta_{i,1}}{\beta_\infty^*}-\frac{\kappa^2}{\sigma_{\omega,1}\sqrt{\beta_\infty^*}} \quad ; \quad \alpha_{\infty,2}=\frac{\beta_{i,2}}{\beta_\infty^*}-\frac{\kappa^2}{\sigma_{\omega,2}\sqrt{\beta_\infty^*}} \tag{2.23}$$

Γ_k and Γ_ω are the effective diffusivities of k and ω which are given by:

$$\Gamma_k=\mu+\frac{\mu_t}{\sigma_k} \qquad ; \qquad \Gamma_\omega=\mu+\frac{\mu_t}{\sigma_\omega} \tag{2.24}$$

In equation (2.25) σ_k and σ_ω are the turbulent Prandtl numbers for k and ω which is given by equation (2.26). μ_t is the turbulent viscosity which is computed by equation (2.27), S is the magnitude of the strain rate tensor.

$$\sigma_k = \frac{1}{\frac{F_1}{\sigma_{k,1}} + (1-F_1)/\sigma_{k,2}} \quad ; \quad \sigma_\omega = \frac{1}{\frac{F_1}{\sigma_{\omega,1}} + (1-F_1)/\sigma_{\omega,2}} \tag{2.25}$$

$$\mu_t = \frac{\rho k}{\omega} \frac{1}{max\left[\frac{1}{\alpha^*}, \frac{SF_2}{\alpha_1 \omega}\right]} \tag{2.26}$$

$$F_1 = \tanh(\Phi_1^4) \quad ; \quad \Phi_1 = min\left[max\left(\frac{\sqrt{k}}{0.09\omega y}, \frac{500\mu}{\rho y^2 \omega}\right), \frac{4\rho k}{\sigma_{\omega,2} D_\omega^+ y^2}\right] \tag{2.27}$$

$$D_\omega^+ = max\left[2\rho \frac{1}{\sigma_{\omega,2}} \frac{1}{\omega} \frac{\partial k}{\partial x_j} \frac{\partial w}{\partial x_j}, 10^{-10}\right] \tag{2.30}$$

$$F_1 = \tanh(\Phi_2^2) \quad ; \quad \Phi_2 = max\left[2\frac{\sqrt{k}}{0.09\omega y}, \frac{500\mu}{\rho y^2 \omega}\right] \tag{2.31}$$

Where y is the distance closest to the wall surface. D_ω is the cross-diffusion term which is defined in equation (2.31) and D_ω^+ is the positive portion of the cross-diffusion term. This term is introduced because the $k-\omega$ SST turbulence model blends the standard $k-\omega$ and standard $k-\varepsilon$ model together which requiring transformation for the $k-\varepsilon$ model into equations based on k and ω.

$$D_\omega = 2(1-F_1)\rho \frac{1}{\sigma_{\omega,2}} \frac{1}{\omega} \frac{\partial k}{\partial x_j} \frac{\partial w}{\partial x_j} \tag{2.32}$$

The term Y_k is the dissipation of k. Unlike the standard $k-\omega$ model, in the $k-\omega$ SST model the f_{β^*} is a constant equal to 1, thus,

$$Y_k = \rho \beta^* k \omega \tag{2.33}$$

$$\beta^* = \beta_\infty^* \left(\frac{4/15 + (Re_t/R_\beta)^4}{1 + (Re_t/R_\beta)^4}\right) \quad ; \quad Re_t = \frac{\rho k}{\mu \omega} \tag{2.34}$$

The term Y_ω represents the dissipation of ω for the $k-\omega$ SST model it is defined as:

$$Y_\omega = \rho \beta \omega^2 \quad ; \quad \beta = F_1 \beta_{i,1} + (1-F_1)\beta_{i,2} \tag{2.35}$$

The model constants are as follows:

$$\alpha_\infty^* = 1, \alpha_\infty = 0.52, \alpha_0 = 0.52, \beta_\infty^* = 0.09, R_\beta = 8, R_k = 6, R_\omega = 2.95,$$

$$\kappa = 0.41, \sigma_{k,1} = 1.176, \sigma_{k,2} = 1.0, \sigma_{\omega,1} = 2.0, \sigma_{\omega,1} = 1.168, \alpha^1 = 0.31$$

$$\beta_{i,1} = 0.075, \beta_{i,2} = 0.0828$$

The Spalart-Allmaras turbulence model:

The Spalart-Allmaras one-equation turbulence model solves a modelled transport equation for turbulent viscosity which was designed for aerospace application involving wall-bounded flows and was proved to be able to give good results for boundary layers subjected to adverse pressure gradients. The transport equation for the S-A model is introduced as follows:

$$\frac{\partial}{\partial_t}(\rho\tilde{v}) + \frac{\partial}{\partial_{xi}}(\rho\tilde{v}u_i) = \frac{1}{\sigma_{\tilde{v}}}\left[\frac{\partial}{\partial_{xj}}\left\{(\mu + \rho\tilde{v})\frac{\partial\tilde{v}}{\partial_{xj}}\right\} + C_{b2}\rho(\frac{\partial\tilde{v}}{\partial_{xj}})^2\right] + G_v - Y_v \qquad (2.36)$$

where G_v and Y_v denote the turbulent viscosity and the destruction of turbulent viscosity that occurs in the near-wall region respectively. $\sigma_{\tilde{v}}$ and C_{b2} are constants and v is the molecular kinematic viscosity. In the S-A model the turbulence kinetic energy, *k*, is not calculated.

For the turbulent viscosity μ_t, it is computed from:

$$\mu_t = \rho\tilde{v}f_{v1} \qquad (2.37)$$

where the viscous damping function f_{v1} is given by:

$$f_{v1} = \frac{\chi^3}{\chi^3 + C_{v1}^3} \quad \text{and} \quad \chi \equiv \frac{\tilde{v}}{v} \qquad (2.38)$$

The production term G_v is modelled as:

$$G_v = C_{b1}\rho\tilde{S}\tilde{v} \qquad (2.39)$$

where

$$\tilde{S} \equiv S + \frac{\tilde{v}}{\kappa^2 d^2}f_{v2} \qquad \text{and} \qquad f_{v2} = 1 - \frac{\chi}{1+\chi f_{v1}} \qquad (2.40)$$

C_{b1} and κ are constants and d is the distance from the wall. S is a scalar measure of the deformation tensor and in ANSYS Fluent, it is defined as:

$$S \equiv |\Omega_{ij}| + C_{prod}min(0, |S_{ij}| - |\Omega_{ij}|) \qquad (2.41)$$

where

$$C_{prod} = 2.0, |\Omega_{ij}| \equiv \sqrt{2\Omega_{ij}\Omega_{ij}}\ , |S_{ij}| \equiv \sqrt{2S_{ij}S_{ij}}$$

The mean strain rate S_{ij} is defined as:

$$S_{ij} = \frac{1}{2}\left(\frac{\partial u_j}{\partial x_j} + \frac{\partial u_i}{\partial x_j}\right) \tag{2.42}$$

The destruction term of the S-A turbulence model is introduced as:

$$Y_v = C_{w1}\rho f_w \left(\frac{\tilde{\nu}}{d}\right)^2 \tag{2.43}$$

where:

$$f_w = g\left[\frac{1+C_{w3}^6}{g^6+C_{w3}^6}\right], \quad g = r + C_{w2}(r^6 - r), r \equiv \frac{\tilde{\nu}}{\tilde{S}\kappa^2 d^2} \tag{2.44}$$

The model constants are as follows:

$$C_{b1} = 0.1355, C_{b2} = 0.622, \sigma_{\tilde{\nu}} = \frac{2}{3}, C_{v1} = 7.1, C_{w1} = 3.2059$$

$$C_{w2} = 0.3, C_{w3} = 2.0, \kappa = 0.4187$$

The Realizable k − ε turbulence model

ANSYS Fluent supports three kinds of k − ε turbulence model which are STD (standard), RNG (renormalization group theory) and Realizable k − ε models. The forms for three models are similar with transport equations for turbulent kinetic energy k and turbulent dissipation ε. They are different because of: 1) the method of calculating turbulent viscosity; 2) the turbulent Prandtl numbers governing the turbulent diffusion of k and ε; 3) the generation and destruction terms in the ε equation.

The Realizable k − ε model is developed from the Standard k − ε model as it has a new formulation for the turbulent viscosity and a new transport equation for the dissipation rate ε (Shih, et al.). It is called 'Realizable' because it satisfies certain mathematical constrains on the Reynolds stress and consistent with the physics of turbulent flows, which the other two k − ε model are not able to meet this requirement.

In ANSYS Fluent, for the incompressible flow, the modelled transport equations for k and ε are introduced as:

$$\frac{\partial}{\partial_t}(\rho k) + \frac{\partial}{\partial_{xj}}(\rho k u_j) = \frac{\partial}{\partial x_j}\left[\left(\mu + \frac{\mu_t}{\sigma_k}\right)\frac{\partial k}{\partial x_j}\right] + G_k + G_b - \rho\varepsilon + S_k \tag{2.45}$$

$$\frac{\partial}{\partial_t}(\rho\varepsilon) + \frac{\partial}{\partial_{xj}}(\rho\varepsilon u_j) = \frac{\partial}{\partial x_j}\left[\left(\mu + \frac{\mu_t}{\sigma_k}\right)\frac{\partial \varepsilon}{\partial x_j}\right] + \rho C_1 S_\varepsilon$$

$$-\rho C_2 \frac{\varepsilon^2}{k+\sqrt{v\varepsilon}} + C_{1\varepsilon}\frac{\varepsilon}{k}C_{3\varepsilon}G_b + S_\varepsilon \tag{2.46}$$

where:

$$C_1 = max\left[0.43, \frac{\eta}{\eta+5}\right], \qquad \eta = S\frac{k}{\varepsilon}, \qquad S = \sqrt{2S_{ij}S_{ij}}$$

In equation 2.45 and 2.46, G_k represents the production of turbulence kinetic energy which is calculated as:

$$G_k = -\rho\overline{u_i' u_j'}\frac{\partial u_j}{\partial x_i} \tag{2.47}$$

And G_b is the generation of turbulence kinetic energy due to buoyancy. For ideal gases, it is calculated as:

$$G_b = -g_i\frac{\mu_t}{\rho Pr_t}\frac{\partial \rho}{\partial x_i} \tag{2.48}$$

where Pr_t is the turbulent Prandtl number for energy which is 0.85 for the Realizable $k-\varepsilon$ turbulence model and g_i is the component of the gravitational vector in the ith direction. S_k and S_ε are user-defined source terms and in the present studies these terms are ignored.

The eddy viscosity is calculated as:

$$\mu_t = \rho C_\mu \frac{k^2}{\varepsilon} \tag{2.49}$$

where:

$$C_\mu = \frac{1}{A_0 + A_S\frac{kU^*}{\varepsilon}} \tag{2.50}$$

$$U^* \equiv \sqrt{S_{ij}S_{ij} + \widetilde{\Omega}_{ij}\widetilde{\Omega}_{ij}} \quad \text{and} \quad \widetilde{\Omega}_{ij} = \overline{\Omega_{ij}} - \varepsilon_{ijk}\omega_k \tag{2.51}$$

In equation 2.51 $\overline{\Omega_{ij}}$ is the mean rate-of rotation tensor viewed in a moving reference frame with the angular velocity ω_k. The constants A_0 and A_s are given by:

$$A_0 = 4.04, A_s = \sqrt{6}cos\phi \tag{2.52}$$

where:

$$\phi = \frac{1}{3}cos^{-1}(\sqrt{6}W), W = \frac{S_{ij}S_{jk}S_{ki}}{\tilde{S}^3}, \tilde{S} = \sqrt{S_{ij}S_{ij}}, S_{ij} = \frac{1}{2}(\frac{\partial u_j}{\partial x_i} + \frac{\partial u_i}{\partial x_j}) \tag{2.53}$$

The model constants are:

$$C_{1\varepsilon} = 1.44, C_2 = 1.9, \sigma_k = 1.0, \sigma_\varepsilon = 1.2$$

2.2.3 The Moving Reference Frame Function

By default, ANSYS FLUENT solves the governing equations and turbulence models of flows in a stationary reference frame. However for some cases such as the rotating blade case in the present work, there are some significant advantages to solve the equations in a moving reference frame. In the stationary reference frame the rotating blade will render the problem unsteady. However with deploying the moving reference frame function and a rotationally periodic boundary condition, the flow of an assigned volume is assumed to be with a constant rotational speed and the non-wall boundaries are surfaces of revolution (for example velocity inlet). Therefore in this situation the blade can be simulated as stationary wall and as a steady-state problem. Such function in ANSYS Fluent can effectively save computational time and resources. In the present work for all 3D CFD study on the rotating blade, the moving reference frame is activated with proper settings for the right rotational speed.

2.3 Literature review: Flow Controls for HAWTs

Researching and optimizing the design of HAWT in the aerodynamic aspect is the most effective way to further improve the HAWTs' performance. So far many scholars have gained some profound achievement in both the numerical and experimental fields. Hansen and Madsen (2011) summarized more than 100 researches on the aerodynamics of wind turbine. The passive and

active flow control devices of wind turbine were comprehensively introduced which including flaps/deformable TE, microtabs, morphing, active twist, suction/blowing, synthetic jets, active VGs and plasma actuators.

2.3.1 Previous Studies on Microtab

The concept of microtab for wind turbine load control which was derived from the Gurney flaps concept for aircraft wings. The conception of Gurney flap was first proposed by an automobile racer Dan Gurney and then his idea was further confirmed by Liebeck (1978, Figure 5) in AIAA journal. Theoretically the Gurney flap increases the lift coefficient (C_l), including the maximum $C_{l,}$ at almost all AOA of the aerofoil when it is deployed on the pressure side. However it will also induced higher drag coefficient (C_d) therefore the lift to drag ration should be considered carefully when such conception is applied in the aircraft design.

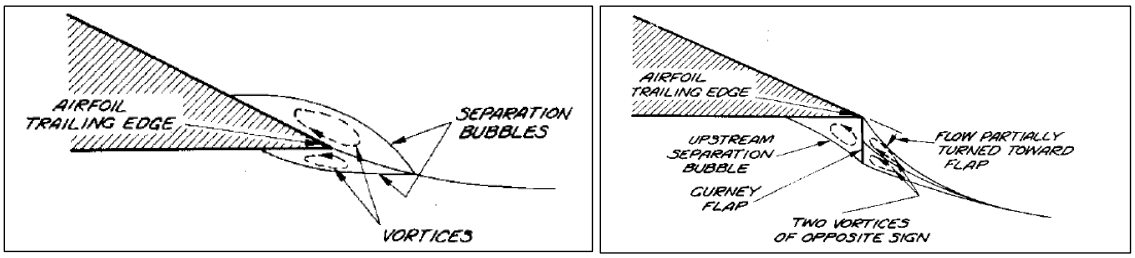

Figure 5. The hypothesis of GF. (Liebeck, 1978)

Unlike aircrafts, the main driving force of HAWTs is the lift force and the drag force is much less important in the design process. Therefore the GF concept is significant for load improvement or control of HAWTs. As an active flow control device some space is required inside the aerofoil for control purpose therefore Van Dam et al. (2001) first proposed the concept of microtab which was deployed from 0% to 10% chord position toward the trailing edge of the aerofoil. The general proposed concept and destination performance estimation for the study can be seen from Figure 6. This study carried out both 2D computational research and experiments on the GU-25-5(11)-8 aerofoil and the detailed working principle of microtab can be seen from Figure 7. Normally for the sharp trailing edge aerofoil, referring to the Kutta condition which is shown on the left of Figure 5(A body with a sharp trailing edge which is moving through a fluid will create about itself a circulation of sufficient strength to hold the rear stagnation point at the trailing edge), a small separation happens around the trailing edge. However deploying microtabs can

shift this separation to the lower edge of the tab, which significantly changes the camber and increases the lift of the aerofoil. In the right of Figure 7, it can be seen that the microtab changes the pressure coefficient of the entire aerofoil with keeping the original aerofoil shape. The CFD results showed predicted the C_l very close to the experimental results especially in lower AOA situations. The results showed that a 1% chord height (3mm) solid microtab at 95% x/C position increased the C_l by up to 50% at 0 degree AOA. Another important conclusion from this study is that for the aerofoil the closer the microtab deployed to the trailing edge the more C_l increases.

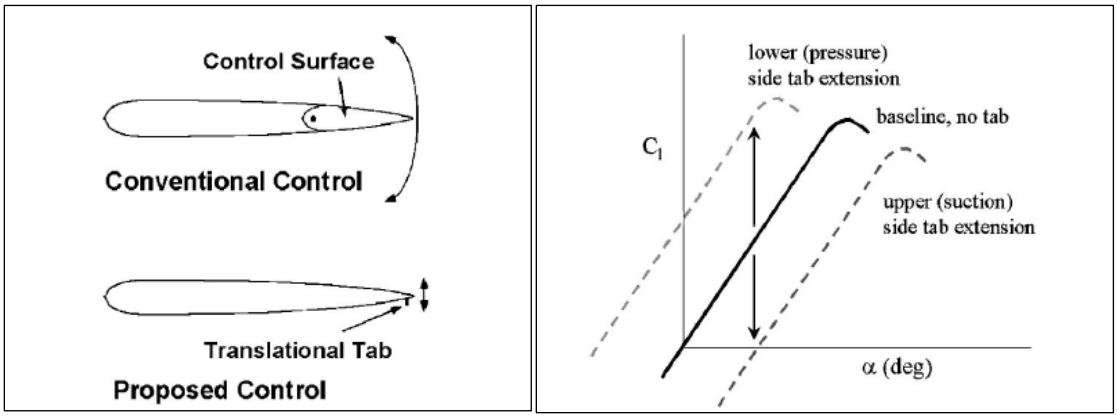

Figure 6. The microtab concept proposed by Van Dam et al. and performance predictions (2001).

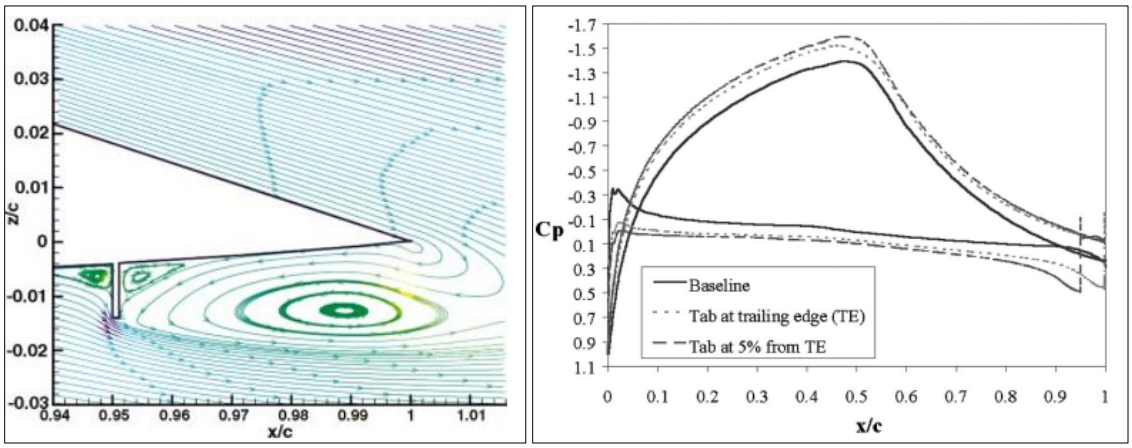

Figure 7. Computed streamlines around the microtab (left) and pressure coefficient comparison (right) which finished by Van Dam et al. (2001).

Nakafuji et al. (2005) investigated the effects of the solidity ratio on the performance of the microtab using a 3D RANS CFD method. In their study the solidity ratio is defined based on

constant height finite microtabs which is: $\sigma = \frac{tab\ width}{tab\ width+gap\ width}$. The results showed that the C_L increment is linearly related to the solidity ratio of the microtab and the microtabs with gaps between each other improved the L/D ratio compared to the solid tab. However whether the gaps could increase or decrease the torque of an integral wind turbine still required to be studied. Zayas et al. (2006) researched into employing the active microtabs at the trailing edge of the cross-section of the wind turbine both experimentally and numerically. The Micon 65 ADAMS model HAWT was both tested experimentally and simulated in CFD method. The CFD results were reasonable but in high AOA it underpredicted the lift coefficient. It was shown that microtab as an active device can not only beneficial for load alleviation but also can improve the energy generation with the microtab in the pressure surface.

Van Dam et al. (2007) numerically investigated the microtab and active microflap around the trailing edge which were used to reduce the aerodynamic fatigue loads on wind turbine blades. The active microflap concept can be seen from Figure 8 which can be rotated towards the pressure side (increasing the camber) for increasing the lift force or the suction side (decreasing the camber) for reducing the lift force of the aerofoil. Similar as the microtab, microflap also change the Kutta condition around the trailing edge. The fatigue loads of wind turbine are caused by the cyclic loading of the structure which could cause failure if some critical level of damage is exceeded. The relevant forces include the gravitational force, the centrifugal force, the wind thrust which is perpendicular to the plane of the wind turbine and other rapidly changing forces because of the stall conditions. The wind thrust forces primarily contribute to fatigue damage therefore for large wind turbines the wind thrust is also important to be investigated. The OVERFLOW2 CFD code was used for the unsteady cases. The results showed that deploying the microtab in around 1% chord length to the trailing edge or moving trailing-edge flaps with around 10% chord length can effectively mitigate high frequency loads of the blade. The high frequency loads means the wind turbine loads are changing in because of the turbulent wind with a frequently changing wind speed. The results of this study showed that this kind of loads can be effectively mitigated with deploying the trailing edge microflap. However, this study is only on the 2D profile.

Holst et al. (2013) investigated into the effects of microtab and Gurney flap on the FX 63-137 aerofoil profile experimentally. The Reynolds number of the tests was Re = 135000, which was relatively low and the number was close to the root side of most modern HAWTs. They further researched into the effects of the gap between microtabs. Their results showed the finite microtabs not only changed the pressure distributions in the area where they were deployed but

also changed the C_P globally. However they only tested one size (1% chord) of the microtabs which ignored the effects of the microtabs when the height exceeded the boundary layer thickness.

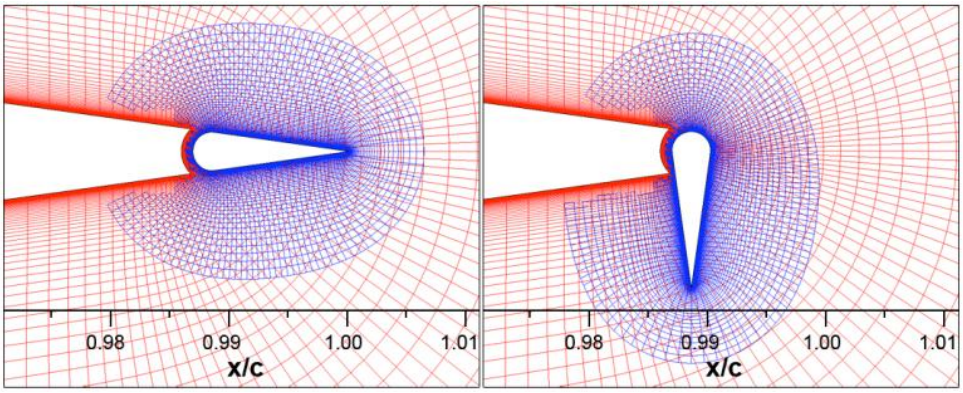

Figure 8. The microflap concept and mesh used in the study of Van Dam et al. (2007).

Bach et al. (2014) researched into both full-span microtab and finite microtab on a span section with AH93W174 aerofoil experimentally. The results showed that the lift force of the span section can be varied by either changing the tab height or the aspect ratio of the finite tabs. Higher tabs led to larger differences on the lift force however they also induced much higher drag force. Moreover they also investigated into the microtab effects on the NREL 5MW reference blade using the BEM code, Qblade, which showed that with 2% chord microtabs deployed on the outer 30% of the blade the bending moment of the blade can be reduced by 13% by suction side tabs and increased by 25% by pressure side tabs.

There were some more previous studies on microtabs using either experimental methods or numerical methods, for example Bæk & Gaunaa (2011) using FLEX5 CFD code for comparing the differences of the effects of the microtabs and trailing edge flaps in 2D condition. Their results showed that the load reduction potential of trailing edge flap was more than twice bigger than that of the microtab. The load reduction for horizontal wind turbine is important at upper rated wind speed to keep the turbine components within torque limits. Because the power of the wind increases proportional to the cube of the wind speed therefore wind turbines needs to be controlled for reducing torque in high winds. The flow controls introduced here control and reduce the torque of the wind turbine in aerodynamic ways. However, because of the limitation of the wind tunnel tests and the computational resources, there is still neither experiment nor numerical study of the microtabs on wind turbine in a real rotating frame.

2.3.2 Previous Study on Microjets

One concept of microjets for flow control on aerofoils is deploying the microjets near the leading edge on the suction side of the aerofoil. The purpose is to reduce the dynamic stall on the suction side of the aerofoil for better performance. The suction side separation is caused by insufficient momentum in the boundary layer to counteract and adverse pressure gradient. Therefore deplying microjet near the leading edge on the suction side can effective increase the momentum of the fluid in the boundary layer, whereby delaying separation (Figure 9). Such concept has been studied for improving the performance of turbine blades. For example Beahan et al. (2014) experimentally studied the microjet effects on NACA0015 aerofoil. They deployed multiple microjets in the first 12% chord of the aerofoil on the suction side. The results showed that microjets effectively suppressed the dynamic stall and separation on the suction side at all AOAs. Koopman & Hoeijmakers (2014) applied tangentially directed synthetic jets on the suction side 30.9% chord away from the leading edge for flow separation control. Their results showed that the synthetic jets could effectively increase the C_L (11%) at higher AOAs and delayed the stall (stall AOA from 13.8 degrees to 16.8 degrees). Such microjet concept is also suitable for stall-regulated HAWTs to improve their aerodynamic performance at higher wind speeds where the induced incidence of the cross-sectional aerofoil is very high.

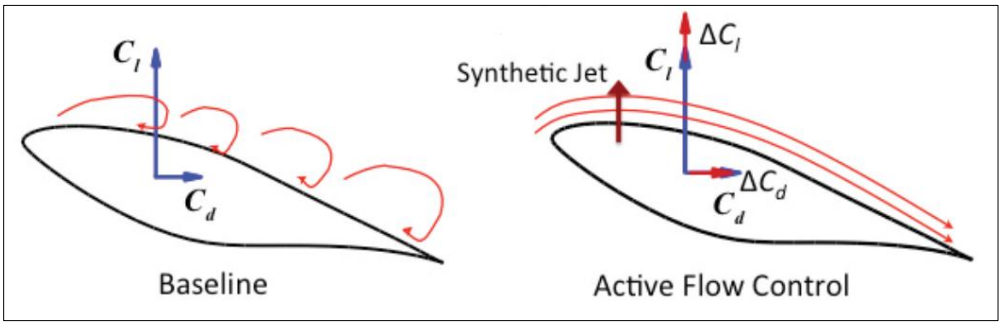

Figure 9. Estimated performance of aerofoil with leading edge synthetic jet (Maldonado et al., 2010)

Maldonado et al. (2010) tested a wind turbine with a cross-section shape of NACA 4415 aerofoil and synthetic jet actuators at proper positions using the PIV technique. This study provided a lot of experimental results and it showed that using synthetic jets can make the flow over the blade fully or partially re-attached depending on the AOA and Reynolds number, and can additionally reduce the blade vibration. Several years later, Taylor et al. (2014) investigated into the leading edge microjets on a finite span S809 blade experimentally. They applied Stereoscopic Particle

Image Velocimetry (SPIV) measurements for capturing the streamlines and vorticity of the blade and relevant results can be seen in Figure 10. The results showed that the deployment of synthetic jets on the suction side near the leading edge effectively delay and relief stall of the S809 finite span blade at higher AOAs.

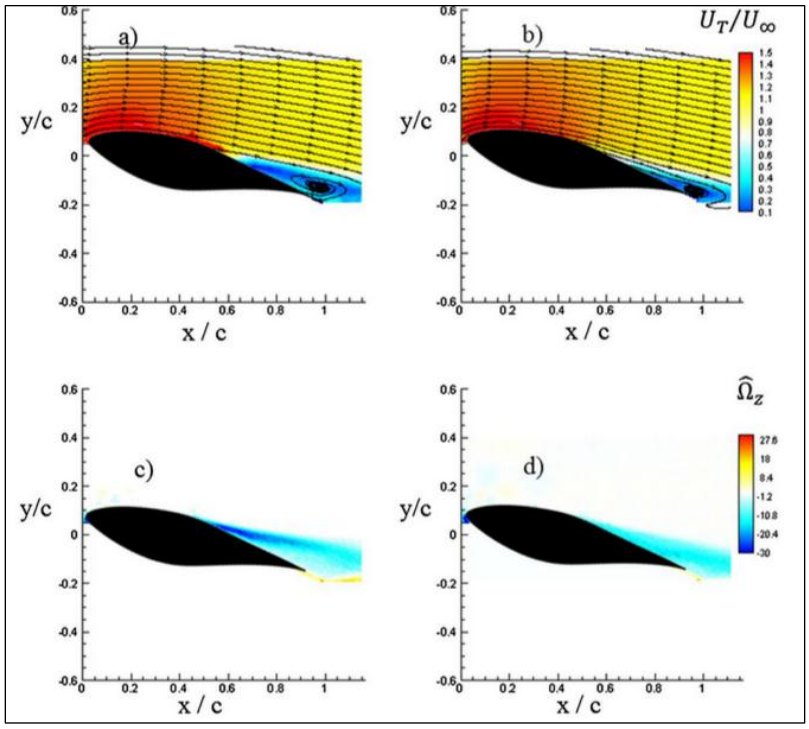

Figure 10. Normalized velocity contour, streamlines and normalized vorticity with jets off and on (Taylor et al., 2014).

Another microjet concept is to deploy the microjets near the trailing edge of the wind turbine blade for load control. This microjet concept is similar to microtab, which is predicted to increase the lift force when deployed near the trailing edge on the pressure side or reduce the lift force when deployed on the suction side. Braylock et al. (2013) numerically researched into the microjets and microtabs on the NACA0012 aerofoil using the CFD solver OVERFLOW-2. Their validation on the microjet compared to the experimental data was quite successful. Their results showed that both the response time and changes to the C_L of the NACA0012 aerofoil from these two types of flow control devices are quite similar except for that the microjet had around 30% lower drag compared to that from the microtab. Their further continuous study (Cooperman et al.

2014) also showed that using microtab and microjet can reduce the lift force variation when wind speed changes, which can effectively protect the HAWT in gust situation.

With the larger and larger size of modern HAWTs, the flapwise root bending moment of the blade should be considered carefully for maintenance issues for wind turbines. Hurley et al. (2016) used a CFD code written by MATLAB and coped with the 2D aerofoil data to simulate the trailing edge microjet effects on the 5MW NREL reference blade. Results showed that deploying a 14 meters microjet from 30-meter span to 44-meter span position of the blade can effectively reduce the flapwise root bending moment of the blade by 3.5%-28% at different wind speeds.

2.3.3 Previous Study on Vortex Generators

Vortex generators are normally applied right to the external surface of aircraft wings or wind turbine blades. They are deployed obliquely for a particular angle of attach with respect to the local flow therefore they can generate relatively stronger tip vortex because they have very small aspect ratio (AR). After the mixture of this kind of high energetic tip vortex and the slow-moving boundary layer, the energy of the boundary layer flow in the adverse pressure gradient can be reinforced. This situation can keep the boundary flow to be attached with the surface for delaying the separation and improving the aerodynamic lift of the aerofoil. This concept has been proved for effective flow separation control around the leading edge on the suction side of the aerofoil (Lin, 2002). As for HAWTs, because the incidence of the cross-sectional aerofoil near the root side is relatively higher than the outer side, flow separation normally happens (Figure 11). Here with the deployment of VGs the stalling can be delayed, whereby improving the aerodynamic performance of the wind turbine.

Vronsky (2000) investigated into the wind turbine performances with air-jets or traditional vane vortex generators. His results of this experimental research showed that the air-jet control was particular significant for the thick airfoils with higher lift coefficient. When compared to the vane VGs, air-jets are easier to control. This study provides a lot of experimental data which are very helpful for CFD study.

Rajendran and Madhu (2011) numerically researched a full wind turbine including the tower using a fully unstructured mesh and Ansys FLUENT CFD code. The chosen turbulence model is the $k-\omega$ SST model. The validation work was also done, however in relatively lower wind speed the results show large differences when compared to experimental data. The reasons were given as some mechanical losses but not shown very clearly. This study involved the CFD analysis of

some passive flow control tools such as winglet on the tip, gurney flap in the trailing edge and vortex generators. Vain VGs were simulated in the study. The results showed that installing VGs at proper positions can improve the power production by 4% and the gurney flap would be very effective in lower wind speeds.

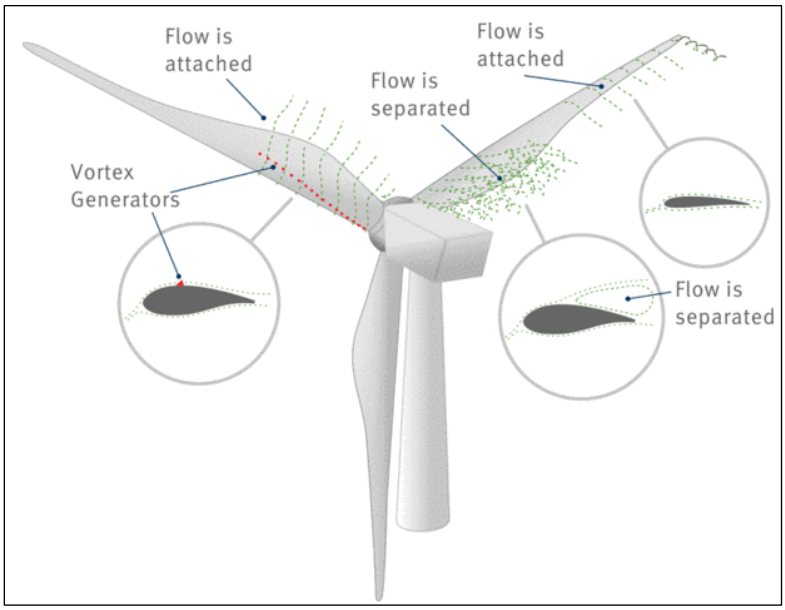

Figure 11. Application sample for VGs on wind turbine blade. (Source from: http://smart-blade.com/products-services/vortex-generators.html

Xue et al. (2010) simulated numerically the VGs on wind turbine blades and introduced the theory and potential performance of the VG. The designing processes were also discussed. However the simulation was just at a cross-section of the wind turbine but not full-scale and the results need to be validated.

Godard and Stanislas (2006) tested three different kinds of vortex generators on the wind turbine which including passive VGs, synthetic jets and round jets with continuous blowing. The comparison among their three types of VGs was performed in both co- and counter-rotating configurations. The results showed that the skin friction increase of the optimized round jet devices and standard passive VGs is similar while the slotted jets are less effective than equivalent passive VGs. Considering the induced drag of the passive VGs, the round steady jets are quite efficient because they will not produce drag when they are turned off.

2.3.4 Overall Reviews of Wind Turbine Flow Control

Barlas and Van Kuik (2010) reviewed over a hundred of current existing researches on the smart rotor control devices for wind turbines including their traditional application in aircrafts and helicopters, design issues and resulting performances. Figure 12 shows the comparison of the lift coefficient differences of different control devices. It can be seen that trailing edge flaps, microtabs and camber control can increase the lift coefficient of the aerofoil largely. However this finding is just for a cross-section of the wind turbine and to what extent the lift coefficient can improve the induced torque is not able to be shown clearly. In addition the CFD method was also discussed and the relevant challenges such as how to model the separated flow conditions, how to accurate model the changed wake environment causing by control devices and so on. Therefore the full scale wind turbine experimental testing and numerical modeling with these flow control devices is necessary.

Saravanan et al. (2012) tested four different winglets at the tip of a small wind turbine and compared their performances. The pressure distribution at three x/C positions were compared and the results showed that the winglet with 2% height of blade radius and 25% curvature ratio can improve the wind turbine performance more significantly. However because in each cross section of the blade there were only three monitors and this condition might lead to less accurate result.

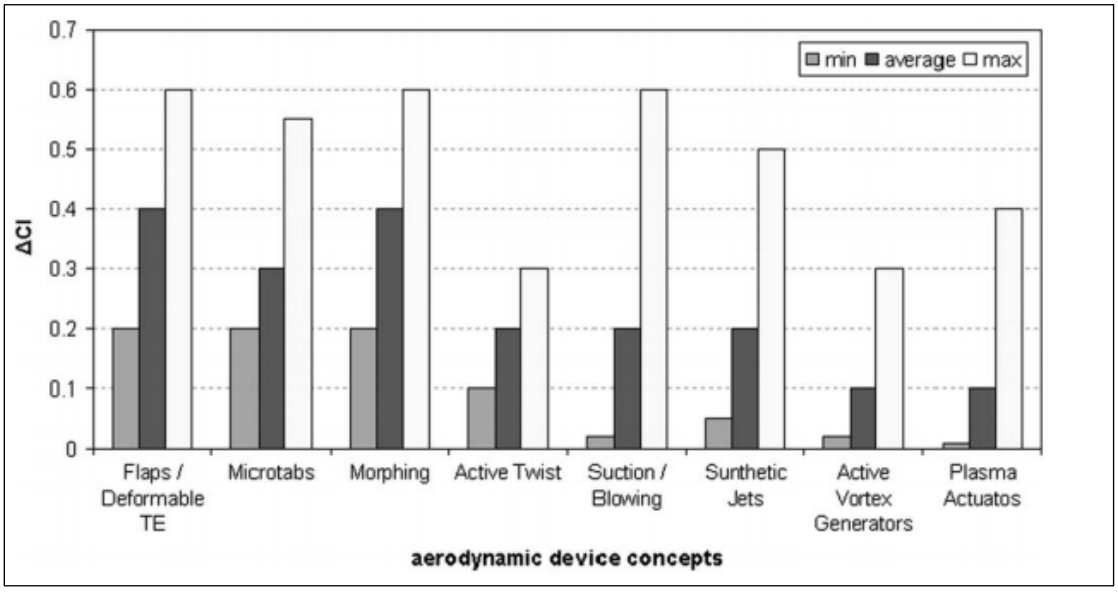

Figure 12. Comparison of control devices in terms of lift control capability (Balas & Kuik, 2010).

The divergent trailing edge is a concept by Henne and Gregg (1991) for aircraft wings, which is proved to be beneficial for high Cl/Cd of aerofoils (Li & Wang 2007). This concept was applied with a large scale divergent trailing edge at 3% chord length for its performance on the wind turbine field. Baker et al. (2006) investigated into the blunt trailing-edge wind turbine aerofoils both experimentally and numerically at a 2D condition. The experimental results showed that by increasing the thickness of the trailing-edge (8.75% and 17.5% chord length thickness were tested in their research), the maximum L/D can be increased from 35.5 to 44 at the Re = 666,000 flow condition and the maximum Cl can be increased from 1.5 to 2.16 for the 17.5% chord length thickness trailing-edge redesigned aerofoil. This study also showed that increasing the thickness of trailing-edge is able to effectively improve the lift force of the aerofoil at the 2D condition.

2.4 Literature Review: CFD Study on HAWTs

As introduced above, CFD has some advantages when compared to experimental research. In recent years since the early 21st century a lot of researchers have done some significant and studies on the aerodynamics of HAWTs numerically due to the fast developing computing resources and the appearance of supercomputers.

Sørensen (2011) reviewed lots of the traditional design models and theories of the HAWT. CFD method has been concerned mostly in recent years however in high wind speed conditions the CFD method still cannot predict very accurate results because of the separated boundary layer.

Sezer-Uzol and Long. (2006) did 3-D time-accurate simulations for analysing the flow fields around the rotor. This research simulated three flow cases: 7m/s with 0^0 yaw, 7m/s with 30^0 yaw and 15m/s with 0^0 yaw with using the PUMA2 solver. A fully unstructured mesh was used in this study with 3.6 million tetrahedral cells. The simulation was run in an inviscid condition and its results were with good agreement with the experimental data except in the 15m/s 0^o situation. Another disadvantage is that the research did not have a comparison with the experimental data on the torque which is one of the most important factors of the wind turbine. Moreover, the research used a full cylinder model without symmetry for simulating the two blades NREL turbine which increased the computation time and cost.

Monier (2011) researched into the winglet and twist aerodynamic design of wind turbine based on the NREL Phase VI wind turbine. He used the $k-\varepsilon$ Launder-Sharma (LS) turbulence model for

simulation and the results showed good quality which may be referred in this study. The $k-\varepsilon$ LS model was developed by Launder and Sharma (1974) which is a classical Low-Re (low Reynolds number) model with benefit of predicting bypass transition.

Esfahanian el al. (2013) combined the 2D CFD aerofoil computational results with a modified blade element momentum method in order to reduce the computation time of the full 3D simulation of wind turbines. Its accuracy was validated with the experimental data of NREL PHASE II wind turbine and showed sufficient accuracy of the power curve. However, the selected NREL phase ii wind turbine is a constant chord wind turbine without local twist angel, which can be rarely seen in recent years.

Sagol et al. (2011) investigated into the turbulence model which can show best performance based on the NREL Phase VI turbine. This research has comprehensive comparisons among different scales of meshes and various turbulence models (RNG $k-\varepsilon$, STD $k-\varepsilon$, k $-$ ω SST, realizable $k-\varepsilon$) in the wind speed = 7m/s situation. A 1.9 million unstructured mesh and the k $-$ ω SST turbulence model was selected to be with the best performance for simulating the wind turbine. The comparison of moments on the blades was simulated in different wind speeds and the results showed that the shaft torque was underestimated by the simulation but the root flap bending moment comparison showed good agreement with the experimental data. This research used fully unstructured mesh and the y+ setting seems to be not small enough for a much more accurate result. Its comparison of the pressure coefficient between its results and the experimental data showed that the results were considerably away from the experimental data.

Carcangir (2008) investigated into the wake, rotational effect and the tip shapes of the HAWT numerically. The NREL Phase VI turbine was also selected as a validation case using the CFD code FLUENT and a fully structured mesh. However the maximum wind speed simulated in this study was 11m/s which showed that the CFD method can predict accurate results in relatively lower wind speeds but cannot show whether such CFD method can still predict accurate result in the stall condition of the wind turbine.

Li el al. (2012) compared the RANS and DES computations of NREL Phase VI experimental wind turbine with using an extremely fine mesh of 57 million grid points. Many cases are simulated including different wind speeds and pitch angels. The computational shaft torques of RANS and DES were both accurately predicted even at 15 m/s condition but DES showed much better transient response. However the mesh used in this research is quite refined and is not affordable by many other researchers.

In conclusion, using CFD method for simulation the flow conditions and performance of wind turbines has been proved to be with reasonable accuracy and effective. Some of these previous studies have shown very good results with simulating the full-length wind turbine blade in a rotating frame. However because of the complexity of the meshing progress and the large mesh size, there is still no research on 3D CFD study on the wind turbine blade with flow control devices (microtabs and microjets) in the rotating frame to study the spanwise flow effects. The present study aims to fill this gap and show extensive CFD computational results of the effects of these two typical flow controls on the rotating wind turbine blade.

Chapter 3 CFD Validation on NREL Phase VI Blade

3.1 Introduction

The NREL Phase VI wind turbine is an experimental wind turbine of NREL which was fully tested in the NASA-Ames wind tunnel in 2001. Because of the comprehensive published information and results, including shaft torque, pressure coefficient, code to experiment comparison and so on. This NREL case was selected by many researchers for their CFD validation and further studies. The present study also selects this famous stall-regulated wind turbine as the validation case. Because of the large separation flow on the suction side of the blade in higher wind speed situations, a big challenge is whether the CFD method can accurately predict the aerodynamic performance (shaft torque, pressure coefficient, etc.) compared to the experimental data.

3.2 Methodology

Basically a full CFD simulation includes four steps: model geometry setup, mesh generation, CFD solver set up and computing, and post processing of the results. In this study a full 3D single wind turbine blade is built and fully structured mesh is used for all cases for good resolution of the viscous boundary layers.

3.2.1 Geometry Model

The geometry model of NREL Phase VI two blade wind turbine is generated in ICEM CFD and SOLIDWORKS. The aerofoils of the turbine blade are generated by inputting coordinates in ICEM CFD and the blade surfaces are generated in SOLIDWORKS. The geometry coordinates and detailed data of the blade are from the official website of the NREL Amestest. Table 3 shows the basic description and parameters of the simulated blade. The present work selects 13 cross-sectional aerofoils for generating the blade geometry and the detailed twist angles of the sections can be found in Appendix 1. Because the NREL Phase VI wind turbine consists of two symmetrical blades, the computational domain is also symmetrical. Therefore just one blade and a semicircle domain are generated for the simulation (Figure 13 & 14). Because there is no detailed explanation for the blade tip of NREL Phase VI turbine, a flat tip shape is used in this project.

Table 3. Basic description of NREL Phase VI blade

Number of blades	2	**Tip pitch angle**	3 degrees
Rotor diameter	10.06m	**Blade profile**	S809
Angular velocity	7.54rad/s	**Blade chord length**	0.358m-0.728m (Linearly tapered)
Cone degree	0	**Twist angle**	Non-liner twist along the span
Rotor location	Upwind	**Blade thickness**	t/c = 20.95%
Power regulation	Stall regulated		

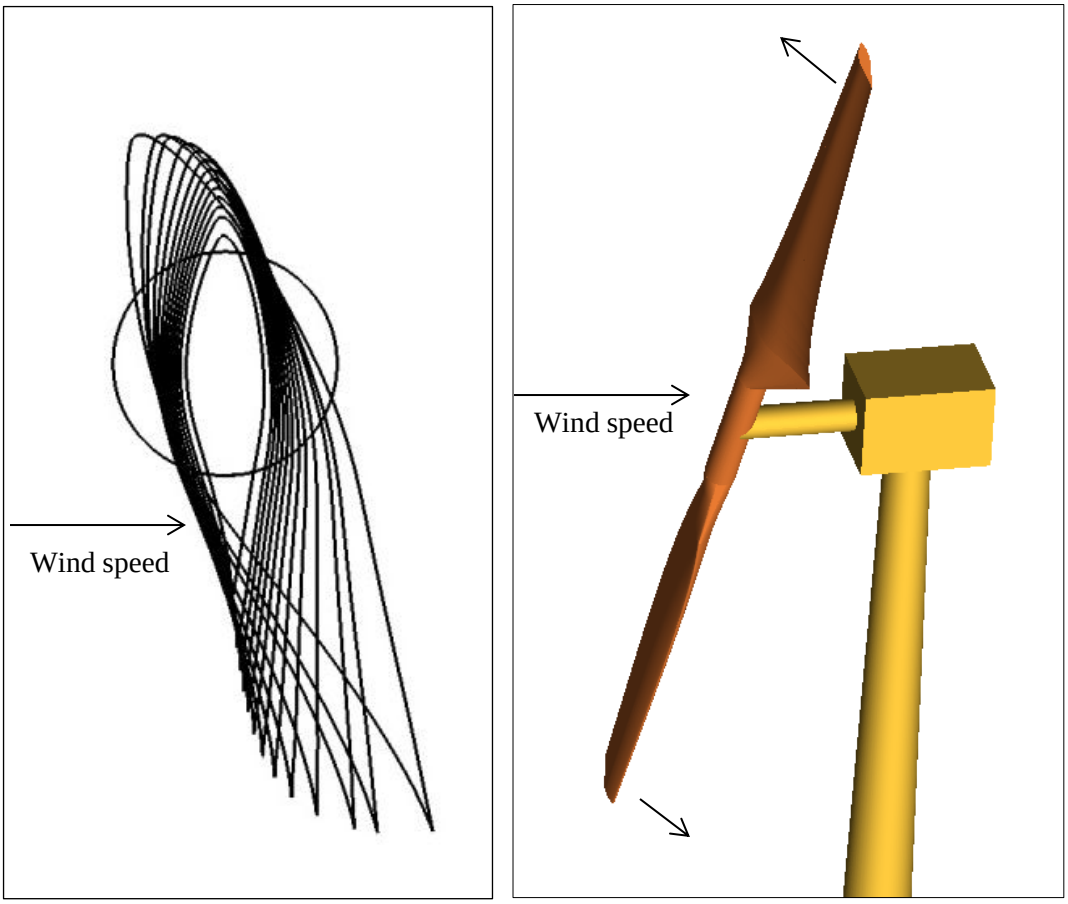

Figure 13. Cross section of the aerofoils of the blade (left) and overview of NREL Phase VI wind turbine (right).

Figure 14 shows the computational domain for the CFD study which is a half cylinder. The hub is not simulated in this study because the effects from the hub to the aerodynamic performance of the blade are very small. Even for the experiment set up for this wind turbine, the hub was also

not included because of the installed monitor in front of the wind turbine. Because of the present study uses fully-structured mesh type therefore considering the mesh topology of the domain, ignoring the hub can effectively reduce the number of computational grids which is quite significant for further complicated study on the blade with flow control devices. Moreover, according to those studies which simulated the full NREL Phase Vi wind turbine with the hub, for example studies as Hsu et al. (2014) and Li et al. (2012), the effects from the hub on the wind turbine blade is extremely small. Therefore because the hub effects on the flow around wind turbine is assumed to be ignorable, many CFD studies, especially those using structured meshing methods, just simulating the blade without the hub (Sezer-Uzol et al., 2006 and Martinez et al., 2015).

The experiment was done in wind tunnel of NASA Ames Research Centre with $24.4m \times 36.6m$ dimensions. The NREL Phase VI wind turbine was tested on a tower with $12.2m$ height therefore the outside domain is designed to be a haft cylinder with $12.2m$ radius in order to replicate the distance between the wind turbine tip and the outer wall. The front surface of the domain (velocity-inlet) is set to be 3R ($15m$) from the blade and the rear surface (pressure-outlet) is set to be 5R ($25m$) away from the blade.

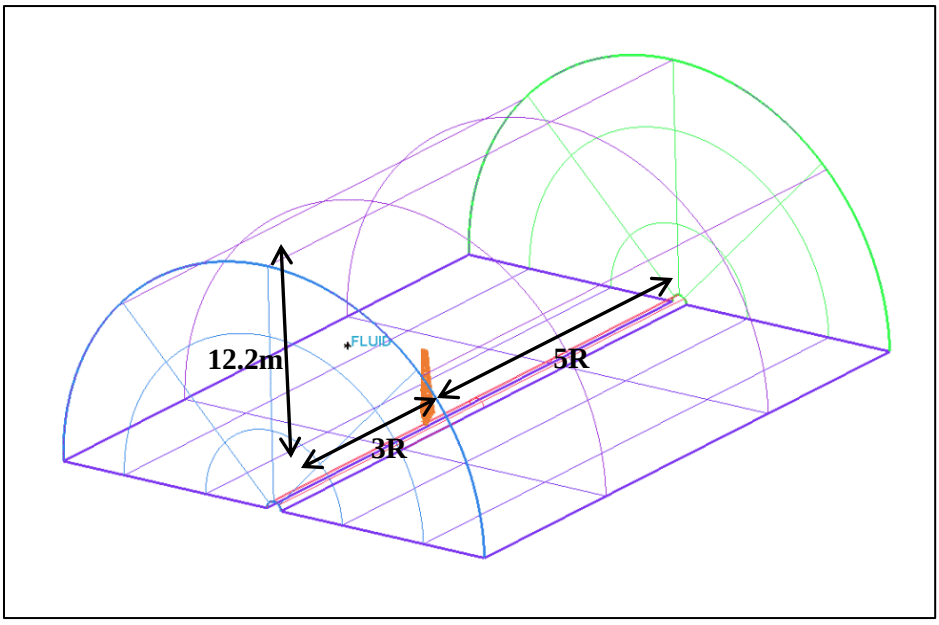

Figure 14.The whole computational domain.

3.2.2 Mesh Generation

Here a fully structured mesh is used for this study using ICEM CFD. As can be seen from Figure 16, an O-type mesh is used around the sectional S809 aerofoil. This is because the NREL Phase VI wind turbine is a flat tip wind turbine therefore for fully structured mesh it is very difficult to generate H-type mesh or C-type mesh around the aerofoil. When using $k-\omega\ SST$ for simulating CFD problems, the wall y^+ needs to be around 1 for accuracy, therefore the mesh needs to be very fine near the blade surface. The first boundary layer height of the blade tip is set to be 0.01mm which lead to the y^+ is around 1 in Fluent. The total elements of the medium mesh for $k-\omega\ SST$ are around 2 million (Figure 15 and 16). After a good effort the mesh quality is controlled as the Determinant 3*3*3 and the Eriksson skewness are above 0.3.

The Determinant can be defined as the relative determinant, which is the ratio of the smallest determinant of the Jacobian matrix divided by the largest determinant of the Jacobian matrix. In this option, the determinant at each corner of the hexahedron is found. The default range is 0–1 with a Determinant value of 1 indicating a perfectly regular mesh element and 0 indicating an element degenerate in one or more edges. Negative values indicate inverted elements.

The Eriksson skewness is an empirical criterion, obtained for a hexahedral element by dividing the volume of the closest parallelepiped by the product of its edges. It measures the shear of the parallelepiped closest to the current element using least squares approximation. The default range of values is 0–1.

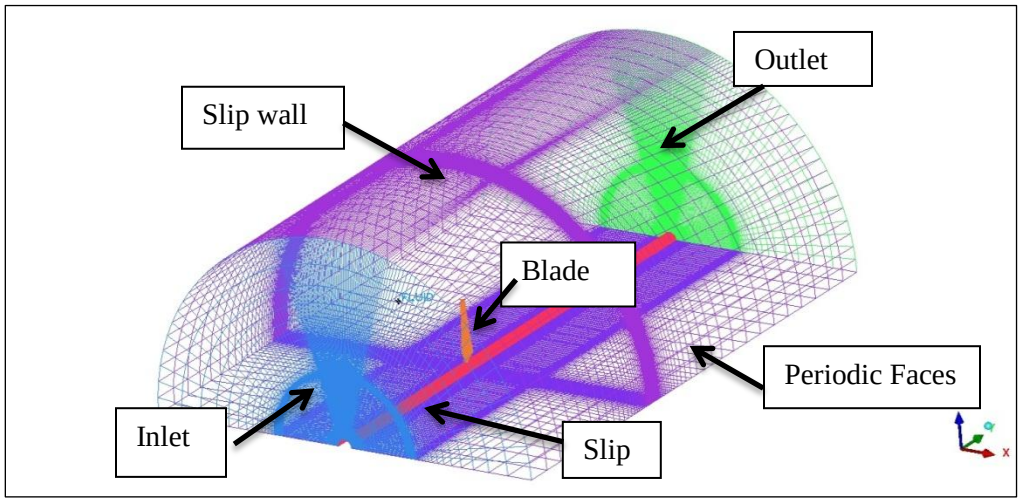

Figure 15. Mesh and boundary conditions of the whole domain

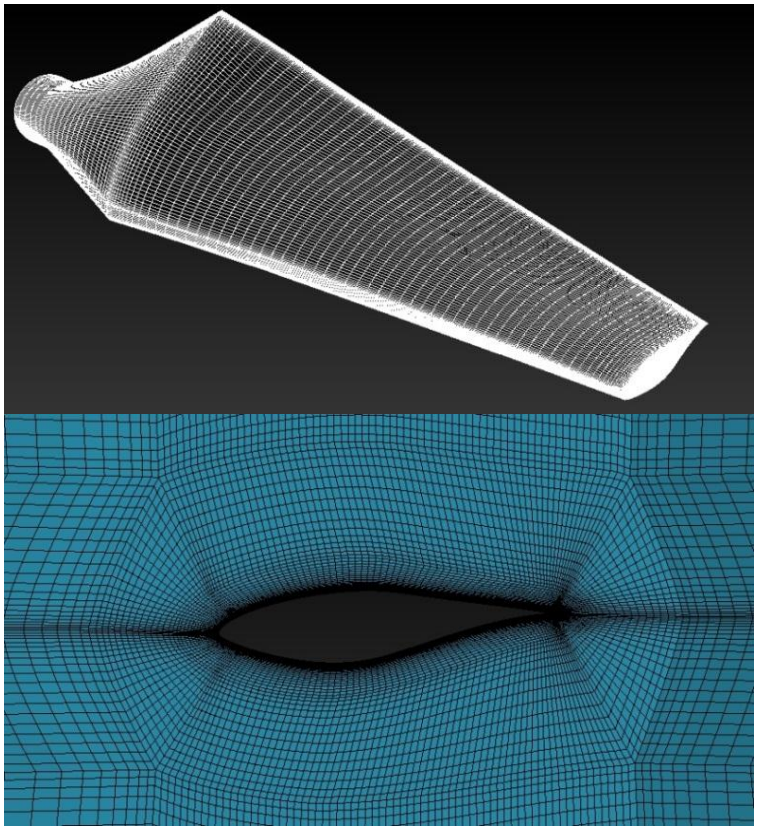

Figure 16.Blade surface mesh (top) and blade cross-sectional mesh (bottom).

3.2.3 Twist angle and AOA (angle of attack) of the blade

The local twist angle plus the blade tip pitch angle is the total twist angle of the cross-section which can be presented as $\beta + \emptyset$, where β is the blade tip pitch angle and $\emptyset$ is the cross-sectional twist angle. This parameter is very important for the blade design because it influences the AOA of the aerofoil in each cross-section, whereby influencing the C_l/C_d. Figure 17 shows the change of $\beta + \emptyset$ from the root to tip of the blade.

Figure 18 shows how the wind turbine generates power from wind. α is the angle of attack which can be determined by the wind speed and the local twist angle of the cross-section. The $F_{effective}$ which is the drive force of the wind turbine in the rotational direction is also introduced here. For the later part of the present work the $F_{effective}$ is used for estimating the aerodynamic performance of 2D cross-sectional aerofoils.

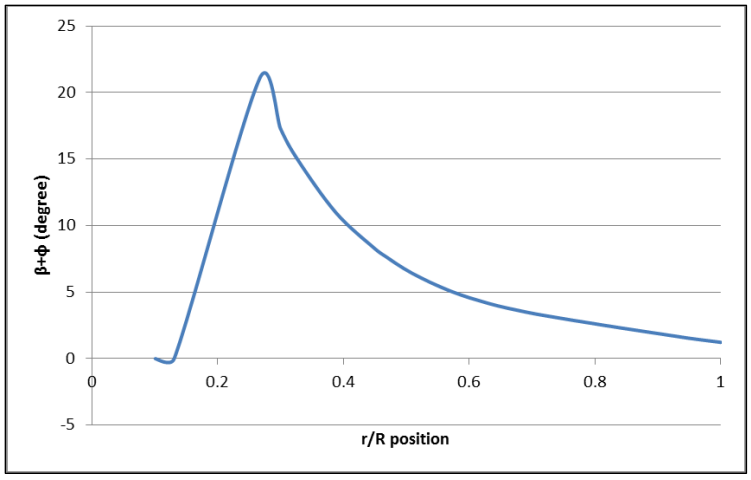

Figure 17. β + ∅ from root to tip of NREL Phase VI wind turbine blade

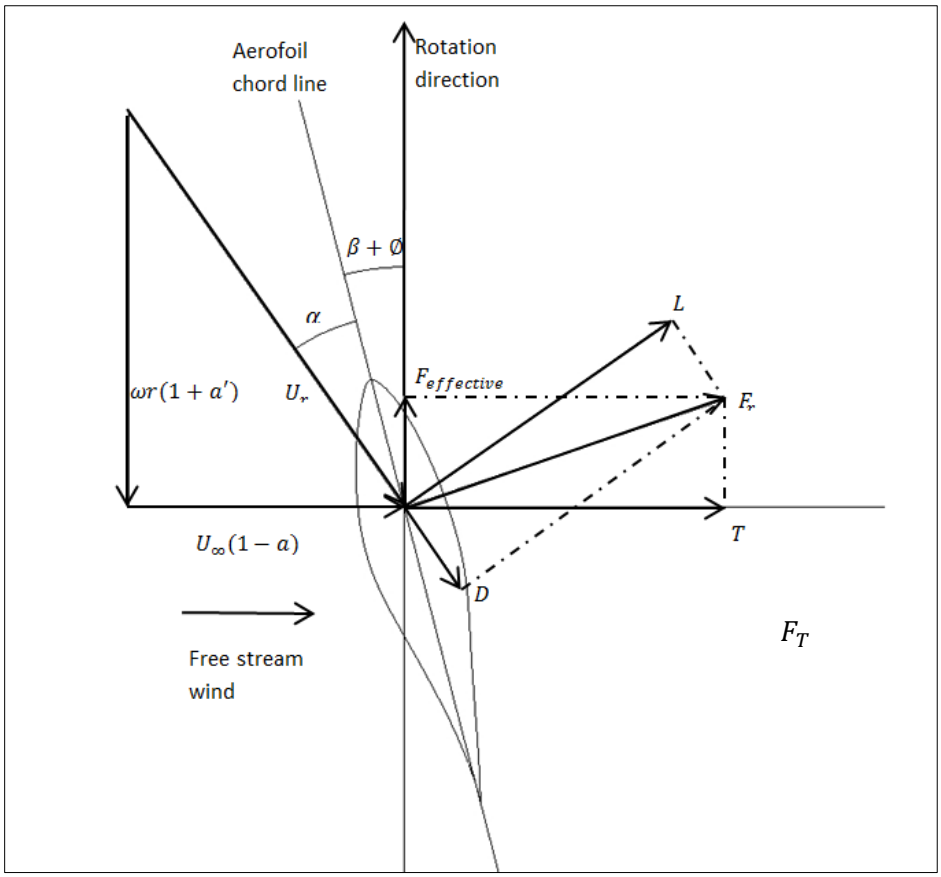

Figure 18. HAWT's cross-sectional aerofoil aerodynamic angles and forces.

In Figure 18, β is the blade tip pitch angle and ∅ is the local twist angle of the sectional aerofoil. Therefore the total pitch angle of the aerofoil chord line to the rotation plane is $\beta + \emptyset$. L and D represent the lift force and drag force of the aerofoil respectively. F_r represents the resultant force

from L and D. F_T represents the induced thrust force from F_r. U_r is the resultant velocity and α is the angle of attack. From the wind turbine vortex system theory (Hansen, 2000), the incoming wind flow is affected by the rotating wind turbine. So the induction factor a and a' are introduced and the resultant flow velocity can be decomposed into axial and tangential component which are $U_\infty(1-a)$ and $\omega r(1+a')$ respectively. This theory is used for studying the 2D aerodynamics of the cross-sectional aerofoil of the wind turbine and it is necessary for the BEM method. In the present work all cases are run with CFD method and proper outer boundary condition settings therefore the induction factors are not input factors.

Figure 19 shows the angle of attack along the blade in different wind speeds. It can be seen that the AOA increases significantly when wind speed is getting high and the AOA will reach an average of about 27 degree along the blade when wind speed is 15m/s. This is a very large AOA and the aerodynamic performance of the aerofoil will keep lowering which leading to very low power coefficient of the wind turbine.

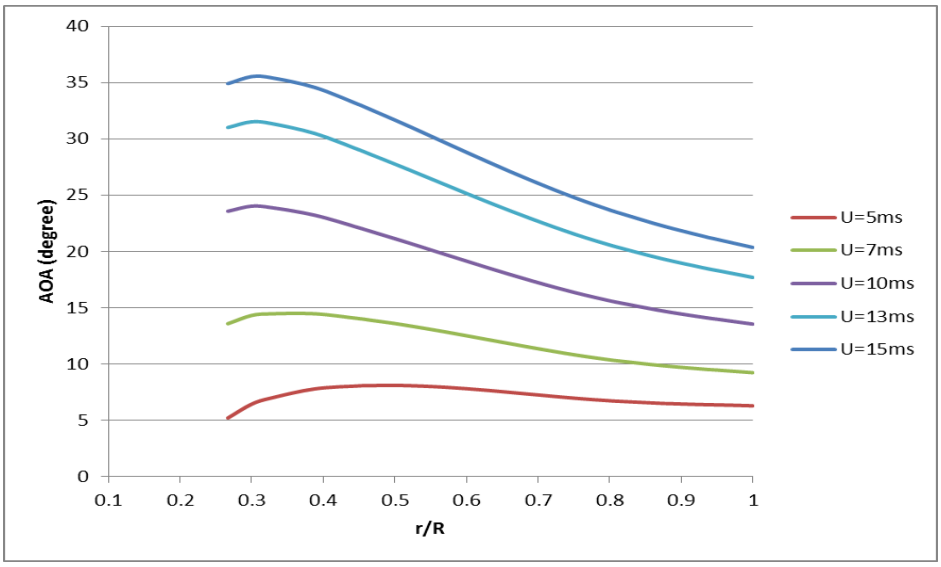

Figure 19. AOA from root to tip of the blade in different wind speeds.

3.2.4 Reynolds number of the blade

As introduced in Chapter 2, Reynolds number is used to help predict whether the flow is laminar flow or turbulent flow. It can be calculated by the equation: $Re = \frac{\rho U_r L}{\mu}$, where L is the chord length of the aerofoil in the cross-section. When the Reynolds number is low, viscous forces are

dominant and the laminar flow occurs while high Reynolds number means the inertial forces dominate and the turbulent flow occurs. Table 4 shows the Reynolds numbers for the root and tip of the NREL Phase VI blade in different wind speeds respectively.

Table 4. Reynolds number at the root and tip of NREL Phase VI blade

Wind speed (m/s)	Reynolds number (root)	Reynolds number (tip)
5	552767	920331
7	602535	927855
10	696585	943642
13	806558	964591
15	885831	981264

According to the results for Reynolds number in table 4, the flow is assumed to be turbulent in all wind speeds and all cross-sections from root to tip.

3.2.5 Fluent setup

The Ansys Fluent 14.0 is selected to be the flow solver for this study.

Boundary conditions

After generating the meshes, the meshes can be imported to Fluent for simulating. The boundary condition setting is one of the most important steps for CFD simulation. The detailed boundary conditions of this study are shown in table 5 and Figure 15.

Table 5. Boundary conditions setting.

Parts	Boundary condition
Blade	No-slip wall
Outer Boundary	Slip wall
Inlet	Velocity inlet
Periodic Faces	Periodic
Outlet	Pressure-outlet
Inner Boundary	Slip wall

The velocity inlet boundary conditions set in the present study is to define the wind velocity on the front surface of the computational domain. Using this boundary condition the total (or stagnation) pressure is not fixed but will rise, in response to the computed static pressure, to whatever value is necessary to provide the prescribed velocity distribution (ANSYS Fluent user guide). Because the present study assumes the flow around the wind turbine blade is incompressible therefore no temperature will be added in the settings. It is noted that because the moving frame motion is activated therefore the velocity must set to be Absolute reference frame in the present study.

As for the wall boundary conditions, which are used to bound fluid and solid regions, the present study uses two types of this boundary condition which are no-slip wall and slip wall. In viscous flows, the no-slip wall boundary condition is applied for the wind turbine blade as stationary because of the activated moving frame motion. The wall roughness effects are not considered in the present study therefore these settings are kept as default. The outer and inner boundaries are set to be slip wall because the wall shear effects at these boundaries are not considered and therefore the wall boundary layer can be ignored. This situation means that there is no wall y^+ requirement for these boundaries which effectively reducing the mesh size of the whole domain.

The pressure outlet boundary condition requires the user to define a specified static (gauge) pressure at the outlet boundary which is the rear surface of the domain in the present study. This value is only used when the flow is subsonic. The static pressure value is relative to the operating pressure (101325 pa as the standard atmosphere pressure) and is set to be 0 in the present study.

The periodic boundary condition is normally applied when the physical feature and expected flow structure have a periodically repeating nature. As for a wind turbine blade, the rotational periodic condition is applied for the two corresponding surfaces of the domain which means all the flow information and solution is the same at these two surfaces.

In this case the moving frame motion of FLUENT is used and the rotating speed of the blade is constantly 7.54 rad/s. According to the experimental setup from the official report, the turbulence intensity and length are set to be 0.1% and 0.02 respectively.

Here even though in realistic the wind turbine is operating in a changing wind speed condition, but it is very hard to simulate such condition in the CFD case. Therefore in this study several wind speeds from 5m/s to 15m/s were simulated respectively and to see the wind turbine's

performances in there conditions. So the velocity-inlet boundary condition was employed with constant wind speed in each case.

As for the symmetry boundary condition, in FLUENT it can be summarized as: 1) zero normal velocity at a symmetry plane; 2) zero normal gradients of all variables at a symmetry plane. Such conditions determine a zero flux across the symmetry plane, which is required by the definition of symmetry. Since the shear stress is zero at a symmetry boundary, it can also be interpreted as a 'slip wall' when used in viscous flow calculations (FLUENT user guide). The present work follows the parameters of the NASA Ames wind tunnel therefore the outer wall is set to be $12.2m$ from the blade tip and is set to be 'symmetry' here for the 'slip wall' boundary condition. Using such boundary condition ignores the boundary layer at the outer wall which leading to smaller mesh size and less computation time.

Solution method

In this project the coupled algorithm and the Green-Gauss Node based discretization scheme are applied. The second order upwind criterion is set for the momentum, turbulent kinetic energy and specific dissipation rate. The simulations were set to be steady flow condition when wind speed is below 10m/s. However when the wind speed is higher than 13m/s, the blade exhibits large scale separation and the flow is no longer steady. Therefore unsteady simulations were carried out for 13m/s and 15m/s wind speed. In these cases, the time-step size was set to be 0.0006s with 20 sub-iterations per time-step. Simulations were run on the university HPC system ICEBERG. In the numerical study, the wind speed U is set varying from 5m/s to 15m/s. The rotational speed of the wind turbine is 7.54 rad/s, leading to the tip speed ratios (TSR) from 2.78 to 7.6 for the different wind speeds.

3.3 Results

In this part, the aerodynamic forces are analysed in the context for wind turbine energy extraction. This is achieved by integrating the pressure and skin friction forces and correspondingly the moment on the blade and projecting them in the direction of rotation. Pressure distributions and streamlines near the blade are also analysed. The comparison of the pressure coefficient distribution with the experimental data is presented. In this study five radial positions are selected for analysis at r/R= 0.3, 0.47, 0.63, 0.8 and 0.95, respectively.

3.3.1 Wall y^+ Study

The turbulence model selected for this study is the k-ω SST which requires a wall y^+ to be around one for accuracy. As shown in Figure 20, the wall y^+ under wind speed = 10m/s is around one on most area of the blade. Moreover, Figure 21 shows y^+ at r/R = 0.8 span section where the value is controlled in the range from 0.2 to 1.8.Because all meshes are with the same first layer height, and the Reynolds number of the blade near root side is relatively lower than the tip side, the wall y^+ varies from 0.1 to 2 along the blade. This range of y^+ is good enough for the turbulence model used to capture the boundary layer near the blade and for computational accuracy.

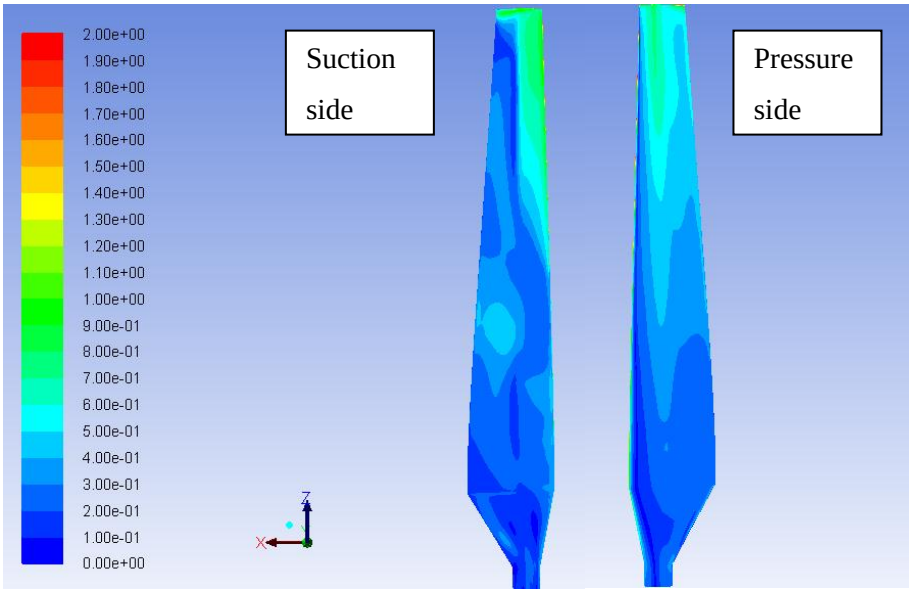

Figure 20. Wall y^+ contour under wind speed = 10m/s.

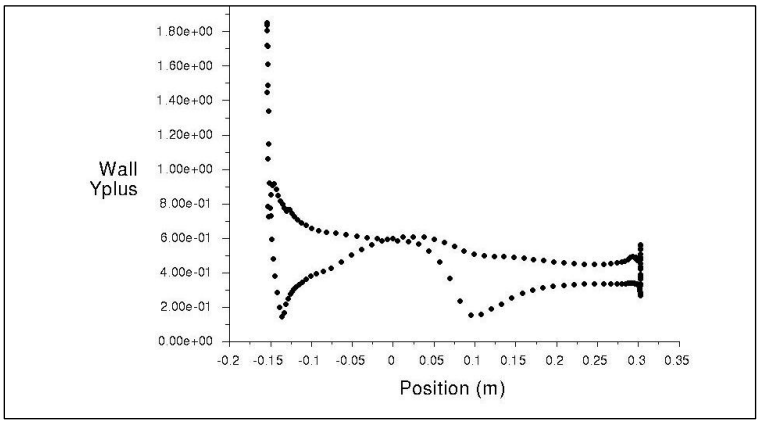

Figure 21. Wall y^+ at r/R = 0.8 span section.

3.3.2 Mesh Sensitivity Study

The mesh sensitivity study is a very important part in numerical simulations. In this study, three mesh sizes are tested, at 1 million, 2 million and 4 million, respectively, at the wind speed of 7m/s. The computed torques of the blade is shown in Table 6. The torque from the experimental result is 780Nm at 7m/s wind speed. According to the table it can be seen that the computed torque shows some small variation with the changes in all three cases. The computational torque at 4 million cells gives a closer comparison with the experimental value, and the comparison is reasonably good. Considering the computational time and resources, the 4 million cell mesh is used in the following study without further refinement. The reason is that the following CFD study on the wind turbine blade with flow control devices will keep increasing the mesh size, for example with the same meshing methodology the mesh size will be as large as 8 million for the turbine blade with microtabs, and the current 4 million mesh has been already proved to be able to predict highly accurate results. Figure 22 and 23 show that the pressure coefficients at r/R = 0.47 and 0.8 are quite similar for the three mesh sizes.

Table 6.Simulated torques of different meshes.

Mesh sizes	Torque (N*m)
1 million	814
2 million	809
4 million	796

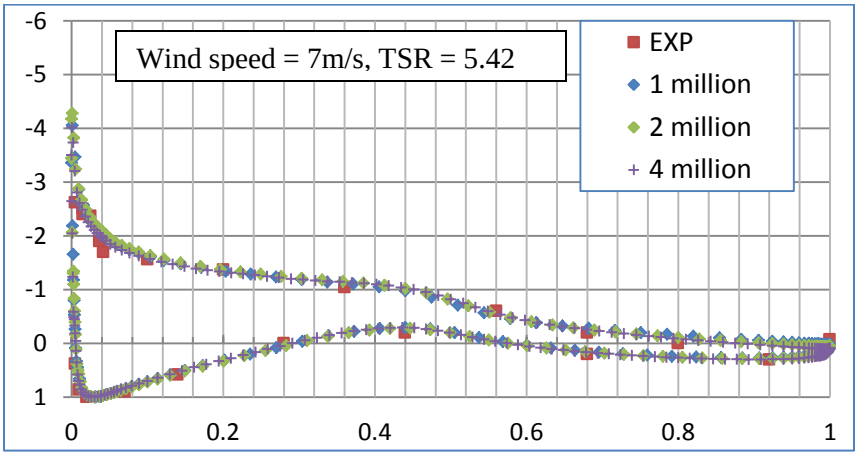

Figure 22. Pressure distribution comparison of 3 meshes at r/R = 0.47 section.

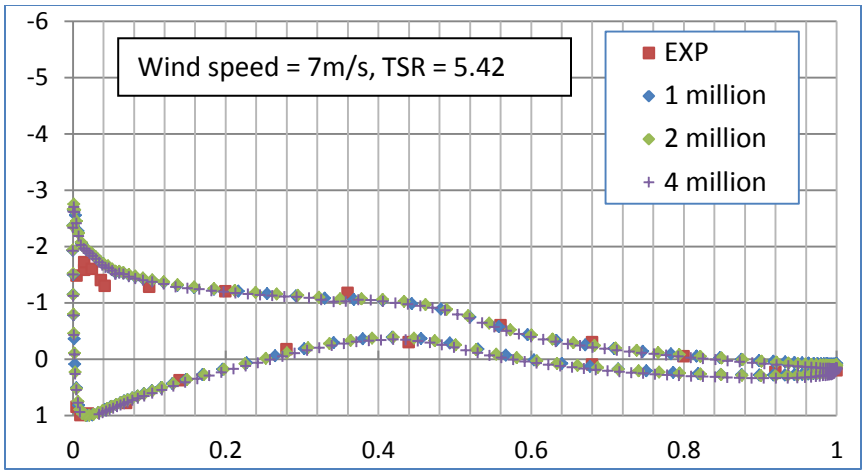

Figure 23. Pressure distribution comparison of 3 meshes at r/R = 0.8 section.

3.3.3 Wind Turbine's Performance under Different TSR

In the initial study of the present work the $k-\omega\ SST$ turbulence model, Realizable $k-\varepsilon$ model and S-A turbulence model are selected to be compared in order to find out which model can predict more accurate results. The equations and details of these three models were introduced in chapter 2. All these three models are tested under RANS solution with the Coupled scheme in ANSYS Fluent. All cases were converged within 7,000 iterations according to the moment coefficient history. The comparison between the computed results and the experimental data is presented in Figure 24. It can be seen that the torque from the Realizable $k-\varepsilon$ turbulence model shows the biggest difference when compared to the experimental torque by over predicting the torque of the blade in all wind speed cases. Both S-A and $k-\omega\ SST$ models show accurate results for 5m/s and 7m/s wind speed cases however the $k-\omega\ SST$ model show much better results at 10m/s and 13m/s wind speeds. For the 15m/s wind speed case, because of the unsteady flow conditions around the blade, both S-A and $k-\omega\ SST$ models are showing some errors. Therefore considering the convergence history and torque predictions from these three models, the k-ω SST turbulence model shows higher and stable accuracy at all speed cases. Therefore considering the further study on the flow control devices, this study chooses the k-ω SST turbulence model for all of the CFD cases.

This part includes results and graphs of the CFD study on the NREL wind turbine blade with comparison to the experimental data in different wind speeds.

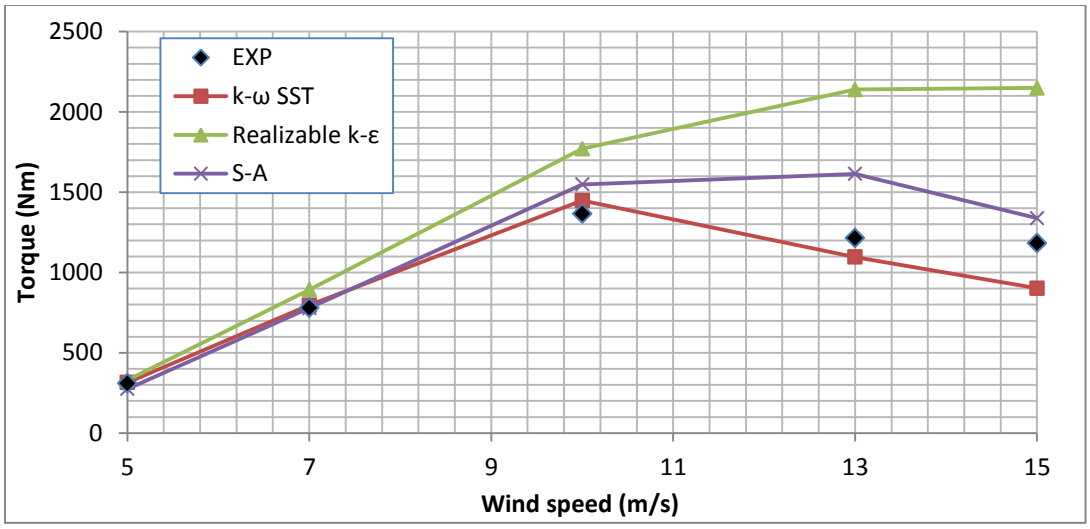

Figure 24. Torque comparison between different turbulence models.

Wind speed = 7m/s, TSR = 5.42

The cut-in wind speed of NREL Phase VI wind turbine is 6m/s so the 7m/s wind speed is a relatively low speed. In this situation, the flow is attached around the blade.

Surface Static Pressure

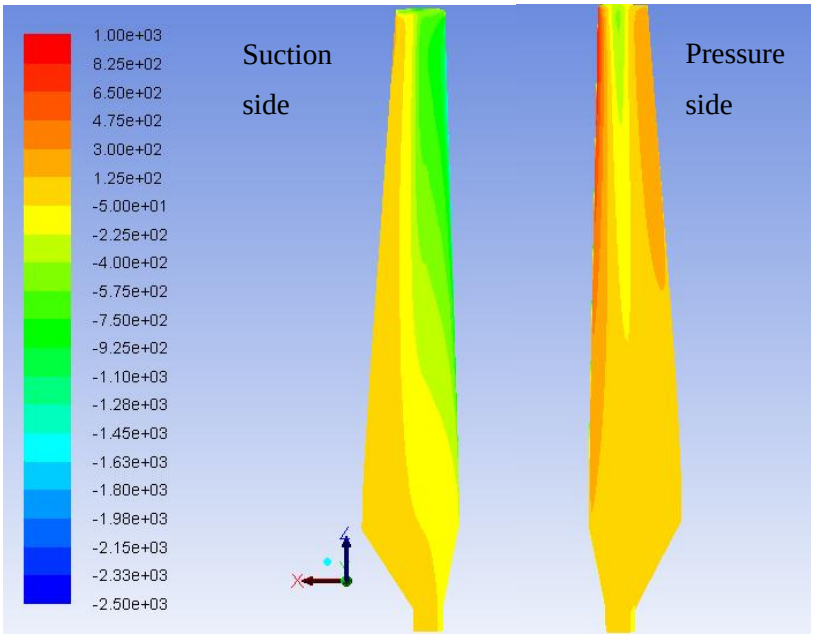

Figure 25. Surface static pressure under wind speed = 7m/s (pascal)

It is noted that here the operating air pressure for the wind turbine is set to the atmospheric pressure which is 101,325 pa. Therefore here the absolute pressure (actual pressure on the surface) is the static pressure plus the atmospheric pressure. This means that the positive value of static pressure means the pressure on the surface is higher than the atmospheric pressure and the negative value means the actual pressure on the surface is lower than the atmospheric pressure. As for the U=7m/s situation which can be seen from Figure 25, the maximum pressure on the upwind surface of the blade is around 900 pascal near the tip on the pressure side. On the suction side the negative static pressure value means that at this area the pressure on the surface is lower than the atmospheric pressure.

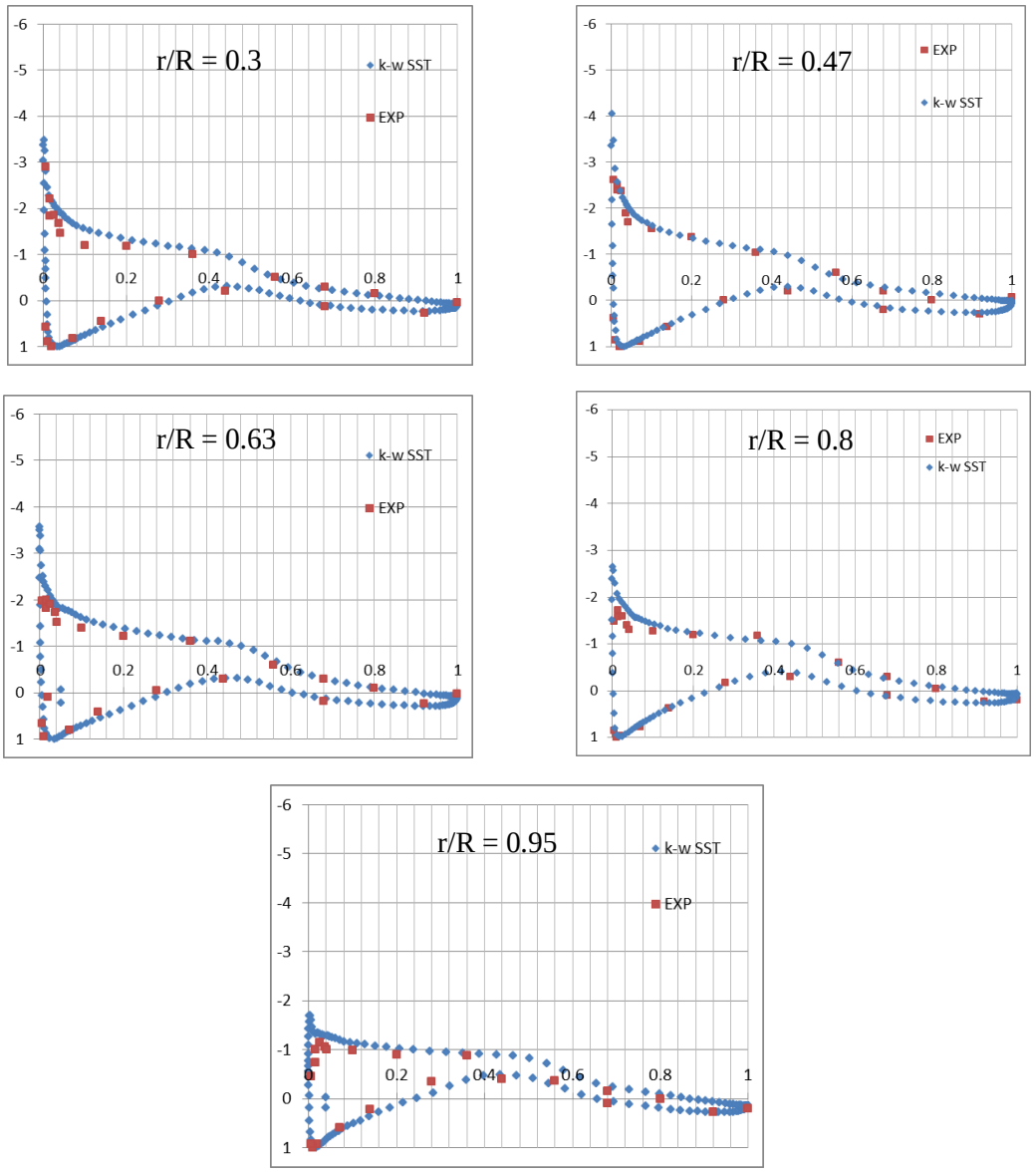

Figure 26. Pressure coefficient comparison at wind speed = 7m/s at different r/R sections

Pressure coefficient (compared with experimental data)

According to Figure 26, the pressure coefficients in different span positions from the computational results are very close to the experimental results. The CFD results predict a relatively higher negative pressure coefficient in the leading edge area around the whole blade. Moreover from the details of pressure distribution, it can be seen that the flow on the suction side of the blade is attached even at r/R = 0.3 span section from the tip.

Velocity streamlines at different r/R positions

Figure 27 shows that when wind speed = 7m/s the streamlines around the whole blade are well attached along the blade. Therefore the lift coefficient and power coefficient could be relatively higher at this wind speed.

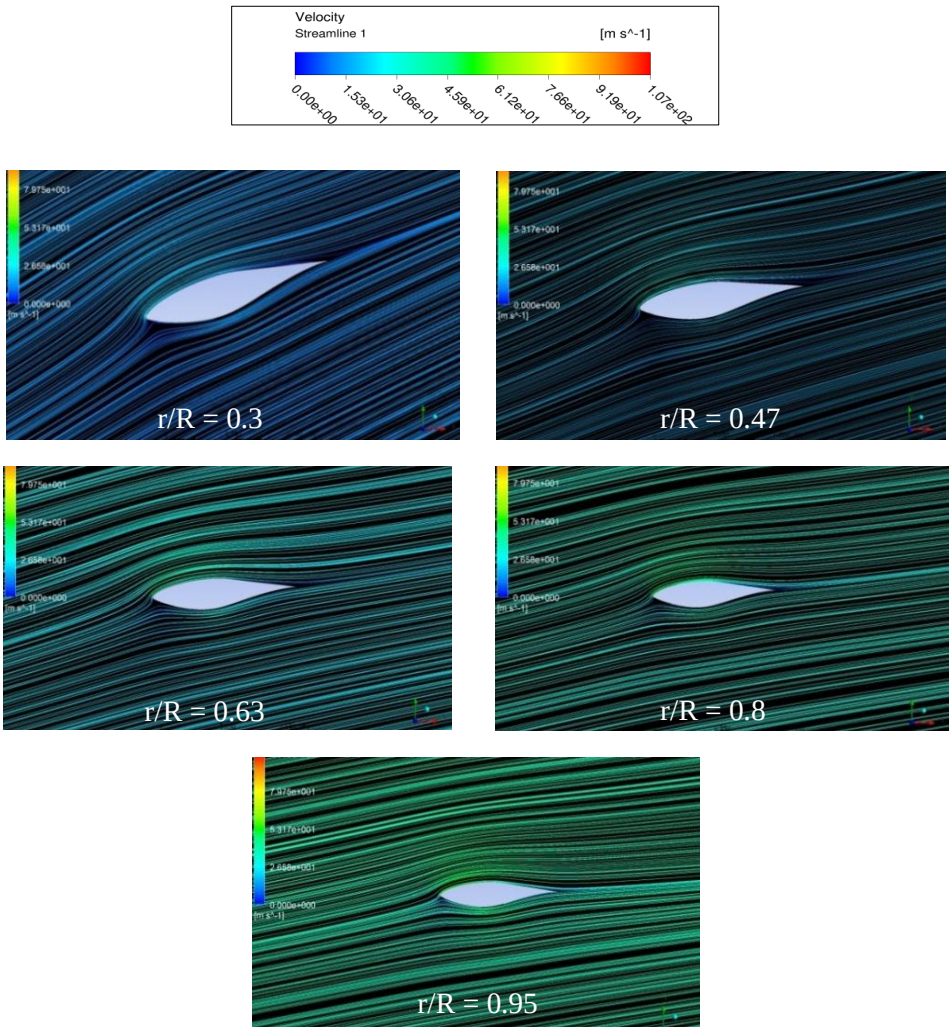

Figure 27. Velocity streamlines around the blade at different span position

Wind speed = 10m/s, TSR = 3.79

When the wind speed reaches 10m/s, stall begins to happen around the bottom area of the blade. The aerodynamic stall leads to wind turbine vibration and lowering the power coefficient of the wind turbine and therefore it is significant to analysis the wind turbine's aerodynamic performance under such situation.

Surface static pressure

Figure 28 shows that when the wind speed reaches 10m/s, the pressure on the suction side near root is not as uniform as that that from the 7m/s case. This condition is mainly due to the flow separation at that area.

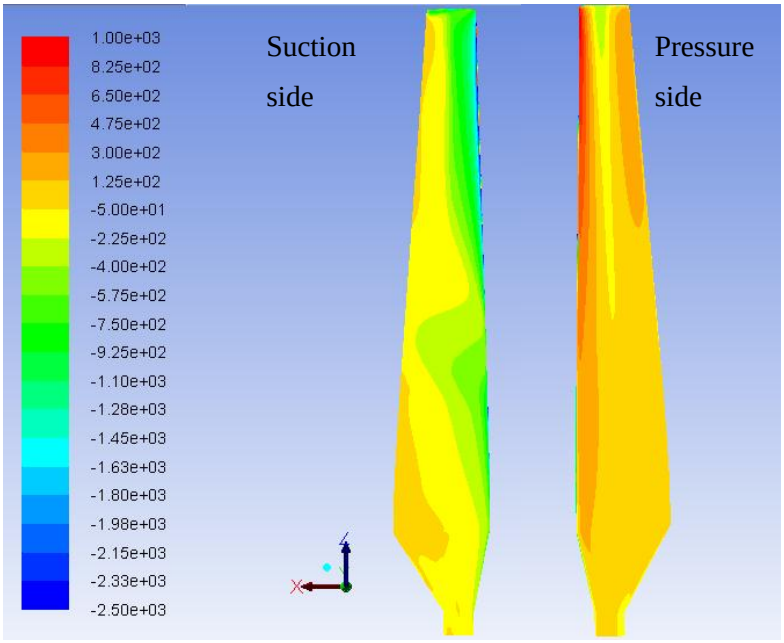

Figure 28. Surface static pressure under wind speed = 10m/s (pascal)

Pressure coefficient (compared with experimental data)

According to Figure 29, when the wind turbine begins to stall, the CFD results predict relatively less accurate results in the stall areas. At r/R = 0.47 span position the pressure in the first half suction side is over predicted and in r/R = 0.63 span position the pressure coefficients are also

underestimated by the CFD results on the suction side. Such situation should probably because of the separation on the suctions side of the blade. Using the current k – ω SST turbulence model with the steady RANS solution may not able to accurately capture the transition point as that from the experiments. However for the other area of the blade where no large separation happens, the current CFD methodology still predicts very accurate results when compared to the experimental data.

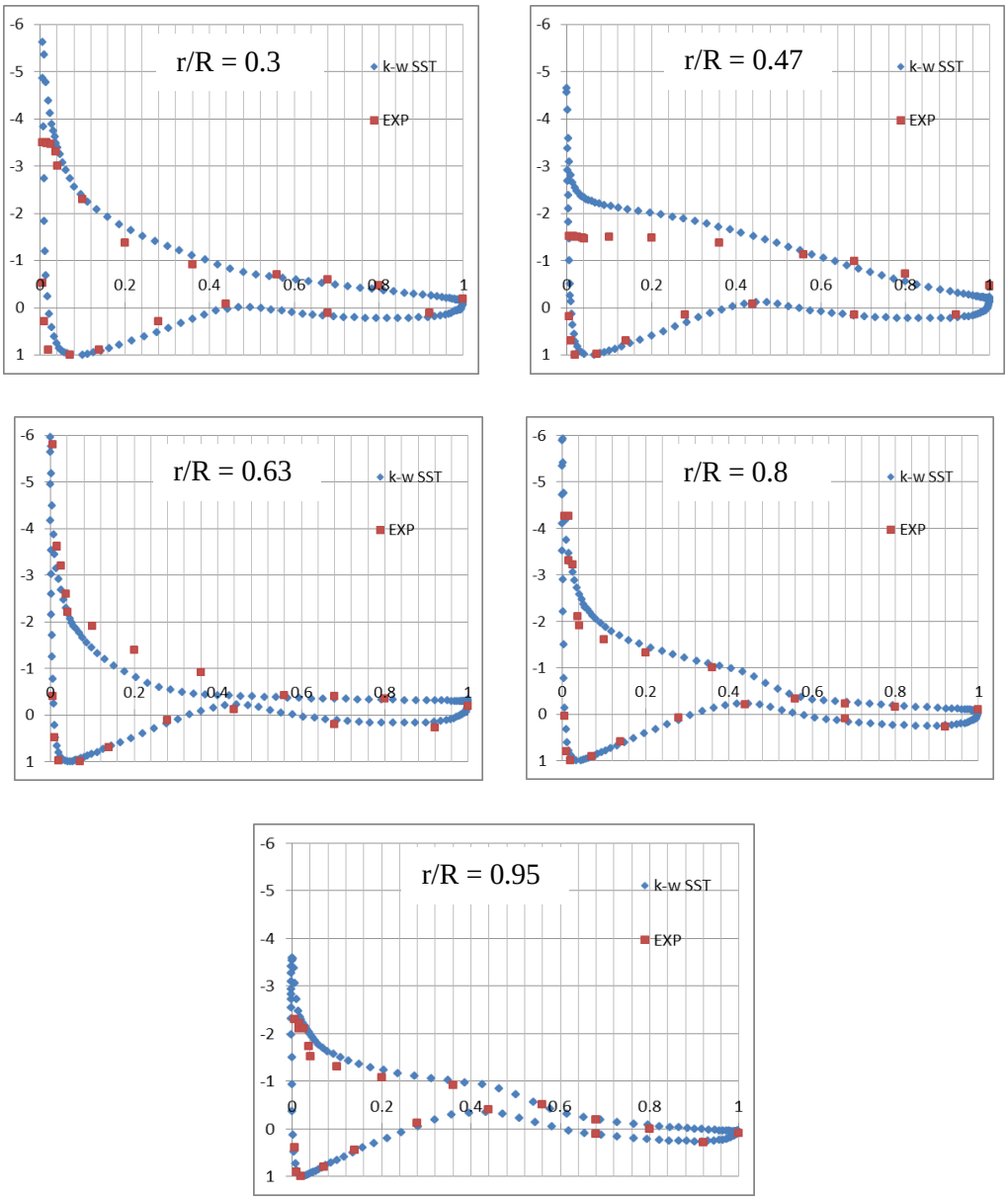

Figure 29. Pressure coefficient comparison at wind speed = 10m/s

Velocity streamlines at different r/R positions

As can be seen from Figure 30, stall happens in the area below the 0.8 r/R span position of the blade. Some obvious detached flows can be seen from the graphs. Stall affects the wind turbine's performance and will decrease its power coefficient and therefore it is significant to reduce stall of the blade.

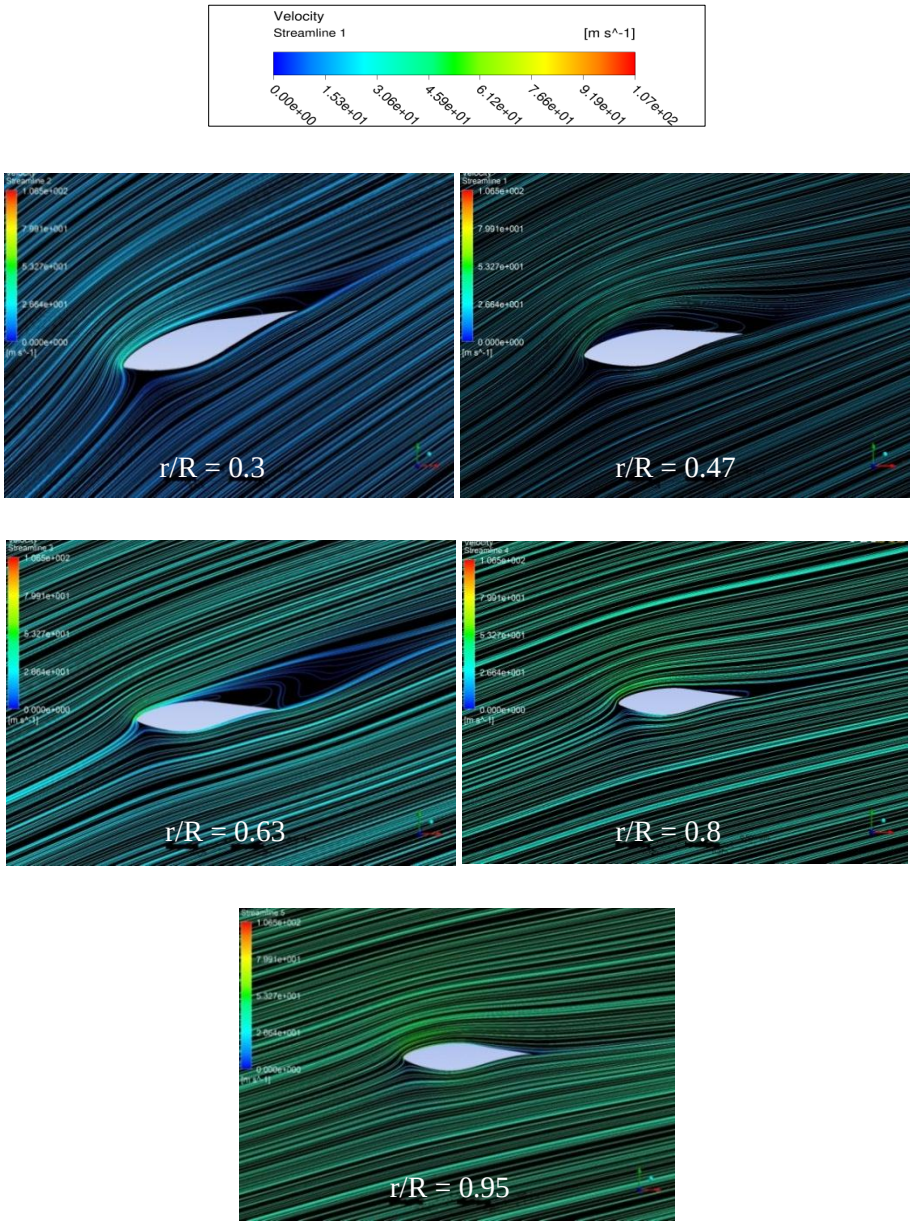

Figure 30. Velocity streamlines at different span positions (U = 10 m/s)

Wind speed = 13m/s, TSR = 2.92

In the 13m/s wind speed situation, the AOAs of most cross-sectional aerofoils of the blade are very large and therefore large separations happens on the suction side from the root to near the tip of the blade. Due to the unsteady conditions from these large separations, the URANS solution is carried out for the 13m/s and 15m/s wind speed cases. The time step is set to be 0.0006s for the time accurate simulations with an auto-save setting for every 400 time steps. Therefore the figures and data below are from an actual time = 2.04s when the shaft torque of the wind turbine is very close to the average value of the torque. In the present study the flow condition of such actual time is assumed to be the average flow condition around the wind turbine. The details of the selection of this instantaneous time can be found in later torque calculation part.

Surface static pressure at time = 2.04s

When wind speed is as high as 13m/s, the flow around the blade separates on most area on the suction side which means the blade is in full-stall situation. From the computed data at the instantaneous time 2.04s, it can be seen that the pressure on the suction side is very irregular because of the large separations (Figure 31).

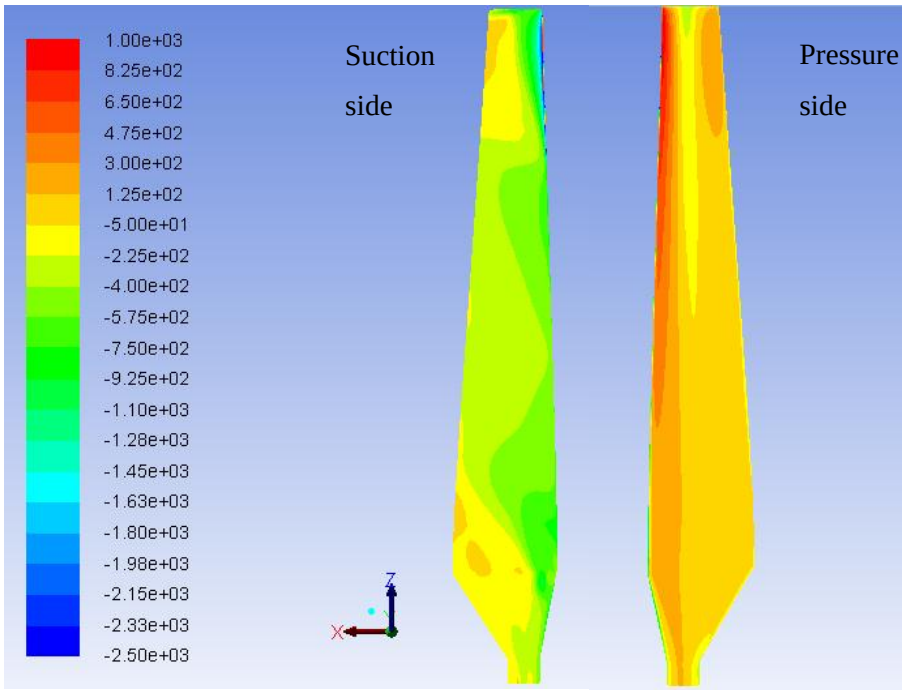

Figure 31. Surface static pressure under wind speed = 13m/s (pascal, time = 2.04s)

Velocity streamlines at different r/R positions (Wind speed = 13m/s, time = 2.04s)

As can be seen from Figure 32, at 13m/s speed, most area of the blade is in the stall situation. At this wind speed the flow is quite unsteady along the suction side of the blade and therefore the Figure is just for an instantaneous time (2.04s).

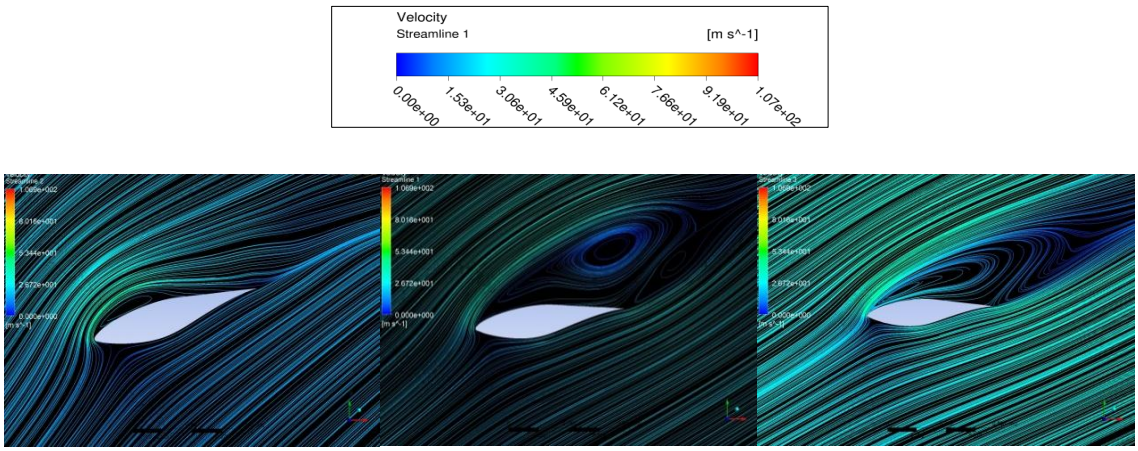

r/R = 0.3 r/R = 0.47 r/R = 0.63

r/R = 0.8 r/R = 0.95

Figure 32. Velocity streamlines at different span positions (U = 13 m/s, time = 2.04s)

Wind speed = 15m/s, TSR = 2.52

Similar as the 13m/s wind speed case, the suction side of the blade has even larger separation. At this situation the unsteady simulation is also applied and some of the detail of the frequency and torque calculation method can be found in later part of this chapter. The instantaneous case at time = 3.12 is selected for presenting the flow condition and pressure coefficient because at this time the wind turbine is generating the mean torque.

Surface static pressure at time = 3.12s

From Figure 33 it can be seen that because of the full span separation on the suction side of the blade, the pressure on the suction side is fully irregular at the instantaneous time = 3.12s.

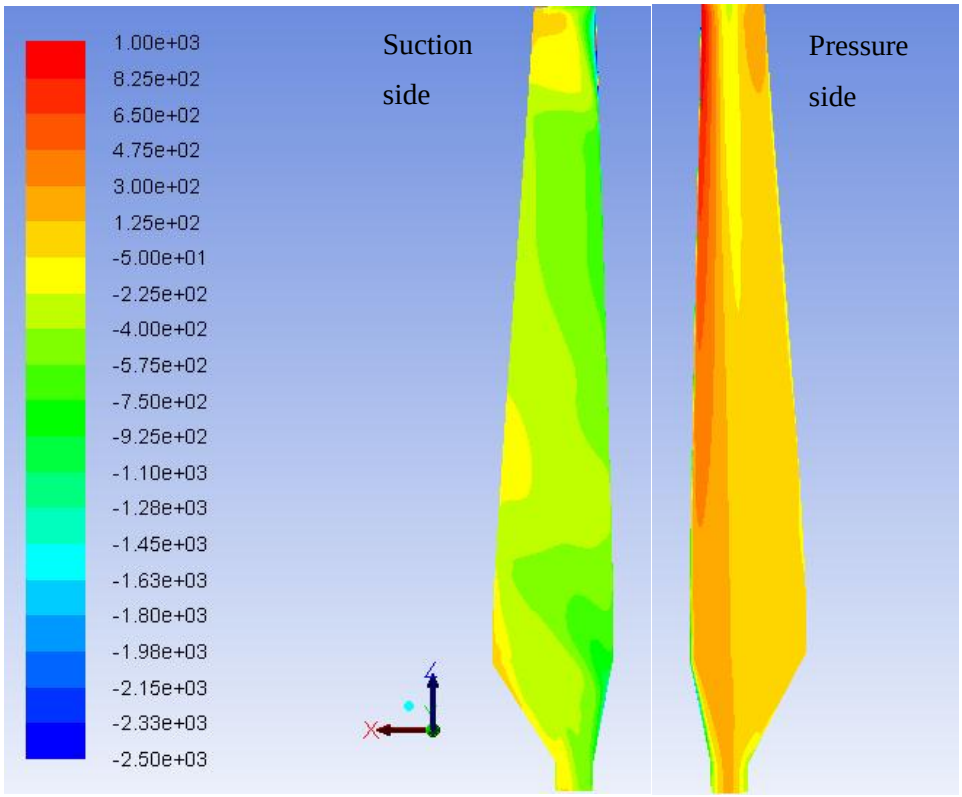

Figure 33. Surface static pressure under wind speed = 15m/s (pascal), time = 3.12s

Pressure coefficient (compared with experimental data, wind speed = 15m/s)

As shown in Figure 34, the CFD simulation predicts a fully stalled situation on the whole blade when wind speed reaches 15m/s. The result is very close to the experimental data except in the near root area of the blade, which is fully stalled in the experimental data.

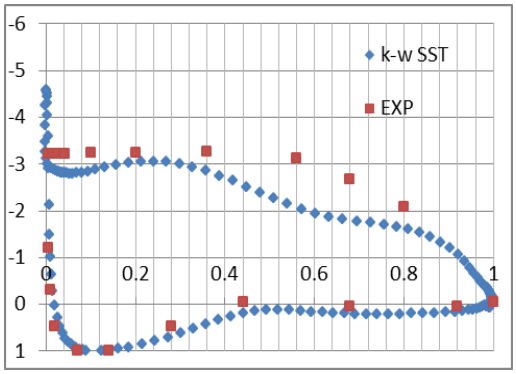

r/R = 0.3

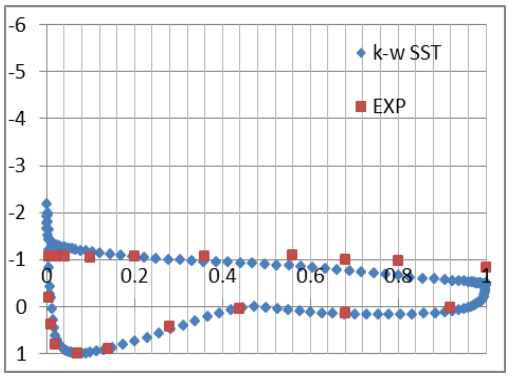

r/R = 0.47

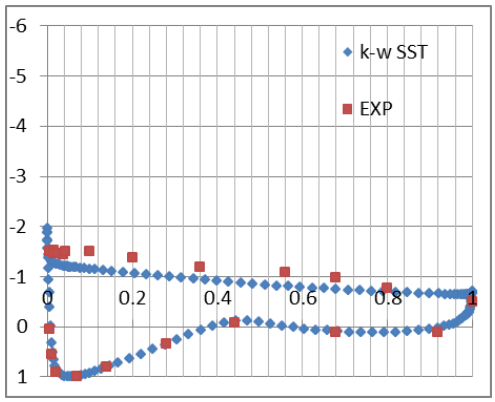

r/R = 0.63

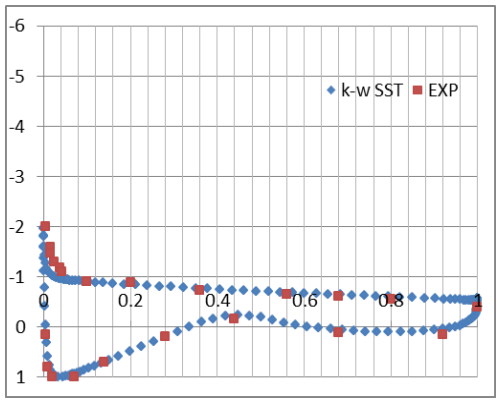

r/R = 0.8

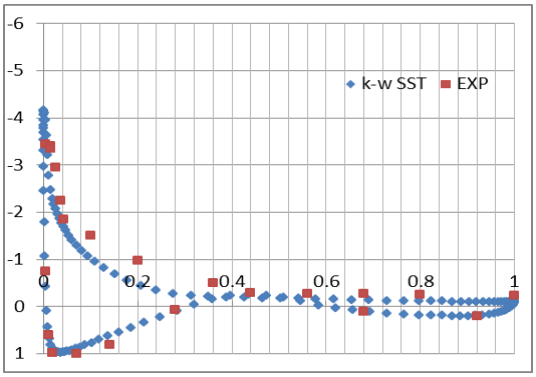

r/R = 0.95

Figure 34. Pressure coefficient comparison at wind speed = 15m/s, time = 3.12s

Velocity streamlines at different r/R positions (Wind speed = 15m/s, time = 3.12s)

Figure 35 shows that the blade is in a completely stalled situation. Even at r/R = 0.95 span section the flow on the suction side is separated. In such situation the wind turbine is not able to perform very well and with a relatively low power coefficient. For the 15m/s wind speed case, the suction side of the blade is full with spanwise flow and Figure 35 only shows the streamlines projected on the 2D cut plane which cannot show the real 3D flow conditions. However it is still worth showing these figures for clear views of the large separation structure on the suction side of the sectional aerofoil.

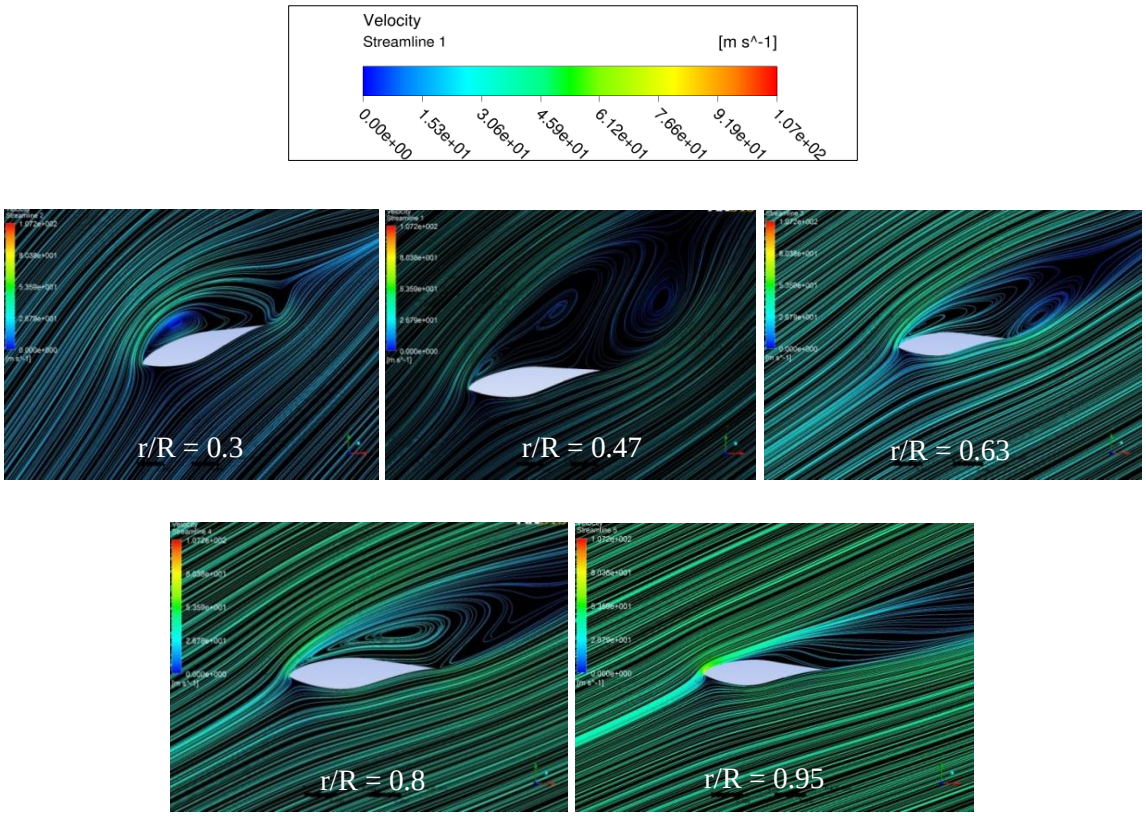

Figure 35. Velocity streamlines at different span positions (U = 15 m/s, time = 3.12s)

In summary, referring to the whole comparison of the pressure distribution between the computational result and experimental data it can be seen that the CFD method is able to predict reasonably the pressure and flow condition along the blade, especially at lower wind speed range where the blade is not stalled. When the blade is fully stalled, using the $k-\omega$ SST turbulence model with the URANS solution show some increasing errors when compared to experimental data in an instantaneous flow condition, but the errors are still in an acceptable range.

3.3.4 Surface Friction lines of Different Wind Speeds

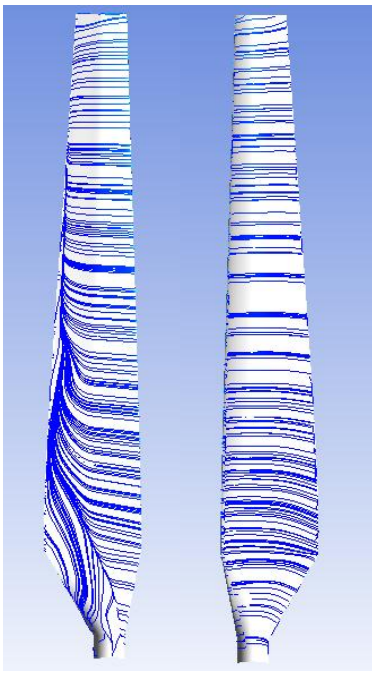

Wind speed = 7m/s

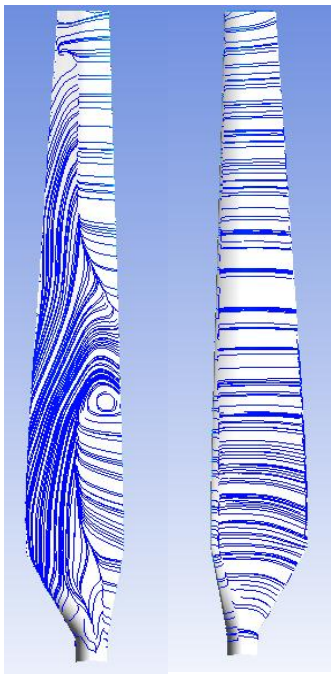

Wind speed = 10m/s

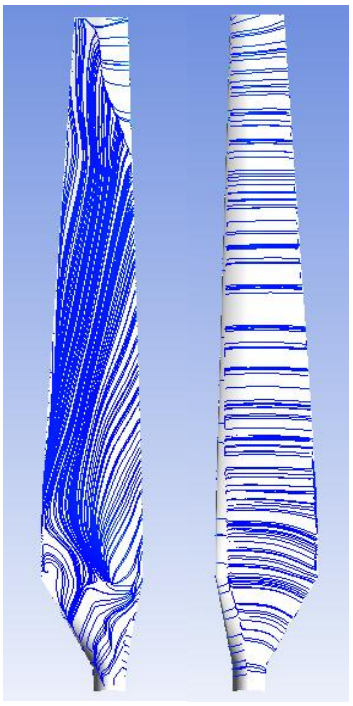

Wind speed = 13m/s (t = 2.04s)

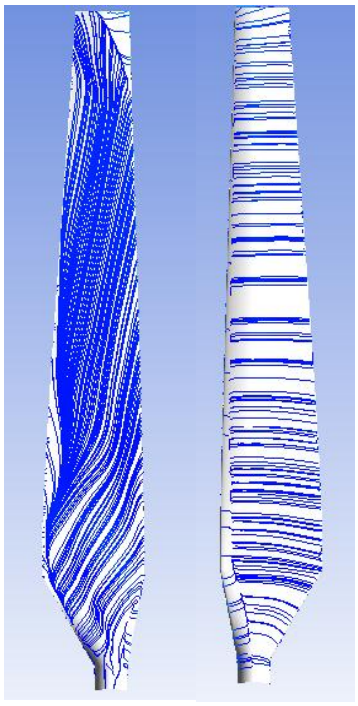

Wind speed = 15m/s (t = 3.12s)

Figure 36. Surface streamlines of the wind turbine from U=7m/s to 15m/s.

Figure 36 shows the surface streamlines of the wind turbine from the wind speed 7m/s to 15m/s. It can be seen that even in the wind speed = 7m/s situation there is some radial flow around the suction side of the blade. When the wind speed is higher than 13m/s, almost the whole blade is stalled. It is noted that when separation happens on the suction side of the blade, the flow becomes spanwise other than streamwise. This condition is because when the separation happens, the energy of the boundary layer is not enough to maintain the flow to be attached to the surface and centrifugal force will draw the flow from root to tip on the suction side area of the blade. According to the figure, for this stall regulated wind turbine, even at its designed wind speed 10m/s the spanwise flow dominates more than half area of the suction side of the blade. This phenomenon also shows that it is significant to simulate the full-length blade in a rotating frame other than just study the wind turbine in aerofoil section because of the spanwise flow interactions.

3.3.5 Torque and Power Coefficient

The CFD solver is able to generate the torque after the computation which has been introduced above. Therefore by using equations (1) Power = angular velocity * torque and (2) $C_P = P/0.5 * \rho * U3 * A$ we can draw a power coefficient curve.

Table 7. Torque and error

Wind speed	Experimental torque (Nm)	CFD torque Nm (Steady cases)	%difference	CFD torque Nm (Unsteady cases)	%difference
5 m/s	310	315	1.6%	317	2.26%
7 m/s	780	796	2.1%	801	2.69%
10 m/s	1366	1448	6%	1455	6.52%
13 m/s	1215	1096	9.8%	1221	0.49%
15 m/s	1183	902	23.8%	1174	0.76%

The torque of the single simulated wind turbine blade can be extracted from the CFD solver directly. Both steady simulations and unsteady simulations are carried out to see the differences compared to the experimental data. Figure 38 shows that in all wind speeds the unsteady flow computation predict the wind turbine performance reasonably well using the k-ω SST model. The biggest discrepancy here is at the 10m/s wind speed condition, which is with a 6.52% over-prediction of the torque.

Table 7 shows the results from both steady and unsteady computations. It can be seen that for cases at 5m/s, 7m/s and 10m/s wind speeds both the steady unsteady simulations can accurately predict the aerodynamic torque of the wind turbine within less than 7% error differences. However for 13m/s and 15m/s wind speeds the steady simulations show much larger errors than that from the unsteady cases which are as high as 23.8% differences at the 15m/s wind speed case. The comparison of both the torque and C_P between the computational and experimental data can be seen in Figure 38 and 39.

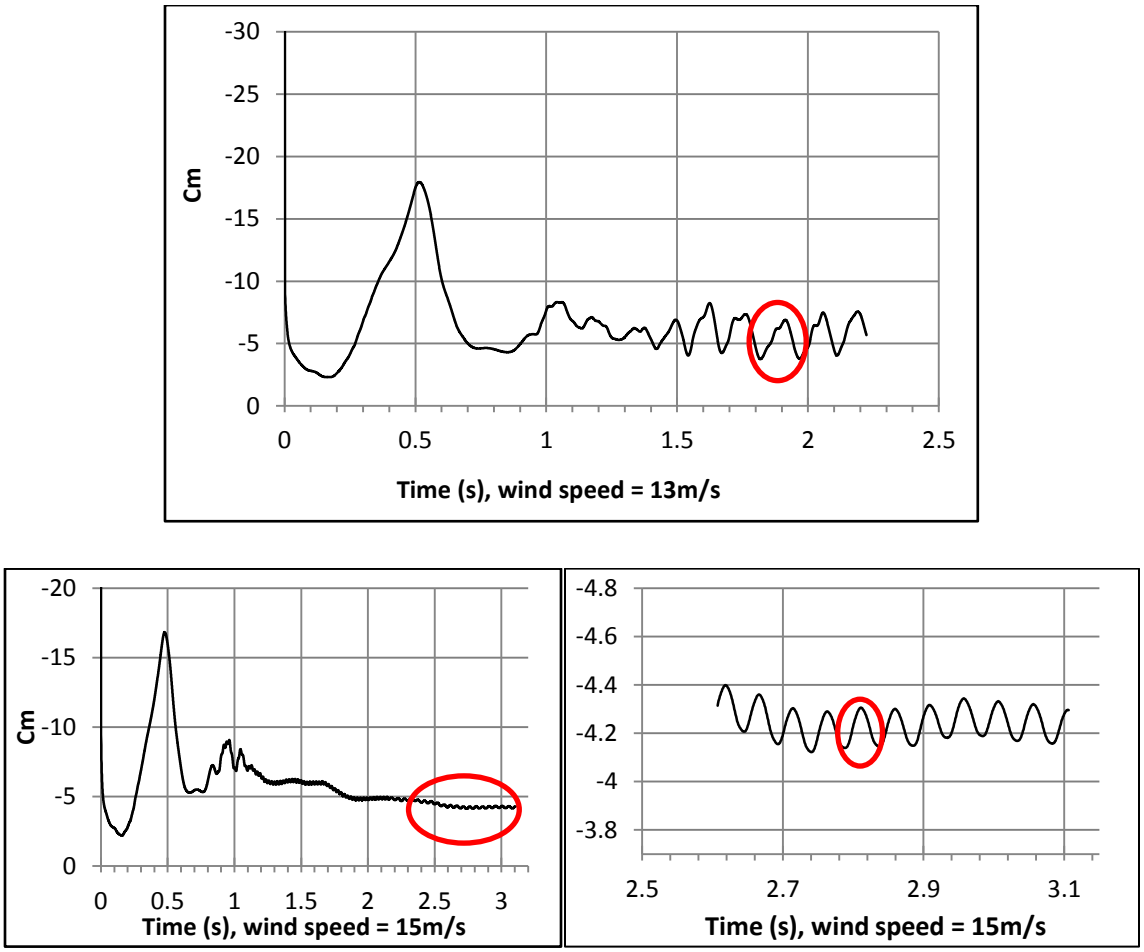

Figure 37. Cm convergence history for the original wind turbine at 13m/s (top) and 15m/s (bottom, the graph is enlarged on the right) wind speed and the mean torque is calculated as shown in the graph.

From the CFD results of the RANS solution at 13m/s and 15m/s wind speeds, the C_m is oscillating with an approximately 20% difference because of the unsteady flow conditions around the blade. Therefore in order to accurately predict the unsteady conditions, the URANS solution

is applied for 13m/s and 15m/s wind speed cases. Therefore for the unsteady simulations at the 13m/s and 15m/s wind speed cases, which are shown in Figure 37, the flow became periodic due to vortex shedding captured in the computational simulation. The torques for the unsteady cases are obtained by averaging the last cycle of the momentum coefficient from the convergence history. In the later part the instantaneous case which is closest to the mean torque is selected for flow condition and pressure coefficient analysis. Therefore considering the computational accuracy and time, the 5m/s, 7m/s and 10m/s wind speed cases will be run in steady flow condition and the 13m/s and 15m/s wind speed cases will be run in the unsteady flow condition in further study on the flow control devices.

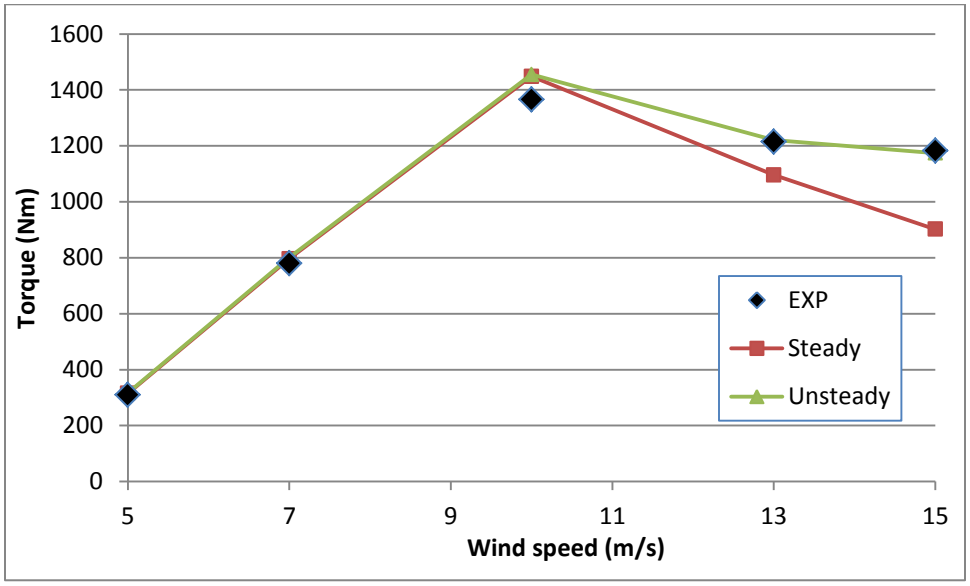

Figure 38. Torque comparison between experimental and computational data.

Figure 40 shows the comparison of the current predicted wind turbine performance with other existing researches which were using different CFD codes. This includes the studies of Sørensen et al. (2002) using EllipSys3D($k-\omega$ SST turbulence model), Pape and Lecanu (2004) using ELSA ($k-\omega$ SST model), Huang el al. (2011) using P-WENO (S-A model), Mo and Lee (2012) using Ansys FLUENT ($k-\omega$ SST model), Mahu el al. (2011) using Fluent ($k-\omega$ SST model), and Potsdam and Mavriplis (2009) using OVERFLOW and NSU3D (S-A model). Most of these studies did the cases from 7m/s wind speed to 15m/s wind speed. Therefore here the torque comparison from 7m/s wind speed to 15m/s wind speed is shown.

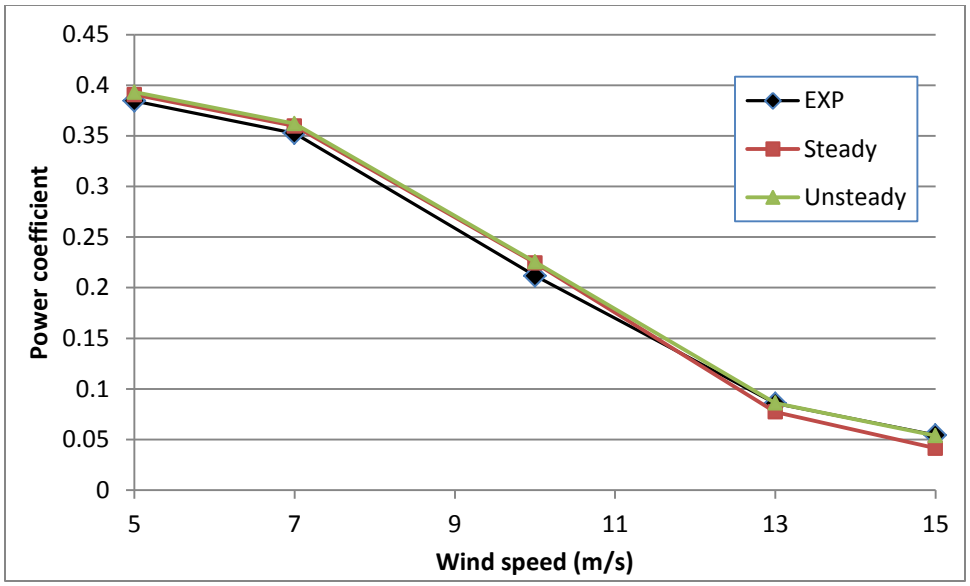

Figure 39. Power coefficient comparison between computational and experimental results.

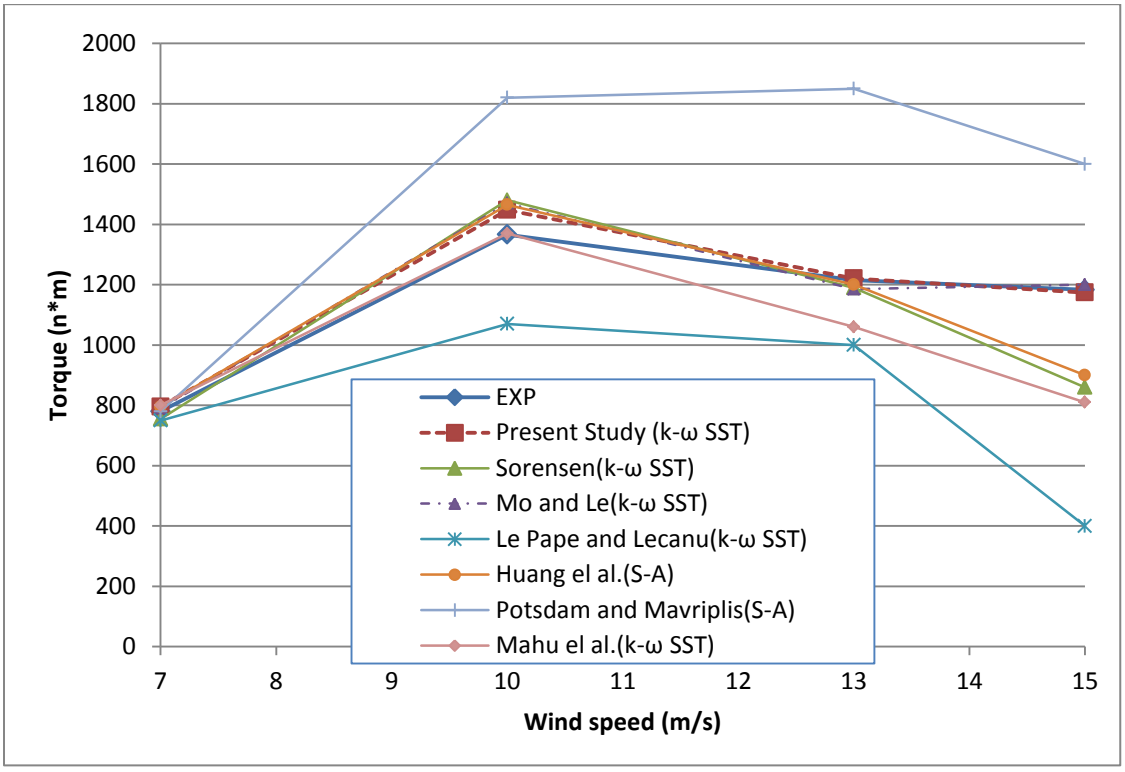

Figure 40. Wind turbine performance comparison with existing studies.

As can be seen from those existing studies, Mo and Lee's (2012) study predicted the most accurate results when using FLUENT with k – ω SST model, which is the same CFD solver and turbulence model used in the present study. With the comparison it can be concluded that with

using different CFD codes and turbulence models, there will be large disagreements among the results. In this study the results is considerably accurate in the non-stall and pre-stall situation. However, as can be seen from Figure 40, for the steady-state simulations, similar as many other studies, when the stall begins to happen, the predicted performances by FLUENT are lower than the experimental data. However for the unsteady-state results, the CFD simulations can accurately predict the torque of the blade at stalled wind speeds. The results from present study accurately meet the experimental results in the torque comparison which is a big challenge in the stalling wind speed range. According to the code to code comparison, it can be seen that using the $k-\omega$ SST turbulence model with the ANSYS FLUENT CFD solver can normally predict reasonably accurate results for this stall regulated wind turbine especially at wind speed from 5m/s to 10m/s range when the blade is not fully stalled. Moreover from the pressure coefficient comparison between the present CFD results and experimental data (Figure 26, 29 and 34), in most cases the CFD results can predict highly consistent results. Therefore the validation case carried out in this chapter show that with using proper turbulence model and boundary condition settings, the CFD method can give accurate predictions for the wind turbine torque and flow structures.

Chapter 4 CFD Study of Trailing Edge Flow Control Devices on NREL Phase VI Wind Turbine

4.1 Introduction

Improving the aerodynamic performance of the wind turbine blade is one of the most significant factors to maximize the efficiency of transforming wind energy into mechanical energy. Great progress has been made in the recent years in blade aerodynamic design and modern HAWT can reach a relatively high power coefficient. However most of present HAWTs are designed with a rated power at a specified wind speed range. Beyond this wind speed range the efficiency of the wind turbine can drop significantly. Considering the manufacturing difficulties of a morphing turbine blade to suit different wind conditions, flow control can offer improved wind turbines' performance for a wider range of wind speed around the rated condition. The present study on this small stall regulated wind turbine is mainly about whether the trailing-edge flow control devices can further increase the performance of the HAWTs in rotating situation. This chapter mainly investigates into the impact of two typical trailing edge flow control devices (microtabs and microjets) along with the concept of the divergent trailing edge for HAWTs.

In this chapter firstly a 2D study on the S809 aerofoil, which is the aerofoil used for the NREL Phase VI wind turbine, is carried out with deploying microtabs, microjets and DTE. This is because most existing studies are in 2D for a span section of the wind turbine and 2D simulations are fast to compute. Then full 3D simulations on the effects of trailing edge flow control devices are carried out in the rotating frame to study the 3D effects. Studies are carried out on the effects of the height and spanwise range of microtabs. The microtab is assumed as an active flow control device deployed near the trailing edge. Therefore considering the thickness of the trailing edge of S809 aerofoil, the height of the microtab tested here is only 1% - 2.3% chord.

4.2 2D Numerical Study of Trailing Edge Flow Control Devices on S809 Aerofoil

4.2.1 Methodology

Before studying the performance of the flow control devices on a 3D rotating turbine blade, 2D simulations of the flow control devices on a blade cross-sectional aerofoil were conducted. Here the selected aerofoil is S809 located at the 80% span of the NREL PHASE VI wind turbine. The details are shown in Table 8. The microtab and the microjet are deployed at the 90% chord length position of the aerofoil section, while a 3% chord length height divergent trailing edge (DTE) is deployed for comparison. The detailed geometries and the 2D meshes are shown in Figure 41. As noted, structured meshes were used to give high accuracy/resolution near the boundary layers and the flow control devices for computational accuracy.

Table 8. 2D study of flow control devices on S809 aerofoil

Chosen wind turbine	NREL PHASE VI
Span location	r/R = 0.8
Rotational speed	7.54 rad/s
Sectional twist angle	2.619 degrees
Wind speed	5m/s –14m/s
Aerofoil chord length	0.457m
Reynolds number	Around 10^6
Microtab size	2% chord length
Microjet speed	60m/s
Divergent trailing edge thickness	3% chord length

For the 2D simulations, the turbulence model is also $k-\omega\ SST$ and all cases are run as steady flow condition. All cases are finished within 10,000 iterations and all the C_l values converge well.

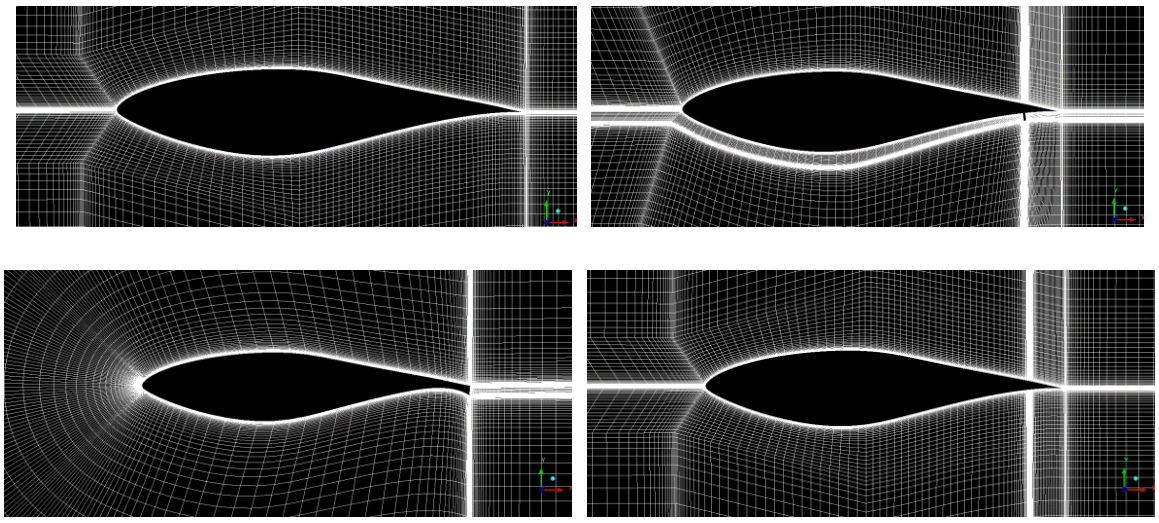

Figure 41. 2D mesh of S809 aerofoil and the aerofoil with 2% chord length microtab (top right), 3% chord length DTE (bottom left) and microjet (bottom right)

4.2.2 Results

As mentioned above, the cross-section S809 aerofoil at the r/R = 0.8 span position of the NREL PHASE VI wind turbine is selected for the 2D flow control devices and DTE study. Considering implementation requirements for the microtab and microjet as active flow control devices, the 3mm width microtab and microjet are deployed at 90% C positions on the pressure side of the aerofoil.

Since the 2D aerofoil is for a wind turbine blade rather than an aircraft wing, focusing just on the lift drag ratio as in many previous literatures can be misleading. Therefore in the present study we investigate directly the effective force in the rotational direction of the blade, which drives the turbine blade around. This effective force is the final resultant force of the cross-section aerofoil contributing to the torque of the wind turbine. Figure 42 shows the effective force comparison between the S809 aerofoil with microtab, microjet and the redesigned 3% chord length DTE aerofoil. The results show that all three flow control devices have positive effects on the effective force from the aerofoil from 7m/s to 10m/s wind speed range. However at 13m/s and 15m/s conditions both DTE and microtab cases show reduction in the force while the microjet case still shows some improvement.

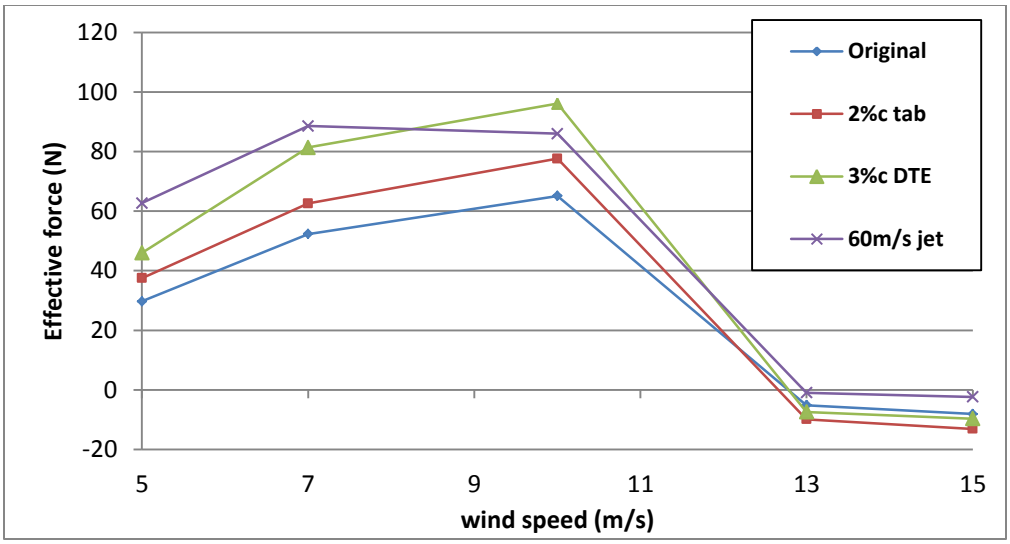

Figure 42. Effective force comparison among different trailing edge flow control devices.

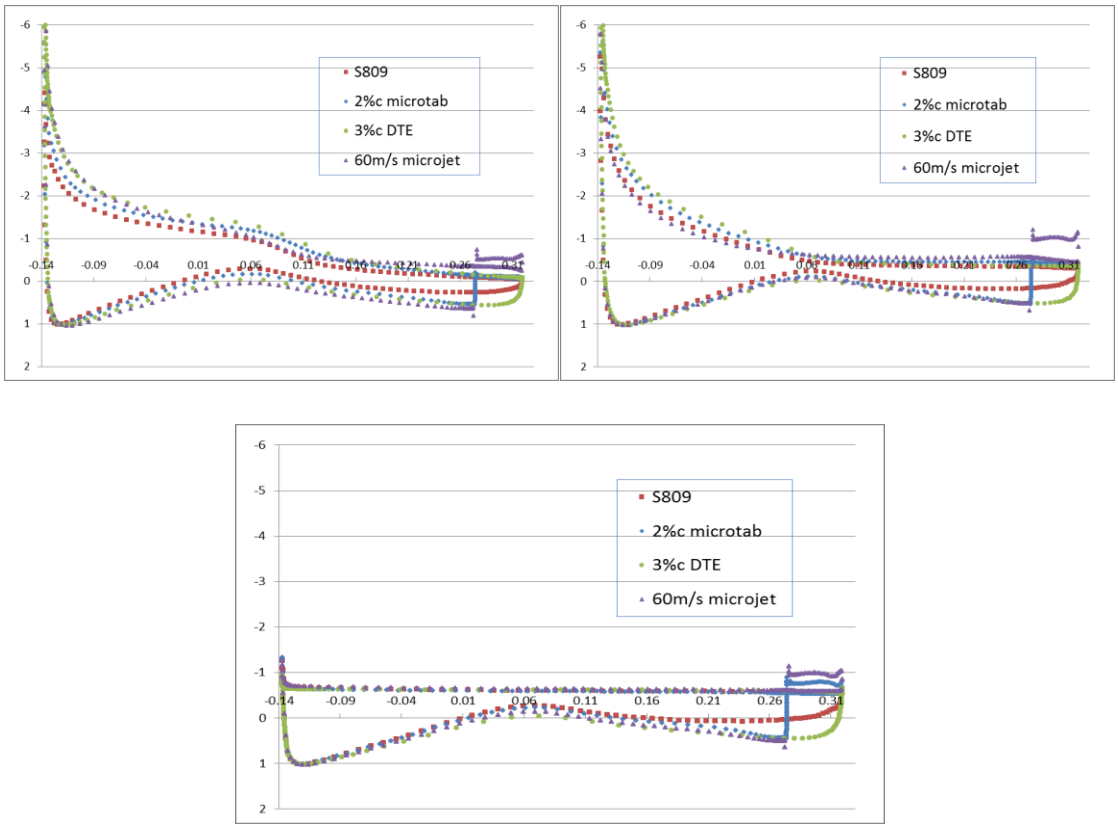

Figure 43. 2D pressure coefficient comparison between different flow control devices. (top left: U = 7m/s; top right: U = 10m/s; bottom: U = 15m/s)

The pressure coefficient comparison between different flow control devices at 7m/s, 10m/s and 15m/s wind speeds can be seen from Figure 43. The results show that the flow control devices increase significantly the differences of the pressure coefficient between pressure side and suction side near the leading edge area of the aerofoil, especially for the lower wind speed case.

Streamlines and pressure contours

Figure 44 to 46 show the streamlines around the aerofoil at 7m/s, 10m/s and 15m/s wind speeds respectively.

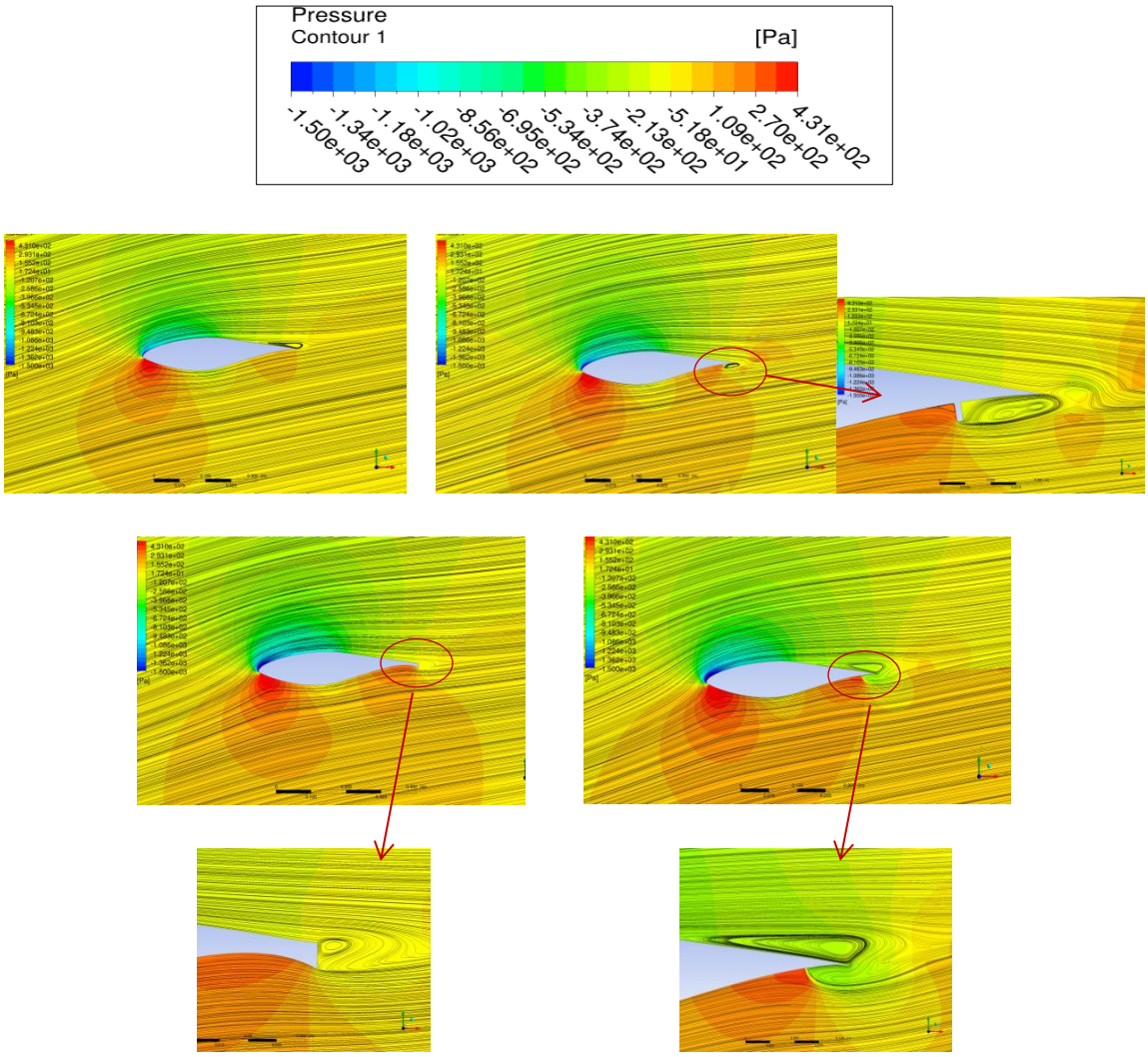

Figure 44. Streamlines overview at 7m/s wind speed. Top left: S809 aerofoil; top right: S809 with 2% chord length microtab; bottom left: S809 with 3%c DTE; bottom right: S809 with 60m/s microjet.

Overall, the 2D computational results show that all flow control devices have local improvement at non-stall wind speeds (5m/s-10m/s) for the S809 aerofoil. However in a real 3D rotating situation as shown in the last section, the flow is much more complicated with strong spanwise flows. For the higher wind speed cases, the 2D flow control results are less relevant.

In Figure 44 it can be seen that there is a very small separation on the suction side of the original S809 aerofoil near the trailing edge which is now happened at the same span section in the 3D validation case. This condition is a sign that the 2D simulation on the sectional aerofoil might not be able to fully transfer to the real situation in the 3D rotating frame situation. Moreover, it is interesting to see that the deployments of the microtab and DTE design on the S809 aerofoil effectively eliminate this small separation at 7m/s wind speed, while the 60m/s microjet makes it even larger.

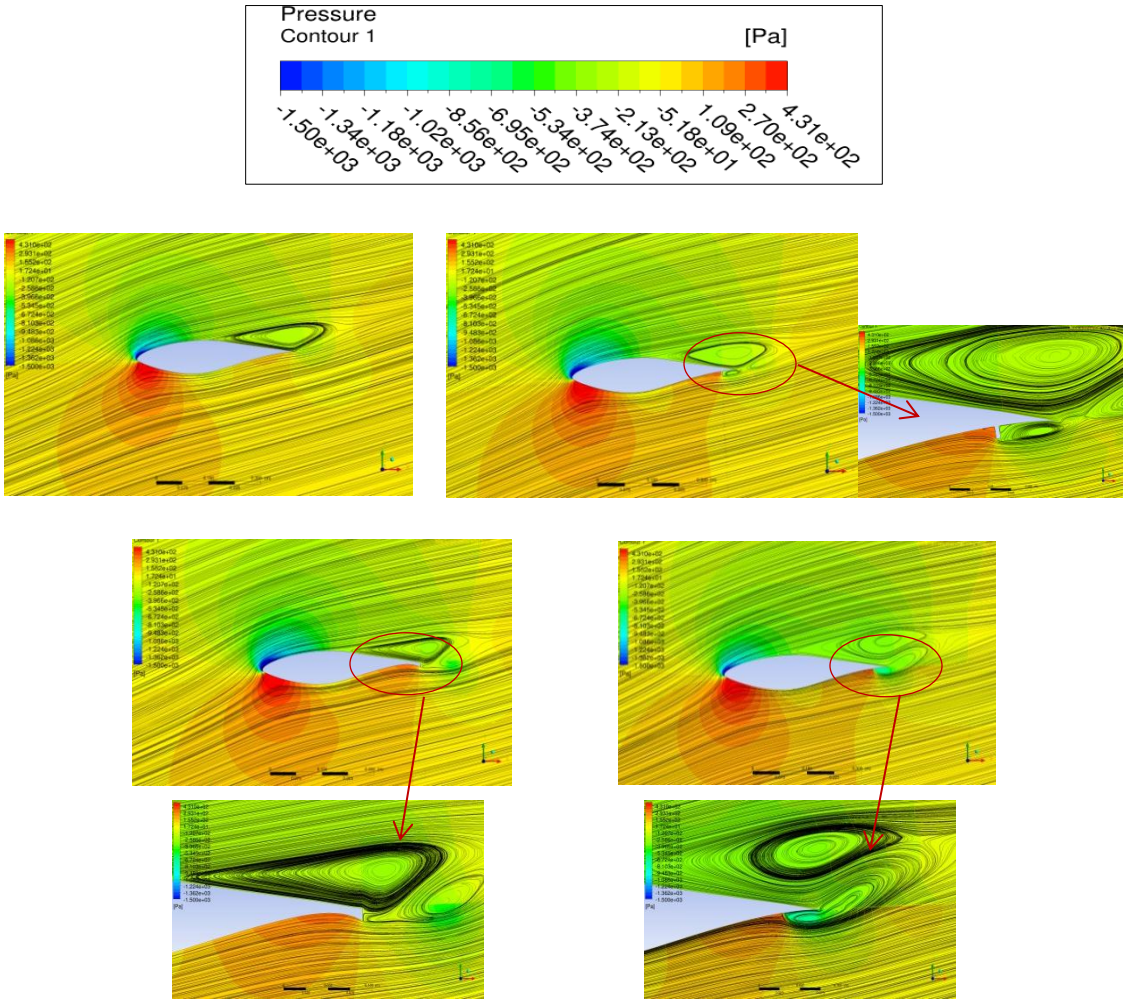

Figure 45. Streamlines overview at 10m/s wind speed. Top left: S809 aerofoil; top right: S809 with 2% chord length microtab; bottom left: S809 with 3%c DTE; bottom right: S809 with 60m/s microjet.

As shown in Figure 45, because of the high incidence of the aerofoil at 10m/s wind speed, the flow controls are not able to cause big changes for the separations on the suction side. However at this incidence because of the changing camber of the aerofoil, these three flow control concepts still show some improvement on the effective force.

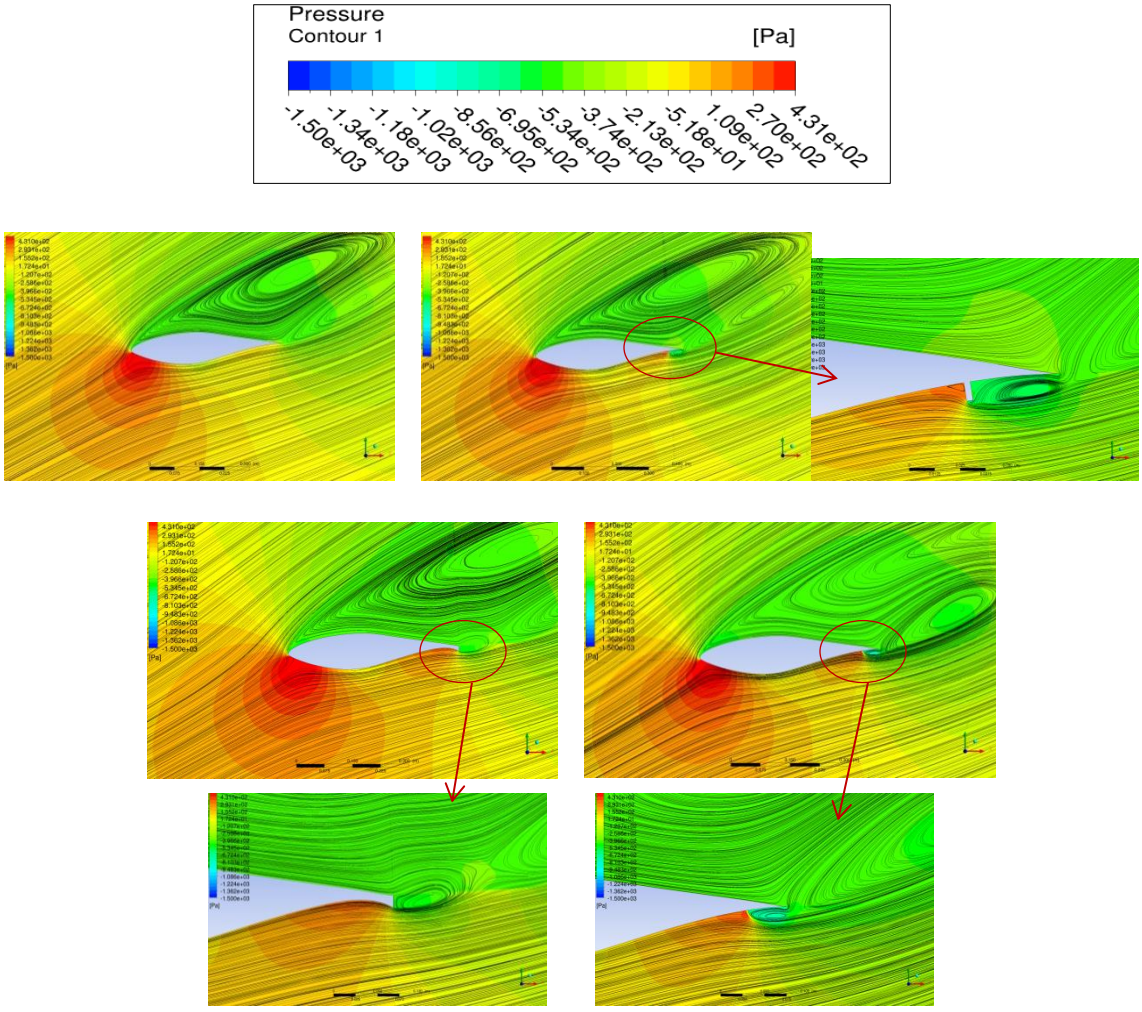

Figure 46. Streamlines overview at 15m/s wind speed. Top left: S809 aerofoil; top right: S809 with 2% chord length microtab; bottom left: S809 with 3%c DTE; bottom right: S809 with 60m/s microjet.

When the wind speed is as high as 15m/s, the flow on the whole suction side of the aerofoil is separated (Figure 46) which leading to fast drop of C_L and $F_{effective}$. Therefore in this situation all the trailing edge flow control concepts are not able to improve the aerodynamic performance of the aerofoil. However because of the large separation which starting from the leading edge on the suction side, the leading edge microjets will be required as the separation control devices for improving the aerofoil performance, which would be studied later.

In conclusion, from the 2D flow control devices study on the S809 aerofoil it can be seen that in the non-stall situation all flow control devices can effectively improve the performance of the aerofoil which contributing to the final torque of the blade. At lower wind speeds such as 5m/s and 7m/s, some of the flow control devices can increase as high as 50%-100% of the performance. However from the validation study it is known that the spanwise flow is also strong for this wind turbine, which is totally ignored in the 2D study. Therefore it is necessary to carry out 3D study on the flow control devices in an actual rotating situation.

4.3 3D Numerical Study of Microjets, Microtabs and DTE

4.3.1 Methodology

The methodology for the 3D simulation of the NREL Phase VI wind turbine with different flow control devices and the 3% chord length height DTE is the same as presented for the validation case. The boundary conditions and turbulence model are the same. In order to meet the wall y^+ requirement the mesh size of the blade with microtab is increased to an 8.2 million grid and a 6.3 million grid for the blade with microjet and a 4.5 million grid for the blade with 3% chord length DTE. Figure 47, 48 and 49 show the mesh overview for the blade with 2%c microtab, microjet and 3%c DTE respectively.

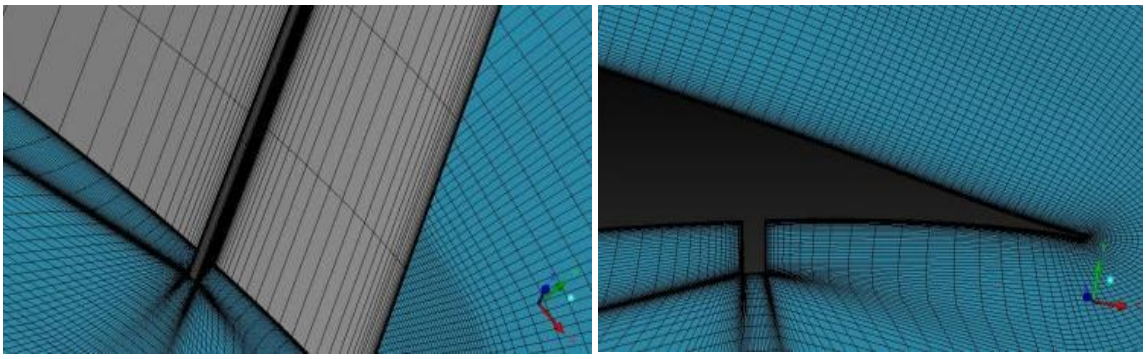

Figure 47. Mesh overview of the blade with 2%c microtab from 70%-97% span of the blade.

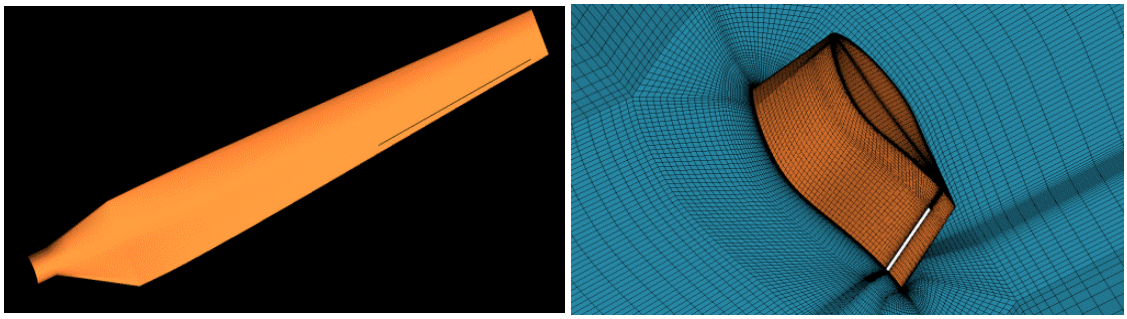

Figure 48. Mesh overview of the blade with microjet from 70%-97% span of the blade.

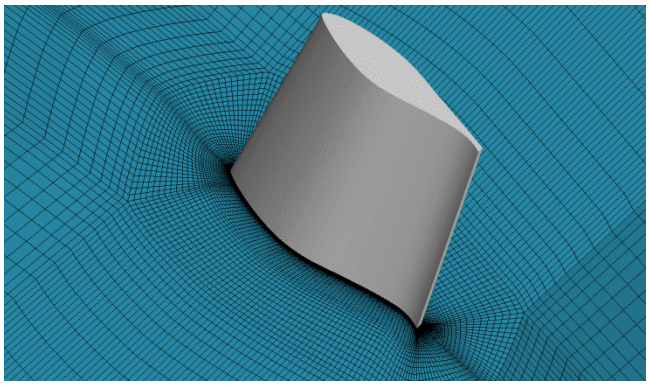

Figure 49. Mesh overview of the blade with 3%c DTE from 70% to tip.

The microtab and the microjet are installed/activated along the blade from 70%-97% along the blade span. The width of both the microtab and microjet is 3mm. The reason for this choice of span location is due to the fact that this is the most energy/torque generating part of the blade, which also the most highly loaded part. For the same reason the DTE is implemented between 70%-100% span.

As mention above, the flow of NREL Phase VI wind turbine blade becomes fully unsteady when wind speed is higher than 10m/s. Therefore here the unsteady simulations are also carried out for 13m/s and 15m/s wind speed cases with a 0.0006s physical time-step size. Other wind speed cases are simulated as steady flows.

4.3.2 Results

For the higher wind speed cases, the flow became periodic due to vortex shedding captured in the computational simulation. The torques for the unsteady cases is obtained by averaging the last cycle of the momentum coefficient from the convergence history. The detailed results of the torque and power coefficient are shown in Figure 51. The 3D results show correspondence with

the 2D results. However for the 5m/s case, the improvement due to flow control from the 3D results is much less than that shown in the 2D case. Moreover, the 3% DTE shows best performance in the 2D aerofoil study while in the 3D rotating blade study it shows the worst performance. All the cases for 13m/s and 15m/s wind speeds are run in unsteady flow simulations and a sample of the momentum coefficient convergence history and the torque calculation can be found in Figure 51.

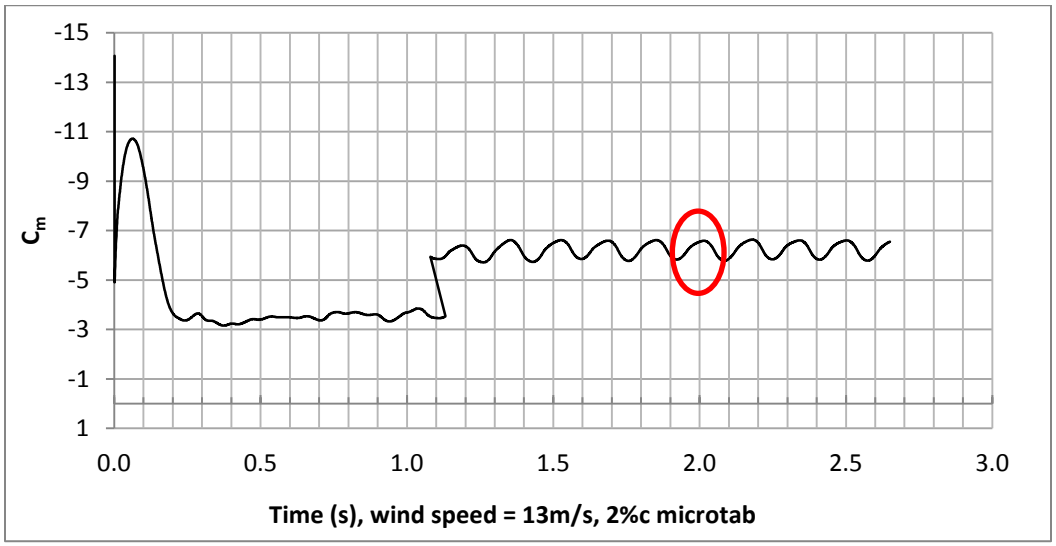

Figure 50. C_m convergence history for the wind turbine with 2%c microtab at 13m/s wind speed, the final mean torque is calculated at one cycle as shown in the graph.

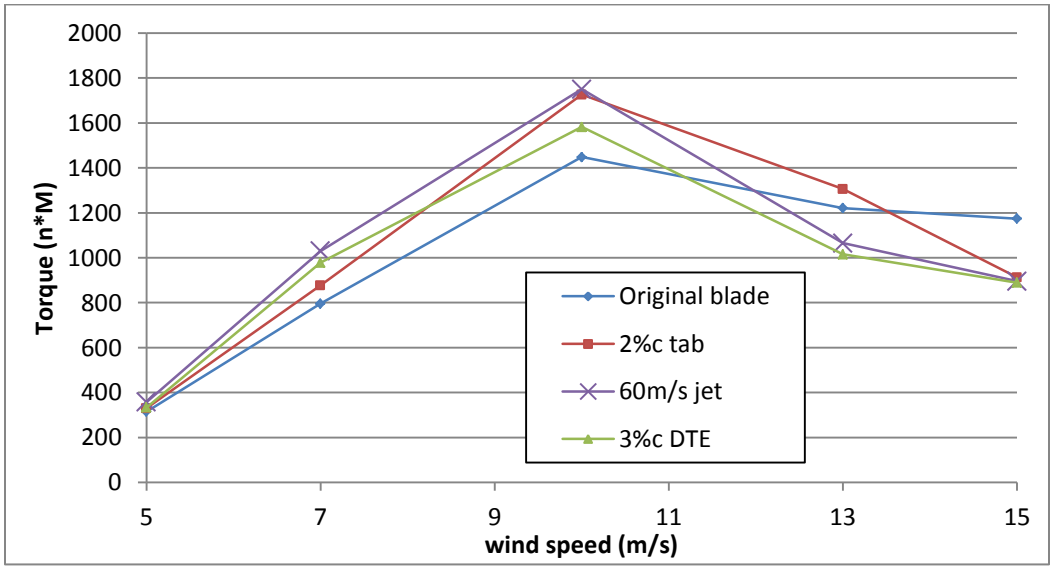

Figure 51. Torque comparison between the original blade and the blade with different flow control devices.

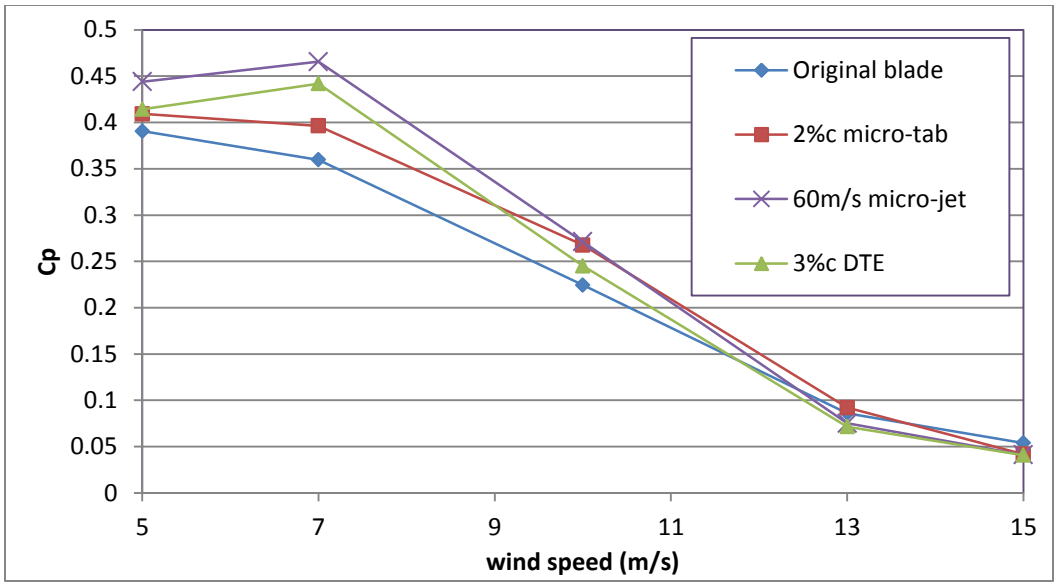

Figure 52. Power coefficient comparison.

In summary, referring to the power coefficient comparison (Figure 52) it can be seen that in the 3D rotating situation, the trailling-edge flow control devices improve a maximum of 29% higer C_p than the original blade (60m/s microjet at 7m/s wind speed). Moreover, even at 10m/s, which is the design speed of the blade, the 2%c height microtab and the 60m/s microjet increase the C_p by 22.2%. However, similar as the 2D results, in the stall wind speed range (higher than 10m/s) the flow control devices decrease the power output of the blade.

Surface pressure comparison

Figure 53, 54 and 55 show the surface pressure of the original blade and the blade with different flow control devices at 7m/s, 10m/s and 15m/s wind speed situations respectively. In order to show clearly the pressre around the flow control devices, only the blade above 0.65 span is shown in the figures. All the pressure contour level settings are the same from -1800 pa to 750 pa (the figure legend can be seen from Figure 53). For all figures, the suction side is on the left while the pressure side of the blade is on the right.

Figure 53 shows that at the relatively lower wind speed, 7m/s, the DTE concept increases the pressure near the trailing edge on the pressure side mostly. The suction side effects of all three kinds of flow control devices are quite similar as the original blade.

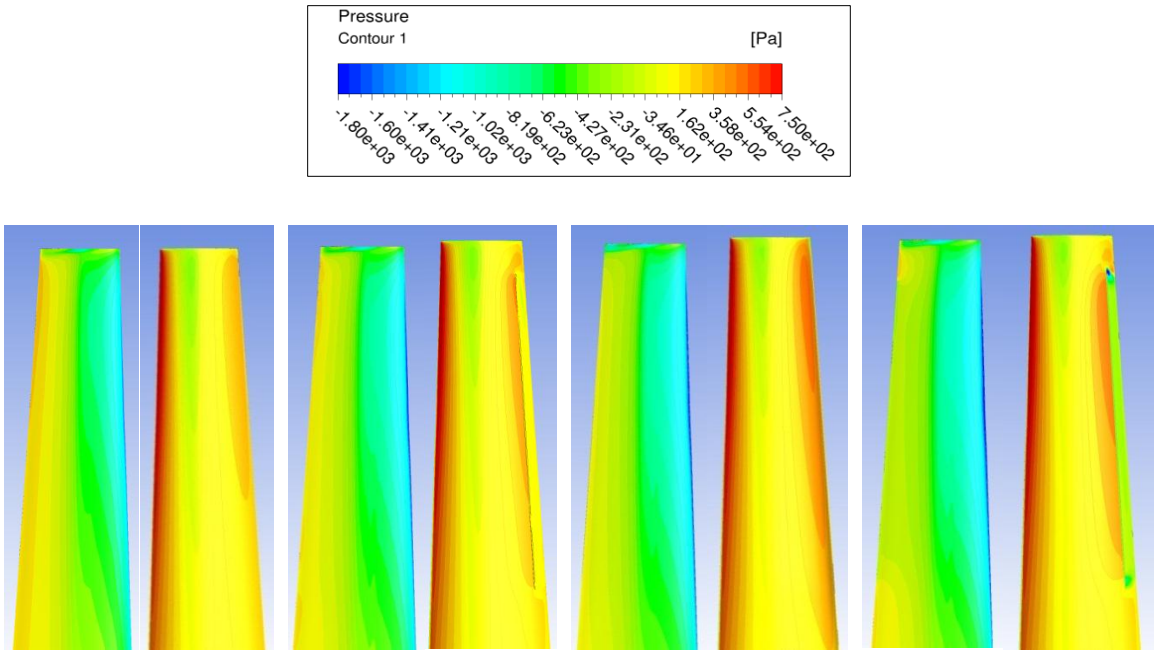

Figure 53. Surface pressure comparison at wind speed = 7m/s.

Figure 54 shows that the DTE shows the biggest effects on increasing the pressure near the trailing edge on the pressure side at 10m/s wind speed. Both the DTE and microjet can to some extent reduce the separation area on the suction side of the blade when compared to the original one.

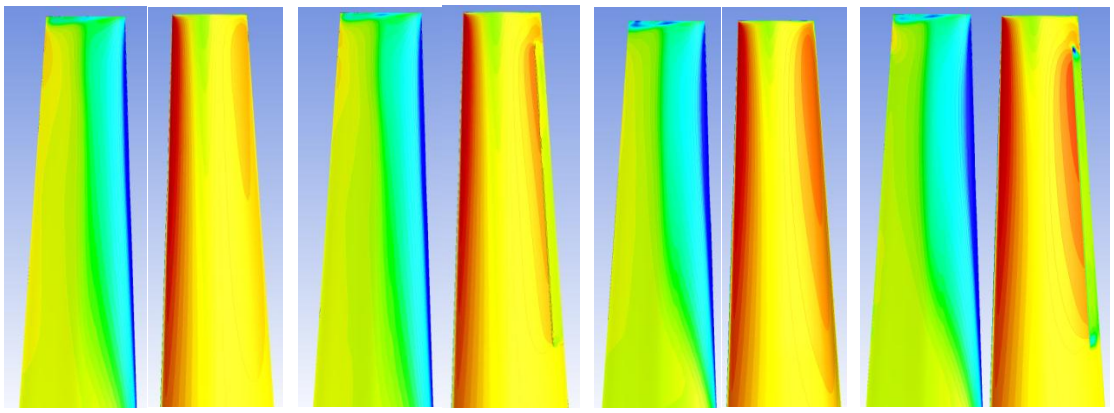

Figure 54. Surface pressure comparison at wind speed = 10m/s.

Figure 55 shows that when the blade is fully stalled at 15m/s wind speed, the flow situation is unsteady in all cases. The pressure contour on the suction side of the blade is fully irregular. At this time even though the flow control devices can still increase the pressure near the trailing edge on the pressure side, the lift force cannot be improved.

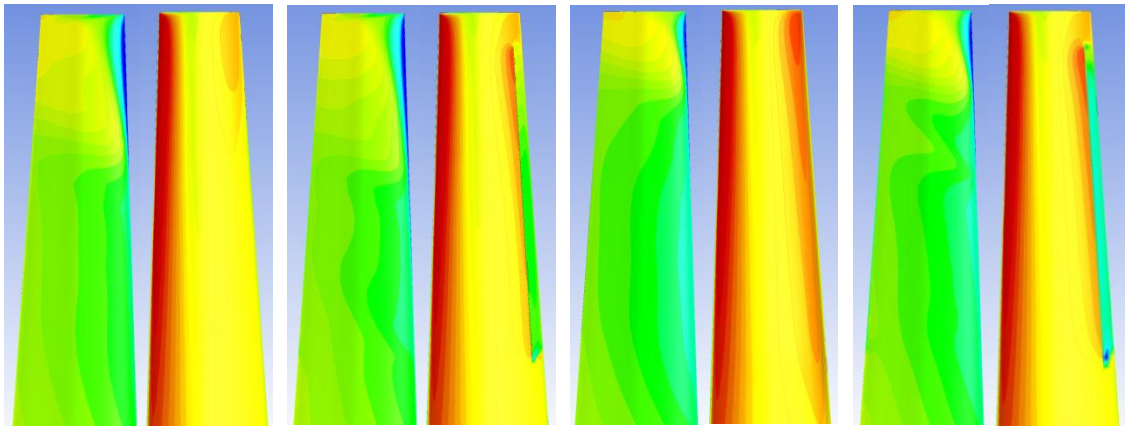

Original 2%c microtab 3%c DTE 60m/s microjet

Figure 55. Surface pressure comparison at wind speed = 15m/s.

Cross-sectional pressure coefficient (C_p) comparison

Figures 56, 57 and 58 show the cross-sectional aerofoil pressure coefficient C_p at two different span positions, r/R =0.47 and r/R = 0.8 respectively. From the figures it can be seen that the trailing edge flow control devices not only change the C_p at where they are deployed but also affect the C_p at the lower part of the blade.

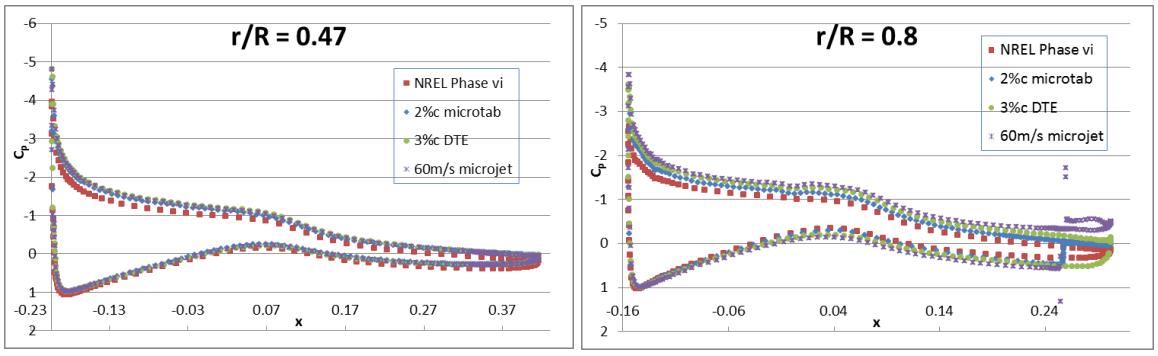

Figure 56. Sectional aerofoil pressure coefficient comparison at wind speed = 7m/s.

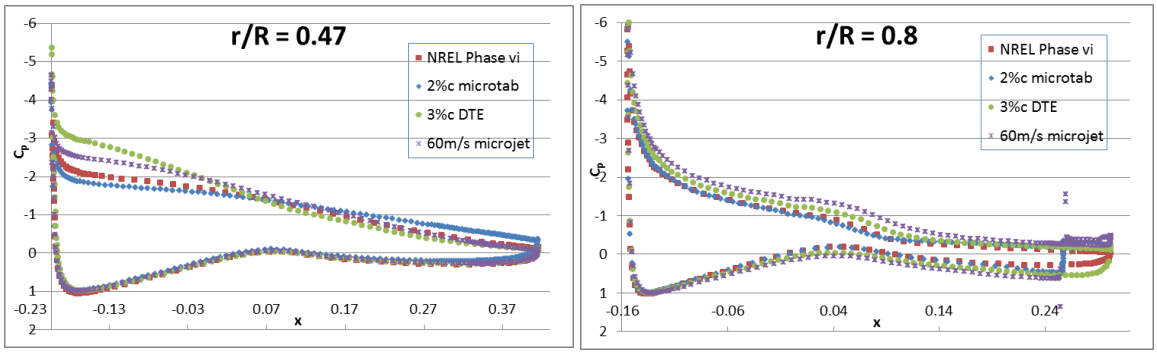

Figure 57. Sectional aerofoil pressure coefficient comparison at wind speed = 10m/s.

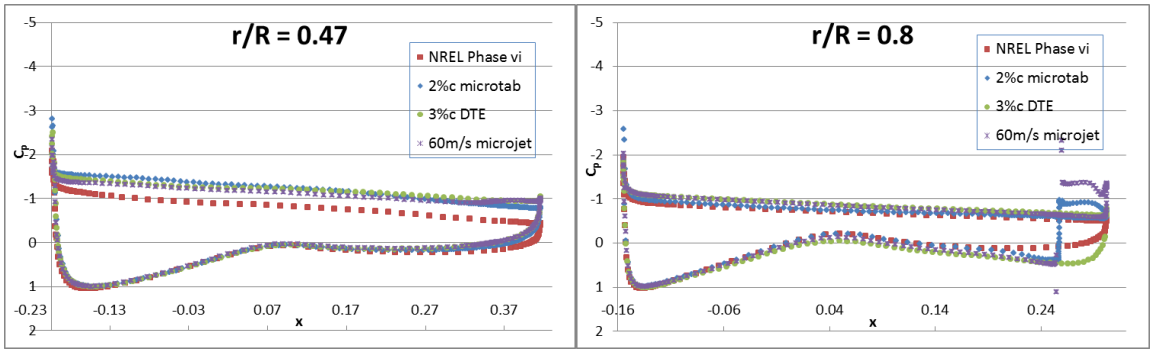

Figure 58. Sectional aerofoil pressure coefficient comparison at wind speed = 15m/s.

The left graph of Figure 56 shows that at 7m/s wind speed, the aerofoil suction side C_p at r/R = 0.47 section is silghtly changed by deploying flow control. The changes from all three kinds of concepts are quite similar which leading to small imprment of the lift force of the sectional aerofoil. The right graph of Figure 56 shows that at r/R = 0.8 section, where the flow control devices are deployed, all flow control concepts improve the aerodynamic lift force of the sectional aerofoil while the 60m/s outlet speed microjet shows the largest improvement.

At 10m/s wind speed, as can be seen from the left graph of Figure 57, the r/R = 0.47 aerofoil section of the blade begins to stall. The 3% chord DTE and microjet delay the stall slightly while the microtab enhances the sectional stall. At r/R = 0.8 section, the C_p of the sectional aerofoil with the microtab is quite similar as the original blade while DTE and microjet show improvement of the aerodynamic lift force.

Figure 58 shows that at 15m/s wind speed, most area of the blade is in stall even for the r/R = 0.8 section. The left graph of Figure 58 shows that at r/R = 0.47, where no flow control are deployed,

all three kinds of flow controls improve the sectional aerodynamic lift force slightly. At r/R = 0.8, which is shown in the right graph, the C_P of the original blade and with flow controls is quite similar where just some minor improvements due to flow controls.

The C_p investigation shows that the flow controls also lead to aerodynamic changes at lower span of the blade where no flow control is deployed. The results to some extent explain the reason for the torque improvement shown above.

Surface wall shear streamlines overview (Suction side on the left, pressure side on the right)

Figure 59-61 show the skin friction lines on the blade surface. It is quite interesting to observe that at the 10m/s wind speed, which is the design speed of the blade, the flow control devices delay stall of the blade on the suction side. The flow on the suction side seperates from 0 to around 0.9 span of the original blade however for the blade with the 60m/s microjet, the seperation on the suction side just happens from 0 to 0.75 span. When the wind speed is as high as 15m/s, because of the high incidence large seperation happens on the suction side along the whole blade and the flow control devices seems to have very little effects (see Figure 61).

In summary, from the surface friction streamlines it can be seen that at lower wind speed range where the blade is not fully stalled and the spanwise flow is not dominanting on the suctionside, the flow control devices can effevtively improve the aerodynamic performance of the blade. However, when the wind turbine is fully stalled and all the suction side of the blade is dominated with spanwise flow, all three kinds of flow control devices are not able to further increase the power output of the blade because the aerodynamic performance of the sectional aerofoils are no longer valid at this situation.

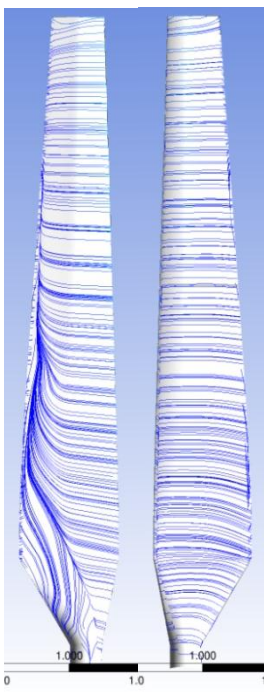

Original blade

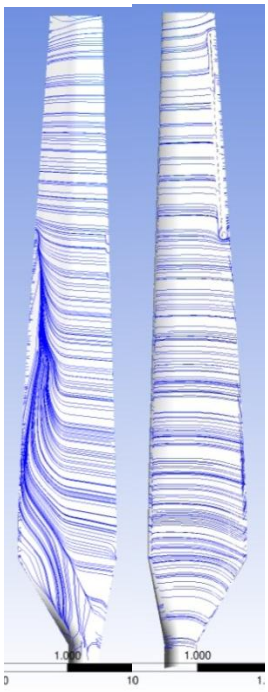

With 2%c microtab

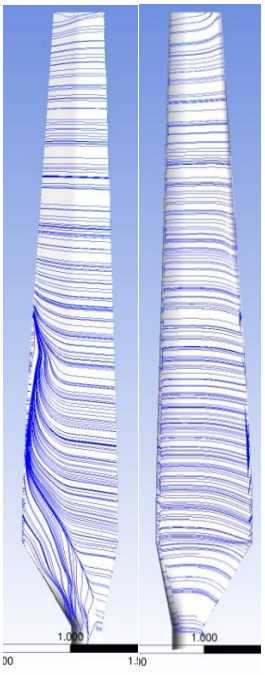

With 3%c DTE

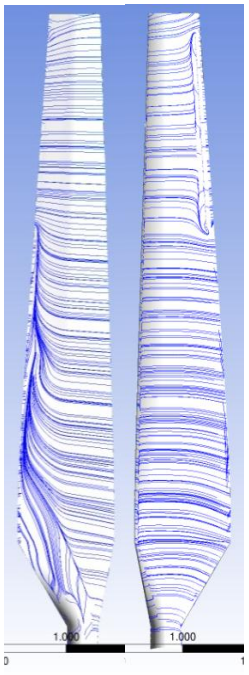

With 60m/s speed microjet

Figure 59. Surface wall shear streamlines comparison at wind speed = 7m/s.

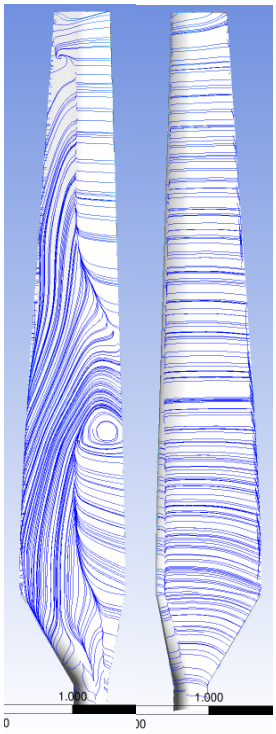

Original blade

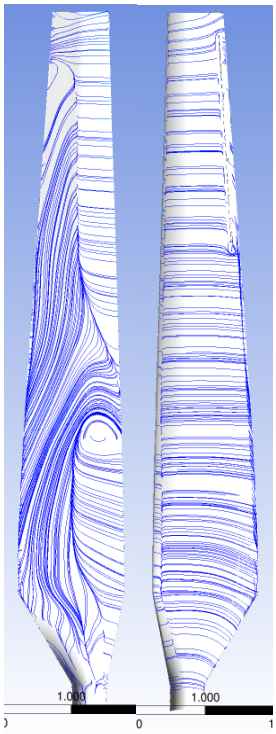

With 2%c microtab

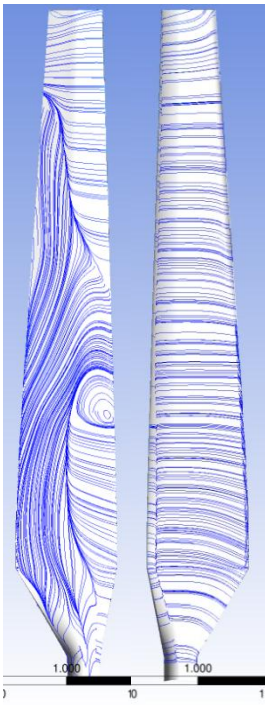

With 3%c DTE

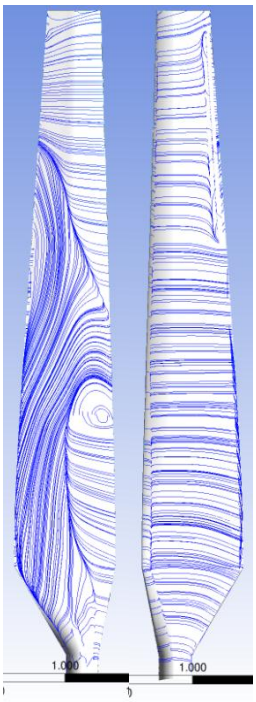

With 60m/s speed microjet

Figure 60. Surface wall shear streamlines comparison at wind speed = 10m/s.

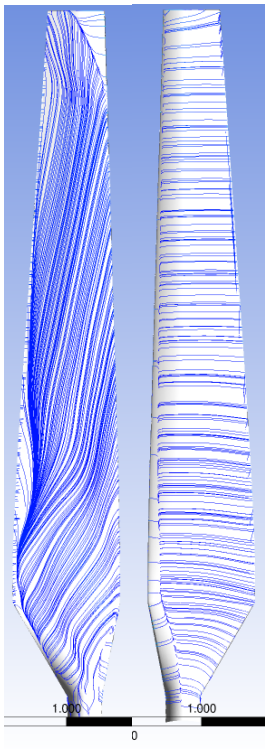

Original blade (t = 2.64s)

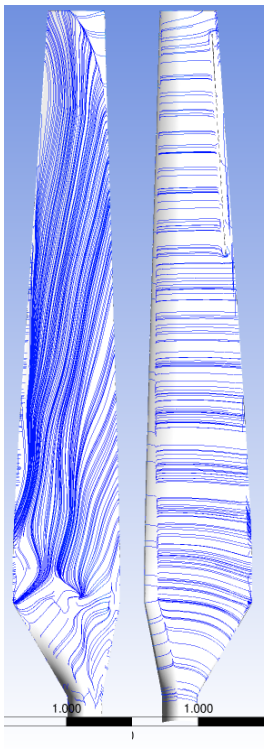

With 2%c microtab (t = 3.48s)

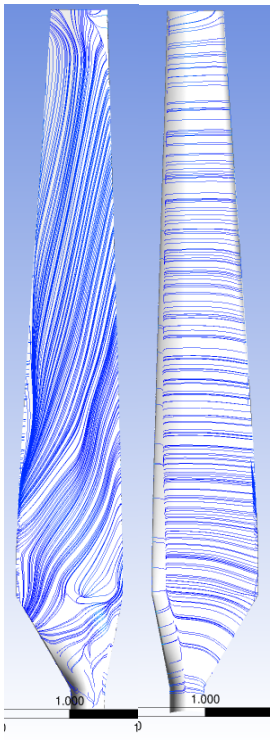

With 3%c DTE (t = 1.8s)

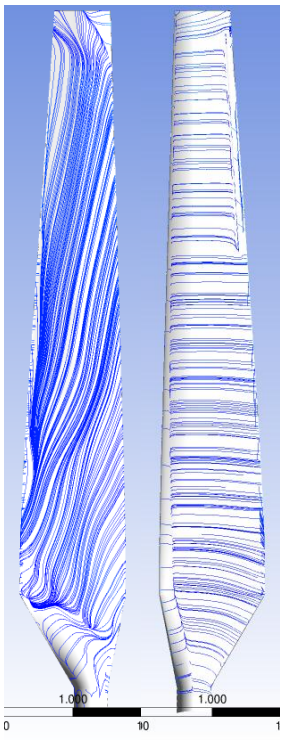

With 60m/s speed microjet (t = 2.16s)

Figure 61. Surface wall shear streamlines comparison at wind speed = 15m/s.

Cross-sectional flow streamlines comparison at r/R = 0.8 span position

Similar as the 2D study, the flow streamlines of the cut-plane of sectional aerofoils are analyzed for clearer views of the effects of flow control devices on the wind turbine blade.

Figure 62 shows the cross-sectional streamlines at r/R = 0.8 position which is the same position as the 2D simulations. Compared to the 2D study above, the flow condition on the suction side is different from the 2D simulations. In the 3D simulation the flow is fully attached on the suction side while the 2D simulation shows a small seperation near the trailling-edge. The streamlines near the trailling-edge on the pressure side of the 3D simulation is very similar as the 2D simulations.

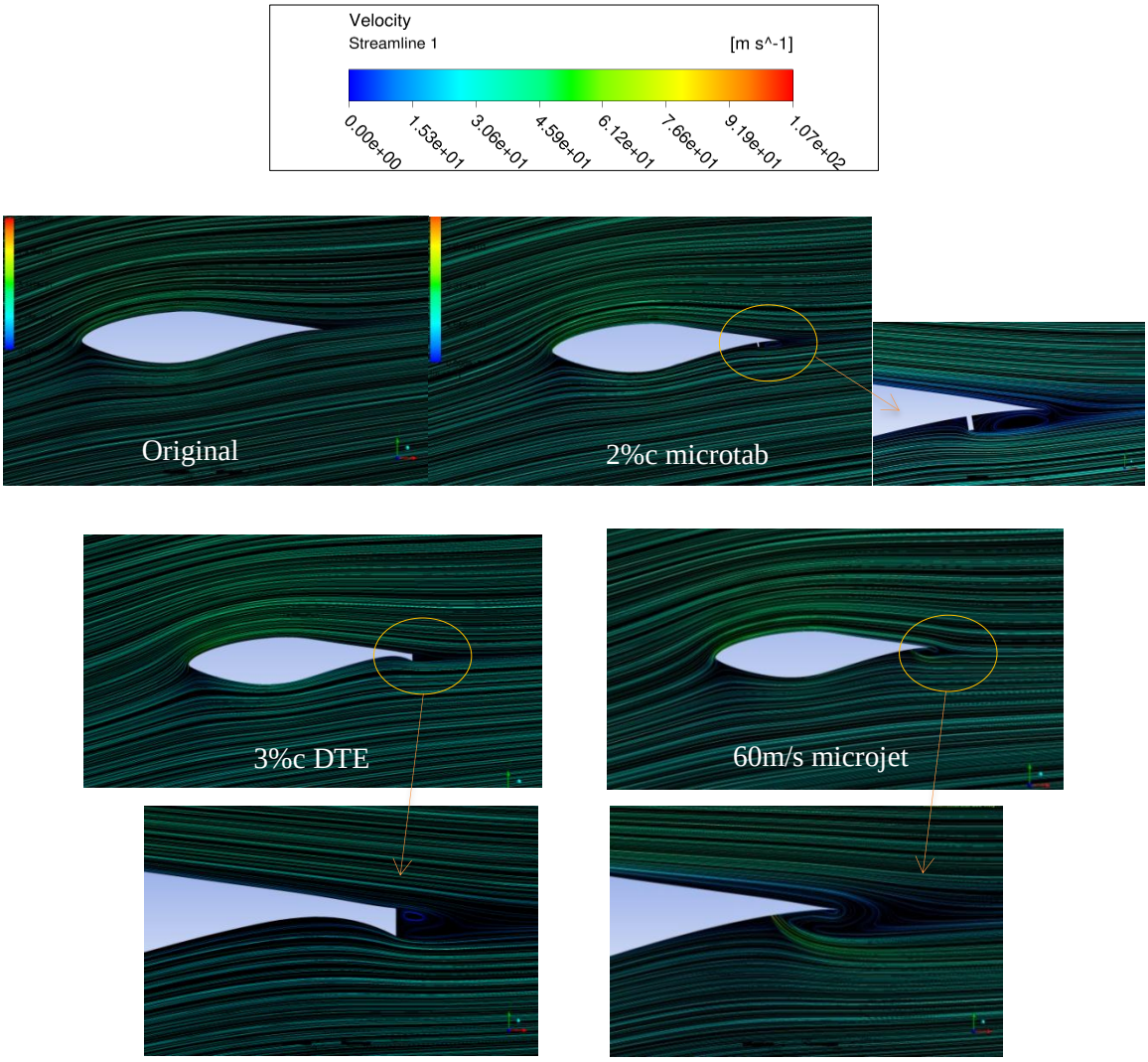

Figure 62. Cross-sectional flow streamlines comparison at 0.8 span at wind speed = 7m/s.

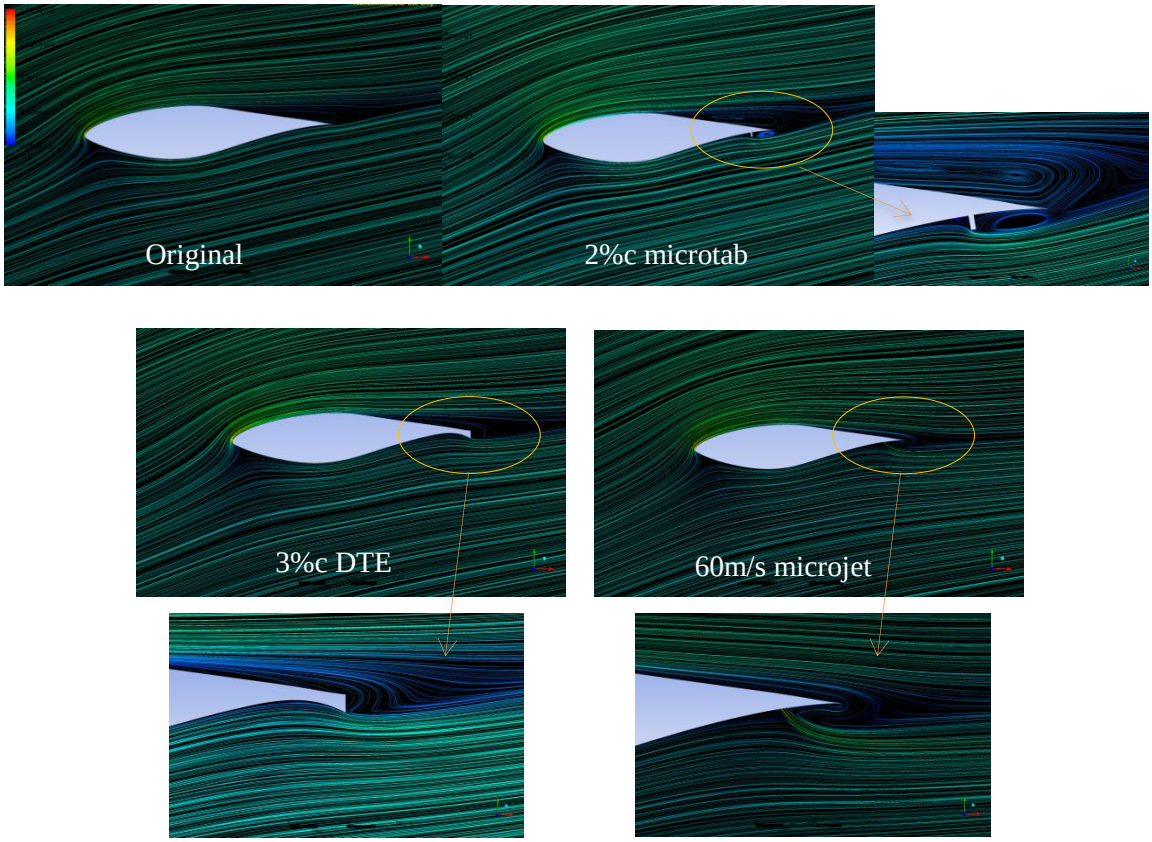

Figure 63. Cross-sectional flow streamlines comparison at 0.8 span at wind speed = 10m/s.

Figure 63 shows the velocity streamlines of the r/R = 0.8 span section at 10m/s wind speed. The 3D results also show a much smaller seperation flow on the suction side compared to the 2D simulation results. An interesting point is that by deploying different flow control devices the flow on the suction side can be changed. The 2%c height microtab sligtly enlarge the seperation on the suction side while the 3%c DTE reduces the detached area of the flow on the suction side and the 60m/s microjet even lead to re-attached flow near the trailing-edge on the suction side. This condition can also be observed in Figure 60.

Figure 64 shows that at 15m/s wind speed, all four cases are with large flow separations starting from the leading edge on the suction side. According to the surface friction lines shown above, these figures are just showing the 3D streamlines mapping on the 2D sectional cut-plane therefore they are not able to present the actual flow conditions around the sectional aerofoil.

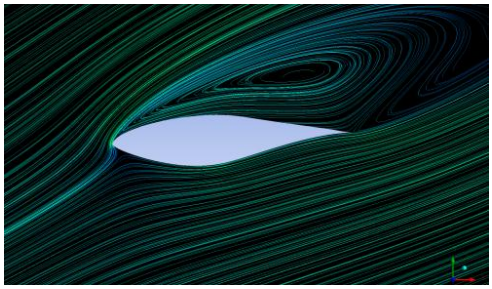

Original blade (t = 2.64s)

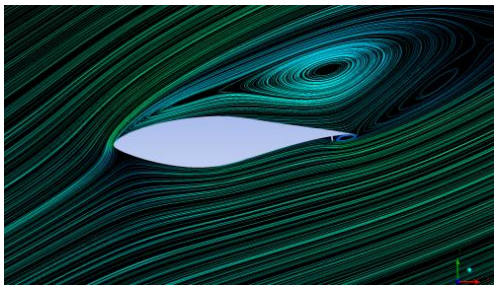

With 2%c micro-tab (t = 3.48s)

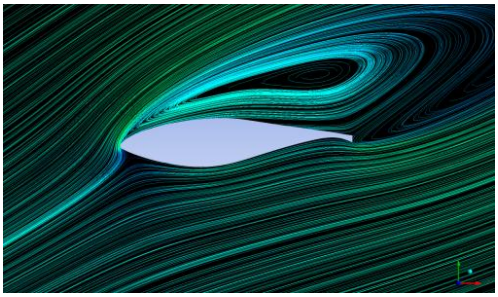

With 3%c DTE (t = 1.8s)

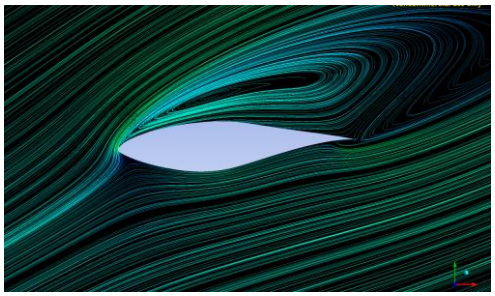

With 60m/s speed micro-jet (t = 2.16s)

Figure 64. Cross-sectional flow streamlines comparison at 0.8 span at wind speed = 15m/s.

4.4 Study of the Height of Microtabs

The previous part of this chapter has investigated one size of the microtab on the wind turbine which is 2% chord of the sectional S809 aerofoil. However the question is to what extend the performance of the aerofoil changes by extending or shortening the microtab. Here some additional studies on the height effects of the microtab would be carried out using both 2D and 3D CFD simulations.

4.4.1 2D Study of Microtabs with Different Heights

Similar to the 2D studies on different flow control devices above, for 2D CFD study on the height effects of the microtabs we also select the S809 aerofoil which locates on the 80% span section for investigation.

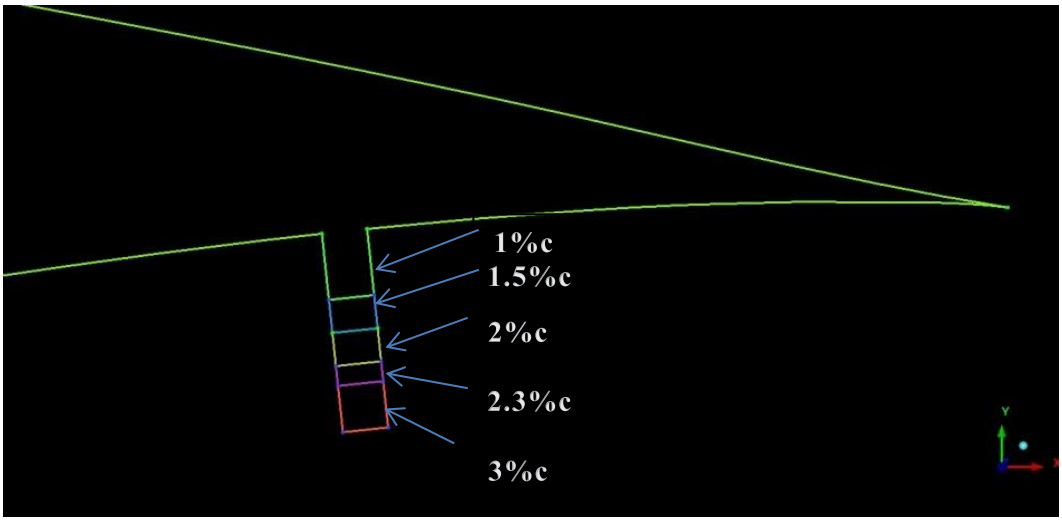

Figure 65. Microtabs with different sizes (1%c, 1.5%c, 2%c. 2.3%c and 3%c) on x/c = 0.9 position.

The trailing edge part for the 2D aerofoil is shown in Figure 65 and five different sizes of microtabs are studied which are 1%, 1.5%, 2%c, 2.3% and 3% chord length, respectively. The microtab with 2.3% chord is chosen because the aerofoil thickness at x/c = 0.9 position is 2.4% of the aerofoil chord length so if the microtab is deployed as an active flow control devices it may not exceed this height for practical manufacturing purpose. Moreover the study on the 3% chord microtab is carried out just for comparison purpose to see the aerofoil performance when increasing the height of the microtab. The mesh size is around 50,000 cells and all cases are run as steady flow conditions.

Results

All cases are converged with 8000 iterations and the C_l of the aerofoil converges very well. Here same as the previous 2D studies, we are not looking into the lift force but the force in direction parallel to the rotating direction of the blade which is $F_{effective}$. Because this force directly contributes to the final torque of the blade so it might be more accurate to use such force than the lift force for the study on the performance of sectional aerofoils.

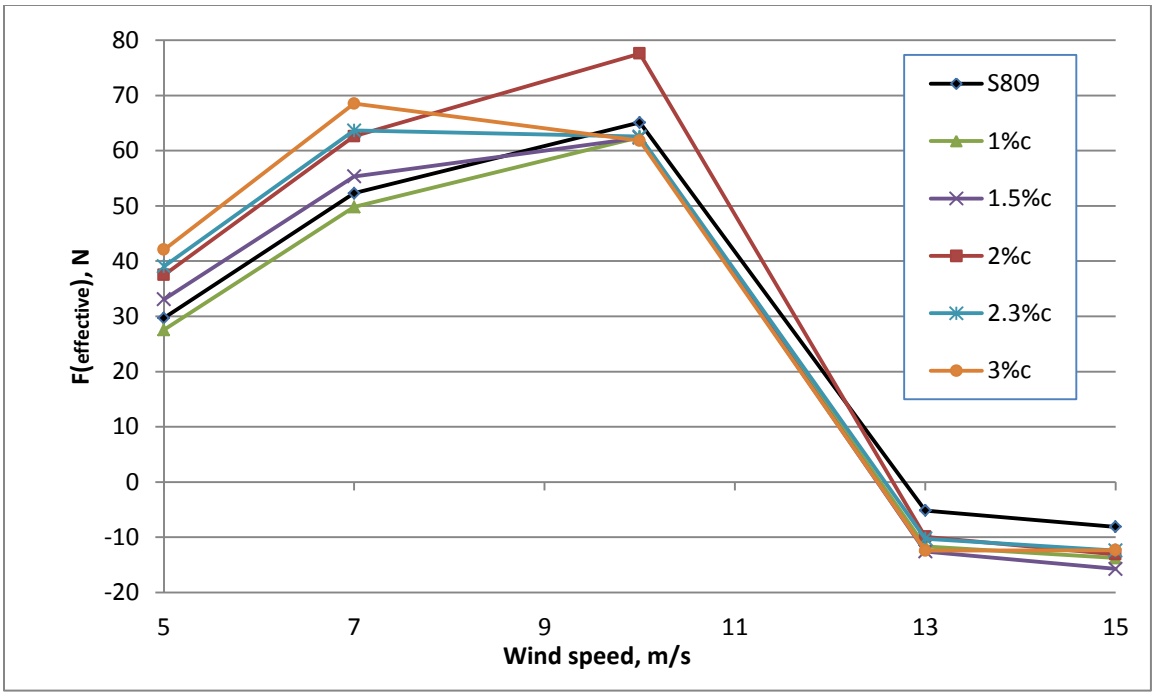

Figure 66. $F_{effective}$ comparison between microtabs with different heights (from 1%c to 3%c).

The $F_{effective}$ comparison among the original S809 aerofoil and that with microtabs of different heights at 80% span section of the blade is shown in Figure 66. It is interesting to see that the microtab with 1% chord height cannot improve the performance of the aerofoil but otherwise slightly reduces $F_{effective}$ in all wind speeds. Moreover, at lower wind speed range (5m/s and 7m/s) where the sectional aerofoil is not stalled, $F_{effective}$ would be improved with increasing the height of the microtabs. The 3% chord microtab is able to increase the $F_{effective}$ by 41.6% at 5m/s wind speed and 31% at 7m/s wind speed. However this situation changes when the wind speed is 10m/s where the sectional aerofoil begins to stall but not totally stalled. From Figure 66 it can be seen that only the 2% chord microtab increases $F_{effective}$ of the sectional aerofoil, more details and analysis of this situation can be found in the later part. A fully stalled wind speeds (13m/s and 15m/s), because of the large separation on the suction side of the aerofoil, the sectional S809 aerofoil with all sizes of microtabs are having negative results to the wind turbine blade which are shown in Figure 66. At this situation the aerofoil with microtabs are performing worse than the original aerofoil.

Pressure coefficient comparison

Figure 67 shows the comparison of pressure coefficients around the S809 aerofoil with different sizes of microtabs. Here only the 1% chord, 2% chord and 3% chord microtabs are selected for comparison. The results are corresponding to the $F_{effective}$ comparison above. It can be seen that at 7m/s wind speed, the 1% chord microtab is not able to improve pressure coefficient along the aerofoil compared to the original one while the 2% chord and 3% chord microtabs increase the pressure coefficient differences between the pressure side and suction side which leads to higher lift force of the sectional aerofoil. At 10m/s wind speed situation, the 2% chord microtab (greed dots) is the only one that can increase the pressure coefficient differences therefore to some extent it explains the $F_{effective}$ results. In the 15m/s wind speed situation, where the aerofoil is fully stalled, from Figure 67, the microtabs are indeed increasing the pressure coefficient differences between the suction side and pressure side of the aerofoil near the trailing edge. Therefore this condition may lead to higher C_l, however from the previous $F_{effective}$ comparison this kind of C_l increment cannot lead to higher torque contribution of the wind turbine blade.

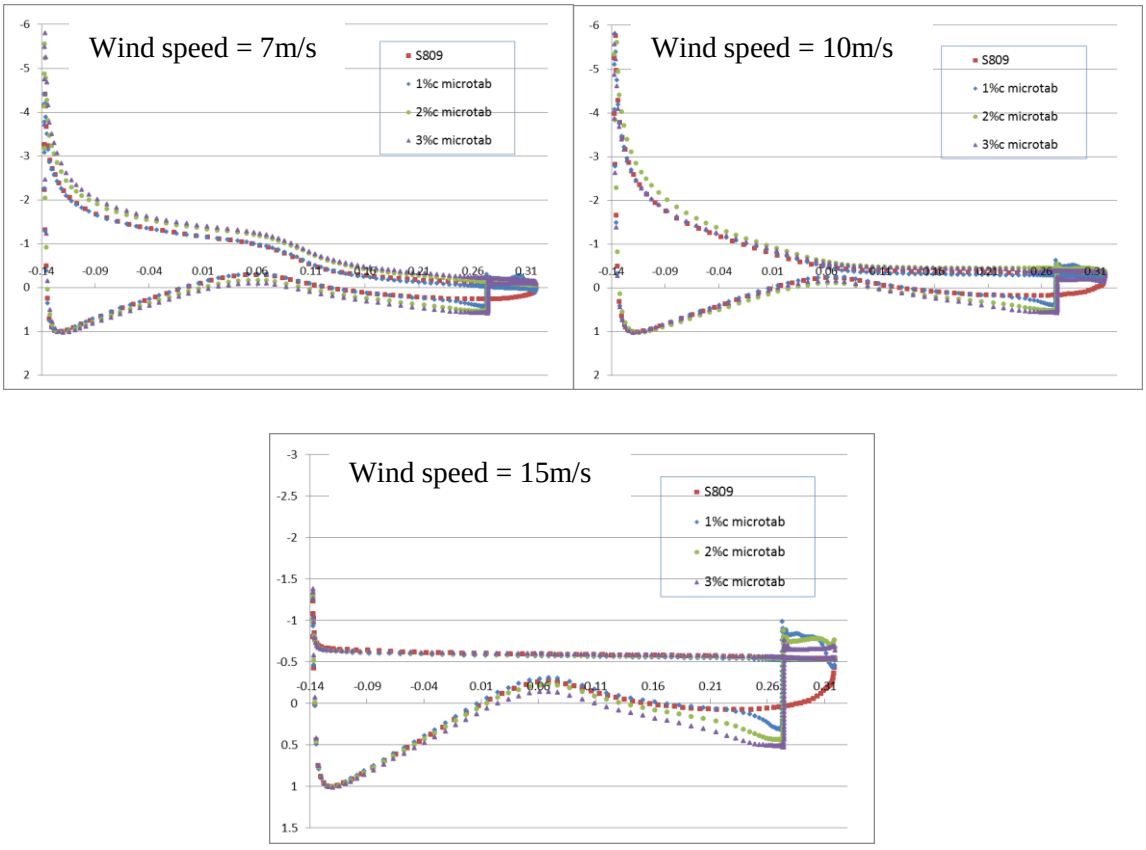

Figure 67. 2D pressure coefficient comparison among S809 aerofoil and microtabs with different sizes.

Streamlines and turbulence kinetic energy overview and comparison

Figures 68, 69 and 70 show the comparison of the streamlines and turbulence kinetic energy contour for S809 aerofoil with different sizes of microtabs. The values of turbulence kinetic energy are from 0 to 30 J/kg (blue to red). As can be seen from Figure 68, at lower wind speed 7m/s, where most part of the flow around the aerofoil is attached except for the small region near the trailing edge on the suction side, the 2% chord and 3% chord microtab can effectively reduce or eliminate the turbulence at that region. However at higher wind speeds where there are large separation flows on the suction side, all sizes of microtabs are not able to improve the performance of the aerofoil by reducing the separation area, generating more separation near the trailing edge on the pressure side.

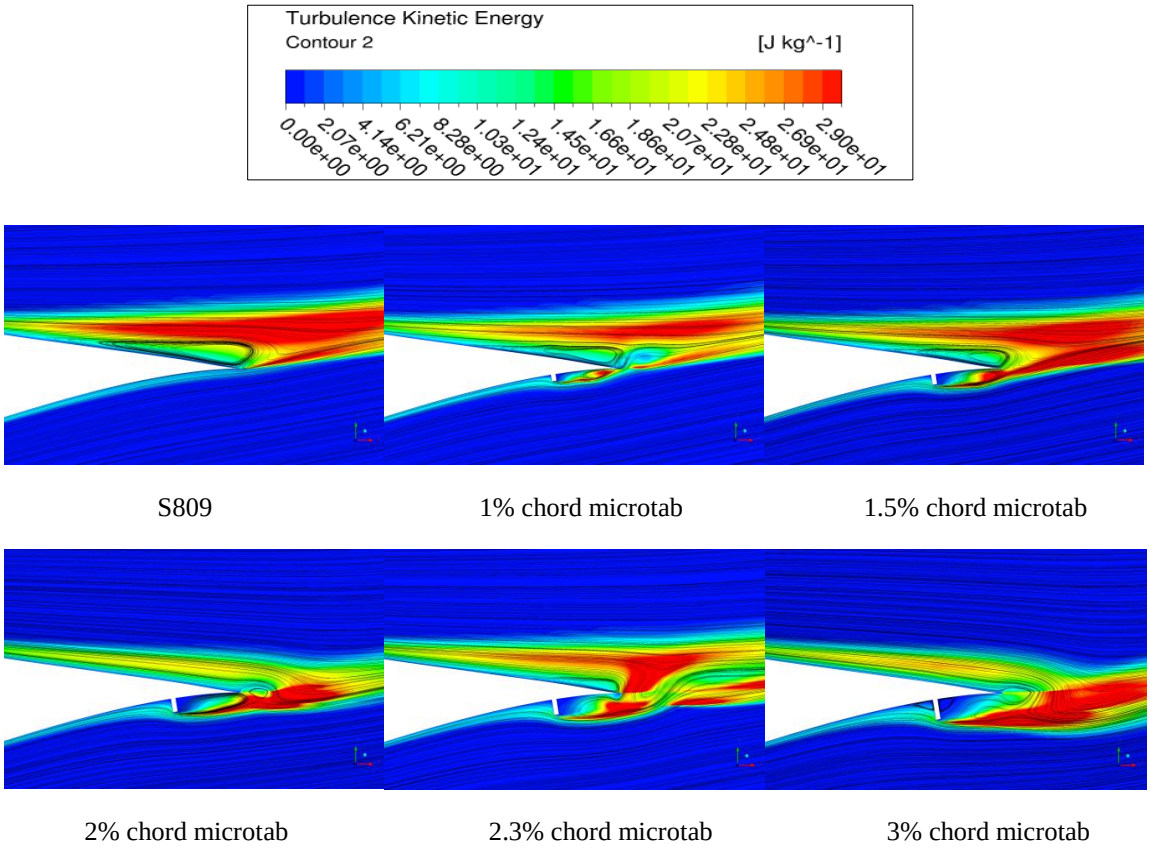

Figure 68. Streamlines and turbulent kinetic energy contour comparison at 7m/s wind speed.

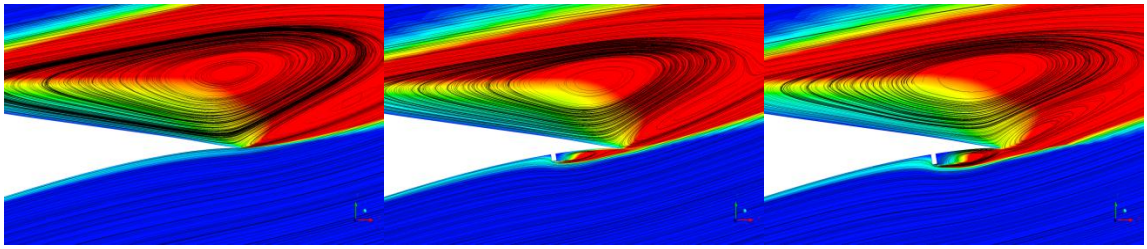

S809 1% chord microtab 1.5% chord microtab

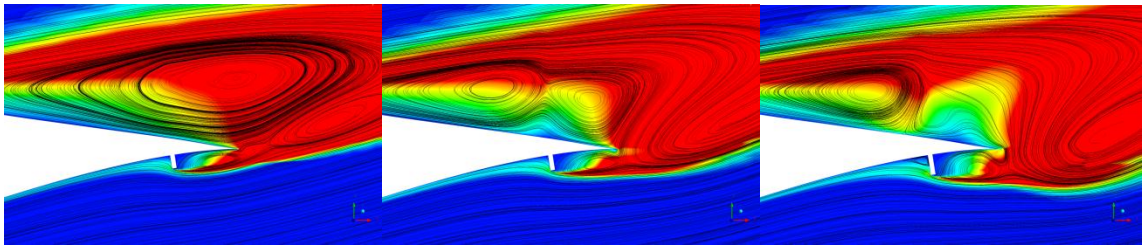

2% chord microtab 2.3% chord microtab 3% chord microtab

Figure 65. Streamlines and turbulent kinetic energy contour comparison at 10m/s wind speed.

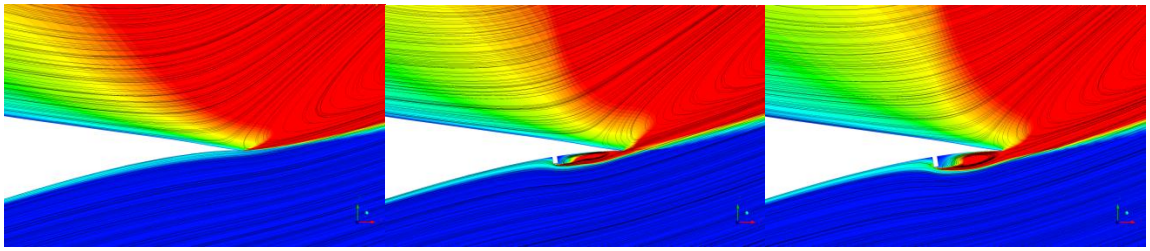

S809 1% chord microtab 1.5% chord microtab

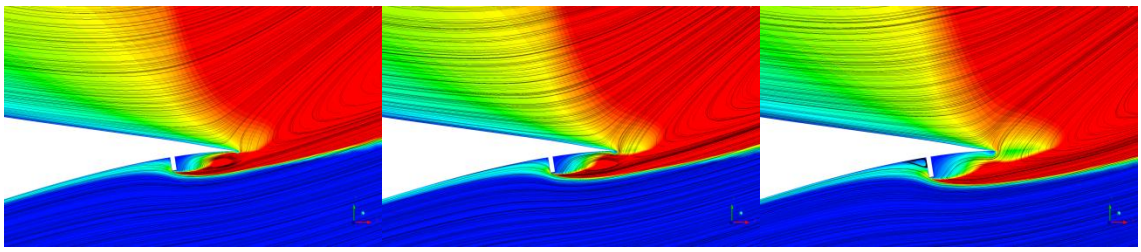

2% chord microtab 2.3% chord microtab 3% chord microtab

Figure 66. Streamlines and turbulent kinetic energy contour comparison at 15m/s wind speed.

In summary, the 2D CFD study on the size effect of microtabs on the pressure side of the S809 aerofoil shows that at non-stall wind speed range (here is 5m/s and 7m/s cases) the sectional aerofoil performance can improve by increasing the height of microtabs. However, when the sectional aerofoil begins to stall, the microtab as a flow control device is no longer effective.

4.4.2 3D Study of Microtabs with Different Heights and Spanwise Ranges

The 2D CFD study on the size effects of microtabs shows that the microtab performance varies a lot due to their heights. In this 3D research the micro-tab is also deployed on the NREL PHASE VI wind turbine. Four different sizes of the micro-tab are simulated which are 1%c, 1.5%c, 2%c and 2.3%c respectively. The reason for not selecting 3% chord microtab is because the microtab is assumed to be an active flow control device and the aerofoil thickness at 90% chord position is just around 2.4% chord length. Therefore the 3% microtab is difficult for installation. Moreover, the micro-tab with 2% chord height is simulated at three different spanwise ranges on the blade (70%-97%, 75%-97% and 80%-97%). Considering the manufacturing possibility, the micro-tab is set to be 3mm width and is located at the 90% chord length position of the cross-sectional aerofoil. In order to simplify the mesh and decrease the mesh size, the micro-tab simulated here is assumed to be integral and with no gaps (Figure 71).

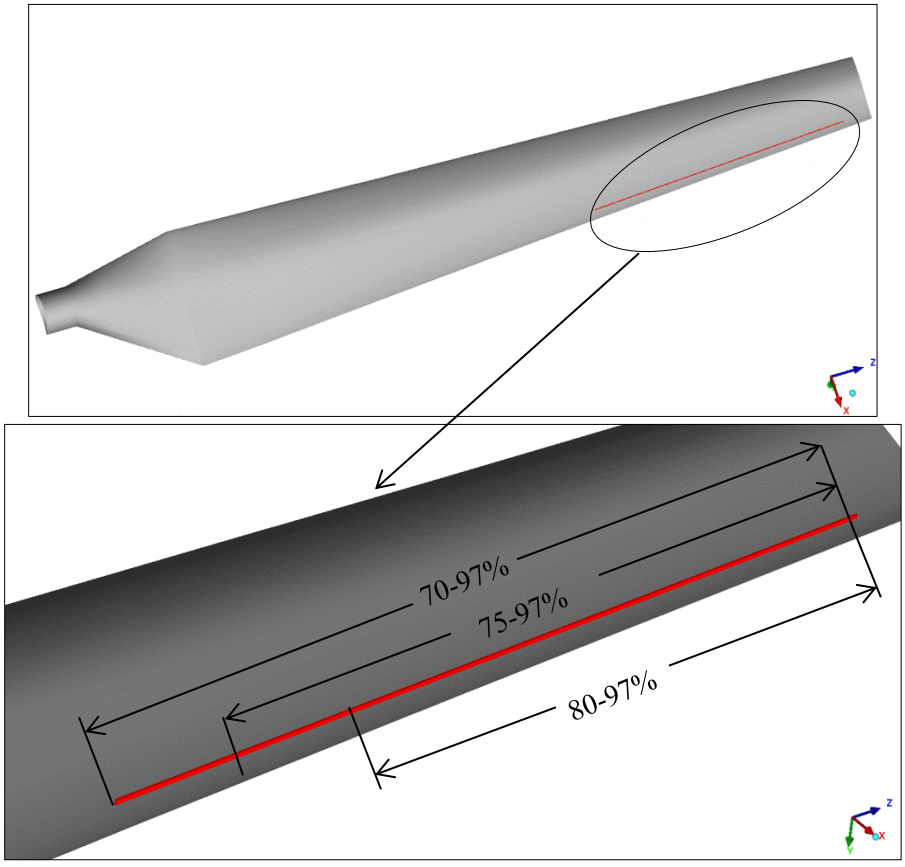

Figure 71. NREL Phase VI blade with 2% chord microtab. Top left: 70%-97% spanwise range; top right: 75%-97% spanwise range; bottom: 80%-97% spanwise range.

Results

Figure 72 show the computed torque from the simulations with comparison between the original blade and that with 1% chord length to 2.3% chord length size micro-tab. The detailed results can be found in Appendix 3. Similar as the 3D simulations in the previous sections, for 5m/s, 7m/s and 10m/s wind speed cases, the simulations are run as steady flow while for 13m/s and 15m/s wind speed cases the simulations are run as unsteady flow conditions.

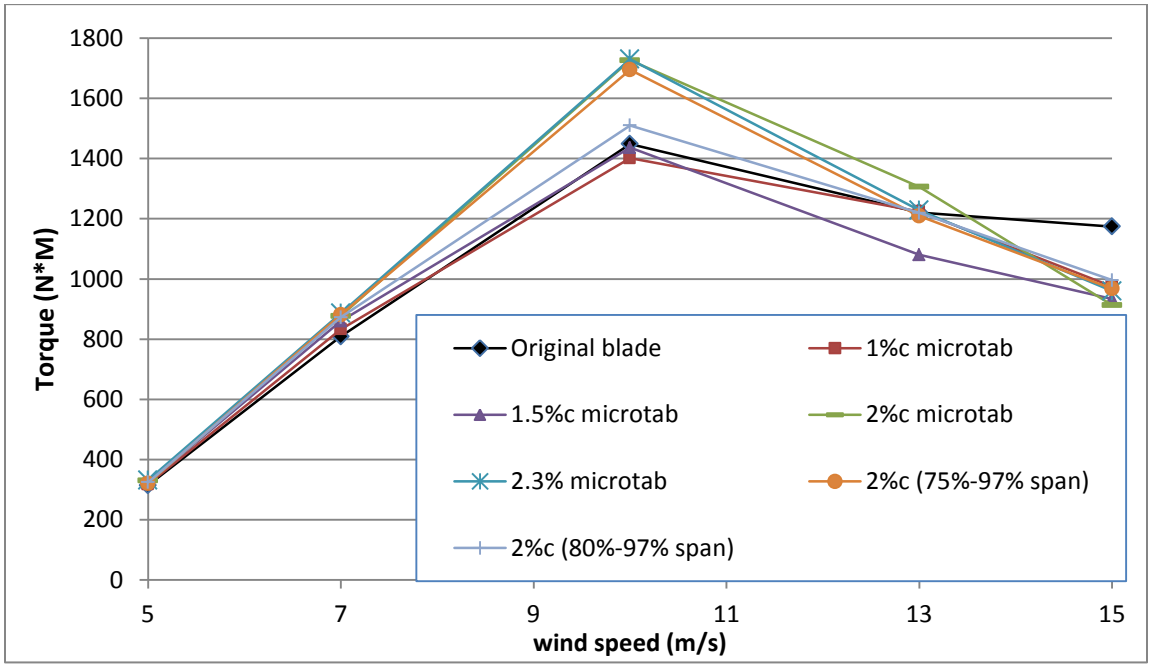

Figure 72. Comparison torque of the NREL PHASE VI blade with different sizes of microtabs.

The results show that the deployment of almost all sizes of micro-tabs is able to increase the torque generated by the NREL wind turbine from wind speed 5m/s to 10m/s except for the 1%c and 1.5% chord length micro-tabs cases. They decrease a very small amount of torque at 10m/s wind speed situation. The 2.3% chord length micro-tab (from 70% to 97% span) and the 2% chord length micro-tab (from 75% to 97% span) can increase the induced torque from the wind turbine by nearly 20% at 10m/s wind speed situation. Considering this stall regulated wind turbine is design with a 10m/s rated wind speed, this improvement is significant. Moreover, the spanwise range of the micro-tab is not seems to be an important factor contribute to the performance of this kind of deployment. The results for these three different spanwise ranges of the 2% chord microtabs (70%-97%, 75%-97%, 80%-97%) show very similar performances. The

80%-97% spanwise range one is showing much less torque improvement than the other two cases. Overall, referring to Figure 72, the 2% chord length deployed at the 70%-97% spanwise range and x/C = 90% location has the best performance and can increase the torque generated by the wind turbine by 20% at its rated wind speed.

Pressure coefficient comparison at r/R = 0.8 span section

Figure 73 shows the pressure coefficient comparison at the 80% span position of the blade corresponding to the 2D studies. Here the original blade, blade with 2.3% chord height (70%-97% span), blade with 1% chord height (70%-97% span) and 2% chord (75%-97% span) microtabs are selected for comparison. The wind speeds selected for the comparison are 5m/s, 10m/s and 15m/s respectively.

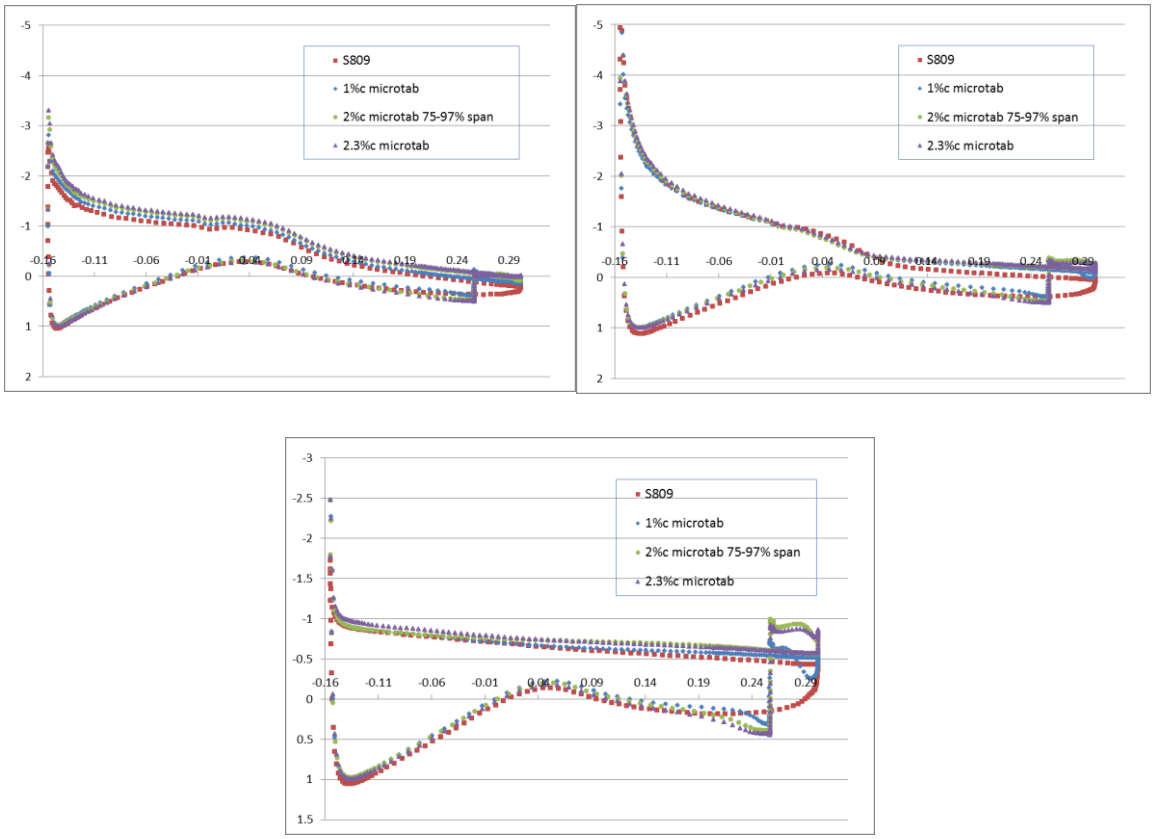

Figure 73. Pressure coefficient comparison between the NREL Phase VI blade and that with 1% (70-97% span), 2% (75-97% span) and 2.3% (70-97% span) chord microtabs. Top left: wind speed = 7m/s; top right: wind speed = 10m/s; bottom: wind speed = 15m/s, t = 2.16s.

From the figure it can be seen that when the wind speed is low, the micro-tab slightly changes pressure coefficient on the suction side of the blade. And at higher wind speeds, the micro-tab leads to higher pressure coefficient near the trailing edge on the pressure side. Overall, it can be seen when compared to the results from 2D simulations, there are some differences between each other especially at higher wind speed such as 10m/s and 15m/s. The 3D simulations predict higher pressure coefficient near the leading edge on the suction side. This maybe because the spanwise flow is dominating on the suction side of the blade which meaning that the 2D simulation of the sectional S809 aerofoil is becoming unreliable.

Surface pressure contour, streamlines and turbulence kinetic energy contour

Figures 74, 75 and 76 show the surface pressure contour of the blade and sectional streamlines and kinetic energy contours. The value range of the kinetic energy contour is the same as that from the 2D studies above which is 0-30 J/kg. Two span sections, at r/R = 0.47 and r/R = 0.8, are selected for investigation. Comparing to the 2D results, there are some obvious differences. At 7m/s wind speed, shown in Figure 74, it can be seen that at r/R = 0.8 section, the 3D results are showing no flow separation near the trailing edge on the suction side of the blade while the 2D results show small separations there. This condition is more obvious when we look into the turbulence kinetic energy contour. This situation also happens at the 10m/s cases as the 3D CFD show much smaller separation and kinetic energy areas than those from the 2D CFD studies. At 15m/s wind speed, as shown in Figure 76, almost the whole blade is stalling and results from both 2D and 3D cases are showing that the microtabs are not able to improve the power output of the blade. The 3D cases here are also run as unsteady flow and the cases at t = 2.16s are selected for comparison.

In summary, at lower wind speeds, increasing the height of microtab can further improve the aerodynamic performance of the blade. However when the blade begins to stall, increasing the height of microtab is not able to further improve the blade torque because of the large separation area on the suction side. This situation also happens at 10m/s wind speed which the designed wind speed of this HAWT.

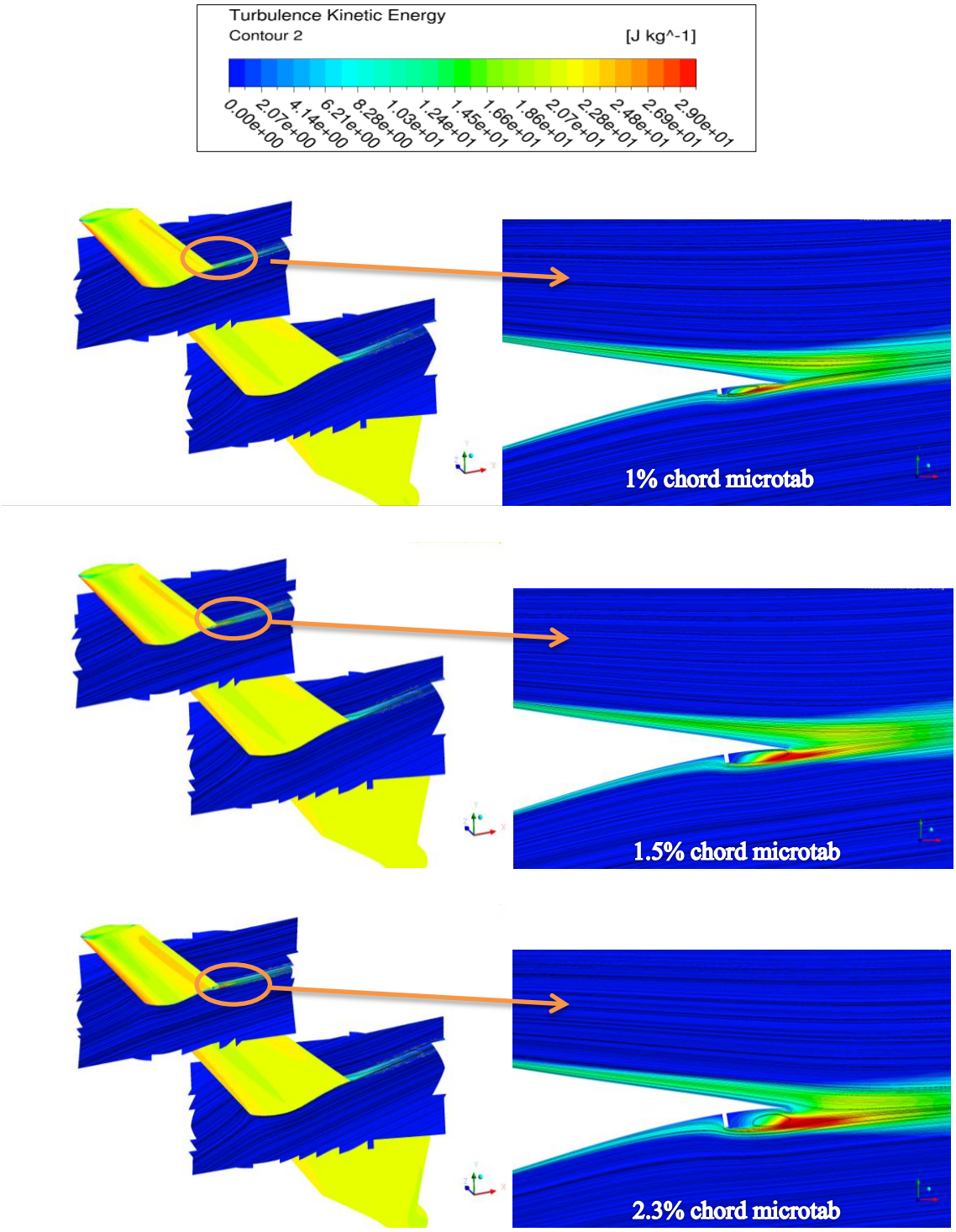

Figure 74. Surface pressure contour, streamlines and turbulence kinetic energy contour at 7m/s wind speed.

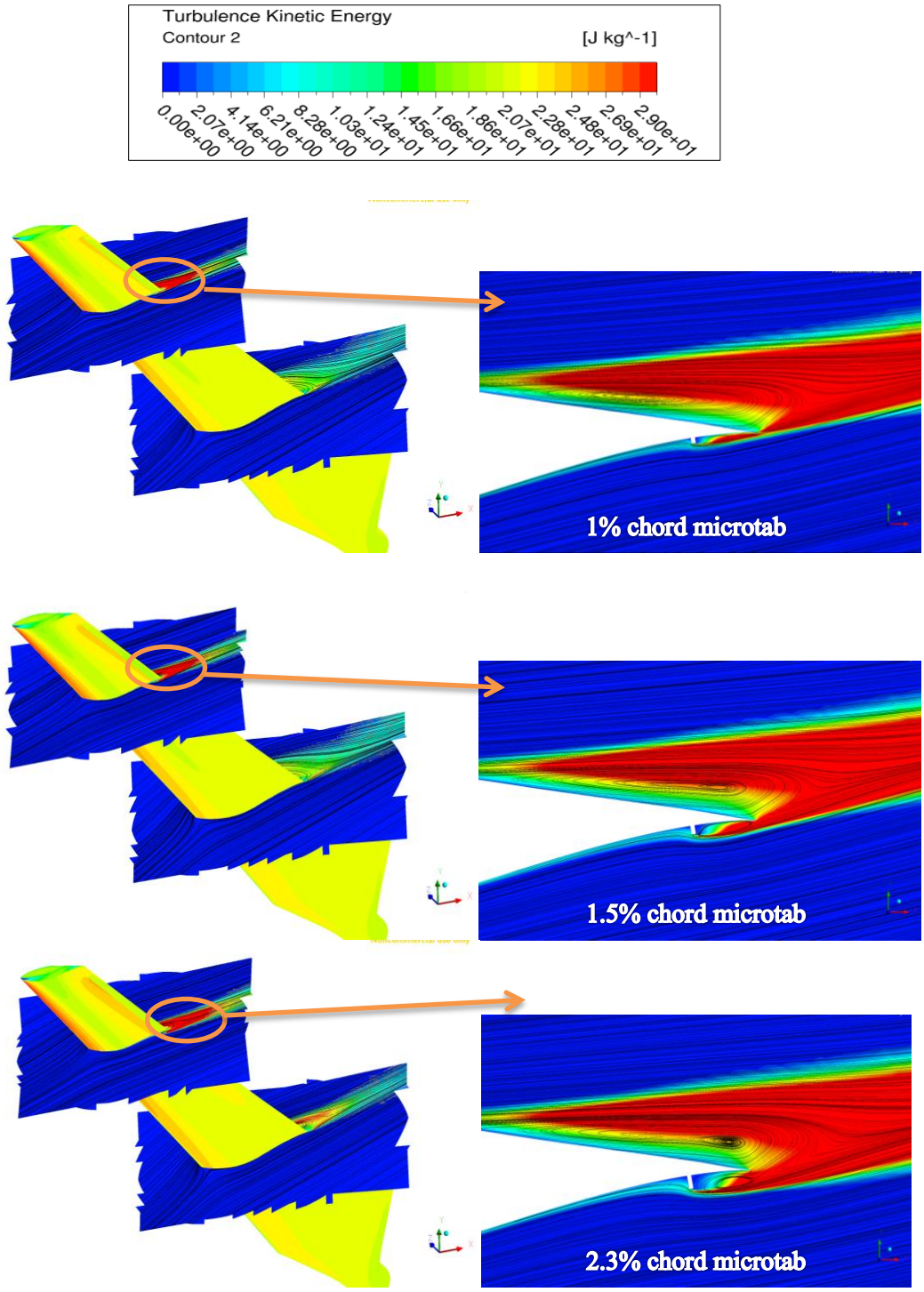

Figure 75. Surface pressure contour, streamlines and turbulence kinetic energy contour at 10m/s wind speed.

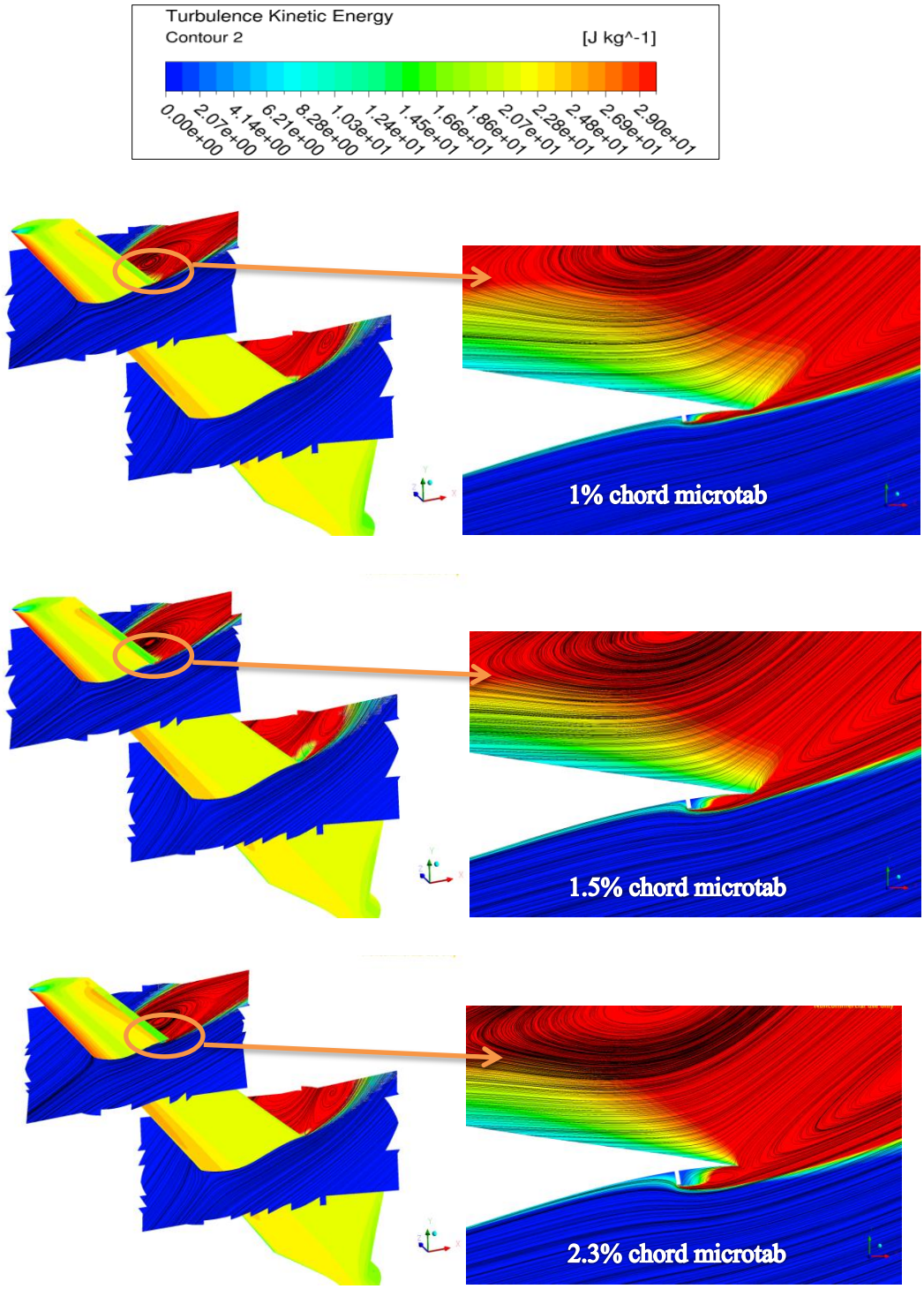

Figure 76. Surface pressure contour, streamlines and turbulence kinetic energy contour at 15m/s wind speed, t = 2.16s.

4.5 Chapter Conclusions

A stall-regulated NREL Phase VI wind turbine is investigated with three trailing edge flow control devices, namely, microtab, microjet and divergent trailing edge. Before simulating the flow control devices in full 3D in the rotating framework, the 2D study of flow control devices on the S809 aerofoil at r/R = 0.8 position of the wind turbine was carried out. The results show that in lower wind speed range when the blade is dominated by attached flows, the flow control devices can effectively improve the performance/torque by as much as 100%.

For more accurate prediction of the effects of the flow control devices, 3D study of flow control devices on this blade in a rotating framework is carried out. Unfortunately, the 2D prediction overestimates the effects of flow control devices. The benefit from the flow control devices in 3D is much less than the 2D cases. For example, at the 5m/s wind speed situation, the 2D simulations show large improvement by deploying the flow control devices but the 3D simulations just show very slight improvement compared to the original blade. And moreover at 10m/s, the 3% DTE does not perform as well as it does in the 2D simulation. For flow control devices, it is essential to include the 3D flow effects and 2D simulations are not reliable for performance prediction.

Some studies on the microtab height and position effects are carried out in this chapter. Totally 6 different geometry model are simulated, which are 1%, 1.5%, 2%, 2.3%c height micro-tabs deployed at 70%-97% spanwise position and 2%c height micro-tab deployed at 75%-97% and 80%-97% spanwise positions. The results show that the 2%c micro-tab deployed at 70%-97% spanwise range and 2.3%c deployed at 70%-97% span position have the best performance, increasing as much as 20% of the torque of the turbine at 10m/s wind speed. The pressure coefficient comparison shows that the micro-tab has very little effects on the pressure coefficient on the pressure side away from the trailing edge region. Comparing the 3D CFD results to the 2D results, it can be seen that the 2D results predict much larger separation and kinetic energy on the suction side of the blade.

Overall from this chapter it can be seen that deploying trailing edge flow control devices can effectively improve the power output of a stall-regulated wind turbine. From the 3D study in the rotating frame, the microjet is more effective at the lower wind condition and the microtab at the higher wind speed condition (Figure 51).

In this chapter, the design parameters for the microtab height, the microjet velocity, and the DTE thickness were chosen from a small number of numerical tests. These parameters along with other

variables may be further tested and optimized in future studies. The study in this chapter is on a relatively small sized stall-regulated wind turbine. Therefore the following study of the trailing edge flow control can be conducted for larger (higher Reynolds number) variable-speed pitch control wind turbines, which dominate the current wind turbine market. This is useful to understand the Reynolds number effects on the performance of the flow control devices.

Chapter 5 CFD Study of Trailing Edge Flow Control Devices on NREL 5MW Off-Shore Wind Turbine

5.1 Introduction

The study in Chapter 4 has researched into the effects of two typical trailing edge flow control devices (microtab and microjet) and the divergent trailing edge concept on a stall-regulated wind turbine. The CFD simulations were carried out for both 2D aerofoil and 3D full-length blade. The results of 2D and 3D simulations show some correspondence and differences. All three kinds of flow control concepts improve the wind turbine's power output at lower wind speed range before the blade is fully stalled. This chapter is mainly about the following research on the effects of these three flow control concepts on a large modern off-shore NREL 5MW wind turbine, which is a three-bladed upwind variable-speed variable-pitch wind turbine. Unlike the previous stall-regulated wind turbine, the NREL 5MW wind turbine will not have large flow separation on the suction side at higher wind speeds because of the pitch control strategy. Therefore for the effects from the flow controls, it is significant to find out the differences between these two types of wind turbines.

The NREL 5MW blade was developed from the DOWEC (Dutch Offshore Wind Energy Converter) project based on the BEM theory and had a 5-MW rating power output (Butterfield, et al., 2009). As a conventional off-shore wind turbine some scholars have researched into its aerodynamic performance using CFD. Bazileys et al. (2011) investigated into the NREL 5MW blade using their NURBS-based (Non-uniform rational B-splines) simulation. Results showed that the computational torque, which is an important value for calculating the wind turbine performance, is quite close to the published data from the BEM code FAST. Moreover the study also illustrated that the efficiency of this wind turbine at 9m/s wind speed, which was 0.527, is close to the maximum efficiency from the Betz's limit theory which was 16/27. Wang et al. (2009) optimized the aerofoil section of NREL 5MW blade using the BEM theory and the structural dynamic model. Their research showed that the chord of the aerofoil around the middle span of the blade can be reduced by 8.2% for keeping the same power output. However this method also ignores the spanwise flow around the blade. Andersen et al. (2009) used the aeroservoelastic multi-body code HAWC2 to research into the deformable trailing edge flaps on the NREL 5MW blade. The results showed that the fatigue load, which means the flapwise

bending moment here, can be reduced by 25% in the blade root moment by deploying a 6.3m long flap at 45m from the root. Berg et al. (2009) researched into the effects of the conventional flap deployed at 90%c position of the aerofoil and morphing trailing edge from 80%c position of the sectional aerofoil (introduced in Figure 77) on the NREL 5MW blade using the NREL FAST/AeroDyn code. These two active flow control devices are all deployed from 25% span t tip of the blade. The maximum deflection is +/-10 degrees and the defection rate limit is 100 degree/sec. The results showed that such active trailing edge control strategy can decrease the fatigue damage causing by the flapwise bending moment and increased the shaft torque at wind speeds lower than the rated wind speed. Vesel & McNamara (2014) optimized the sectional aerofoil of the NREL 5MW blade based on the aerofoil data computed from XFOIL and the wind turbine loads and performance computed from the NREL FAST code. Their study showed that with the optimization of the thickness and control variables of the sectional aerofoils of the blade, the COE (cost of energy, defined as: $\mathrm{COE} = \frac{Capital\ cost + Operation\ cost + Maitenace\ cost}{Lift\ time\ energy\ production}$) can be decrease by over 6%.

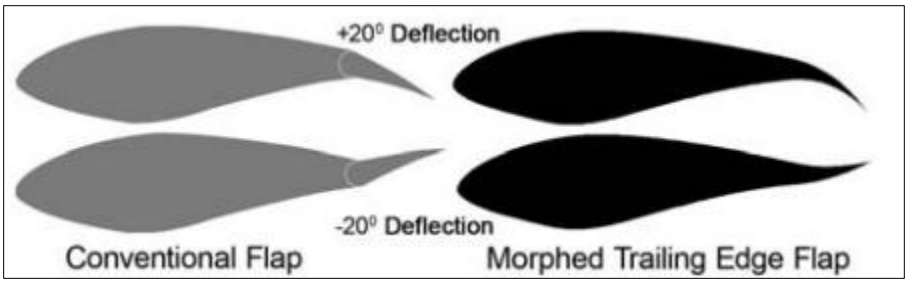

Figure 77. Conventional flap and morphing trailing edge flap (Berg et al., 2009)

In summary, the existing studies showed some significant progresses about the aerodynamic performance of the trailing edge flow control devices in both experimental and CFD method. However most of those studies are just for a span section of the blade with a specified aerofoil i.e. 2D simulation. Last chapter showed that microtab, microjet and the DTE concept can effectively improve the small stall-regulated wind turbine, however for modern large off-shore wind turbine with variable speed and variable pitch whether these flow control concepts still perform well is questionable. This part of the study firstly researches into the aerodynamic performance of the NREL 5MW blade, then carries out both 2D CFD study of the NACA 64-618 aerofoil and 3D CFD study of the blade with microtab, microjet and DTE concepts deployed at specified span locations.

5.2 CFD Study on NREL 5MW Wind Turbine

The CFD study on the NREL 5MW wind turbine is shown in this part which includes the generation of the geometry and mesh, blade surface pressure contour and friction lines, cross-sectional flow streamlines, wake study, torque distribution study and power output comparison.

5.2.1 Geometry and Mesh Generation

The NREL 5MW blade is a large off-shore upwind three-blade wind turbine with 63m radius, which consists of DU (Delft University) series aerofoils from 10m to 40m span and NACA 64-618-618 aerofoil from 40m span to tip. The detailed information of the sectional aerofoils is shown in Appendix 4 and Figure 78. The Twist Centre represents the ratio between the distance of the twist axis of the cross-section aerofoil to its leading edge and the chord length of the aerofoil. I.e. Twist Center = 0.375 means that the twist axis is located at x/c = 0.375 on the chord line. All these details can be found in the official definition report of the NREL 5MW wind turbine (Jonkman et al., 2009).

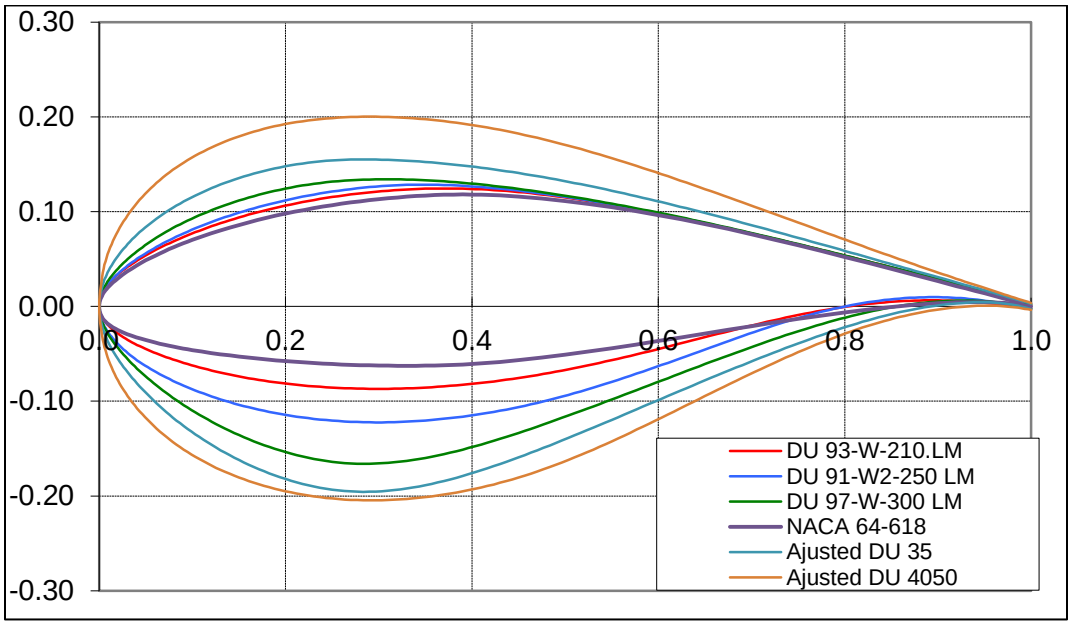

Figure 78. Overview of the used aerofoils for the NREL 5MW wind turbine.

Its cut in, rated and cut-out wind speed are 3m/s, 11.4m/s and 25m/s, respectively with a rated power output of 5MW. The rotational speed of the wind turbine grows from 6.9rpm at cut-in

speed to 12.1rpm at rated wind speeds and is kept constant from rated wind speed to cut-out speed. As defined before, the blade pitch angel is the pitch angle of the blade tip section which is normally zero. As a variable-speed variable-pitch wind turbine, the pitch angle of the blade is zero below the rated wind speed and then grows gradually with the higher and higher wind speed to as large as 23.47degrees at 25m/s wind speed. The details of the pitch angle and the rotational speed at different wind speeds of the wind turbine can be found in Appendix 5.

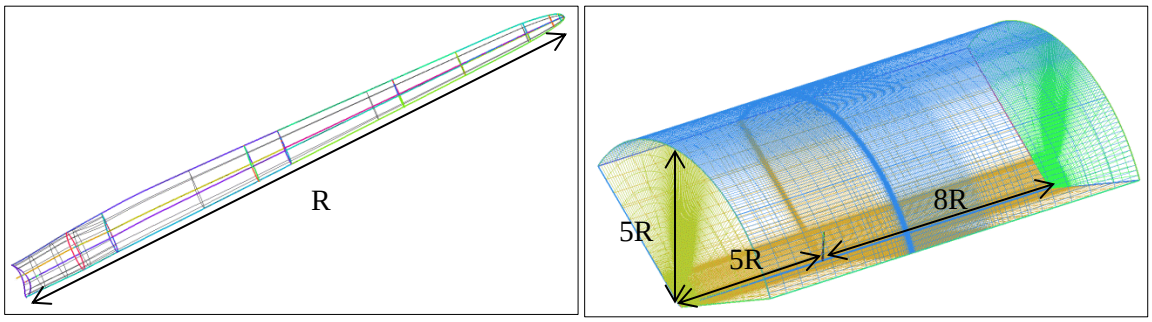

Figure 79. 5MW blade geometry setup (left) and overview of the computational domain and mesh (right).

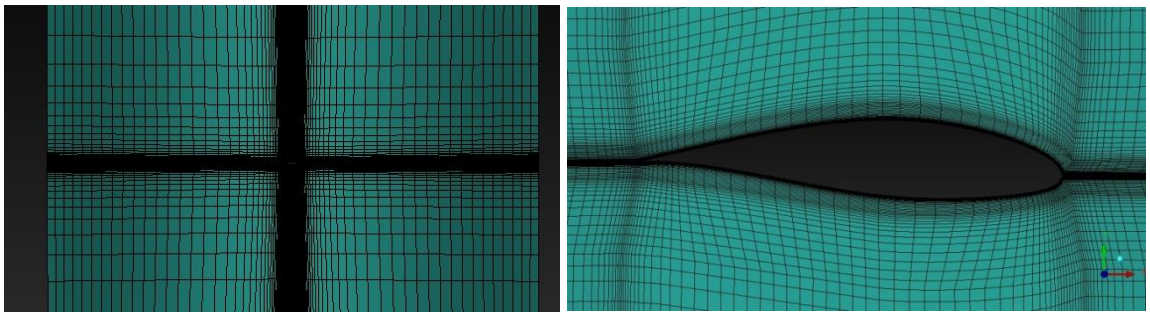

Figure 80. Cross-sectional cut plane and aerofoil mesh overview of the 5MW blade.

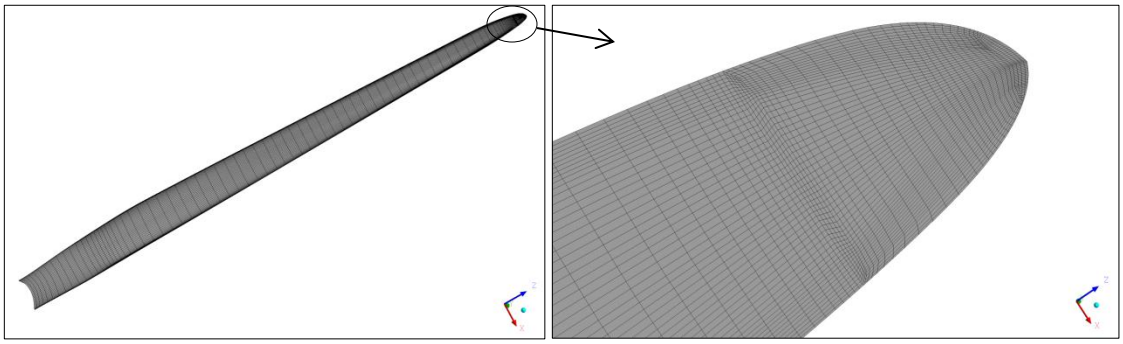

Figure 81. Blade surface mesh (left) and the O-mesh around the blade tip (right).

In this study the flow condition of all three blades is assumed to be repeated periodically therefore the periodic boundary condition is used for the two sides of the domain which is similar as the previous CFD domain of the validation case. This means that all the flow conditions are the same for the two periodic surfaces and the flow information will transfer through these two surfaces. Therefore the outer domain is a third cylinder and just one blade is simulated. The effect of the hub is neglected in present study as an approximation because in later study the mesh size might be very big for the blade with the flow control devices and the hub. The geometry detail can be found from the official published paper of the NREL 5MW blade and is generated in ICEM CFD software. As can be seen from Figure 79, the outer domain is with a radius of 5 times the radius of the blade, and the velocity inlet is 5 times blade radius far away from the blade where the pressure outlet is 8 time blade radius from the blade.

The geometry and mesh are generated in ICEM CFD. Unlike the stall-regulated wind turbine with a flat tip shape, the NREL 5MW wind turbine has a sharp tip therefore an H-type mesh is used in order to effectively capture the wake along the trailing edge (see Figure 80). For the tip region, an O-mesh is employed in order to improve the mesh quality which is shown in Figure 81. The mesh of the NREL 5MW wind turbine has 3.63 million cells in total. As mentioned above, this wind turbine is a pitch control wind turbine which means that at that the blade pitch angle will be changed after rated wind speeds which is 11.4m/s (Appendix 5), therefore the geometry and mesh will also be changed to corresponding pitch angles at different wind speeds.

5.2.2 CFD Solver Setup

This study also uses the same CFD solver as the study above – ANSYS FLUENT. Most of the boundary condition settings are the same as the previous case except the top surface of the outer domain is set to be pressure outlet instead of symmetry in the part-one study. This is because the validation case of previous study is a wind tunnel test and here the pressure outlet boundary condition is more reasonable for the real flow condition. The moving frame motion is also activated here for simulating the constant rotational speed of the blade. The Coupled scheme is used for the simulation and each simulation is carried out for around 10,000 iterations. All the cases in different wind speeds are steady and the momentum coefficient of the blade converges well. In this study only the shaft torque of the blade is researched which aims to show the wind turbine performance and to what extent can the trailing edge flow control devices influence the blade performance.

5.2.3 Results

Figure 82 shows the wake of the full NREL 5MW wind turbine at 11m/s wind speed with showing the Iso-surface of vorticity magnitude. It can be seen the strongest vortex exists at the trailing edge near the tip. The wake of wind turbine is very important for wind farm establishments because it will influence the wind velocity directly and increase turbulent intensity for other wind turbines in the farm. According to Figure 82, the wake from the wind turbine is mostly in the same direction of the coming wind speed. According to the right figure of Figure 82, the vorticity energy mainly distributes in a sector area with about 40 degrees besides the wind turbine blade. Because practically the wind turbine blade is rotating therefore this region is revolving behind the wind turbine. In the present study the wind turbine wake is not a primary research objective therefore the detailed wake region range and effects are not studied.

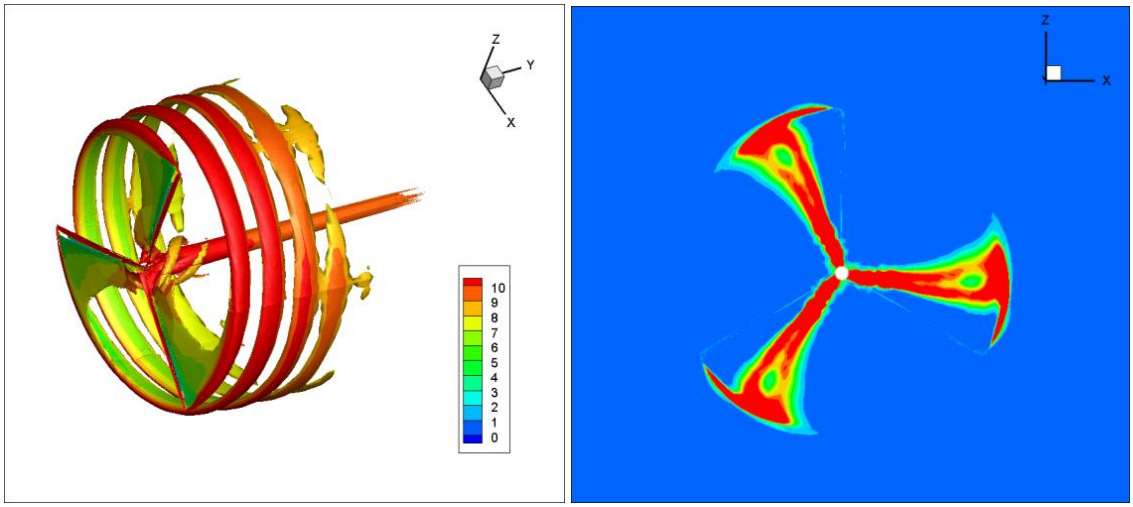

Figure 82. Wake study at 11m/s wind speed. Left: Iso-surface of Vorticity magnitude and contour of velocity magnitude; right: contour of vorticity magnitude at 2 meters behind the wind turbine.

Researching into the torque distribution of the blade provides the detailed information of what part of the blade contributes most of the energy output. Figure 83 shows that the blade is separated into eight parts to find out the torque density along the span of the blade. The parts are not separated averagely because aerofoil shapes at some specified span locations are defined by the official definition and it is more convenient to keep these sections for simplifying the mesh topology. Table 9 shows the result from the simulation. It can be seen that the upper part of the

blade from r = 37.8 to tip contributes 63.9% of the total power output of the blade. The following table 9 and Figure 84 show that the highest torque density is at around 80% span region. With such information this study mainly concerns the flow control devices around this high torque density region of the blade.

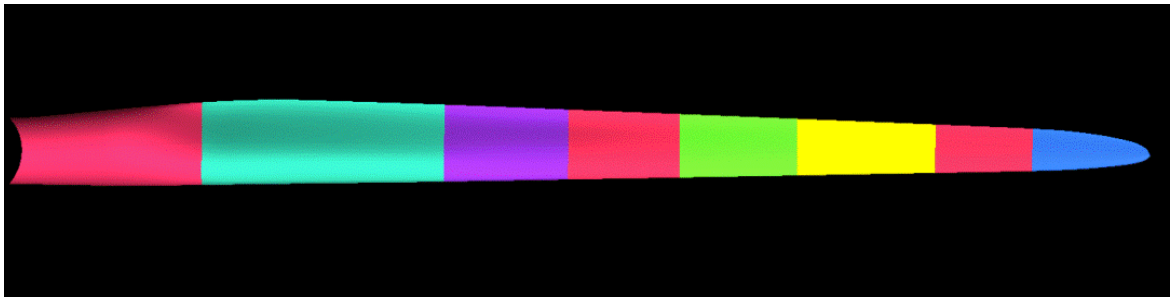

Figure 83. Segmenting the blade for torque distribution study.

Table 9. Torque distribution along the span of the NREL 5MW blade

r (m)	r/R	Torque (n*m)	Torque % of total	Torque per meter
0- 12.2m	0 - 0.194	17596	1.41%	1442
12.2 -25.2m	0.194 - 0.4	150981	12.15%	11614
25.2 - 31.84m	0.4 - 0.505	130961	10.54%	19723
31.84 - 37.8m	0.505 - 0.6	148997	11.99%	24999
37.8 - 44.1m	0.6 – 0.7	190559	15.33%	30247
44.1 - 51.4m	0.7 - 0.0.816	260092	20.93%	**35629**
51.4 - 56.7m	0.816 – 0.9	187562	15.09%	**35389**
56.7 - 63m	0.9 - 1	155921	12.55%	24749
Total		1242673		

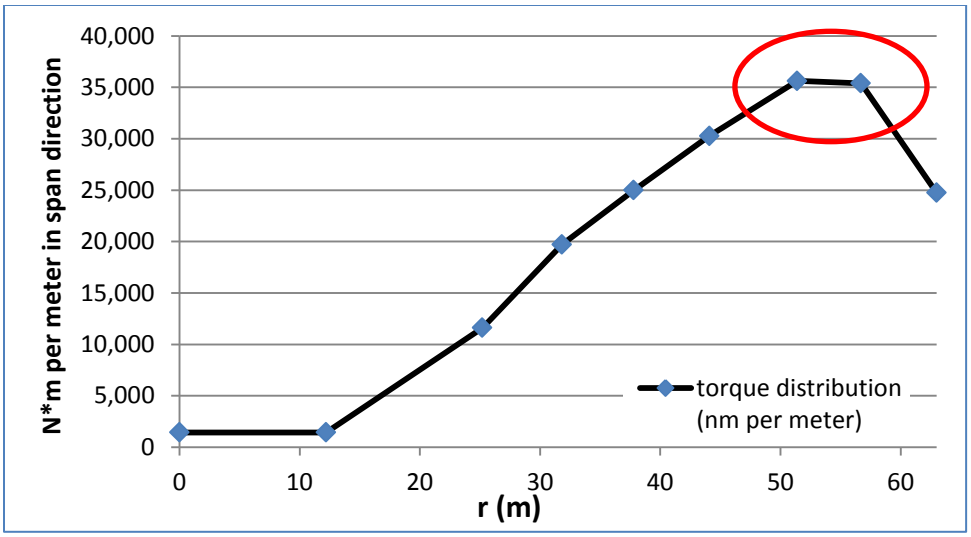

Figure 84. Torque distribution along the span of the NREL 5MW blade. The red circle shows the highest torque density of the blade region is from r = 51.4 to r = 56.7.

The surface pressure contour and friction lines of the blade can be seen from chapter four of this paper in order to comparing with the blade with different flow control concepts. It can be seen that unlike the previous NREL Phase VI wind turbine, in all wind speeds even as high as 20m/s the flow around most part of the blade is attached except just a small detached flow near the root region at the suction side. Moreover it is also interesting to see a small separation at the pressure side near the trailing edge at 5m/s wind speed.

The NREL 5MW offshore wind turbine is designed to have a 5MW power output at the 11.4m/s rated wind speed and keep a constant 5MW power output from rated to cut-out speed based on the NREL FAST BEM code. From the CFD results of the present study, the power output of the blade is lower than that predicted by the BEM code. Moreover the power keeps dropping from rated wind speed to cut-out speed. Compared to other published paper, Chow & Dam (2011) used the CFD code OVERFLOW2 with the $k-\omega$ SST turbulence model to simulate the NREL 5MW wind turbine. Compared to the results from the BEM code, their results over-predicted the power output of the wind turbine when the wind speed is higher than 11m/s which is the rated wind speed. This study also focused on the separation on the suction side near the root. They deploy a fence around the largest aerofoil neat the root and get a 1% increase of the power output of the wind turbine at 8m/s wind speed condition. Sørenson & Johansen (2007) used their code EllipSys3D with the $k-\omega$ SST model to study the aerodynamics of the NREL 5MW blade and their results are close to that from the present study using FLUENT (Figure 85). Overall, according to the pressure coefficient comparison done in the validation case (Figure 26), the

present CFD methodology can accurately predict flow condition and also the shaft torque of the wind turbine in non-stall situation. From Figure 97, 100, 103 it can be seen that the blade surface is mostly dominated by attached streamwise flow with just very small separation area near the root on the suction side. Therefore for the NREL 5MW wind turbine the present CFD method can probably show very accurate results for the shaft torque and flow structure around the blade using RANS solution. Moreover with the code to code comparison with some other published research works, the results from the present study is assumed to be with reasonably good accuracy.

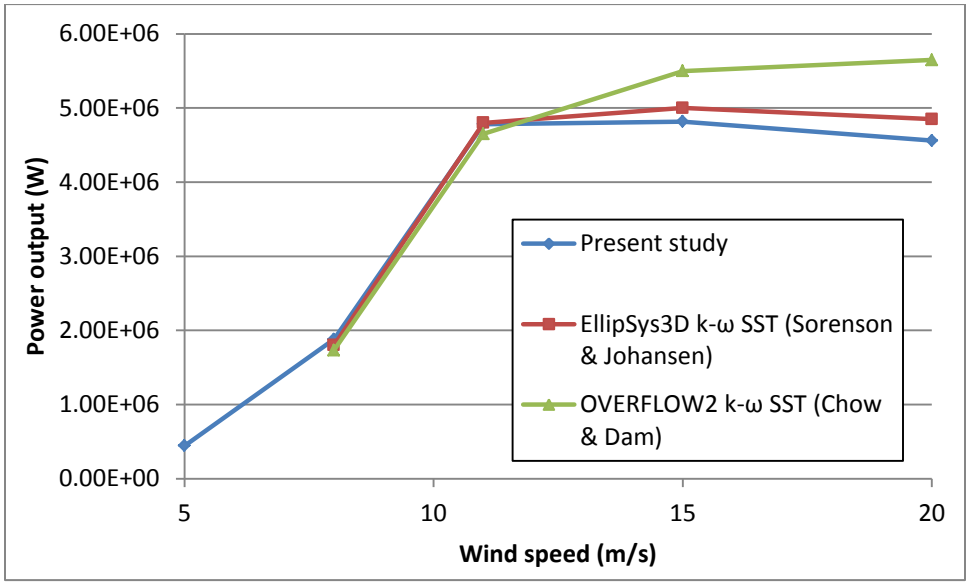

Figure 85. CFD code to code comparison of the power output of the 5MW wind turbine.

5.3 2D Aerofoil Study with Microtab, Microjet and DTE

The study above showed that the region near the 80% span position of the NREL 5MW blade has the highest contribution to the torque. Therefore the NACA 64-618 aerofoil at r/R = 0.8 span section is selected for the 2D CFD study.

5.3.1 2D Geometry and Mesh

The NACA 64-618 aerofoil at 80% span of the blade is with 2.659m chord length and 1.9 degrees twist angle. The mesh detail of NACA 64-618 aerofoil and that with flow control devices is

shown in Figure 86. All cases are using an H-type mesh except for the DTE case which is using C-type mesh. The mesh size of all cases is from 35,000 to 70,000 grids. The right and bottom edges of the outer domain are set to be velocity-inlet while the top and left edges are set to be pressure-outlet. The flow velocity is the same as the sectional relative wind speed of the wind turbine in rotating situation. Both the microtab and microjet are deployed at 90%c position of the aerofoil with 1 centimeter thickness.

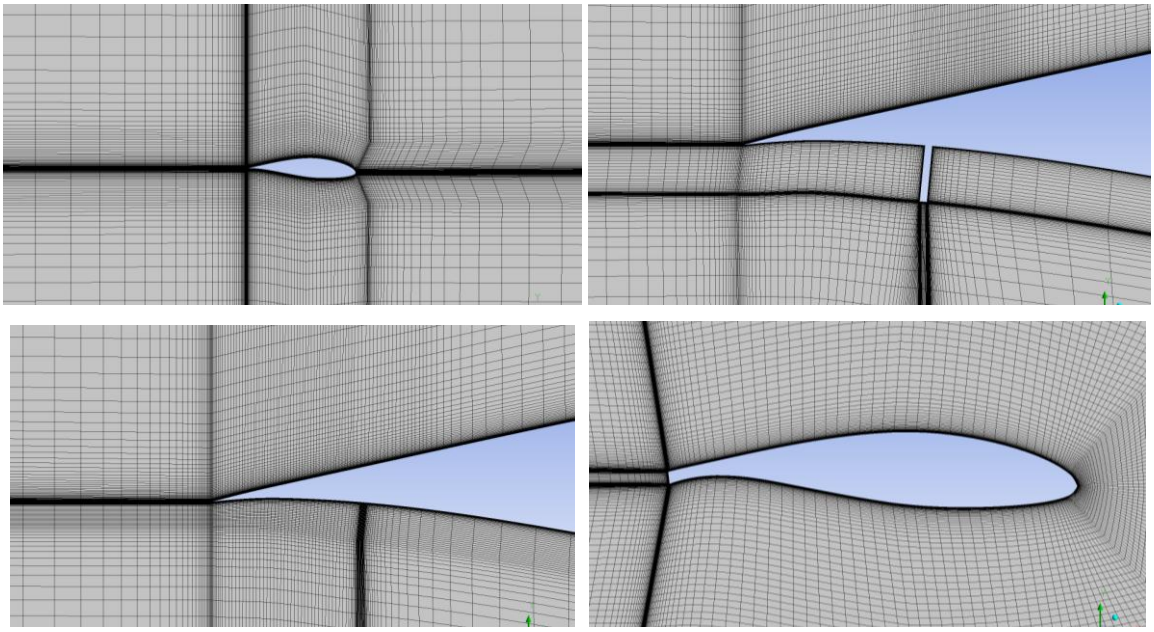

Figure 86. 2D CFD meshes. Top left: mesh of NACA 64-618 aerofoil; top right: mesh of NACA 64-618 aerofoil with 3% chord microtab; bottom left: NACA 64-618 aerofoil with 100m/s outlet speed microjet; bottom right: NACA 64-618 aerofoil with 3% chord with DTE design.

5.3.2 Results

The right and bottom edges of the outer boundary are set to be velocity-inlet, while the top and left edges are set to be pressure-outlet. The X velocity of the velocity-inlet is the calculated V_X = R*ω*0.8, where R is the radius of the blade (63m), ω is the rotational speed of the blade (rad/s) which changes with different wind speeds. The Y velocity of the velocity-inlet is the working wind speed of the wind turbine. Here the 5m/s, 8m/s, 11m/s, 15m/s and 20m/s wind speeds are studied.

The results of the 2D NACA 64-618 aerofoil and that with different trailing edge flow control concepts are shown, including pressure distribution comparison, streamlines comparison and effective force comparison. All cases are run in steady flow field conditions for this pitch control wind turbine case.

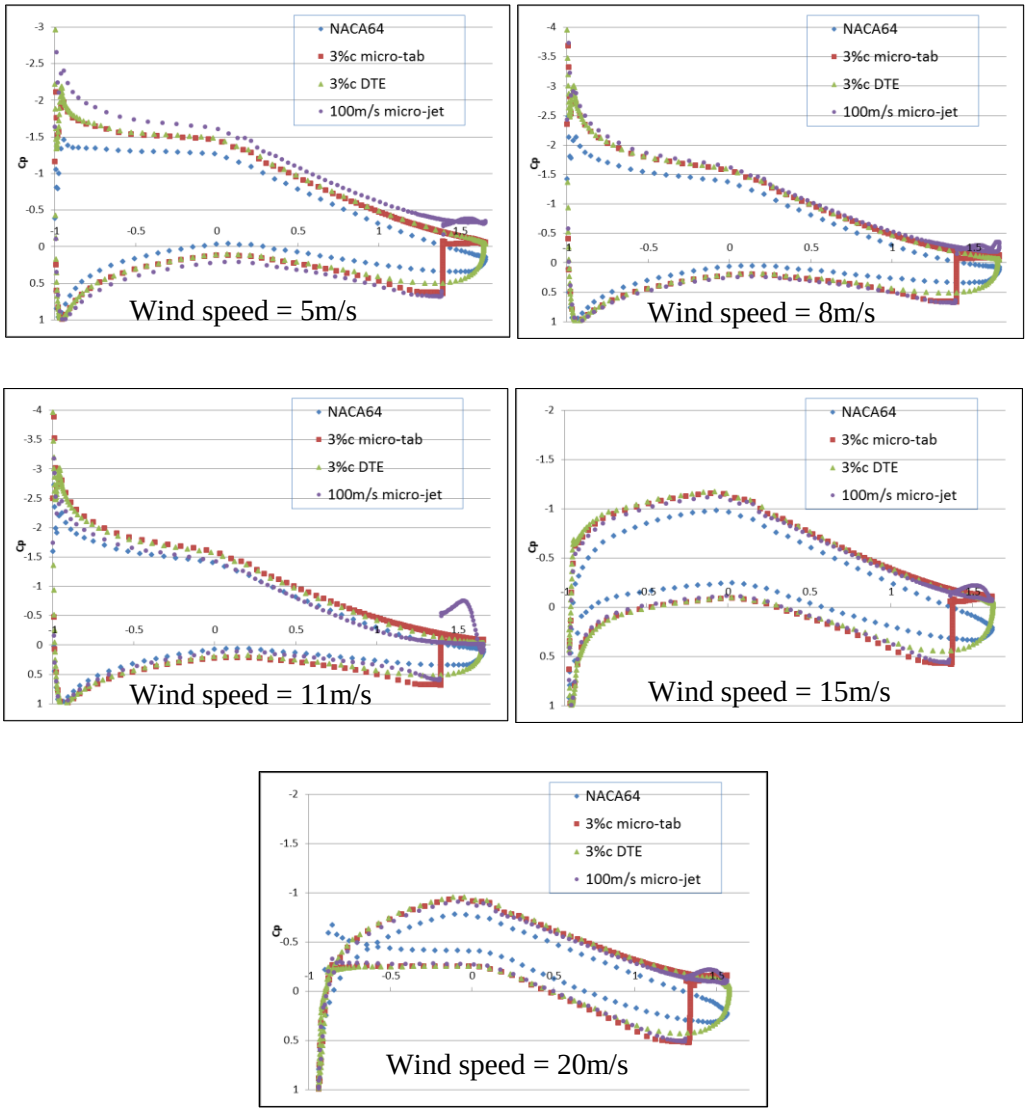

Figure 87. Comparison of pressure coefficient (C_p) between NACA 64-618 aerofoil and that with 3% chord microtab, 100m/s speed microjet and 3% chord DTE.

The pressure distribution of the NACA 64-618 aerofoil and that with microtab, microjet and DTE from 5m/s to 20m/s wind speeds is shown in Figure 87. At lower wind speeds such as 5m/s and 8m/s, the 100m/s outlet speed microjet shows the best performance while the 3% chord microtab

and DTE show quite similar C_p except for the trailing edge area. At 11m/s which is the rated wind speed of the blade, the 3% chord microtab and DTE show better performance than that of the 100m/s speed microjet and all flow control concepts show improvement over the original NACA 64-618 aerofoil. At higher wind speeds such as 15m/s and 20m/s, because the blade is pitched to large angles, the angle of attack becomes negative and at this situation the flow control concepts show large improvement due to the difference between the pressure side and suction side of the aerofoil leading to big increase of the lift force.

From Figure 88 to 82 the streamlines and pressure contour of the NACA 64-618 and that with deployment of trailing edge flow control concepts are shown clearly. All the flow control concepts increase the pressure on the pressure side of the aerofoil. Moreover, the pressure side endures the highest pressure at 11m/s wind speed, leading to the highest thrust. The flow control devices and DTE increase the pressure in the front region near the flow controls (from flow control devices towards leading edge) which can be seen very clearly at 15m/s and 20m/s wind speed situations.

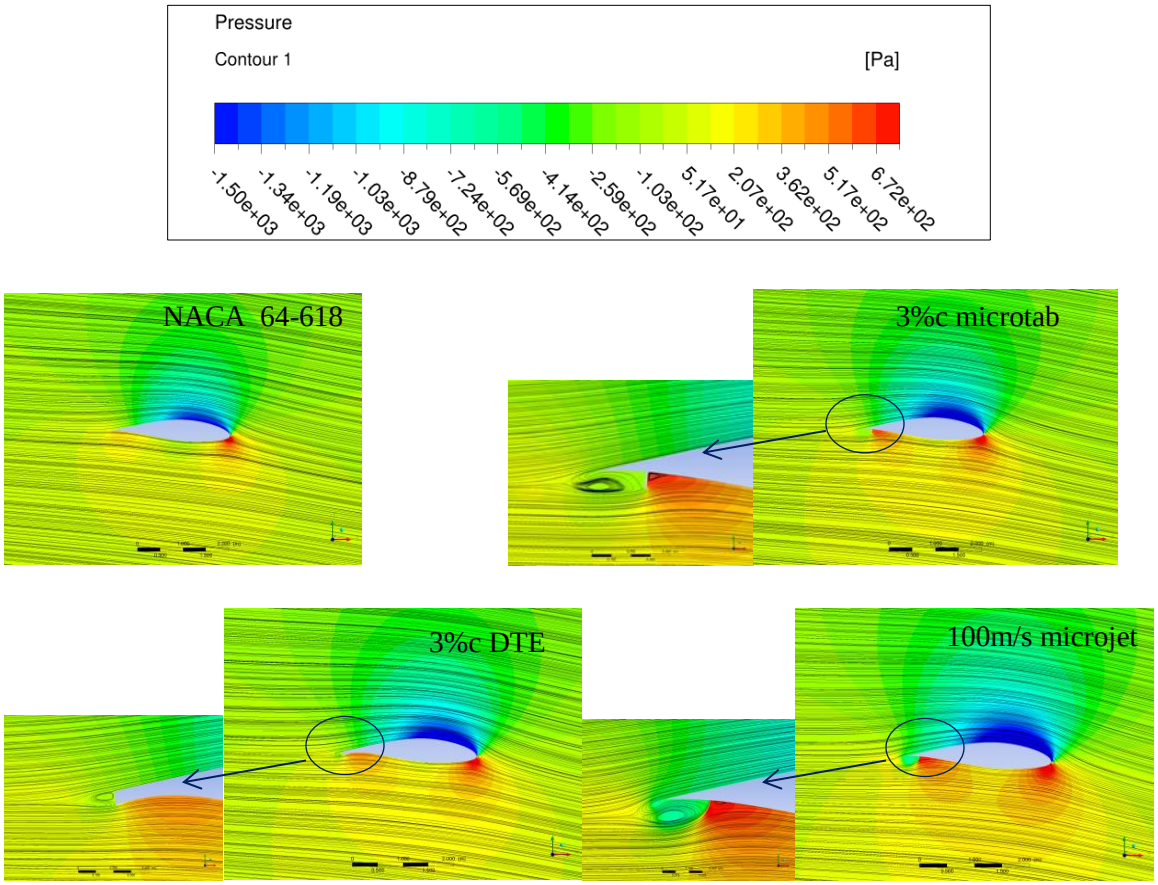

Figure 88. Streamlines and pressure contour of 2D simulations at 5m/s wind speed.

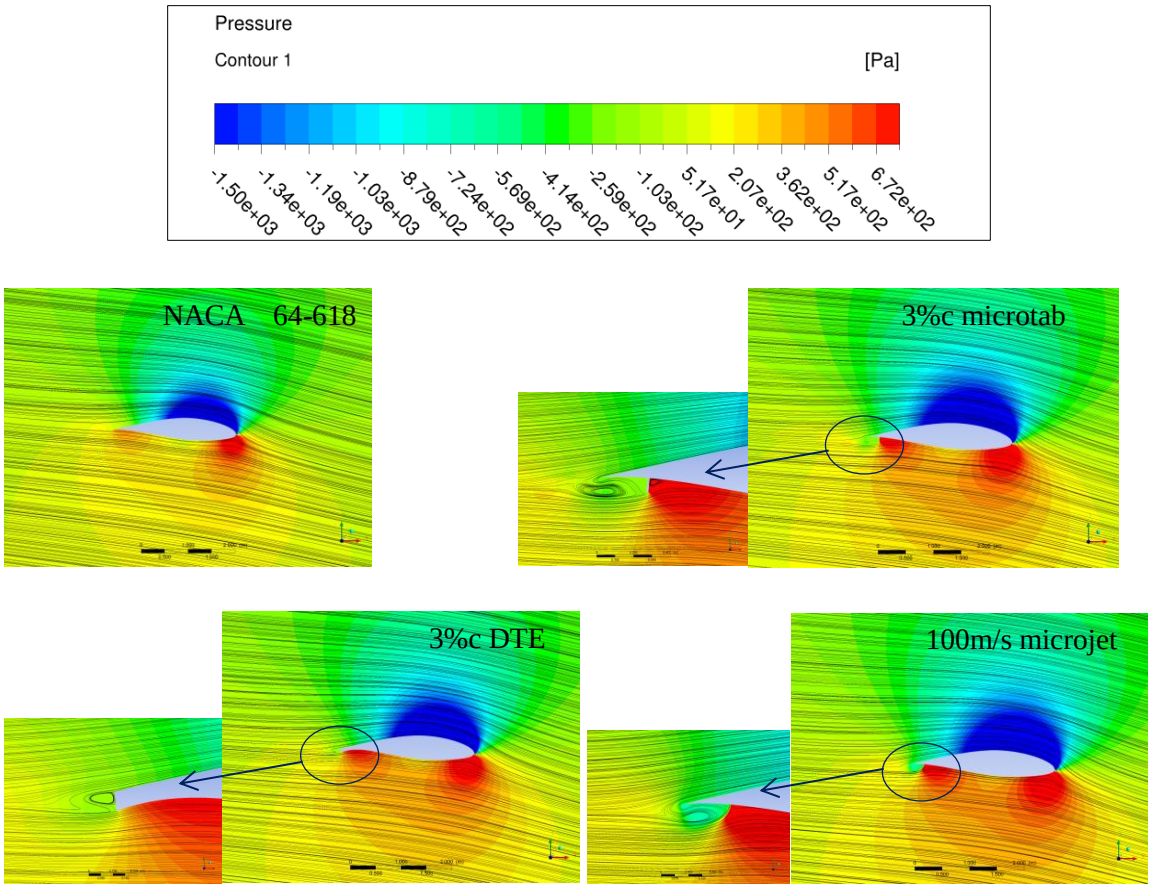

Figure 89. Streamlines and pressure contour of 2D simulations at 8m/s wind speed.

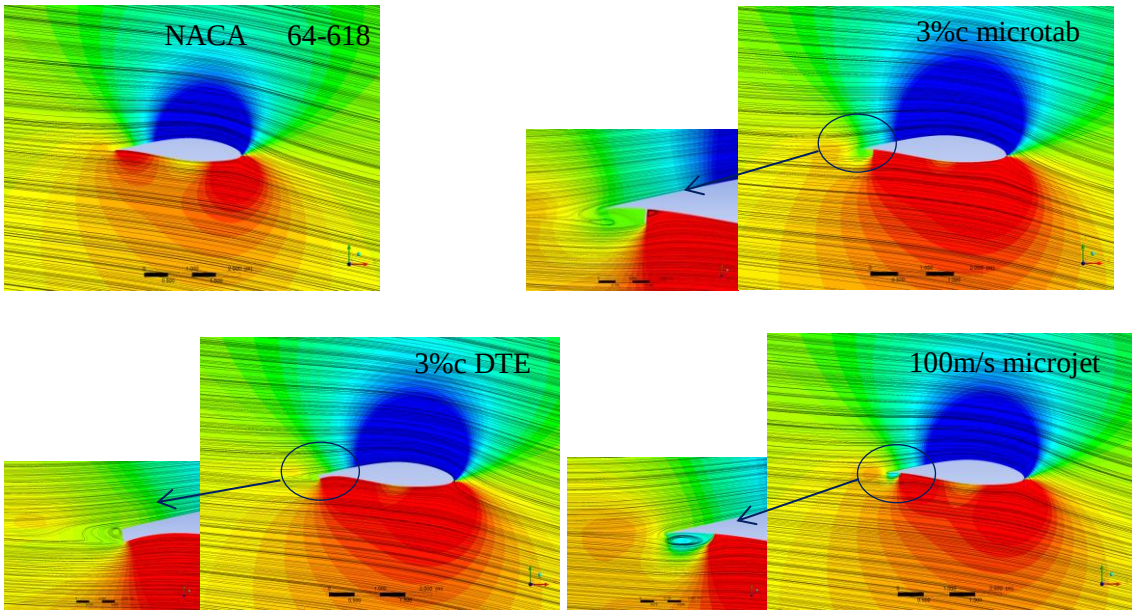

Figure 90. Streamlines and pressure contour of 2D simulations at 11m/s wind speed.

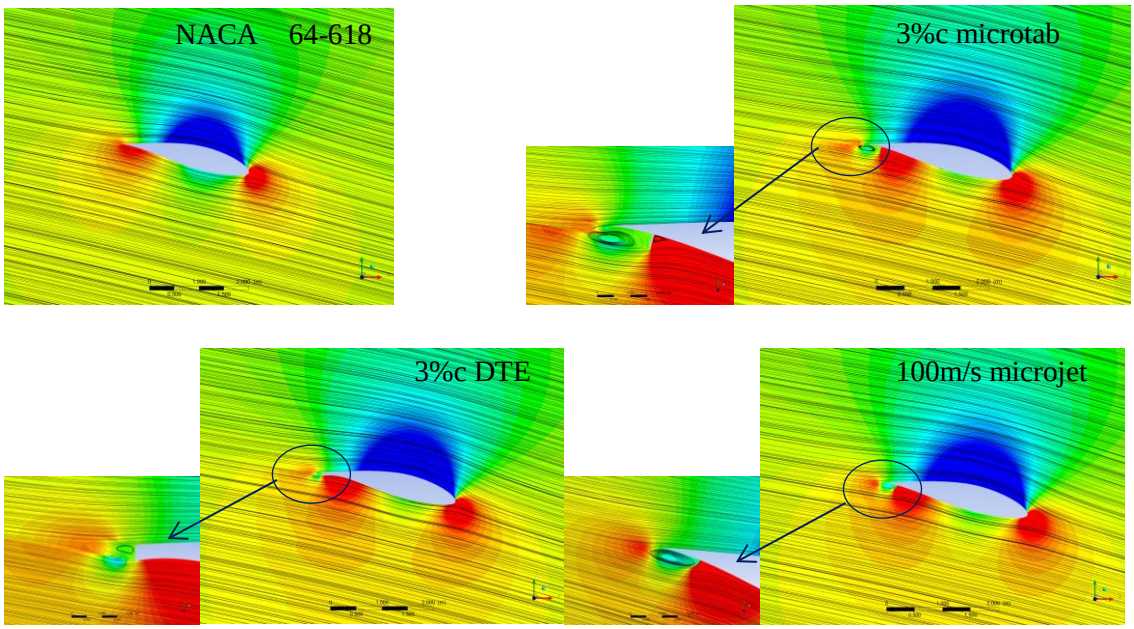

Figure 91. Streamlines and pressure contour of 2D simulations at 15m/s wind speed.

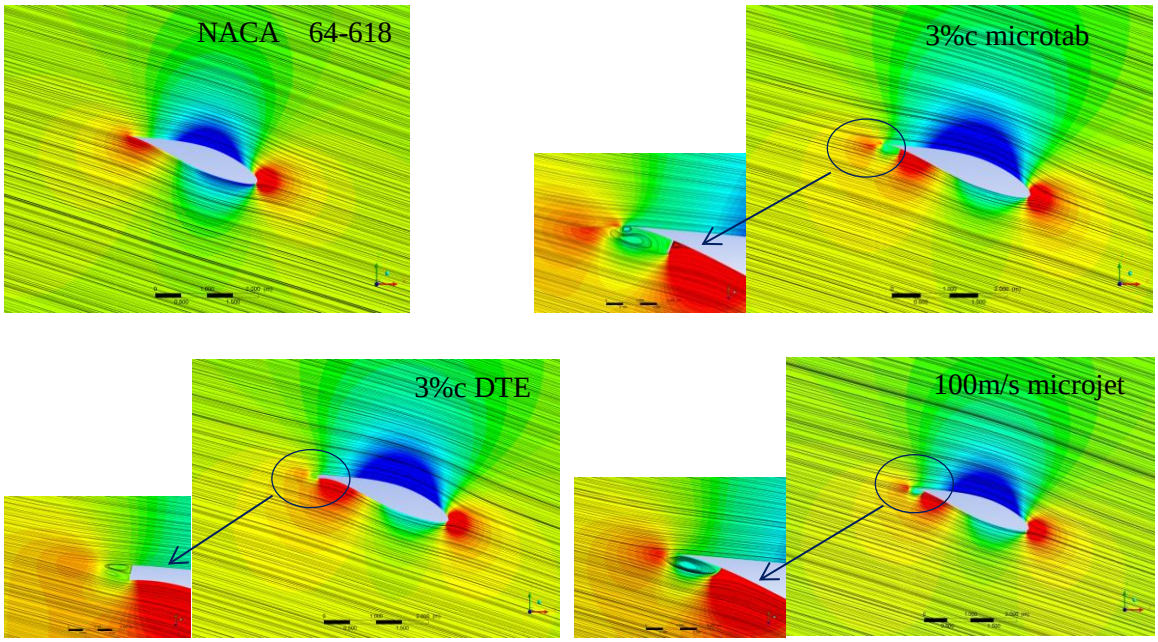

Figure 92. Streamlines and pressure contour of 2D simulations at 20m/s wind speed.

The effective force $F_{effective}$ is introduced in Figure 18 of chapter 2, which is the drive force for the wind turbine blade. Here the effective force in all 2D simulations is the force in X direction. Figure 93 shows the comparison of the effective force between the NACA 64-618 aerofoil and that with 3% chord microtab, 100m/s speed microjet and 3% chord DTE. The results show that all three trailing edge flow control concepts increase the effective force of the section of the wind

turbine blade, directly leading to higher power output of the blade. The 100m/s outlet speed microjet has the largest improvement at lower wind speed range below the rated wind speed while the aerofoil with 3% chord DTE shows the largest increase at higher wind speeds (15m/s and 20m/s). At the rated wind speed of the blade all three trailing edge flow control concepts show an around 21% increase than the original NACA 64-618 aerofoil.

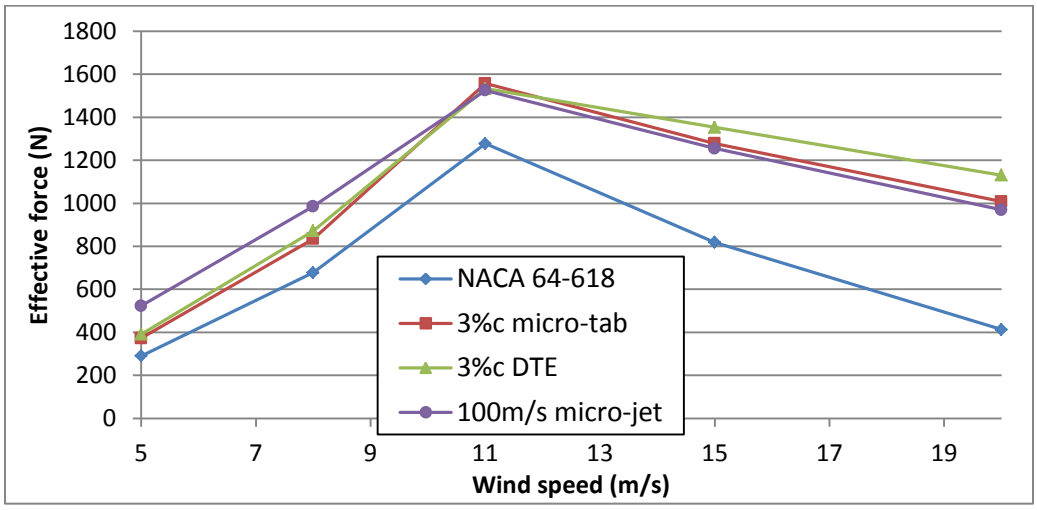

Figure 93. Effective force comparison between NACA 64-618 and that with flow control concepts.

5.4 3D CFD Study on NREL 5MW Blade with Microtab, Microjet and DTE

The 2D numerical study on the sectional aerofoil NACA 64-618 shows that the 3% chord microtab, 100m/s speed microjet and 3% chord DTE can effectively increase the torque of the blade. However the sectional simulations ignore the spanwise effects while the blade is in rotating situation which might lead to misleading results. Therefore this paper carries out the 3D numerical research into whether these trailing edge concepts are still working effectively when deploying on the blade in rotating situation.

5.4.1 Geometry Modification and Mesh Generation

Referring to the torque distribution study of the NREL 5MW wind turbine which is shown in Table 9 and Figure 84, the region near r/R = 0.8 span contributes the largest amount of the generated power of the blade. Therefore this area is assumed to the most sensitive area for

contributing the power output of the wind turbine. Improving the aerodynamic performance around this area could have much larger effects on changing final shaft torque of the blade. Therefore two different spanwise ranges are selected for the deployment of the microtab, microjet and DTE, which are 71% - 97% and 82% - 97% span.

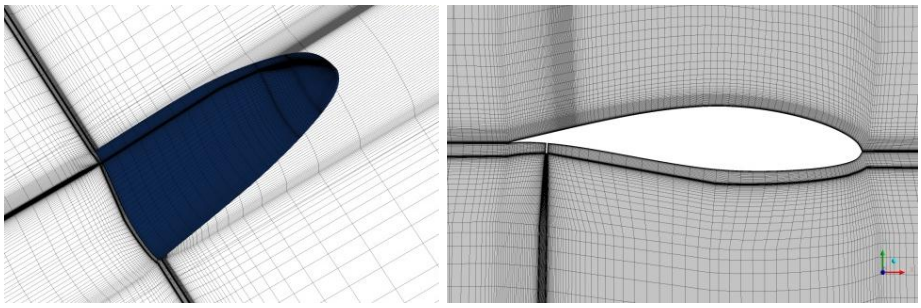

Figure 94. Mesh detail of the blade and cut-plane with 3%c microtab from 71% to 97% span.

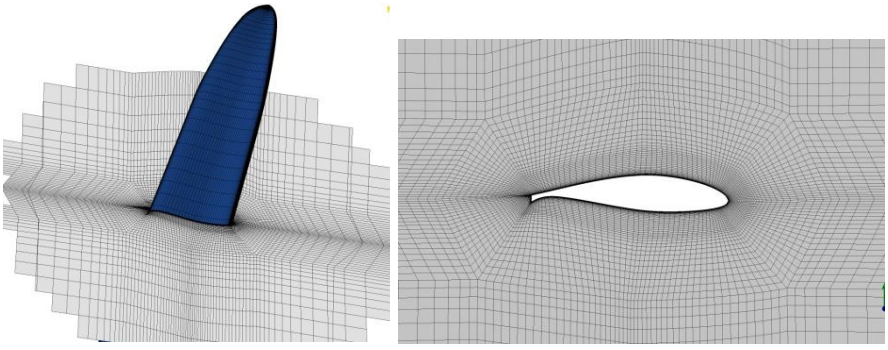

Figure 95. Mesh detail of the blade and cut-plane with 3%c DTE from 71% to 97% span.

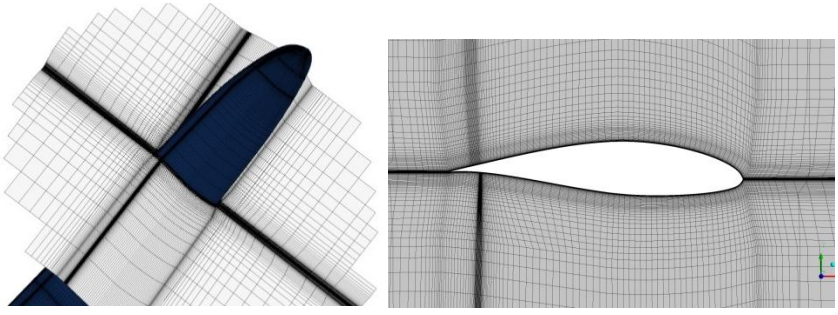

Figure 96. Mesh detail of the blade and cut-plane with 100m/s microjet from 71% to 97% span.

The width of the microtab and microjet is set to 1 centimeter. The height of the microtab is set to 3%c of the local aerofoil and that means the height is decreasing from root side to tip side of the blade. The lengths of the microtab and microjet are mentioned above as located at 71% - 97% or 80% -97% span of the blade which corresponding to a length of 16.38m or 10.71m. A fully

structured mesh is used for all cases. The meshes of the blade with microtab and microjet are still generated with an H-type mesh around the blade while an O-type mesh is used for the blade with 3% chord DTE. The mesh sizes of the blade with flow control devices and DTE are from 5 million to 8 million grids. The details of the geometry and mesh generation are shown from Figure 94 to 96.

5.4.2 Results

The results here are mainly about the surface wall shear friction lines with the pressure contour of the blade and the sectional flow streamlines and pressure contour. The selected sections for the blade are the r/R =0.5 and r/R =0.85 section. Because there are a large amount of simulations, here only the original blade, blade with 3%c microtab from 71-97% span, 3% DTE from 71-97% span and 100m/s microjet from 71-97% span at 5m/s, 11m/s and 20m/s cases are shown.

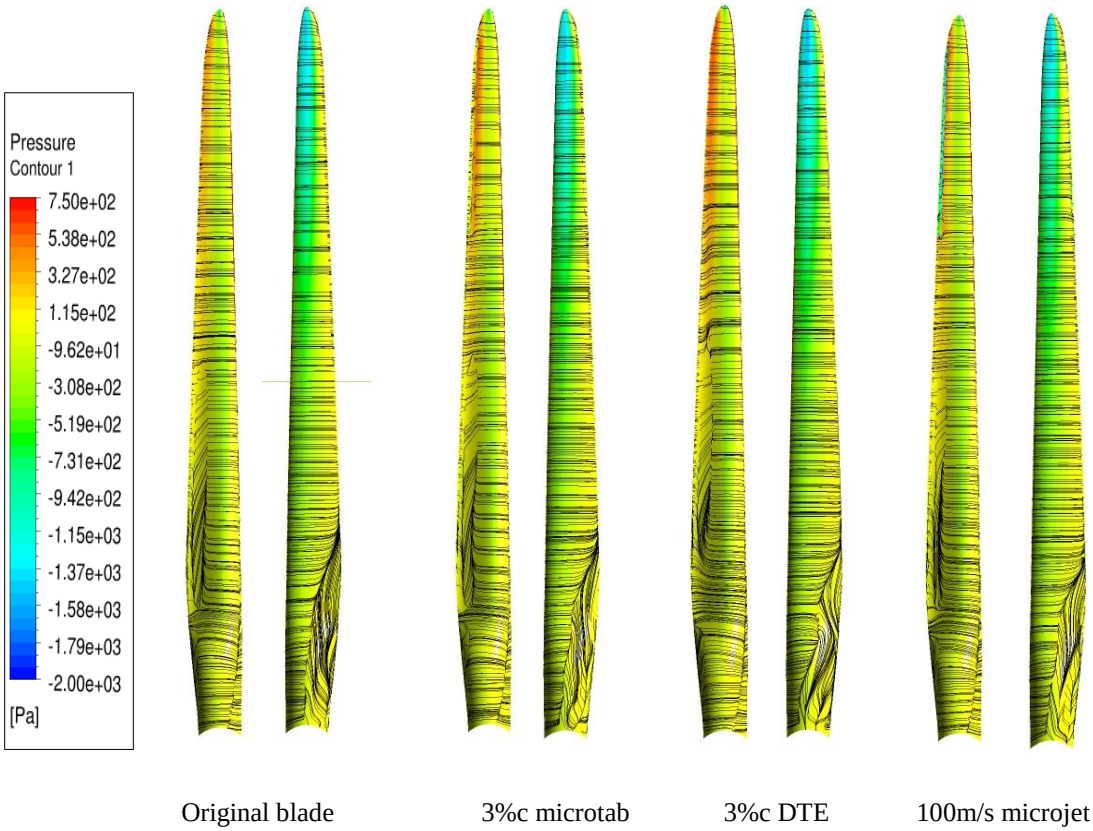

Figure 97. Blade surface friction lines and pressure contour at 5m/s wind speed.

Figure 97 shows the blade surface friction lines and the pressure contours at 5m/s wind speed. It can be seen that the trailing edge flow control devices and DTE do not changing the flow condition along the blade except for the deployment area. A small separation bubble can be seen from 20-50% span on the pressure side near the trailing edge is shown clearly in Figure 99.

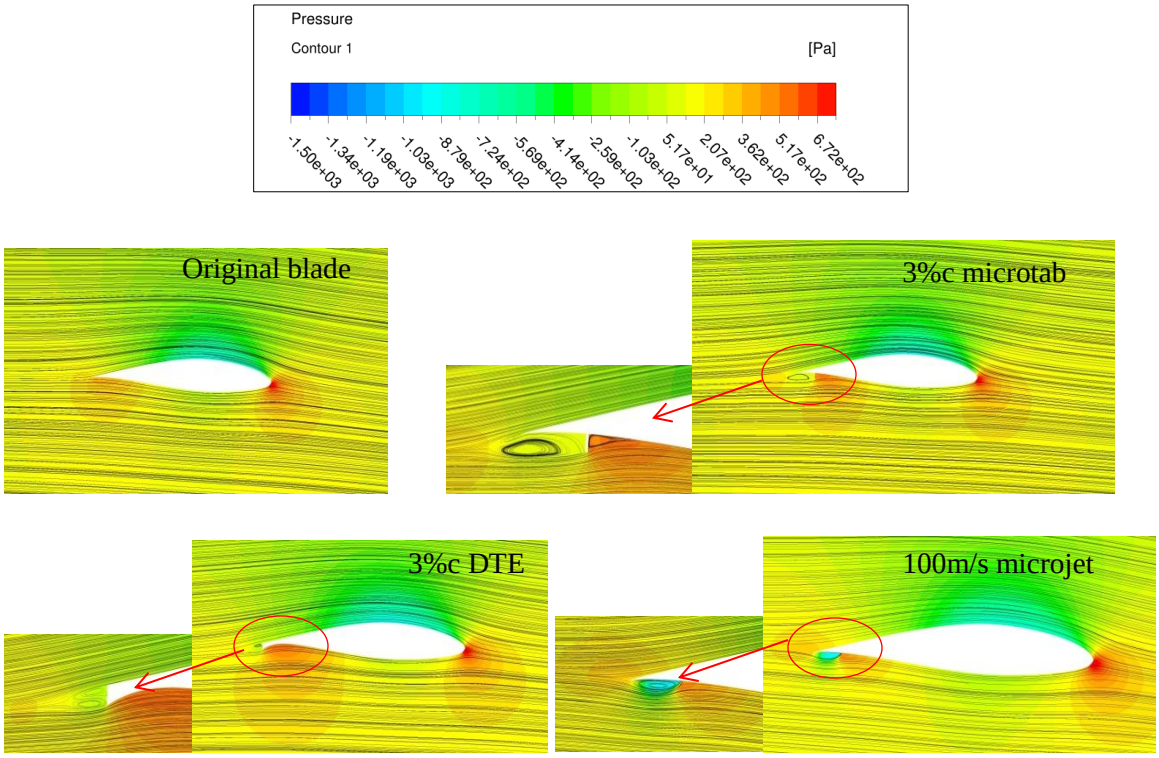

Figure 98. Streamlines and pressure contour at r/R = 0.85 span section at 5m/s wind speed.

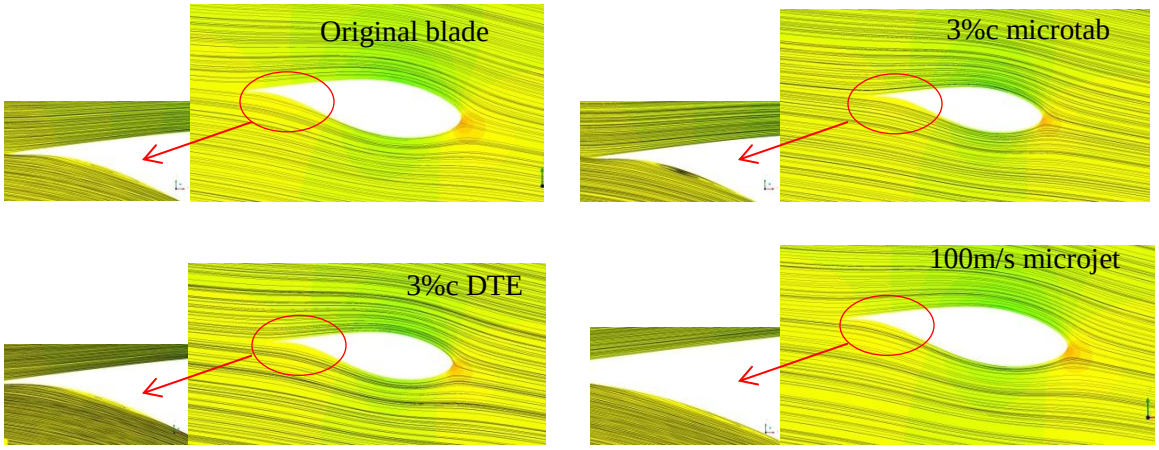

Figure 99. Streamlines and pressure contour at r/R = 0.5 span section at 5m/s wind speed.

At 11m/s wind speed which is quite close to the rated wind speed of the NREL 5MW wind turbine, it can be seen that microtab, microjet and DTE all increase the pressure near the trailing edge on the pressure side of the blade (Figure 100). Moreover, the small separation bubble from 20-50% span near the trailing edge disappears (Figure 102).

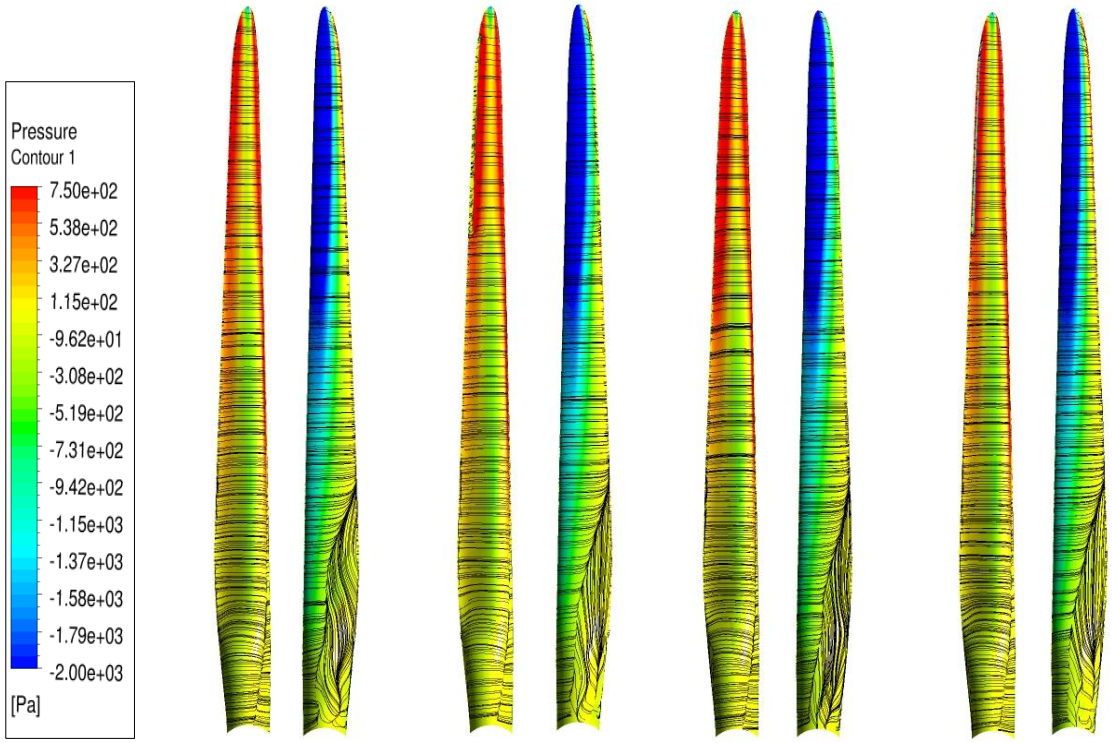

Figure 100. Blade surface friction lines and pressure contour at 11m/s wind speed.

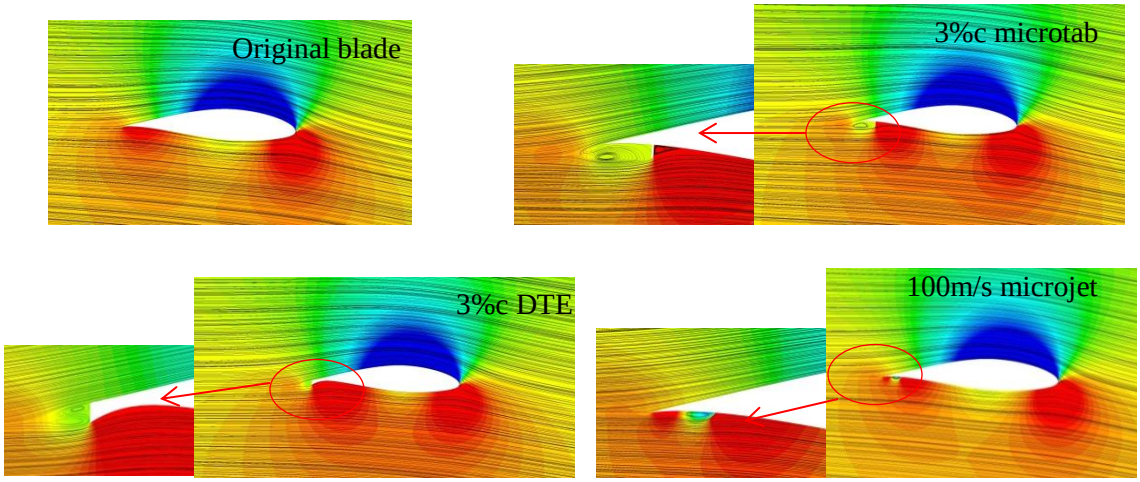

Figure 101. Streamlines and pressure contour at r/R = 0.85 span section at 11m/s wind speed.

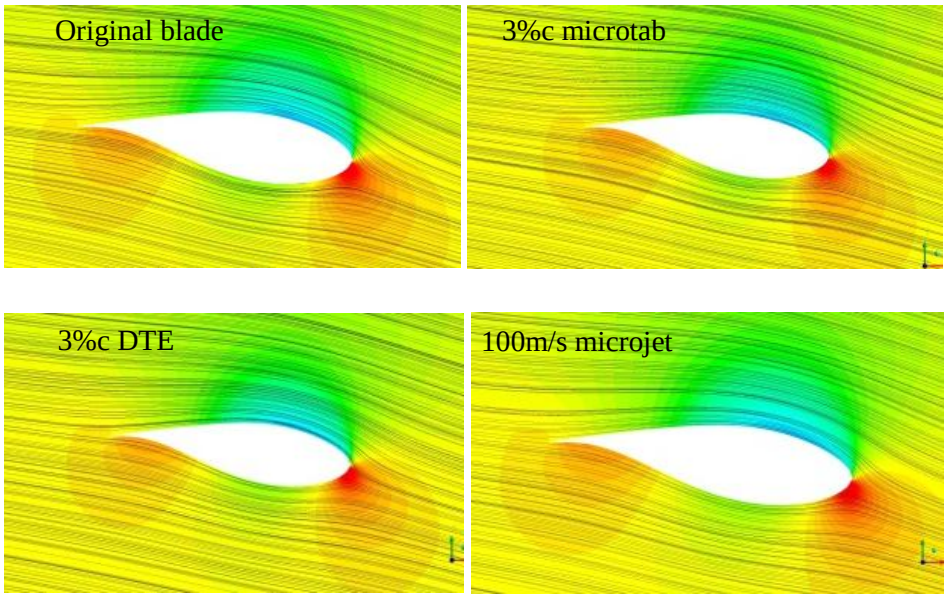

Figure 102. Streamlines and pressure contour at r/R = 0.5 span section at 11m/s wind speed.

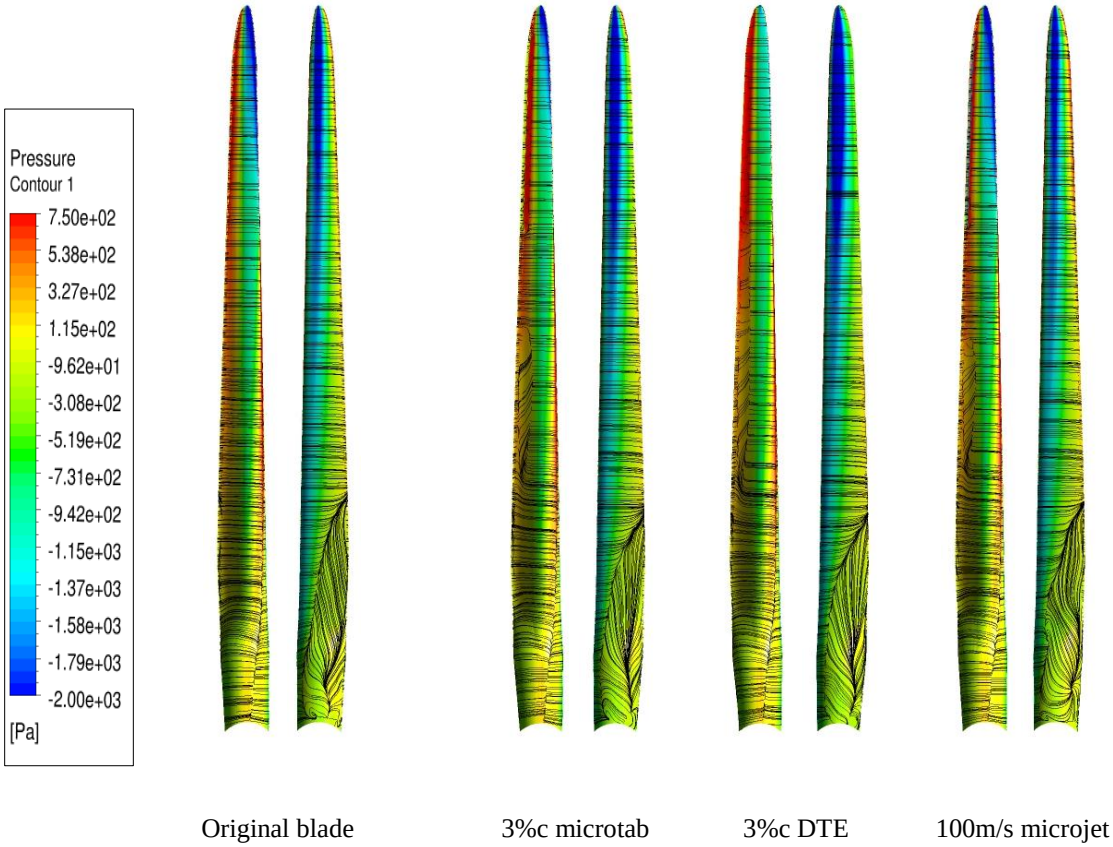

Figure 103. Blade surface friction lines and pressure contour at 20m/s wind speed.

Figure 103, 104 and 105 show that when the wind speed reaches 20m/s and the blade is pitched by 17.47 degrees, the AOA of the aerofoil near the tip is negative. In this situation the trailing edge flow control devices and the DTE concept decrease the pressure on the suction side of the blade. It is also interesting to see that all microtab, microjet and DTE induce a separation bubble on the pressure side near the trailing edge at lower spanwise range, which can be seen clearly from Figure 103 and 105. This condition is not able to be presented by 2D aerofoil study.

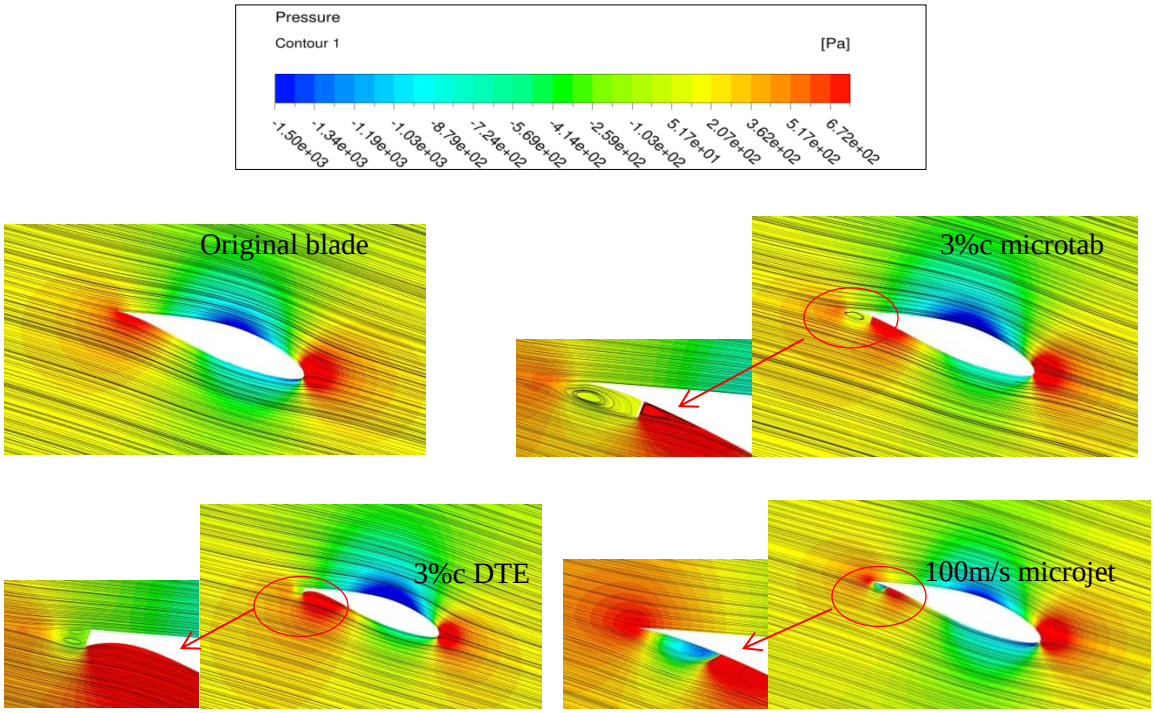

Figure 104. Streamlines and pressure contour at r/R = 0.85 span section at 20m/s wind speed.

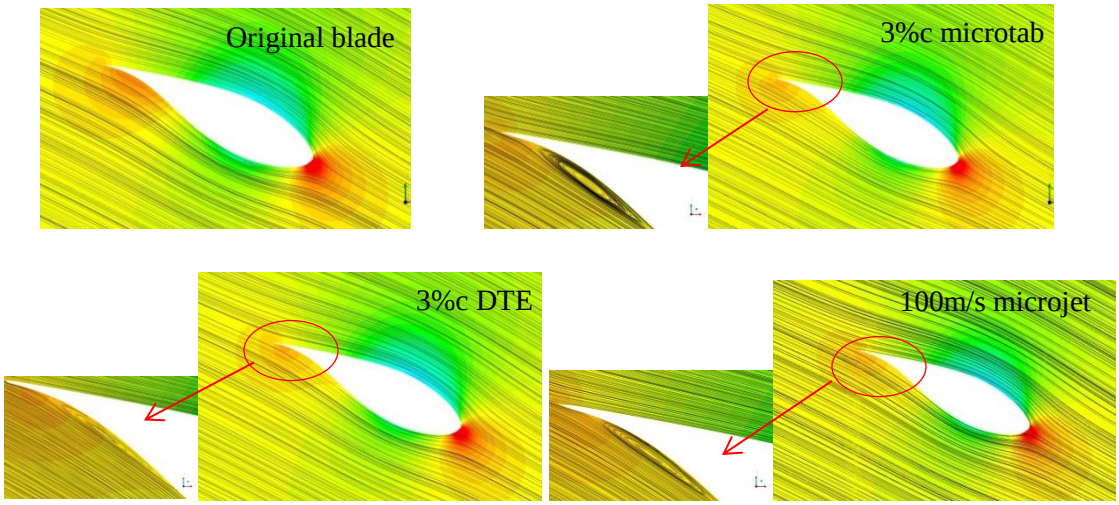

Figure 105. Streamlines and pressure contour at r/R = 0.5 span section at 20m/s wind speed.

5.4.3 Power and Thrust Comparison

The computational power output of the NREL 5MW wind turbine and that with microtab, microjet and DTE are shown in Figure 106. The results show large difference referring to the 2D aerofoil study. None of the flow control concepts show improvement of the power output of the blade below the rated wind speed except for just a small increase of the power of the microjet at 5m/s wind speed, which is quite different from 2D numerical predictions. However at higher wind speed above the rated wind speed such as 15m/s and 20m/s, the wind turbine with microtab and DTE concept show some increase of power output than the original one. The wind turbine with 3% chord DTE increases the power by 40% and 62.4% than the original blade at 15m/s and 20m/s wind speed respectively. However at this higher wind speed rang, the microjet method still decrease the power output which is also different from the 2D results.

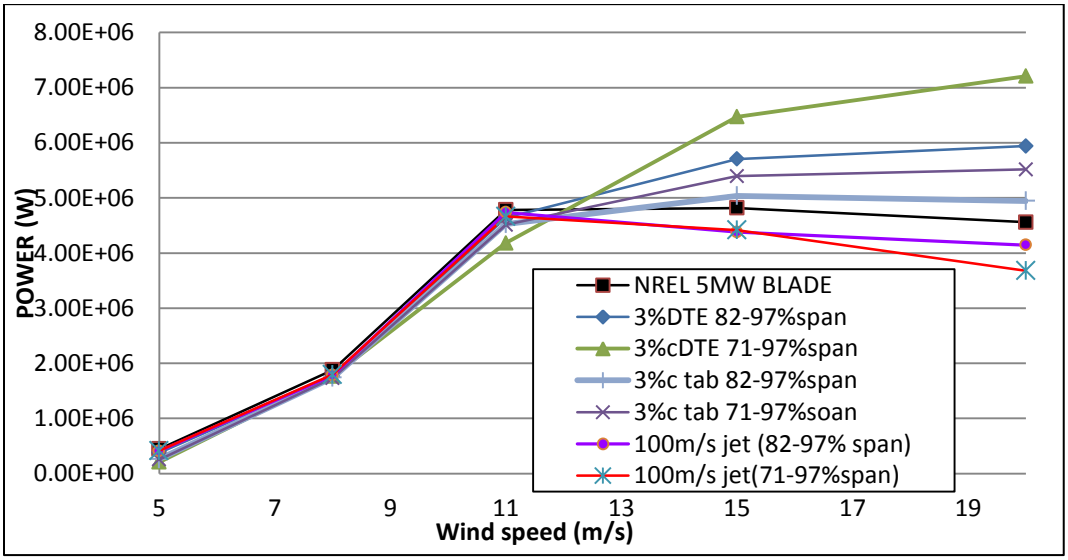

Figure 106. Comparison of the power output of the NREL 5MW wind turbine and that with microtab, microjet and DTE

Another interesting finding is that for the power coefficient of the wind turbine shown in Figure 107, it can be found that the effectiveness of the flow control concepts is highly related to the current C_p of the wind turbine. According to the Betz's limit theory, the maximum C_p of the HAWT is 0.593. The NREL 5MW wind turbine has a relatively high C_p (above 0.4) from 5m/s to 11m/s wind speed and much lower C_p at higher wind speed such as 15m/s and 20m/s (lower than 0.2). From Figure 107 it can be seen that the flow control concepts are hard to show their

effectiveness when the C_P of the wind turbine is high but is effective at lower C_P wind speed range.

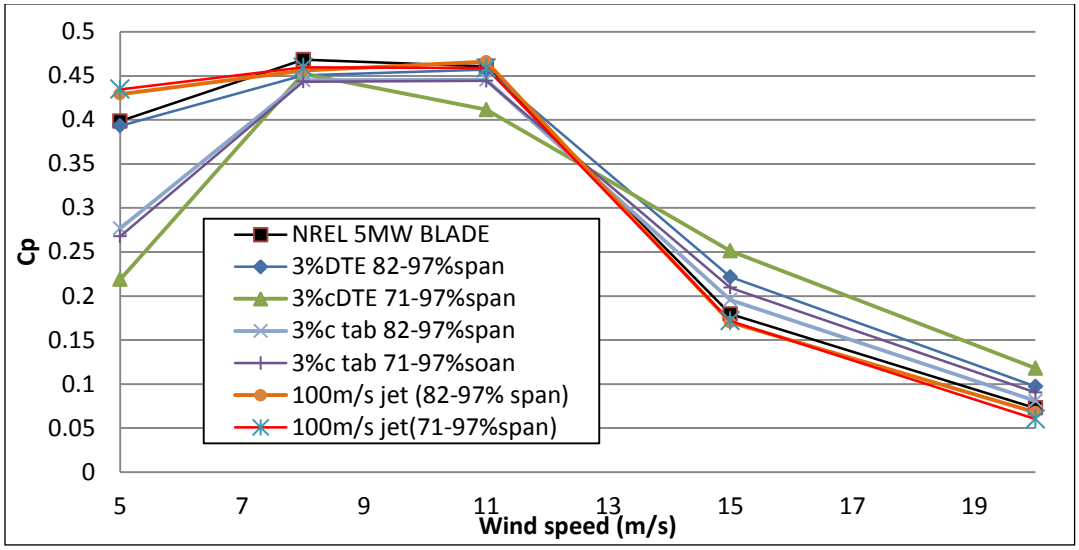

Figure 107. Comparison of the power coefficient of the NREL 5MW wind turbine and that with microtab, microjet and DTE

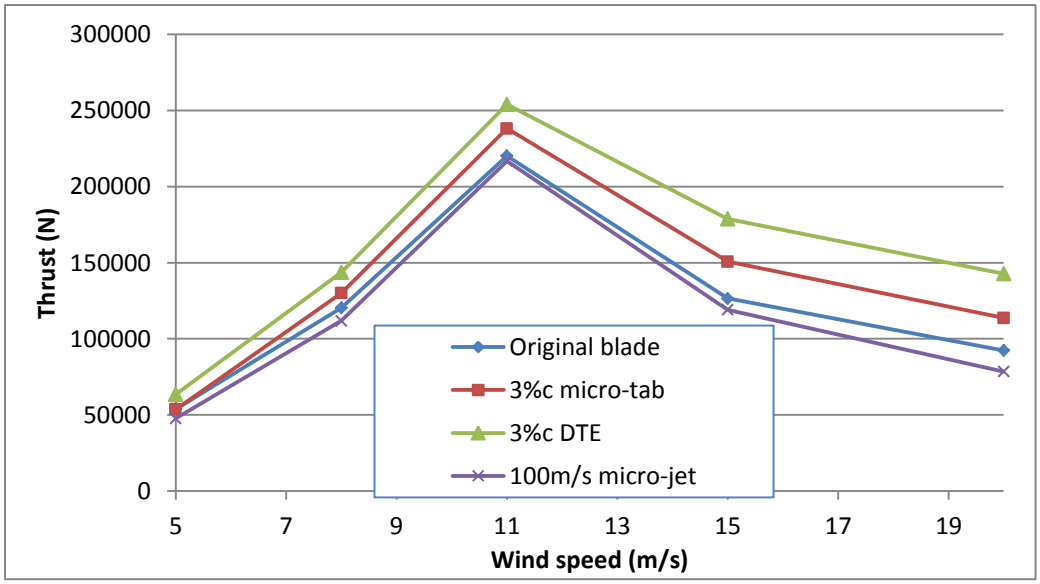

Figure 108. Thrust comparison between NREL 5MW wind turbine and that with flow controls.

The thrust of the wind turbine is also an important factor for large wind turbine design because of the structural strength issues. Figure 108 shows the thrust of the NREL 5MW wind turbine and that with deployment of flow control concepts from 71% to 97% span. The results show that 3% chord microtab and DTE increase the thrust of the wind turbine while the microjet decreases the

thrust at all wind speeds. This condition is also studied by Hurley et al. (2016) who used BEM method and their results showed that deploying microjet on the pressure side trailing edge is able to reduce the flapwise bending moment of the blade.

5.4.4 Pressure Coefficient Comparison

The pressure coefficients of cross-sectional aerofoils of the NREL 5MW blade are shown in the following figures. Two sections are selected for the comparison between the original blade and the blade with flow control devices. The r/R = 0.5 section is chosen in order to find out whether the flow control devices can affect the flow conditions at the spanwise range where they are not deployed. The r/R = 0.85 section is selected for analysis to see how the flow control devices change the flow and pressure conditions after they are deployed.

As can be seen from the left of Figure 109, when the wind speed is 5m/s, the pressure coefficient at 50% span section of the original blade and other with flow control devices are quite the same and all of these cases are showing there is a small separation bubble on the pressure side near the trailing edge which is highlighted in the figure. The right hand side of Figure 109 shows that the 3%c microtab and DTE enlarge the differences between the pressure side and suction side of the blade at 80% span section near the trailing edge. However this condition does not lead to improvement of the power output of the blade. Moreover, comparing to the 2D CFD results for the NACA 64-618 aerofoil at 80% span section of the blade, the C_p shown in the 3D CFD results is very different. The differences of the C_p near the leading edge of the sectional aerofoil of the 3D results are much smaller those from the 2D aerofoil CFD results which might be the main reason that why the flow control devices in the 3D simulations are not able to give any improvement of the power output of the blade. This situation also happens at other wind speeds as the 2D CFD results predict higher C_p differences between the pressure side and the suction side of the blade.

It is also interesting to see that from Figure 110, the 3% chord thickness DTE concept slightly reduces the difference of the C_p near the leading edge at 50% span section. And moreover from the C_p shown on the right of Figure 110 the flow control devices are actually improving the lift force of the sectional aerofoil except for the 100m/s outlet speed microjet. However from the final power output comparison shown above, none of the flow control device actually improves the performance of the blade.

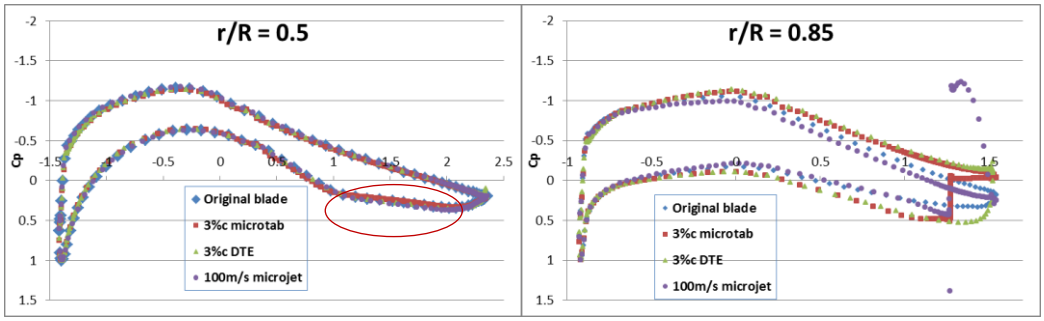

Figure 109. C_P of NREL 5MW blade and with different flow control devices at 5m/s wind speed.

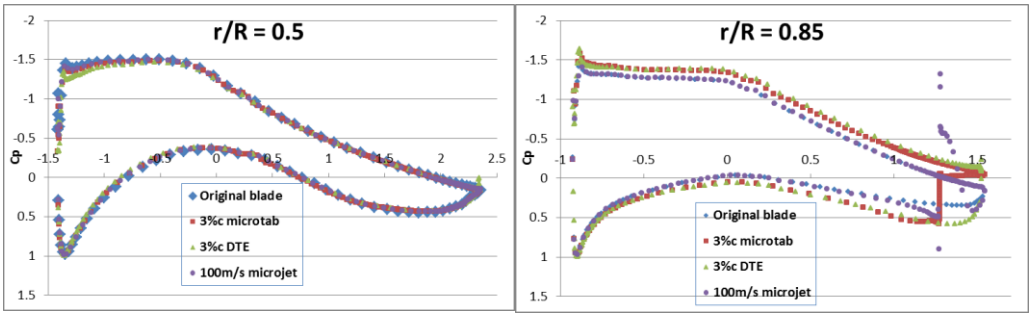

Figure 110. C_P of NREL 5MW blade and with different flow control devices at 11m/s wind speed.

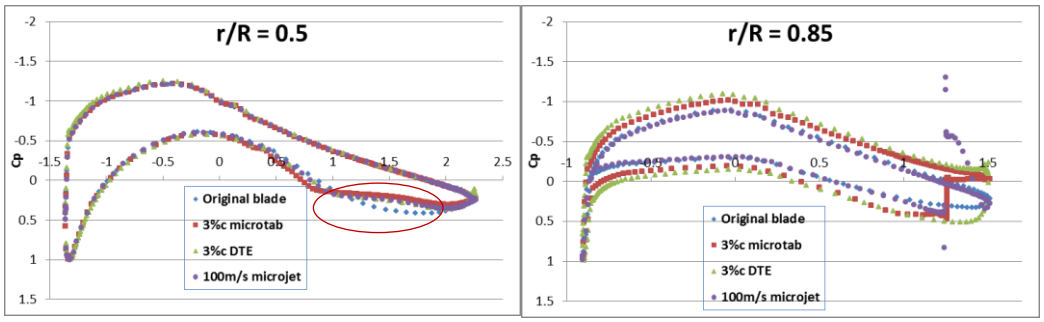

Figure 111. C_P of NREL 5MW blade and with different flow control devices at 15m/s wind speed.

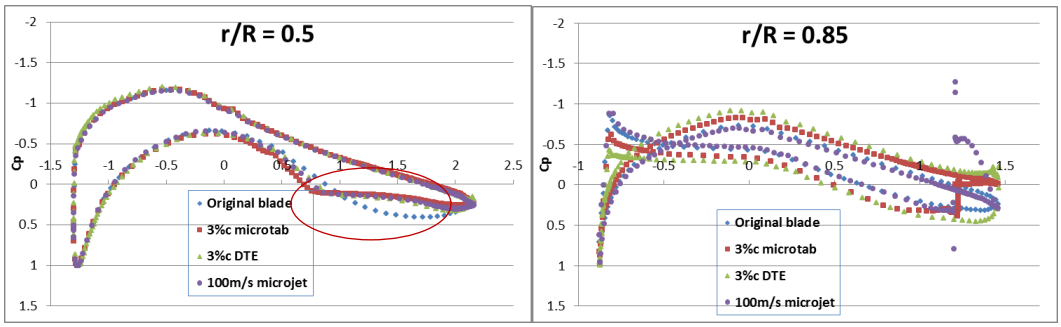

Figure 112. C_P of NREL 5MW blade and with different flow control devices at 20m/s wind speed.

From the highlighted area in Figure 111 and 112 which are for high wind speed cases (15m/s and 20m/s), it can be seen that all the flow control devices which are deployed from 71% to 97% spanwise range are changing some flow situations at the 50% span section near the trailing edge on the pressure side. The C_p around this area is showing some separation bubble which can also be found in Figures 104 and 106. Moreover from the right hand side of Figure 111 and 112, the 3%c microtab and DTE are improving the performance of the sectional aerofoil obviously. This is corresponding to the power output comparison before. Another very interesting finding is that the microjet in the 3D CFD studies performs much worse than those from the 2D CFD simulations where almost has none improvement in any cases. In other words, the 2D prediction gives wrong results due to inaccurate 2D assumption.

5.5 Deploying Microtab for Load Alleviation

Nowadays the HAWT as one of the biggest machines on land or offshore, the maintenance issues for HAWTs have been carefully considered by engineers. One big challenge is the brake system for the large HAWTs because of their huge shaft torque. Normally there are two kinds of brake systems of wind turbines, mechanical brake and aerodynamic brake. The mechanical brake normally consists of a steel brake disc between the gearbox and the shaft which is used to stop the wind turbine in emergency situation such as extreme gust event. The aerodynamic brake system is more benign than mechanical brakes and is usually used for normal shut-downs for wind turbine because it can effectively decrease the shaft torque without causing mechanical damage on the gearbox. For modern wind turbines the aerodynamic brake design mainly includes active pitch control, pitching blade tip and some other flow control devices such as microtabs and microflaps. Migliore et al. (1995) proposed the aerodynamic brakes for wind turbines using five different trailing-edge devices.

Using the gearbox for as mechanical brake system for HAWTs might cause high wastage of the gears and shortening the lifetime of the wind turbine. Designing an active aerodynamic brake system on the blade is significant for modern large HAWTs. From previous studies Johnson et al. (2010), deploying microtabs on the suction side of the blade can decrease the lift force of the sectional aerofoil of the wind turbine blade. However so far there is still lack of research on the suction side microtab effects on the HAWTs in rotating frame. Here the NREL 5MW reference is

also selected for investigation and similar as the studies above, both 2D sectional aerofoil CFD study and 3D study are carried out.

5.5.1 2D Study on NACA 64-618 Aerofoil at r/R = 0.8 of NREL 5MW Blade

Similar as the previous studies on the flow control devices on the wind turbine blade, the 2D CFD study on the NACA 64-618 aerofoil at r/R = 0.8 span section of the NREL 5MW blade is carried out. The suction side microtab is deployed at x/c = 0.9 position of the aerofoil which is the same as the pressure side microtab. The direction of microtab is vertical to the suction side surface and three different sizes are tested which are 1% chord, 2% chord and 3% chord height. The design details can be found in Figure 113.

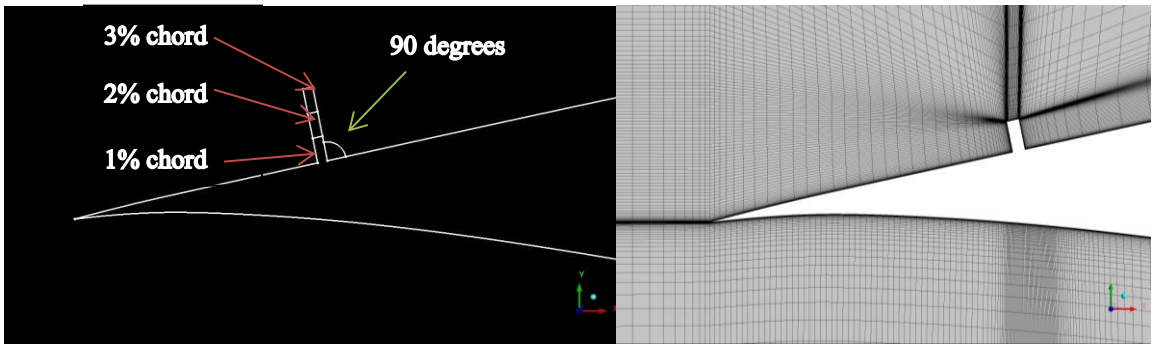

Figure 113. Geometry and meshing detail of suction side microtabs.

Results

The sectional aerofoil pitch angles conditions are following the definition of the NREL 5MW blade. The pitch angle is zero degree below the rated wind speed (11.4m/s) and grows to 10.4 degrees when the wind speed is 15m/s and reaches 17.47 degrees when the wind speed is 20m/s. For the 2D simulations all cases are run as steady flow because the C_L of the sectional aerofoil or with suction side microtabs converges very well and become constant after 10,000 iterations. Here also the $F_{effective}$ is chosen for comparison as it directly contributes to the turbine torque.

From Figure 114 it can be seen that the microtab deployed on the suction side of the sectional NACA 64-618 aerofoil has the opposite performance than that deployed on the pressure side which is shown in Figure 96. Especially at high wind speeds such as 15m/s and 20m/s cases, even

the 1% chord height suction side microtab can decrease the $F_{effective}$ hugely or even leading to negative values. This condition means that at this situation, this section of the span is supposed to provide the momentum on the direction opposite to the rotating direction of the blade. Overall, from the 2D CFD study on the sectional aerofoil of the NREL 5MW blade, deploying the suction side microtab as an active flow control device for wind turbine brake system is very effective but more details should be concerned in the 3D rotating frame such as the thrust.

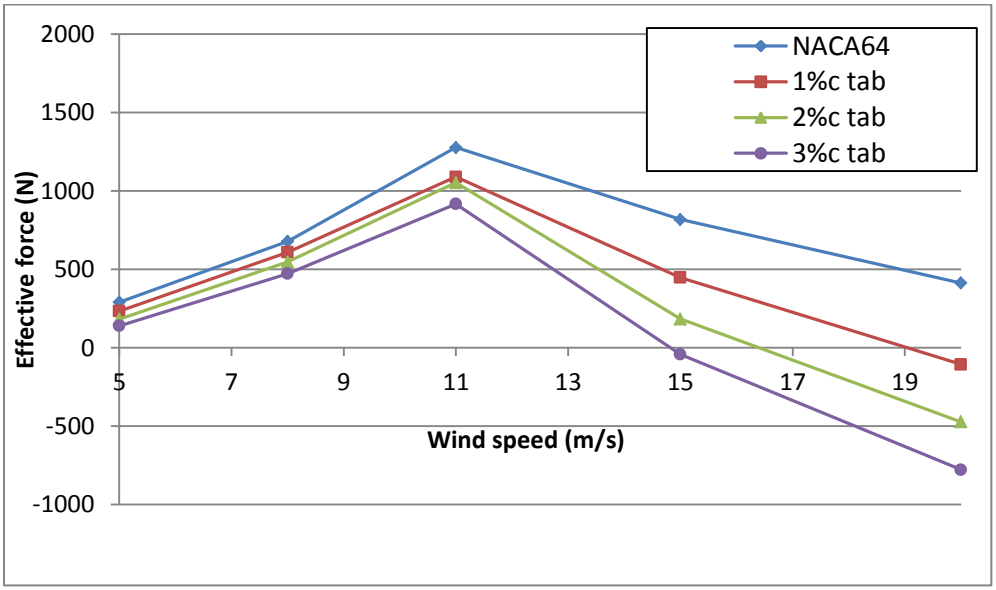

Figure 114. Effective force comparison between NACA 64-618 and that with suction side microtabs.

Pressure contour and streamlines

The following figures show the pressure contour and streamlines of the sectional NACA 64-618 aerofoil at 5m/s, 11m/s and 20m/s wind speeds respectively. The contour value of the pressure is from -1500 Pa to 1500 Pa and the color is from blue to red.

From Figure 117 it can be found that at 20m/s wind speed (with the 17.47 degrees pitch angle of the blade), the deployment of the suction side microtab totally changes the flow situation of the sectional aerofoil. The suction side microtab changes the chamber of the aerofoil to an opposite side which meaning the pressure side and suction side have been switched at this situation. This is the reason why the $F_{effective}$ is showing negative value at this condition.

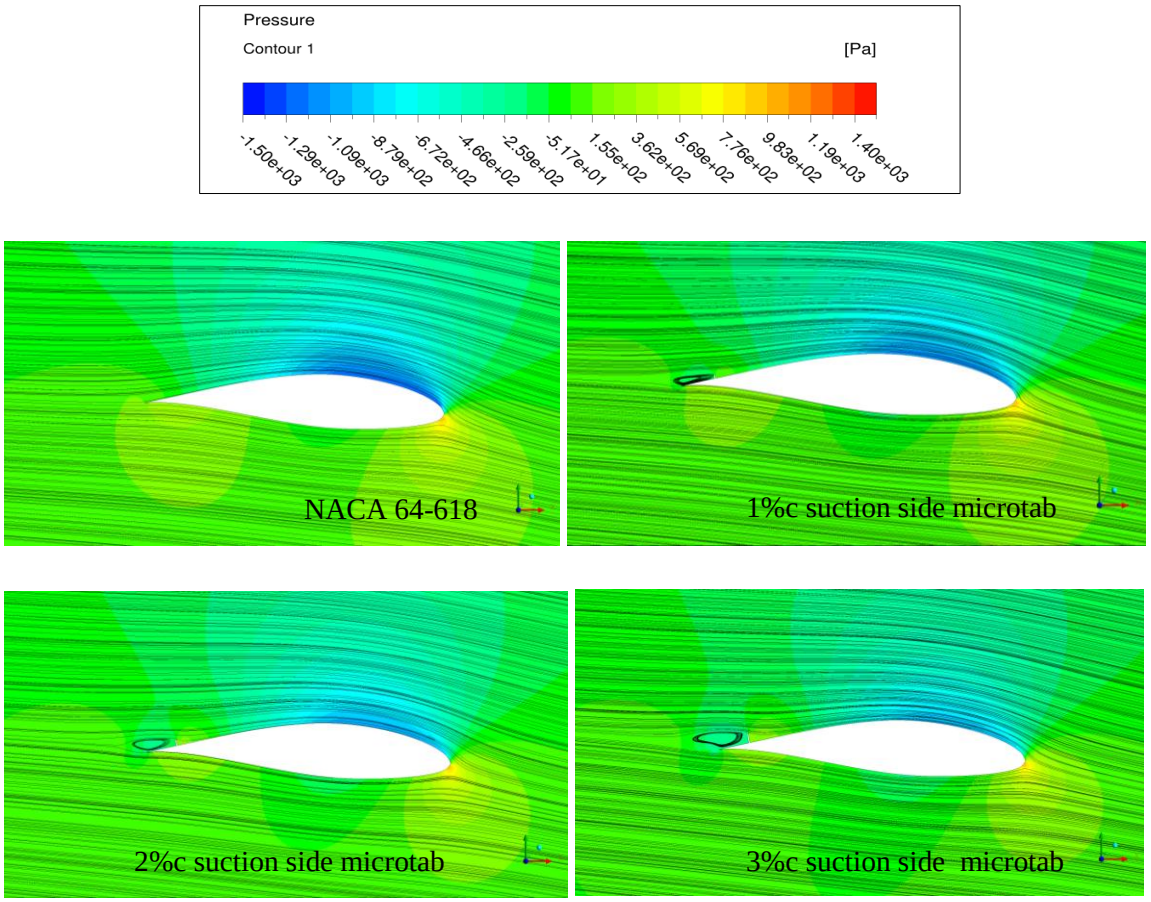

Figure 115. 2D sectional pressure contour and streamlines at 5m/s wind speed.

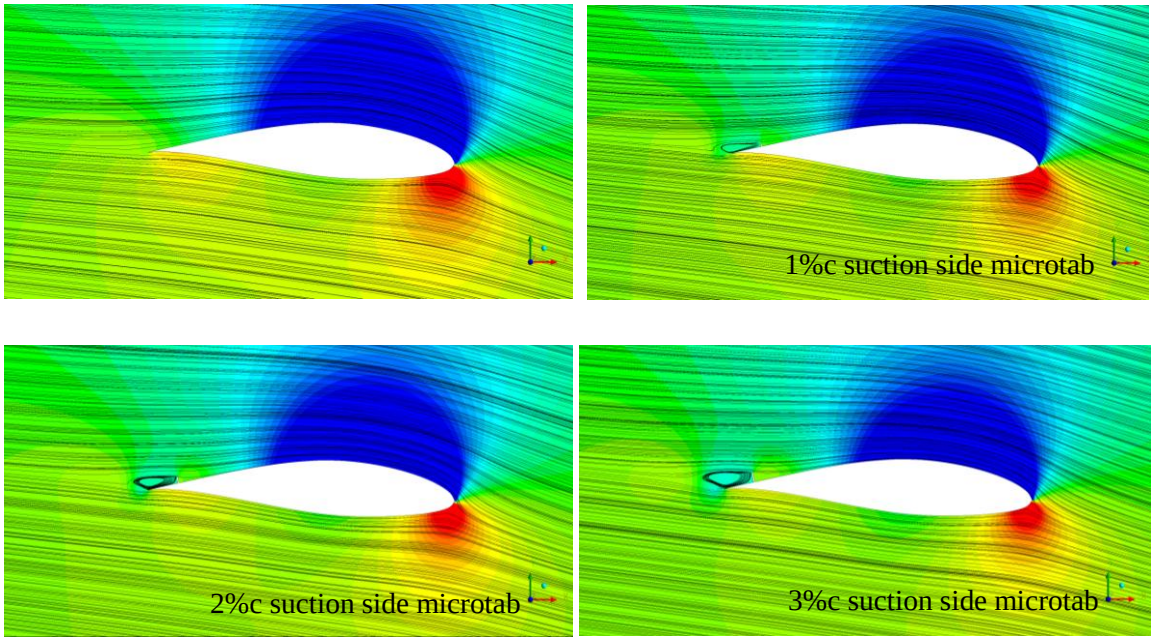

Figure 116. 2D sectional pressure contour and streamlines at 11m/s wind speed.

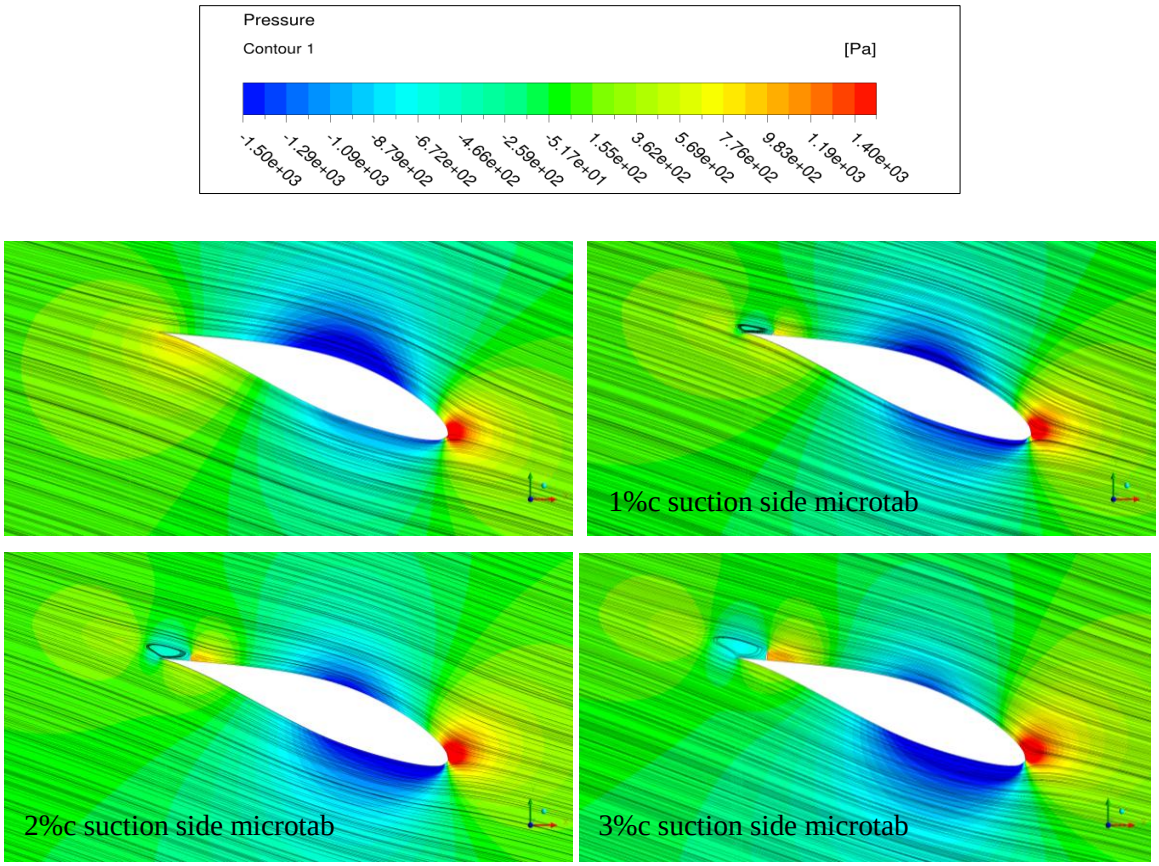

Figure 117. 2D sectional pressure contour and streamlines at 20m/s wind speed.

Pressure coefficient comparison

Figure 118 shows the pressure coefficient of the 2D sectional aerofoil of the NREL 5MW blade at r/R = 0.8 span and that with suction side microtabs in different sizes. It can be seen that from 5m/s to 15m/s wind speed, deploying suction side microtabs on the aerofoil would reduce the C_p differences between the pressure side and suction side which leads to reduction of the lift force and $F_{effective}$. Moreover, by increasing the height of the microtabs, the effects of the suction side microtabs are stronger. At 20m/s wind speed, because the AOA of the sectional aerofoil is negative and the suction side microtabs make this condition even stronger, which can be assumed that the pressure side and suction side of the aerofoil is switched. Therefore at this situation the sectional aerofoil is providing the force opposite to the rotating direction of the blade.

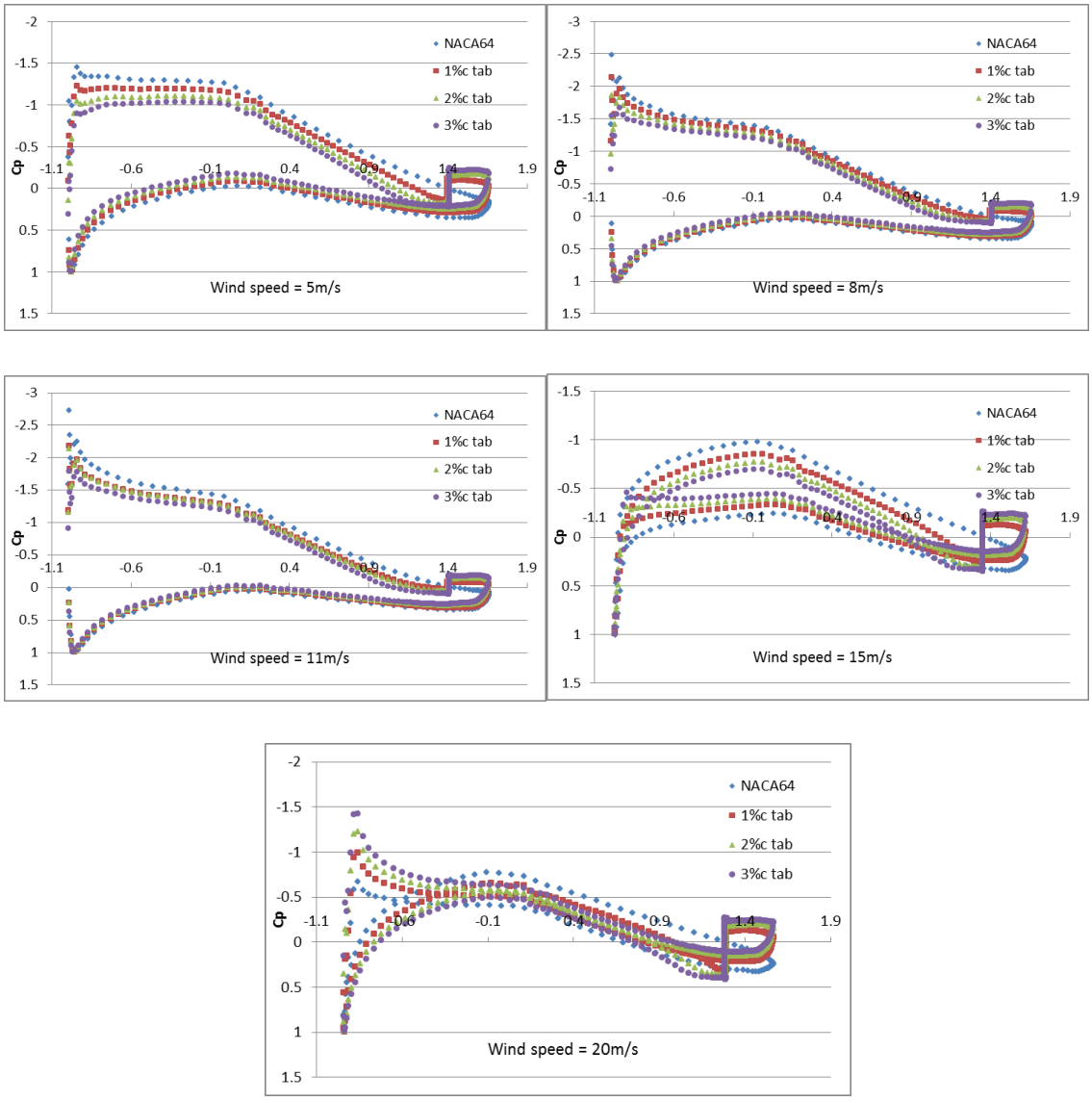

Figure 118. Comparison of pressure coefficient (C_p) between NACA 64-618 aerofoil and that with different sizes of suction side microtabs.

5.5.2 3D CFD Study on Suction Side Microtabs for Aerodynamic Brake of HAWT

The 2D CFD study on the r/R = 0.8 span sectional aerofoil shows that deploying microtabs on the suction side of the blade can effectively reduce the shaft torque of the wind turbine therefore it can be assumed to be an active flow control device for the brake system. However referring to the previous CFD study of trailing edge flow control devices on the pressure side of the wind turbine

blade, 3D CFD study on the suction side microtabs of the blade in rotating frame should also be carried out because of the inconsistence between the 2D and 3D CFD results.

From the previous torque distribution study of the NREL 5MW blade, the r/R = 0.7 to r/R = 0.9 span range of the blade has the highest torque density which means that decreasing the aerodynamic performance of this span range of the blade can be more effective to the wind turbine brake. Therefore the suction side microtab is deployed from 71% to 97% span of the blade. Because of the mesh size and computational resources, here only the integral microtab with no gaps is simulated and the mesh has seven million cells (Figure 119). Similar as the 2D CFD study, three different sizes (1% chord, 2% chord and 3% chord) of the suction side microtabs are simulated for comparison. All 3D CFD simulations are run in steady flow condition.

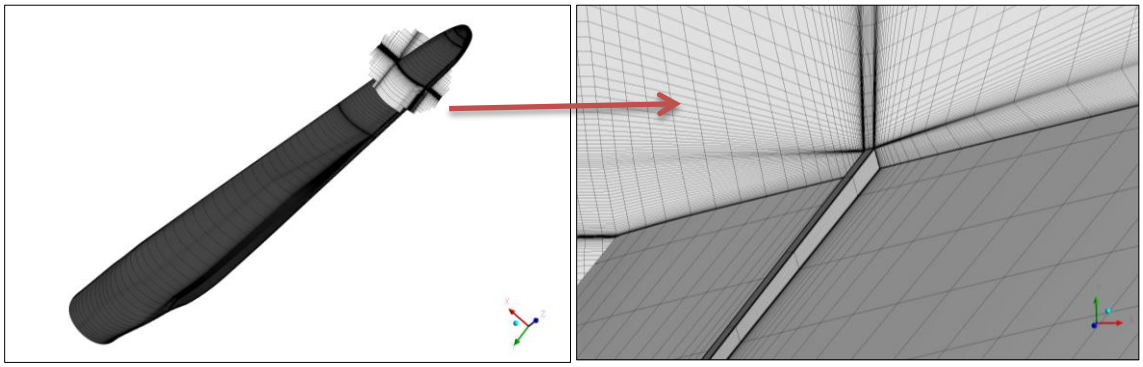

Figure 119. Mesh details of the NREL 5MW blade with 2% chord suction side microtab.

Power and thrust comparison

The suction side microtab is deployed for the aerodynamic brake system of the wind turbine as an active flow control device. Figure 120 shows the comparison of the power output of the blade before and after deploying the suction side microtab from 71% to 97% span range. It can be seen that similar as the 2D CFD results, in the 3D rotating frame of the whole wind turbine blade, the microtab can effectively decreasing the aerodynamic torque of the blade.

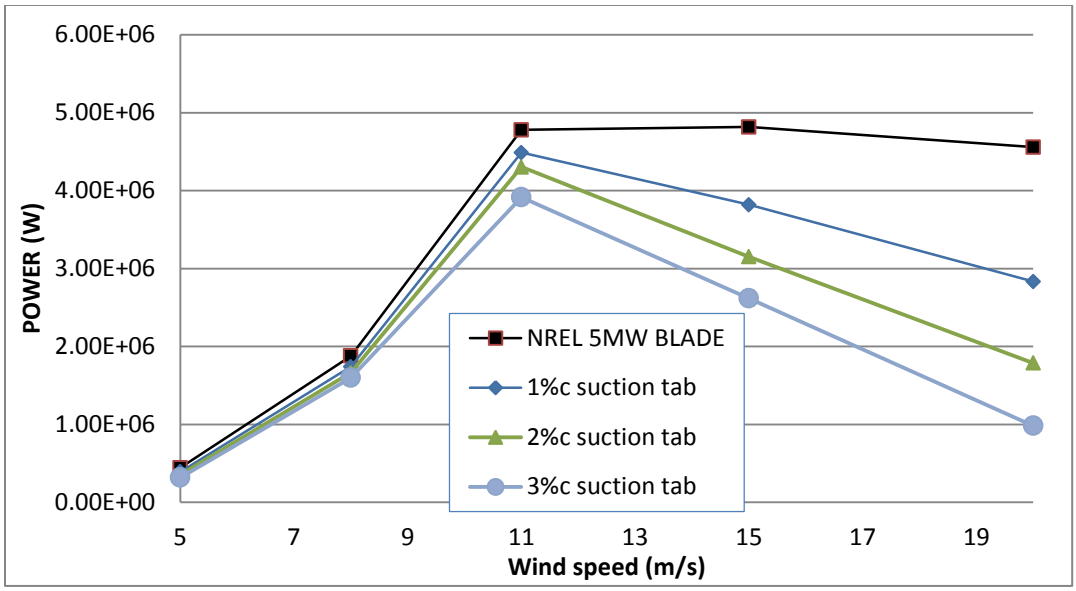

Figure 120. Power comparison between the NREL 5MW blade and that with 1% to 3% chord suction side microtabs.

From Figure 120 it can be seen that at lower wind speed range from 5m/s to 11m/s which is very close the rated wind speed of the blade, the suction side microtab decrease the generated power of the wind turbine gradually. The 3% chord suction side microtab decreases the power output of the wind turbine by 16.3% at 11m/s. The power dropping effect from the suction side microtab is becoming stronger and stronger when the wind speed exceeds the rated wind speed. Even the microtab with only 1% chord height can reduce the power output of the blade by 37.8% at 20m/s while the 3% chord microtab reduces it by 78.4%.

The thrust comparison between the original blade and the blade with suction side microtabs can be found in Figure 121, it can be seen that deploying suction side microtabs from 71% to 97% span near the trailing edge of the blade decreases the thrust which means lower flapwise bending moment. According to the power output and thrust comparisons, it can be concluded that deploying microtabs on the suction side near the trailing edge of the blade can be an effective method for large offshore HAWTs' aerodynamic brake system. The torque of the blade would be dropped rapidly with the suction side microtab at higher wind speeds.

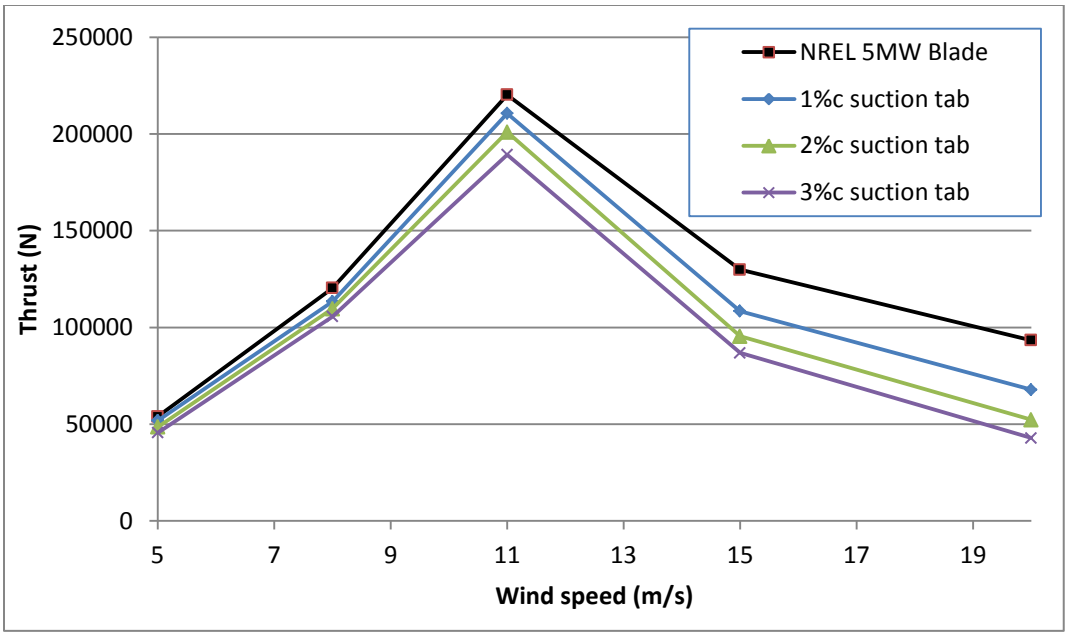

Figure 121. Thrust comparison between the NREL 5MW blade and that with 1% to 3% chord suction side microtabs.

Surface wall shear friction lines and sectional streamlines at r/R = 0.8

Figure 122, 123 and 124 show the blade surface contour along with the wall shear friction lines and a cut plane at r/R = 0.8 section to show the sectional streamlines and turbulence kinetic energy contour. The pressure contour value on the surface is set to be from -2500 to 1500 Pa with 30 levels of colors (blue to red) and the turbulence kinetic energy contour value is set to be from 0 to 50J/kg (Figure 122). From the figures it can be seen that the effects of the suction side microtabs become stronger when the wind speed increases. At 20m/s wind speed, the suction side microtabs change the entire aerodynamic performance of the sectional aerofoil. This is because with the changed camber and the minus angle of attack, this aerofoil section is no longer generating the driving lift force for wind turbine but an adverse force instead, which is actually driving the wind turbine back from its rotating direction.

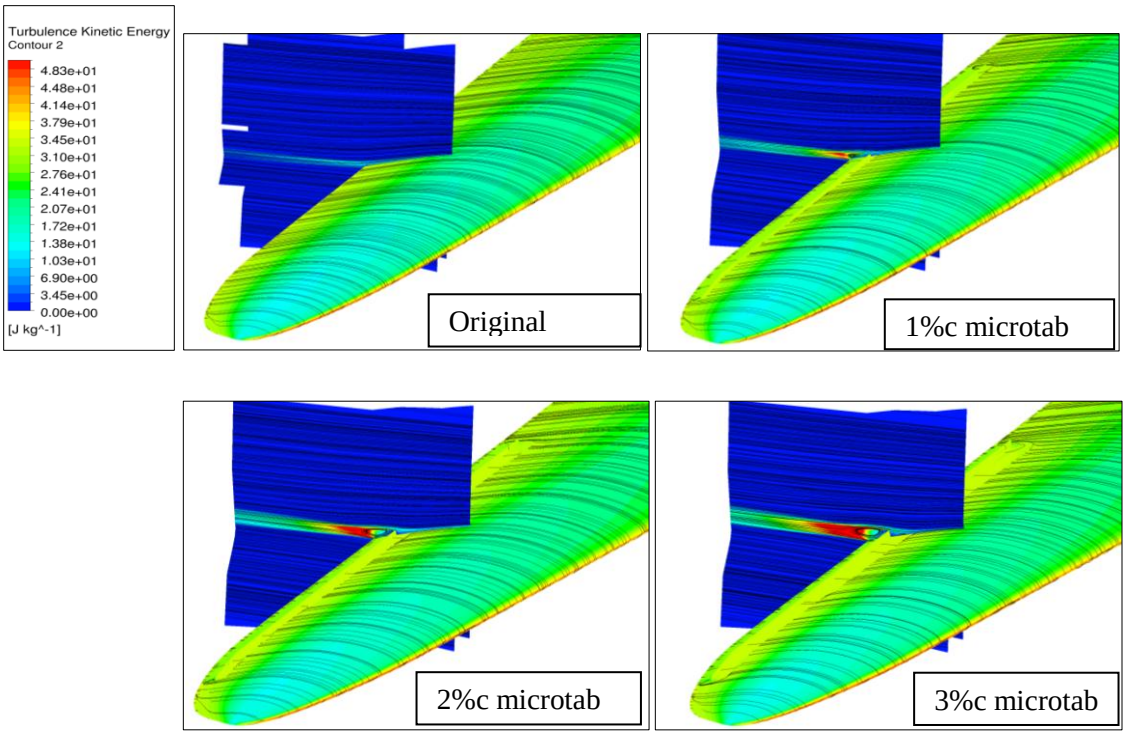

Figure 122. Surface pressure contour and wall shear friction lines plus cross-sectional turbulence kinetic energy contour and streamlines at r/R = 0.8 span, wind speed = 5m/s.

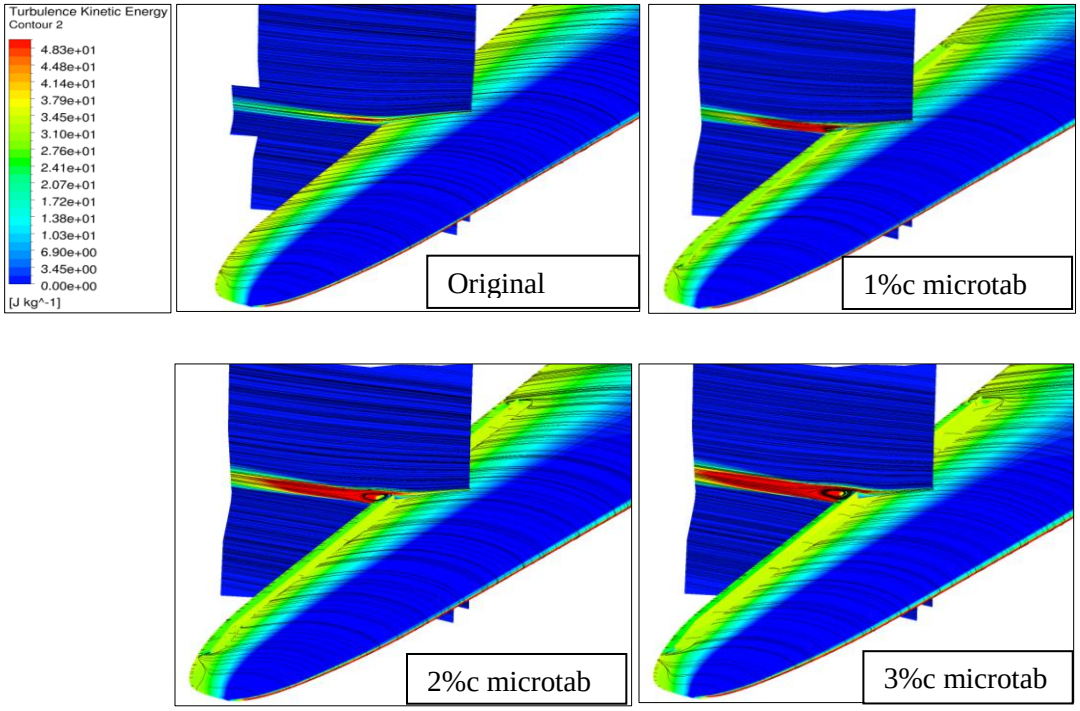

Figure 123. Surface pressure contour and wall shear friction lines plus cross-sectional turbulence kinetic energy contour and streamlines at r/R = 0.8 span, wind speed = 11m/s.

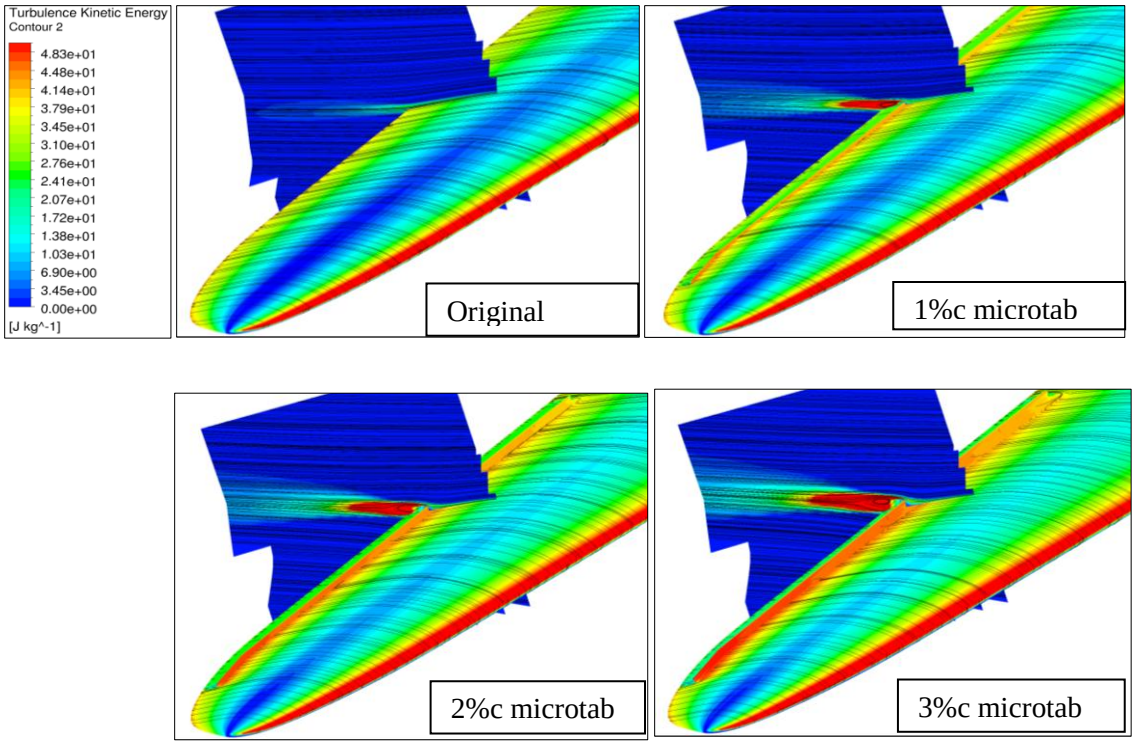

Figure 124. Surface pressure contour and wall shear friction lines plus cross-sectional turbulence kinetic energy contour and streamlines at r/R = 0.8 span, wind speed = 20m/s.

Pressure coefficient comparison at r/R = 0.8 span

The pressure coefficient comparison between the original NREL 5MW blade and that with different sizes of suction side microtabs at r/R = 0.8 span section is shown in Figure 125. It can be seen that compared to the 2D CFD results, the pressure coefficient from 3D results show some differences at the same r/R = 0.8 span section of the blade. The 2D CFD simulations seem to overestimate the aerodynamic performance of the sectional aerofoil when comparing the C_p with each other. Moreover, the effect from the suction side trailing edge microtab is quite similar for both 2D and 3D CFD results. Deploying suction side microtabs effectively drops down the differences of the C_p between the suction side and pressure side of the sectional aerofoil from 5m/s to 15m/s wind speed. For the 20m/s wind speed case, the suction side trailing edge microtabs change the entire pressure coefficient of the sectional aerofoil which switching the pressure side to be suction side. This condition would be enlarged when increasing the height of the suction side microtab.

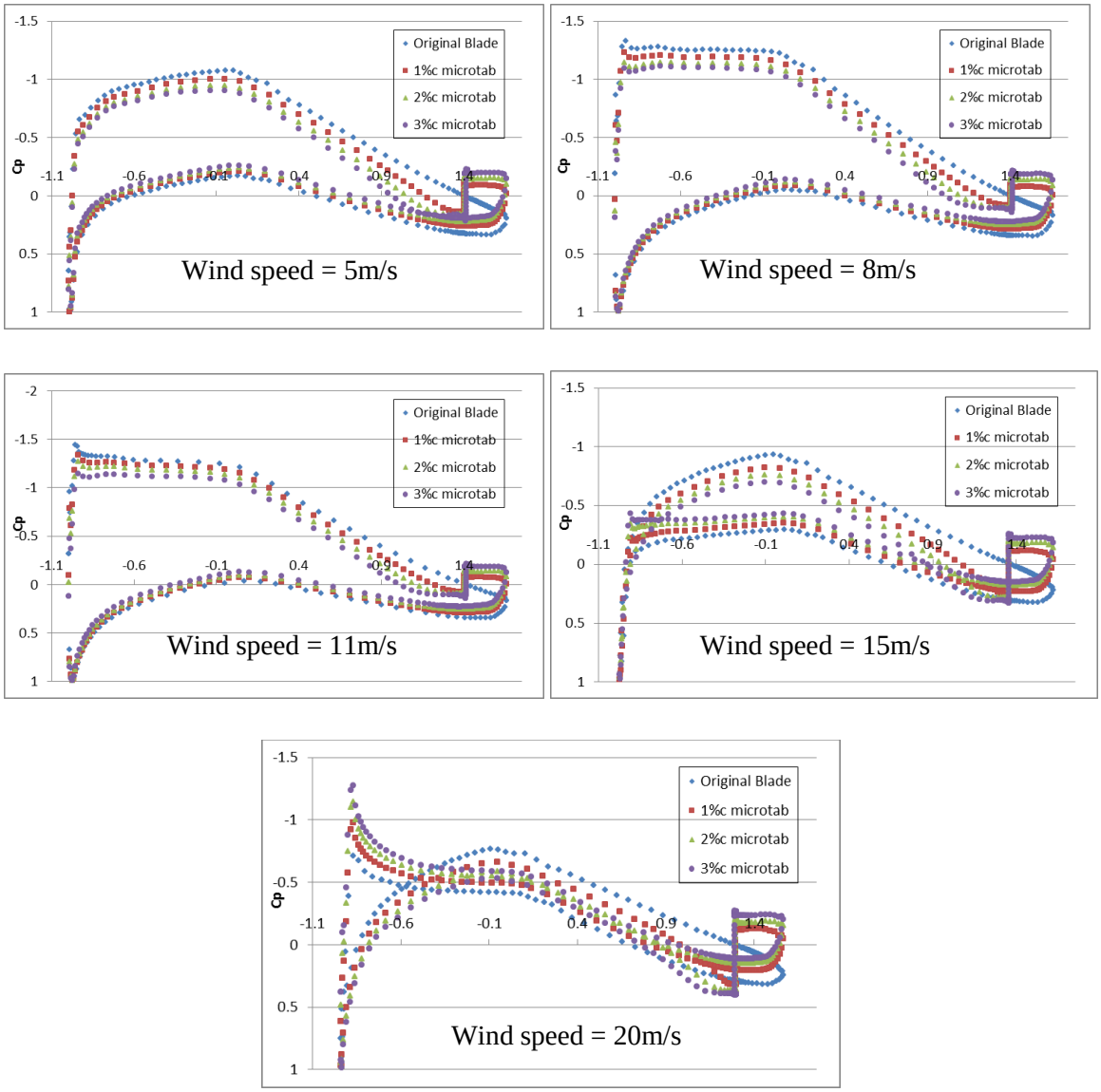

Figure 125. Comparison of pressure coefficient (C_p) between the original NREL 5MW blade and that with different sizes of suction side microtabs at r/R = 0.8 span section.

5.6 Chapter Conclusions

This chapter researches into the effects of three kinds of trailing edge flow control concepts (microtab, microjet and DTE) on a large off-shore NREL 5MW wind turbine. Because the lack of experimental data of this reference wind turbine so only code to code comparison is carried out

for validation. The problem is we cannot say which one is more accurate. The torque distribution study shows that the near r/R = 0.8 span area of the blade contributes the highest torque of the blade and therefore for this study the flow control devices and DTE are mainly deployed at this range.

The 2D CFD study on the NACA 64-618 and that with deploying 3% chord microtab, 3% chord DTE and 100m/s outlet speed microjet shows that all three kinds of trailing edge concepts increases the effective force at all wind speeds, which directly contributing to the final torque of the blade. Even at the rated wind speed 11m/s the flow control methods increase the force by around 21%.

However unlike the previous study on the small stall-regulated wind turbine, the 3D CFD results show large differences in power output predictions compared with the 2D results from 5m/s to 11m/s wind speed. Only the 100m/s outlet speed microjet shows a very small increase at 5m/s wind speed. All other cases from 5m/s to 11m/s show that the flow control devices and DTE are not able to improve the power output of the wind turbine or even damage its performance. However microtab and DTE work at higher wind speed 15m/s and 20m/s, which increase the power output of the blade by 11.2% to 62.4% than the original blade. The 100m/s speed microjet still slightly decrease the power output of the blade which is totally in contrast to the 2D simulation results, indicating the inaccuracy of the 2D predictions.

Referring to the previous study on the small stall-regulated wind turbine, a very interesting point is that the extent of trailing edge flow control concepts is highly relevant to the power coefficient C_p. From Betz's law the maximum C_p of the wind turbine is 0.593 and the C_p of NREL 5MW blade reaches 0.468 and 0.460 at 8m/s and 11m/s wind speeds respectively, which are higher than 75% of the maximum C_p. From the 3D CFD simulations it can be observed that the trailing edge flow control concept is hard to further improve the power output of the blade at the high C_p wind speed range (5m/s – 11m/s). At the higher wind speeds 15m/s and 20m/s where the C_p of the wind turbine is lower than 0.2, the flow control devices microtab and the DTE design show some obvious increase of the power output. In addition, from the results of the thrust it can be seen that microtab and DTE increase the thrust of the wind turbine while the microjet slightly decreases the thrust at all wind speeds.

Moreover, the concept of suction side microtabs is also carried out with full 3D CFD study for the aerodynamic brake system of the NREL 5MW wind turbine. The results show that deploying suction side microtabs on x/c = 0.9 chordwise position from 71% to 97% span can effectively

decrease the shaft torque and thrust of the wind turbine blade. The effect of suction side microtabs becomes stronger and stronger when the wind speed increases and the 3% chord microtab can lead to a 78.4% reduction of the turbine torque at 20m/s wind speed. Although both 2D and 3D CFD simulations predicted the same effect from deploying suction side microtab, the 2D results are unreliable due to 3D effects.

In conclusion, the main purpose of this part of study is to investigate the aerodynamic performance of two typical trailing edge flow control devices and the DTE on a real modern large off-shore wind turbine. The results of 2D sectional aerofoil and flow control concepts are not able to accurately predict the performance of the wind turbine in 3D rotating situation.

Chapter 6 Conclusions, Limitations and Potential Further Studies

6.1 Summary of the Study

The present study mainly investigates into the aerodynamics of modern HAWTs with flow control concepts using CFD method with the commercial software ANSYS ICEM CFD for meshing and ANSYS FLUENT as the solver. The validation case, which is very important in CFD study, selects the well documented experimental stall-regulated NREL Phase VI wind turbine which has extensive experimental results for comparison. The $k-\omega\ SST$ turbulence model and the Coupled scheme have been selected for all the simulations. Compared to the experimental data, the CFD results show that at lower wind speeds (5m/s – 10m/s) where the blade is not stalled, the steady flow simulations can predict the torque of the blade very accurately while at higher wind speeds (13m/s and 15m/s) the steady flow simulations are no longer valid and underpredicts the turbine torque because of the large separation flow on the suction side of the blade. Therefore some unsteady flow simulations are carried out for the 13m/s and 15m/s wind speed cases and results show that the torque of the blade is unstable at these wind speeds. The mean torques from the unsteady simulations are very close to the experimental data. Therefore for the following studies on NREL Phase VI wind turbine, steady flow simulations are carried out for 5m/s to 10m/s wind speeds and unsteady flow simulations are selected for 13m/s and 15m/s cases. The validation case is reasonable according to comparison of the pressure coefficient at different r/R span section and the wind turbine torque for this case. The surface friction lines show that the at higher wind speeds (13m/s and 15m/s), the flow on the suction side of the blade is mainly spanwise other than streamwise because of the stall.

Three different flow control concepts are studied for comparison using the validated CFD method, which are microtab, microjet and the divergent trailing edge (DTE), respectively. The DTE is selected for comparison because it is also proposed to improve the aerodynamic lift force of the aerofoil which is the same purpose of the pressure side microtabs and microjets. Because most of the previous studies on the flow control devices on wind turbine blade is in 2D condition or just a span section of the blade but not in the real 3D rotating frame, before simulating the flow control devices on the 3D rotating blade firstly the 2D CFD study on the sectional S809 aerofoil at r/R = 0.8 span of the NREL Phase VI blade is carried out. Here $F_{effective}$ is introduced because the 2D

aerofoil is for a wind turbine blade rather than an aircraft wing, focusing just on the lift drag ratio as in many previous literatures can be misleading. The effective force $F_{effective}$ is in the rotational direction of the blade, which drives the turbine blade around. The 2D CFD results show that all three kinds of flow control devices can effectively improve the effective force at lower wind speeds (5m/s to 10m/s) when there is no or just small separation on the suction side of the aerofoil. However at 13m/s and 15m/s cases, because of the large separation on the suction side of the aerofoil, all flow control concepts are not able to increase the effective force. At 7m/s wind speed when looking into the streamlines around the aerofoil, the 2% chord microtab and 3% chord DTE eliminate the small separation near the trailing edge on the suction side when compared to the original S809 aerofoil.

The 3D CFD study of these three flow control devices on the blade in the rotating frame show some corresponding results when compared to the 2D CFD results. The 60m/s outlet speed microjet has the largest improvement of the turbine torque from 5m/s to 10m/s wind speed. At the rated wind speed which is 10m/s of the wind turbine, deploying the 60m/s outlet speed microjet from 70% to 97% span increases the torque of the blade by 20.8% while the 2% chord microtab (same spanwise range) increases it by 19.2%. Because the microjet requires extra energy for blowing therefore the microtab is assumed to be the best flow control device for improving the turbine torque before stalling wind speed for the small stall-regulated wind turbine among the three. At higher wind speed where the blade is stalling, the spanwise flow is dominating on most area of the blade's suction side and at this situation the flow control devices are not able to further improve the aerodynamic performance of the blade but slightly decrease the turbine torque. From the figures of surface wall shear friction lines it can be seen that some of the flow control concepts can reduce the separation area on the suction side of the blade at 7m/s and 10m/s wind speeds. Then additional study on the height and spanwise range effects of the microtabs is carried out in both 2D and 3D simulations. The results show that the 2%c micro-tab deployed at 70%-97% spanwise range and 2.3%c deployed at 70%-97% span range have the best performance which can increase as high as 20% of the torque of the turbine at 10m/s wind speed.

With the development of the control system and manufacturing capacity, large offshore HAWTs with variable speed and pitch control are becoming more popular because of their large and stable power output. Therefore besides the experimental NREL Phase VI wind turbine, a typical variable speed and pitch control NREL 5MW reference wind turbine is selected for CFD investigation. Because there is no available experimental data for this large offshore wind turbine, only code to code comparison is carried out. The results show very close predictions of the power

output when compared to Sφrenson and Johansen's (2009) study. Moreover the torque distribution study on 11m/s wind speed is carried out and the 70% to 90% span part of the blade was found to contribute the highest torque.

Similar to the CFD study on the small stall-regulated wind turbine, both 2D and 3D CFD studies are carried out for the investigation on the flow control devices. However for the NREL 5MW wind turbine the 2D and 3D CFD results show some inconsistence of the power output and sectional pressure coefficient. The 2D CFD simulations seem to overpredict the sectional aerofoil performance than that from the 3D simulations in the rotating frame. At lower wind speeds from 5m/s to 11m/s (rated wind speed is 11.4m/s), the pressure microtab and DTE are not able to improve the power output of the wind turbine and only the 100m/s outlet speed microjet has very small improvement than the original wind turbine. However when the wind speed exceeds the rated wind speed (15m/s and 20m/s cases), the pressure side microtab and DTE can improve the power output of the wind turbine except for the microjet. Another interesting finding is that deploying the pressure side trailing edge microjet can reduce the thrust of the blade which can be considered as a concept for flapwise bending moment alleviation method for large HAWTs. The additional study on deploying suction side microtab for aerodynamic brake system of HAWTs is also carried out in 2D and 3D CFD simulations. Although there is also some inconsistences of the pressure coefficient between the 2D and 3D CFD results, but they all show that the suction side trailing edge microtab can reduce the power output of the wind turbine effectively at all wind speeds. Deploying an 3% chord height microtab at x/c = 0.9 position from 71% to 97% span can reduce the power output of the blade by 78.4% at 20m/s wind speed.

Overall, this study aims to provide detail information of the effects from some typical flow control concepts on HAWTs in 3D rotating frame using CFD method, which is missing from existing studies. From the results it can be seen that for the small stall-regulated wind turbine (NREL Phase VI), the CFD results of the 2D aerofoil overestimate the improvement from the flow control devices when compared to the 3D full-length blade simulation in the rotating frame, especially at 5m/s wind speed (Figure 42 and 51). Moreover, the blowing microjet with 60m/s outlet speed shows the largest improvement at non-stall wind speeds (5m/s – 10m/s) according to the 3D CFD results while the 3%c DTE shows the best performance in the 2D aerofoil study. For the large off-shore NREL 5MW wind turbine with variable speeds and pitch control, the 2D aerofoil results show even larger differences when compared to the 3D computational results (Figure 93 and 106). When the wind speed is lower than 11m/s, which is the designed rated wind speed for this wind turbine, none of the flow control devices can improve the power output of the

blade which is total in contrast with the 2D aerofoil predictions. However for 15m/s and 20m/s wind speeds, the 3D computational results show that the flow control devices can improve the power output of the wind turbine which is corresponding to the predictions from the 2D aerofoil CFD results. According to the Betz limit, the theoretical maximum coefficient for a HAWT is no greater than 0.593. From the present computational results from Figure 52 and 107, it can be seen that when the power coefficient is close to the Betz limit value, deploying the flow control devices on the pressure side near the trailing edge of the blade is very hard to improve the consequent shaft torque. The flow control devices are effective only when the power coefficient is low such as 0.25 which is shown in Figure 107, or are used for reducing the load of the wind turbine for aerodynamic braking purpose as shown in Figure 121.

6.2 Limitations and Suggestions for Further Study

The limitations and suggestions for further study are as follows:

1) The 3D CFD simulations ignore the hub of the HAWTs to save computing time. Although the effect of the hub is very small but it is still worth including the hub with the wind turbine blade for further study. Moreover, all simulations are just for one blade of the wind turbine using periodic boundary conditions because the flow conditions are assumed to be all the same for all three blades. Further study on the full wind turbine in wind shear with three (two) blades and the hub should be carried out and compare the results from the simulations on just one blade using periodic solutions.

2) There are many existing flow control concepts for HAWTs but in the present thesis only two typical concepts are selected for investigation (microtabs and microjets). Further study on other flow control devices such as plasma actuator, moving trailing edge, vortex generator and circulation control can be carried out in 3D rotating frame other than 2D or sectional studies. Some of these cases might require very large size of mesh because the geometry is quite complicated such as for vortex generators. From the NREL Phase VI cases it can be seen that large separation flows happens on the suction side of the blade at higher wind speeds. Therefore deploying leading edge microjets as an active flow control devices at higher wind speeds could be effective for separation control of the blade which might leading to power output improvement.

3) Although many studies have been carried out for the microtab effects on wind turbine with different sizes, this study does not look into the gap effect of the microtabs. The microtab is assumed to be integral in the present study because the mesh size would be quite large if using microtabs with gaps between each other. Further study could look into the gap effect of microtabs and compare the result with the integral microtab.

4) The studies on the NREL 5MW offshore wind turbine show that the pressure side trailing flow control concepts are not able to increase the power output which is inconsistent with the 2D CFD result predicted. The reason for this situation can be investigated more carefully for further study. Moreover, from the surface wall shear friction lines it can be seen that there is some separation flows on the NREL 5MW blade at lower span range (Figure 98). Therefore some further optimization work can be carried out to see whether deploying flow control devices on this area can improve the aerodynamic performance of the blade.

References

Andersen, P. B., Henriksen, L., Gaunaa, M., Bak, C., & Buhl, T. (2010). Deformable trailing edge flaps for modern megawatt wind turbine controllers using strain gauge sensors. *Wind Energy, 13*(2- 3), 193-206.

Anon (2013). The historical development of the wind turbine. *NTNU environmental studies: Wind power.*

Ansys Fluent user guide. Available at: http://users.ugent.be/~mvbelleg/flug-12-0.pdf

Bach, A. B., Lennie, M., Pechlivanoglou, G., Nayeri, C. N., & Paschereit, C. O. (2014). Finite microtab system for load control on a wind turbine. In *Journal of Physics: Conference Series* (Vol. 524, No. 1, p. 012082). IOP Publishing.

Bæk, P., & Gaunaa, M. (2011). Modelling the temporal response of a microtab in an aeroelastic model of a wind turbine. *49th AIAA Aerospace Sciences Meeting, 2011-348.*

Baker, J. P., Mayda, E. A., & Van Dam, C. P. (2006). Experimental analysis of thick blunt trailing-edge wind turbine airfoils. *Journal of Solar Energy Engineering*, *128*(4), 422-431.

Barlas, T. K., & Van Kuik, G. A. M. (2007, July). State of the art and prospectives of smart rotor control for wind turbines. In *Journal of Physics: Conference Series* (Vol. 75, No. 1, p. 012080). IOP Publishing.

Barlas, T. K., & Van Kuik, G. A. M. (2010). Review of state of the art in smart rotor control research for wind turbines. *Progress in Aerospace Sciences*, *46*(1), 1-27.

Barlas, T., & Lackner, M. (2008). Smart rotor blade technology applied to the Upwind reference turbine. In *Proceedings of the IEA topical expert meeting on the application of smart structures for large wind turbine rotor blades, Sandia National Labs, Alberquerque, USA.*

Bazilevs, Y., Hsu, M. C., Akkerman, I., Wright, S., Takizawa, K., Henicke, B. & Tezduyar, T. E. (2011). 3D simulation of wind turbine rotors at full scale. Part I: Geometry modeling and aerodynamics. *International Journal for Numerical Methods in Fluids*, *65*(1- 3), 207-235.

Beahan, J. J., Shih, C., Krothapalli, A., Kumar, R., & Chandrasekhara, M. S. (2014). Compressible dynamic stall control using high momentum microjets. *Experiments in Fluids*, *55*(9), 1-11.

Berg, D. E., Wilson, D. G., Resor, B. R., Barone, M. F., Berg, J. C., Kota, S., & Ervin, G. (2009). Active aerodynamic blade load control impacts on utility-scale wind turbines. In *Proc. of WindPower Conf. & Exhib.*

Betz, A. (1966). *Introduction to the theory of flow machines.* Pergamon Press, 99-109.

Blaylock, M., Chow, R., & Van Dam, C. P. (2010). Comparison of Microjets With Microtabs for Active Aerodynamic Load Control. *AIAA Paper*, 2010-*4409*.

Butterfield, S., Musial, W., & Scott, G. (2009). Definition of a 5-MW reference wind turbine for offshore system development. *Golden, CO: National Renewable Energy Laboratory*.

Carcangiu Carlo, E. (2008). CFD-RANS Study of Horizontal Axis Wind Turbines. *Supervisors: Mandas N. y Cambuli F. Thesis for the degree of Doctor of Philosophy, Universit├ á degli Studi di Cagliari Dipartimento di Ingegneria Meccanica Dottorato di Ricerca in Progettazione Meccanica XX Ciclo-Ing-Ind/09*.

Carlin, P. W., Laxson, A. S., & Muljadi, E. B. (2003). The history and state of the art of variable- speed wind turbine technology. *Wind Energy*, *6*(2), 129-159.

Chen, Z. J., & Przekwas, A. J. (2010). A coupled pressure-based computational method for incompressible/compressible flows. *Journal of Computational Physics*, *229*(24), 9150-9165.

Chow, R., & Dam, C. P. (2012). Verification of computational simulations of the NREL 5 MW rotor with a focus on inboard flow separation. *Wind Energy*, *15*(8), 967-981.

Chow, R., & Dam, C. V. (2006). Unsteady computational investigations of deploying load control microtabs. *Journal of Aircraft*, *43*(5), 1458-1469.

Cooney, J., Williams, T., & Corke, T. (2013). Increasing Wind Turbine Power Generation Through Optimized Flow Control Design. *Bulletin of the American Physical Society*, *58*.

Cooperman, A., Blaylock, M., & van Dam, C. P. (2014). Experimental and simulated control of lift using trailing edge devices. In *Journal of Physics: Conference Series* (Vol. 555, No. 1, p. 012019). IOP Publishing.

Elfarra, M. A., Sezer- Uzol, N., & Akmandor, I. S. (2014). NREL VI rotor blade: numerical investigation and winglet design and optimization using CFD. Wind Energy, 17(4), 605-626.

ELFARRA, M. A. (2011). *Horizontal Axis Wind Turbine Rotor Blade: Winglet and Twist Aerodynamic Design and Optimization Using CFD* (Doctoral dissertation, MIDDLE EAST TECHNICAL UNIVERSITY).

Esfahanian, V., Pour, A. S., Harsini, I., Haghani, A., Pasandeh, R., Shahbazi, A., & Ahmadi, G. (2013). Numerical analysis of flow field around NREL Phase II wind turbine by a hybrid CFD/BEM method. *Journal of Wind Engineering and Industrial Aerodynamics*, *120*, 29-36.

Esfahanian, V., Salavati Pour, A., Harsini, I., Haghani, A., Pasandeh, R., Shahbazi, A., & Ahmadi, G. (2013). Numerical analysis of flow field around NREL Phase II wind turbine by a hybrid CFD/BEM method. *Journal of Wind Engineering and Industrial Aerodynamics*, *120*, 29-36.

Gai, S. L., & Palfrey, R. (2003). Influence of trailing-edge flow control on airfoil performance. *Journal of Aircraft*, *40*(2), 332-337.

Geyler, M., & Caselitz, P. (2007). Individual blade pitch control design for load reduction on large wind turbines. In *European Wind Energy Conference (EWEC 2007), Milano, Italy, May* (pp. 7-10).

Global Wind Report 2014. Global Wind Energy Council (GWEC). Available at: http://www.gwec.net/

Godard, G., & Stanislas, M. (2006). Control of a decelerating boundary layer. Part 1: Optimization of passive vortex generators. *Aerospace Science and Technology*, *10*(3), 181-191.

Godard, G., & Stanislas, M. (2006). Control of a decelerating boundary layer. Part 3: Optimization of round jets vortex generators. *Aerospace science and technology*, *10*(6), 455-464.

Godard, G., Foucaut, J. M., & Stanislas, M. (2006). Control of a decelerating boundary layer. Part 2: Optimization of slotted jets vortex generators.*Aerospace science and technology*, *10*(5), 394-400.

Hand, M. M., & Balas, M. J. (2007). Blade load mitigation control design for a wind turbine operating in the path of vortices. *Wind Energy*, *10*(4), 339-355.

Hansen, A. D., & Hansen, L. H. (2007). Wind turbine concept market penetration over 10 years (1995–2004). *Wind energy*, *10*(1), 81-97.

Hansen, M. O. (2000). *Aerodynamics of wind turbines: rotors, loads and structure* (Vol. 17). Earthscan.28-30.

Hansen, M. O., & Aagaard Madsen, H. (2011). Review paper on wind turbine aerodynamics. *Transactions of the ASME-I-Journal of Fluids Engineering*, *133*(11), 114001.

Hardy, C. (2010). Renewable energy and role of Marykirk's James Blyth. *The courier. DC Thomson & Co. Ltd, Dundee (06/07/2013)*.

Henne, P. A., & GREGG, III, R. D. (1991). New airfoil design concept. *Journal of Aircraft*, *28*(5), 300-311

Herrero Barandica, A., & Solana Arocena, Í (2012). Experimental study of the performance of microtabs for load alleviation in wind turbines. *Master thesis, Erasmushogeschool Brussel.*

Holst, D., Bach, A. B., Nayeri, C. N., & Paschereit, C. O. (2013, June). Influence of a Finite Width Microtab on the Spanwise Lift Distribution. In *ASME Turbo Expo 2013: Turbine Technical Conference and Exposition* (pp. V008T44A011-V008T44A011). American Society of Mechanical Engineers.

Hsu, M. C., Akkerman, I., & Bazilevs, Y. (2014). Finite element simulation of wind turbine aerodynamics: validation study using NREL Phase VI experiment. *Wind Energy*, *17*(3), 461-481.

Huang, J. C., Lin, H., Hsieh, T. J., & Hsieh, T. Y. (2011). Parallel preconditioned WENO scheme for three-dimensional flow simulation of NREL Phase VI rotor. *Computers & Fluids*, *45*(1), 276-282.

Hurley, O. F., Chow, R., Blaylock, M. L., & Van Dam, C. C. P. (2016). Blade Element Momentum Based Study for Active and Passive Microjets Systems on the NREL 5-MW Turbine. In *34th Wind Energy Symposium* (p. 1263).

Jang, C. S., Ross, J. C., & Cummings, R. M. (1998). Numerical investigation of an airfoil with a Gurney flap. *Aircraft Design*, *1*(2), 75.

Johansen, J., Madsen, H. A., Gaunaa, M., Bak, C., & Sørensen, N. N. (2009). Design of a wind turbine rotor for maximum aerodynamic efficiency. *Wind Energy*, *12*(3), 261-273.

Johnson, S. J., Baker, J. P., Van Dam, C. P., & Berg, D. (2010). An overview of active load control techniques for wind turbines with an emphasis on microtabs. *Wind Energy*, *13*(2- 3), 239-253.

Jowit J. (2012). Windfarms axed as UK loses its taste for turbines. *The Guardian*, available at: http://www.guardian.co.uk/environment/

Koopmans, E., & Hoeijmakers, H. W. M. (2014). Experimental research on flow separation control using synthetic jet actuators. In: *29th Congress of International Council of Aeronautical Sciences*, ICAS 2014, 07-09-2014 - 12-09-2014, Bonn (pp. 1 - 17).

Launder, B. E., & Sharma, B. I. (1974). Application of the energy-dissipation model of turbulence to the calculation of flow near a spinning disc. *Letters in heat and mass transfer*, *1*(2), 131-137.

Li, Y., Paik, K. J., Xing, T., & Carrica, P. M. (2012). Dynamic overset CFD simulations of wind turbine aerodynamics. *Renewable Energy*, *37*(1), 285-298.

Liebeck, R. H. (1978). Design of subsonic airfoils for high lift. *Journal of aircraft*, *15*(9), 547-561.

Lin, J. C. (2002). Review of research on low-profile vortex generators to control boundary-layer separation. *Progress in Aerospace Sciences*, *38*(4), 389-420.

Lu, X., McElroy, M. B., & Kiviluoma, J. (2009). Global potential for wind-generated electricity. *Proceedings of the National Academy of Sciences*,*106*(27), 10933-10938.

Macquart, T., Maheri, A., & Busawon, K. (2014). Microtab dynamic modelling for wind turbine blade load rejection. *Renewable Energy*, *64*, 144-152

Mahu, R., Popescu, F., Frunzulică, F., &Dumitrache, A. (2011). 3D CFD Modeling and Simulation of NREL Phase VI Rotor. In *AIP Conference Proceedings* (Vol. 1389, p. 1520).

Maldonado, V., Farnsworth, J., Gressick, W., & Amitay, M. (2010). Active control of flow separation and structural vibrations of wind turbine blades. *Wind Energy*, *13*(2- 3), 221-237.

Maldonado, V., Farnsworth, J., Gressick, W., & Amitay, M. (2010). Active control of flow separation and structural vibrations of wind turbine blades. *Wind Energy*, *13*(2- 3), 221-237.

Martinez, j., Doerffer, p., Szulc, o., & Tejero, f. (2015). Aerodynamic analysis of wind turbine rotor blades. *Task Quarterly: Scientific Bulletin of Academic Computer Centre in Gdansk, 19*(2), 129-140.

Mayda, E. A., Van Dam, C. P., & Yen-Nakafuji, D. (2005). Computational investigation of finite width microtabs for aerodynamic load control. *AIAA paper*, *1185*, 2005.

McCoy, T., & Griffin, D. (2006, January). Active control of rotor aerodynamics and geometry: statues, methods, and preliminary results. In *44th AIAA Aerospace Science Meeting and Exhibit, 2006-605*.

Menter, F. R. (1994). Two-equation eddy-viscosity turbulence models for engineering applications. *AIAA journal*, *32*(8), 1598-1605.

Migliore, P. G., Miller, L. S., & Quandt, G. A. (1995). Wind turbine trailing edge aerodynamic brakes (No. NREL/TP--441-7805; CONF-950309--2). *National Renewable Energy Lab., Golden, CO (United States).*

Miller, S. L. (1996). Experimental investigation of aerodynamic devices for wind turbine rotational speed control: Phase II (No. NREL/TP--441-20507). *National Renewable Energy Lab., Golden, CO (United States).*

IPCC. (2011). Summary for Policymakers. In: *IPCC Special Report on Renewable Energy Sources and Climate Change Mitigation* [O. Edenhofer, R. Pichs- Madruga, Y. Sokona, K. Seyboth, P. Matschoss, S. Kadner, T. Zwickel, P. Eickemeier, G. Hansen, S. Schlömer, C. von Stechow (eds)], Cambridge University Press, Cambridge, United Kingdom and New York, NY, USA.

Mo, J. O., & Lee, Y. H. (2012). CFD Investigation on the aerodynamic characteristics of a small-sized wind turbine of NREL PHASE VI operating with a stall-regulated method. *Journal of Mechanical Science and Technology*, *26*(1), 81-92.

Nakafuji, D. Y., Van Dam, C. P., Smith, R. L., & Collins, S. D. (2001). Active load control for airfoils using microtabs. *Journal of Solar Energy Engineering*,*123*(4), 282-289.

Pape, A. L., &Lecanu, J. (2004). 3D Navier–Stokes computations of a stall- regulated wind turbine. *Wind Energy*, *7*(4), 309-324.

Potsdam, M. A., & Mavriplis, D. J. (2009). Unstructured mesh CFD aerodynamic analysis of the NREL Phase VI rotor. *AIAA paper*, *1221*, 2009.

Rajendran, C. (2011). Techniques for Enhancing Wind Energy Generation-A CFD Based Multibody Dynamics Approach in Horizontal Axis Wind Turbines. *(Doctoral dissertation, Cochin University of Science & Technology).*

Richter, K., & Rosemann, H. (2002). Experimental investigation of trailing-edge devices at transonic speeds. *Aeronautical Journal*, *106*(1058), 185-193.

Sagol, E., Reggio, M., & Ilinca, A. (2012). Assessment of two-equation turbulence models and validation of the performance characteristics of an experimental wind turbine by CFD. *ISRN Mechanical Engineering*, vol. *2012*.

Saravanan, P., Parammasivam, K. M., & Rajan, S. (2012). Pressure distribution of rotating small wind turbine blades with winglet using wind tunnel. *Journal of Scientific & Industrial Research*, *71*, 425-429.

Schreck, S., Hand, M., & Fingersh, L. J. (2001). NREL unsteady aerodynamics experiment in the NASA-Ames wind tunnel: a comparison of predictions to measurements. *Golden, CO, USA: National Renewable Energy Laboratory.*

Sezer-Uzol, N., & Long, L. N. (2006). 3-D time-accurate CFD simulations of wind turbine rotor flow fields. *AIAA paper*, *394*, 2006.

Shih, T. H., Liou, W. W., Shabbir, A., Yang, Z., & Zhu, J. (1995). A new k-ϵ eddy viscosity model for high Reynolds number turbulent flows. *Computers & Fluids*, *24*(3), 227-238.

Simms, D., Hand, M., Fingersh, L. J., Jager, D. W., & Cotrell, J. R. *Unsteady aerodynamics experiment phase v: Test configuration and available data campaigns*. *Technical report, National Renewable Energy Laboratories*, 1617 Cole Boulevard, Golden, Colorado, United States of America, 2001. NREL/TP-500-29491.

Sørensen, J. N. (2011). Aerodynamic aspects of wind energy conversion. *Annual Review of Fluid Mechanics*, *43*, 427-448.

Sorensen, J. N., & Shen, W. Z. (2002). Numerical modeling of wind turbine wakes. *Journal of Fluids Engineering*, *124*(2), 393-399.

Sørensen, N. N., Michelsen, J. A., &Schreck, S. (2002). Navier–Stokes predictions of the NREL Phase VI rotor in the NASA Ames 80 ft × 120 ft wind tunnel. *Wind Energy*, *5*(2- 3), 151-169.

Standish, K. J., & Van Dam, C. P. (2005). Computational Analysis of a Microtab- Based Aerodynamic Load Control System for Rotor Blades. *Journal of the American Helicopter Society*, *50*(3), 249-258.

Takizawa, K., Henicke, B., Tezduyar, T. E., Hsu, M. C., & Bazilevs, Y. (2011). Stabilized space–time computation of wind-turbine rotor aerodynamics. *Computational Mechanics*, *48*(3), 333-344.

Taylor, K., Leong, C. M., & Amitay, M. (2015). Load control on a dynamically pitching finite span wind turbine blade using synthetic jets. *Wind Energy*,*18*(10), 1759-1775.

Taylor, K., Leong, C., & Amitay, M. (2010). Performance Enhancement of a Wind Turbine Blade using Synthetic Jets. *Bulletin of the American Physical Society*, *55*.

Tongchitpakdee, C., Benjanirat, S., & Sankar, L. N. (2006). Numerical studies of the effects of active and passive circulation enhancement concepts on wind turbine performance. *Journal of Solar Energy Engineering*, *128*(4), 432-444.

Van Dam, C. P., Chow, R., Zayas, J. R., & Berg, D. E. (2007). Computational investigations of small deploying tabs and flaps for aerodynamic load control. In *Journal of Physics: Conference Series* (Vol. 75, No. 1, p. 012027). IOP Publishing

Van Dam, C. P., Yen, D. T., & HW Vijgen, P. M. (1999). Gurney flap experiments on airfoil and wings. *Journal of Aircraft*, *36*(2), 484-486.

Vesel, R. W., & McNamara, J. J. (2014). Performance enhancement and load reduction of a 5 MW wind turbine blade. *Renewable Energy*, *66*, 391-401.

Vronsky, T. (2000). High performance cost-effective large wind turbine blades using air-jet vortex generators. *Atomic Energy Research Establishment, Energy Technology Support Unit, New and Renewable Energy Programme.*

Wang, J. J., Li, Y. C., & Choi, K. S. (2008). Gurney flap—Lift enhancement, mechanisms and applications. Progress in *Aerospace Sciences*, *44*(1), 22-47.

Wind in power: 2012 European statistics. Available at: http://www.ewea.org/

Wright, A. D., Fingersh, L. J., & Stol, K. A. (2007, January). Designing and testing controls to mitigate tower dynamic loads in the controls advanced research turbine. In *45th AIAA Aerospace Sciences Meeting and Exhibit, Wind Energy Symposium, Reno, Nevada (USA)*.

Xudong, W., Shen, W. Z., Zhu, W. J., Sørensen, J. N., & Jin, C. (2009). Shape optimization of wind turbine blades. *Wind Energy*, *12*(8), 781-803.

Xue, S., Johnson, B., Chao, D., Sareen, A., & Westergaard, C. (2010, April). Advanced aerodynamic modeling of vortex generators for wind turbine applications. In *European Wind Energy Conference (EWEC), Warsaw Poland*.

Yen, D. T., Van Dam, C. P., Bräeuchle, F., Smith, R. L., & Collins, S. D. (2000). Active load control and lift enhancement using MEM translational tabs. *AIAA paper*, *2422*, 2000.

Zayas, J. R., van Dam, C. P., Chow, R., Baker, J. P., & Mayda, E. A. (2006, February). Active aerodynamic load control for wind turbine blades. In *European Wind Energy Conference*.

Appendix

1. Sectional aerofoil details of NREL Phase VI blade.

(Source from: http://www.nrel.gov/docs/fy02osti/29955.pdf)

Radial Distance r (m)	Span Station[1] (r/5.532 m)	Span Station[1] (r/5.029 m)	Chord Length (m)	Twist[2] (degrees)	Thickness (m)	Twist Axis (% chord)
0.0	0.0	0.0	Hub - center of rotation	Hub - center of rotation	Hub – center of rotation	Hub - center of rotation
0.508[3]	0.092	0.101	0.218 (root hub adapter)	0.0 (root hub adapter)	0.218	50 (root hub adapter)
0.660[4]	0.120	0.131	0.218[5]	0.0	0.218	50
0.883	0.160	0.176	0.183[5]	0.0	0.183	50
1.008	0.183	0.200	0.349[5]	6.7	0.163	35.9
1.067	0.193	0.212	0.441[5]	9.9	0.154	33.5
1.133	0.205	0.225	0.544[5]	13.4	0.154	31.9
1.257	0.227	0.250	0.737[5]	20.040	0.154	30
1.343	0.243	0.267	0.728	18.074	20.95% chord	30
1.510	0.273	0.300	0.711	14.292	20.95% chord	30
1.648	0.298	0.328	0.697	11.909	20.95% chord	30
1.952	0.353	0.388	0.666	7.979	20.95% chord	30
2.257	0.408	0.449	0.636	5.308	20.95% chord	30
2.343	0.424	0.466	0.627	4.715	20.95% chord	30
2.562	0.463	0.509	0.605	3.425	20.95% chord	30
2.867	0.518	0.570	0.574	2.083	20.95% chord	30
3.172	0.573	0.631	0.543	1.150	20.95% chord	30
3.185	0.576	0.633	0.542	1.115	20.95% chord	30
3.476	0.628	0.691	0.512	0.494	20.95% chord	30
3.781	0.683	0.752	0.482	-0.015	20.95% chord	30
4.023	0.727	0.800	0.457	-0.381	20.95% chord	30
4.086	0.739	0.812	0.451	-0.475	20.95% chord	30
4.391	0.794	0.873	0.420	-0.920	20.95% chord	30
4.696	0.849	0.934	0.389	-1.352	20.95% chord	30
4.780	0.864	0.950	0.381	-1.469	20.95% chord	30
5.000	0.904	0.994	0.358	-1.775	20.95% chord	30
5.305	0.959	1.055	0.328	-2.191	20.95% chord	30
5.532	1.000	1.100	0.305	-2.500	20.95% chord	30

2. Detailed results of the torque and C_p of the NREL Phase VI wind turbine with flow control devices.

Wind speed (m/s)	Original (n*m)	2%c tab (n*m)	60m/s jet(n*m)	3%c DTE (n*m)
5	315	330	358	334
7	796	877	1030	978
10	1448	1726	1750	1582
13	1221	1306	1065	1015
15	1174	913	896	889
	C_p	C_p	C_p	C_p
5	0.390641	0.409243	0.443967	0.414204
7	0.359736	0.396343	0.465488	0.441988
10	0.224464	0.267558	0.271279	0.245236
13	0.086152	0.092149	0.075145	0.071617
15	0.053923	0.041935	0.041154	0.040832

3. Torque comparison between original NREL Phase VI blade and the blade with different sizes of mocrotabs.

U (m/s)	Original (N*m)	1%c	1.5%c	2%c	2.3%c	2%c (75%-97%)	2%c (80%-97%)
5	315	318	324	330	332	321	325
7	809	833	860	877	886	881	873
10	1448	1401	1436	1726	1730	1695	1510
13	1221	1224	1080	1306	1228	1290	1318
15	1174	975	934	913	960	968	996

4. Aerofoil geometry definition of the NREL 5MW wind turbine (Jonkman et al., 2009).

Radius(m)	Twist Angle (deg.)	Chord (m)	Twist Centre(-)	Aerofoil
2.8667	0.000	3.542	0.5000	Cylinder
5.6000	0.000	3.854	0.4682	Cylinder
8.3333	0.000	4.167	0.4417	Cylinder
11.7500	13.308	4.557	0.4035	Adjusted DU 4050
15.8500	11.480	4.652	0.3750	Adjusted DU 35
19.9500	10.162	4.458	0.3750	Adjusted DU 35
24.0500	9.011	4.249	0.3750	DU 97-W-300 LM
28.1500	7.795	4.007	0.3750	DU 91-W2-250 LM
32.2500	6.544	3.748	0.3750	DU 91-W2-250 LM
36.3500	5.361	3.502	0.3750	DU 93-W-210 LM
40.4500	4.188	3.256	0.3750	DU 93-W-210 LM
44.5500	3.125	3.010	0.3750	NACA 64-618
48.6500	2.310	2.764	0.3750	NACA 64-618
52.7500	1.526	2.518	0.3750	NACA 64-618
56.1667	0.863	2.313	0.3750	NACA 64-618
58.9000	0.370	2.086	0.3750	NACA 64-618
61.6333	0.106	1.419	0.3750	NACA 64-618
62.9000	0.000	0.700	0.3750	NACA 64-618

5. Operational details of the NREL 5MW wind turbine (Jonkman, et al., 2009)

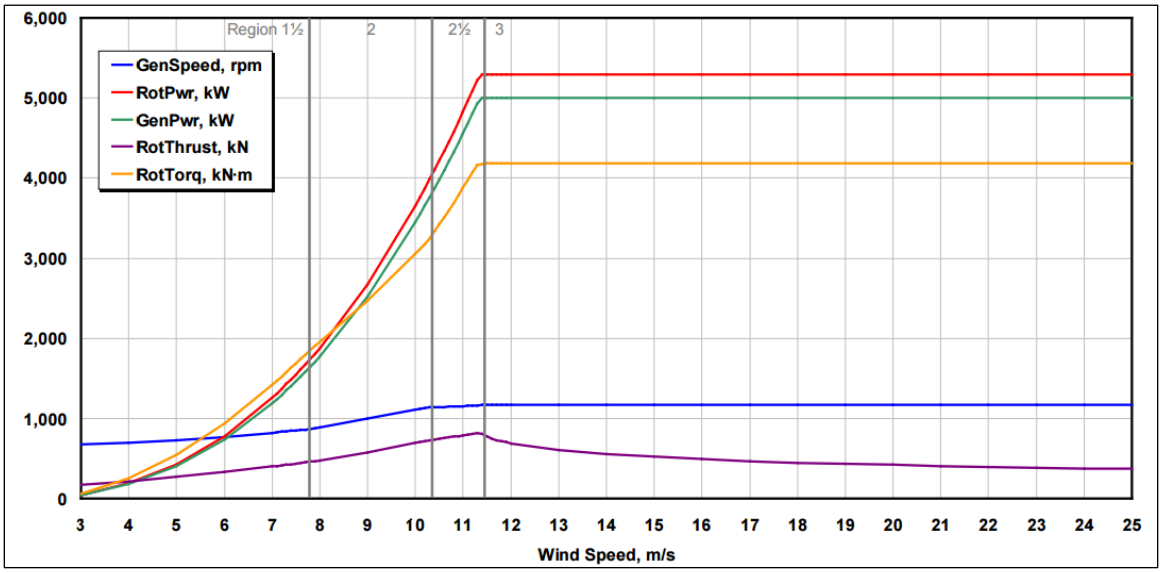

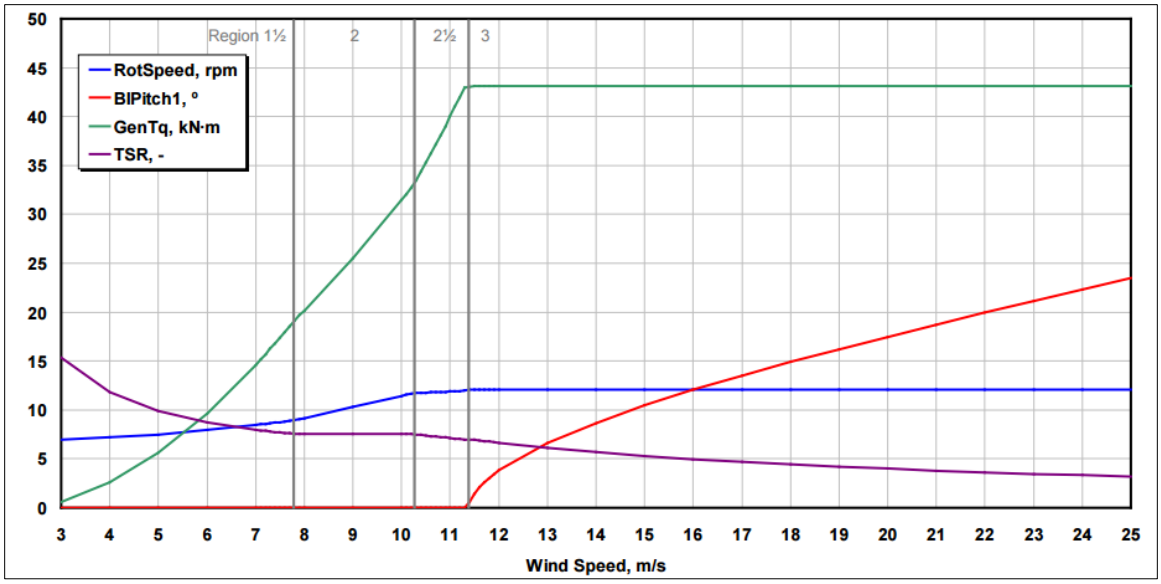

The RotSpeed represents the rotational speed (rpm) of the wind turbine; the RotPwr represents the mechanic power output of the wind turbine and it is calculated and compared in the present work (Chapter 5); BlPitch1, ^{0} represents the pitch angle (β) of the blade tip. The power output of the wind turbine is estimated by using the typical aerodynamic modeling software FAST, which is a BEM based code usually used for wind turbine rotor computations.